

# **A novel approach to Landau damping of transverse collective instabilities in future hadron colliders**

**Thèse N° 9298**

Présentée le 25 mars 2019

à la Faculté des sciences de base

Laboratoire de physique des accélérateurs de particules

Programme doctoral en physique

pour l'obtention du grade de Docteur ès Sciences

par

**Michael SCHENK**

Acceptée sur proposition du jury

Prof. F. Mila, président du jury

Prof. L. Rivkin, Dr K. S. B. Li, directeurs de thèse

Dr E. Shaposhnikova, rapporteuse

Prof. K. Oide, rapporteur

Prof. M. Q. Tran, rapporteur

2019



*Curiosity is one of the permanent and  
certain characteristics of a  
vigorous intellect.*

Samuel Johnson

To Ειρηνούλα and my family





# Acknowledgements

My doctoral studies have been a challenging and inspiring journey defined by an extraordinary professional and personal growth. With the following lines I would like to thank all the people who contributed to my achievements in one way or another.

First of all, I express my sincere gratitude to my thesis director, Prof. Lenny Rivkin, for the opportunity to carry out my research at the Laboratory for Particle Accelerator Physics at EPFL and for his support throughout the entire time. I would, furthermore, like to thank him for the possibility to gain more experience as a teaching assistant. I particularly enjoyed and learned a great deal from preparing and giving one of the lectures on accelerator physics at EPFL.

It is hard to imagine a better PhD advisor than Dr. Kevin Li and I cannot thank him enough for doing such an amazing job on the supervision of my project. Throughout, I always felt to get exactly the right amount of support from him without ever compromising my freedom to explore my own ideas. I was particularly impressed by and learned a lot from his ability to bring a clear structure into new results, breaking down complex processes, and being creative without losing view of the big picture. It was a true pleasure for me to work with him and an honour to be his first PhD student.

I would like to thank Prof. Frédéric Mila, Prof. Katsunobu Oide, Prof. Minh Quang Tran, and Dr. Elena Shaposhnikova for being the experts of my thesis committee and for their valuable feedback on my project.

A big thank you also goes to my group leader Gianluigi Arduini and section leader Dr. Elias Métral for their support of my doctoral studies and their interest in the project, for creating opportunities to travel to conferences and to attend schools.

I was very lucky to be able to rely on another great source of knowledge and wisdom at CERN – Dr. Giovanni Rumolo. I thank him for all the discussions and ideas that I got over the past years.

I express my gratitude to Dr. Alexej Grudiev for his proposal of the rf quadrupole for Landau damping which developed into such an exciting PhD project for me. His interest in the matter as well as his creative inputs were always inspiring and beneficial. I also thank Dr. Kai Papke for the pleasant collaboration when defining the requirements of the rf quadrupole cavity in terms of beam dynamics and rf design.

A big thank you goes to Antoine Maillard and Dr. Xavier Buffat for an extremely fruitful collaboration whose output was the analytical theory on beam stabilisation with nonlinear chromaticity. This work had a great impact on the understanding of the entire project. The publication on analytical studies of beam stabilisation with nonlinear chromaticity as well as an essential chapter of my thesis would not have been possible without their help.

## Acknowledgements

---

I would like to acknowledge Drs. Riccardo de Maria and Stéphane Fartoukh for their invaluable help in the design of a second-order chromaticity knob for the LHC. Their contribution made the LHC measurements possible. Furthermore, I thank Drs. Massimo Giovannozzi, Xavier Buffat, Roderik Bruce, Lee Carver, and the members of the Optics and Measurement Corrections team, in particular Drs. Rogelio Tomás, Ewen Maclean, and Lukáš Malina, as well as the LHC operator, machine protection and coordination crews for their support in the planning and execution of the measurements.

I am very grateful to Drs. Hannes Bartosik, Michele Carlà, and Verena Kain for their advice and their support during the machine studies with nonlinear chromaticity and amplitude detuning in the SPS. Furthermore, I thank Mario Beck for the excellent teamwork when planning and executing the measurements. I would also like to thank the SPS operators, in particular Stéphane Cettour-Cave, for the enjoyable work atmosphere and their help with the operation of the SPS.

Throughout my time at CERN I was able to profit from the broad knowledge and experience of many colleagues and friends across the HSC section, in particular from Drs. Giovanni Iadarola, Lotta Mether, Nicolas Mounet, Adrian Oeftiger, Benoit Salvant, and Carlo Zannini. Thank you all for your valuable contributions to my thesis and for enjoyable moments outside of work.

To the co-members of the office 6/R-006 aka. the CERN Bureau of Jokes: Drs. Lee Carver, Fabien Plassard, and Mr. Felix Carlier. I am very glad to have spent most of my time at CERN with you guys in a wonderful work atmosphere. Thanks for the professional discussions on countless subjects, for keeping the quality of our plots at a high level, for many memorable stories, and do not forget: there is always time for a *good joke*.

A huge, heartfelt thank you goes to my family and friends, especially my parents and brothers from whom I have received unconditional support throughout my entire life. Without them, none of what I have achieved would have been possible.

Δεν μπορώ να εκφράσω με λέξεις το πόσο ευγνώμων νιώθω για τον πιο σημαντικό άνθρωπο στη ζωή μου, αλλά παρόλα αυτά θα προσπαθήσω: Ειρήνη σε ευχαριστώ πολύ για αυτό που είσαι, για όλη την αγάπη σου και την ατελείωτη υποστήριξη σου. Με έχεις βοηθήσει τόσο πολύ όλο αυτόν τον καιρό σε όλα τα επίπεδα ...

Geneva, February 2019

Michael

# Abstract

Transverse collective instabilities induced by the beam-coupling impedance of the accelerator structure lead to beam quality degradation and pose a major limitation to the machine performance. Landau damping, a powerful stabilising mechanism that can be employed against various types of instabilities, is present in the transverse planes when there is a betatron frequency spread among the beam particles. Traditional approaches use octupole magnets to introduce betatron detuning with the transverse particle oscillation amplitudes. Their damping efficiency depends on the transverse geometric beam emittances which decrease with increasing beam energy and brightness. For the Future Circular Collider (FCC) they may hence no longer be the most suitable instability mitigation tool. Within the framework of this PhD thesis a novel approach to Landau damping is studied from the theoretical, numerical, and experimental points-of-view. The novelty of the method is to introduce the betatron frequency spread through detuning with the longitudinal instead of the transverse amplitudes. This is motivated by the fact that in typical high-energy proton machines the longitudinal emittance is several orders of magnitude larger compared to the transverse ones. Two equivalent detuning schemes are considered: a radio-frequency (rf) quadrupole cavity and nonlinear chromaticity.

The first achievement of the project is the development of the Vlasov theory for nonlinear chromaticity to provide the analytical foundation for the novel Landau damping technique. The formalism is validated successfully against the circulant matrix model and the PYHEADTAIL tracking code. Based on the new theory, two beam dynamics effects introduced by detuning with longitudinal amplitude are identified: Landau damping and a change of the effective impedance altering the head-tail instability formation mechanism. Second, the first numerical proof-of-concept of an rf quadrupole for Landau damping is realised in PYHEADTAIL. A two-family scheme for rf quadrupoles is also evaluated for FCC operational scenarios demonstrating an improved overall damping performance of the device. In particular, the required active magnetic length of the rf quadrupole is significantly shorter compared to octupole elements. Third, the numerical models and the theory are validated against measurements in the Large Hadron Collider (LHC) and the Super Proton Synchrotron (SPS) at CERN. In the two machines, the second-order chromaticity is successfully enhanced using a sextupole and an octupole scheme respectively and the measured nonlinear optics parameters are shown to be consistent with MAD-X calculations. The stabilisation of single bunches by means of a betatron frequency spread produced by nonlinear chromaticity is demonstrated in the LHC which marks the first experimental proof of the novel Landau damping method. The measurements are in good agreement with detailed PYHEADTAIL simulations. In particular, the two effects predicted by the theory are consistently observed in both experiments and simulations confirming a thorough understanding of the involved beam dynamics.

**Keywords:** particle accelerator physics, beam dynamics, collective effects, head-tail instability, Landau damping, nonlinear optics, Vlasov theory, particle tracking simulations, Future Circular Collider



# Kurzfassung

Transversale kollektive Instabilitäten in Teilchenbeschleunigern werden u.a. durch die Strahlkopplungsimpedanz der Beschleunigerstruktur verursacht. Sie vermindern die Strahlqualität und limitieren so die Luminosität eines Speicherrings. Die Landau-Dämpfung kann solche Instabilitäten verhindern indem eine Verteilung in den Betatronfrequenzen der Strahlteilchen eingeführt wird. Herkömmliche Methoden verwenden dazu Oktupolmagnete, die eine Verbreiterung der Frequenzverteilung als Funktion der transversalen Amplituden der Teilchenschwingungen erzeugen. Die Dämpfungseffizienz hängt von den transversalen geometrischen Strahlemittanzen ab, die mit zunehmender Strahlenergie und -brillanz abnehmen. Daher sind Oktupolmagnete für den Future Circular Collider (FCC) möglicherweise nicht das bevorzugte Mittel zur Strahlstabilisierung. Im Rahmen dieser Dissertation wird anhand von analytischen und numerischen Modellen, sowie Experimenten ein neuer Ansatz zur Landau-Dämpfung untersucht. Die Neuheit des Verfahrens besteht darin, die Betatronfrequenzverteilung als Funktion der longitudinalen anstelle der transversalen Amplitude zu generieren, was dank der massiv größeren longitudinalen Emittanz die Dämpfungseffizienz steigert. Zwei äquivalente Techniken werden analysiert: eine Hochfrequenz- (HF) Quadrupolkavität und die nichtlineare Chromatizität.

Der erste Meilenstein des Projekts ist die Erweiterung der Vlasov-Theorie um die Strahldynamik unter der Berücksichtigung der nichtlinearen Chromatizität zu beschreiben. Dies schafft die analytische Grundlage für diese neuartige Landau-Dämpfung. Der Formalismus wird durch das zirkulante Matrixmodell und mit PYHEADTAIL Simulationen erfolgreich validiert. Basierend darauf werden die zwei Strahldynamikeffekte untersucht, die die nichtlineare Chromatizität und ein HF-Quadrupol mit sich bringen: Landau-Dämpfung und eine Veränderung der effektiven Impedanz, die den Mechanismus zur Bildung von Head-Tail Instabilitäten beeinflusst. Zweitens wird ein erster numerischer Beweis für einen HF-Quadrupol für Landau-Dämpfung in PYHEADTAIL erbracht. Ausserdem wird eine zwei-Familien Konfiguration mit verbesserter Gesamtdämpfungsleistung für den FCC ausgewertet. Es wird gezeigt, dass die erforderliche magnetische Länge des HF-Quadrupols im Vergleich zu Oktupolelementen signifikant kürzer ist. Drittens werden die numerischen Modelle und die entwickelte Theorie mit Messungen im Large Hadron Collider (LHC) und im Super Proton Synchrotron (SPS) am CERN verglichen. In beiden Maschinen wird die Chromatizität zweiter Ordnung unter Verwendung eines Sextupol- bzw. Oktupolschemas erfolgreich erhöht. Die gemessenen Parameter der nichtlinearen Optik stimmen dabei gut mit MAD-X Modellberechnungen überein. Die Stabilisierung von einzelnen Strahlpaketen durch die von der nichtlinearen Chromatizität erzeugten Frequenzverteilung wird durch die LHC Messungen bestätigt und liefert den ersten experimentellen Nachweis der neuartigen Landau-Dämpfung. Das Experiment ist in guter Übereinstimmung mit PYHEADTAIL Simulationen. Insbesondere werden die beiden von der Theorie vorhergesagten Effekte im Experiment und im Simulationsmodell reproduziert.

**Stichwörter:** Teilchenbeschleuniger, Strahldynamik, kollektive Effekte, Head-Tail Instabilität, Landau-Dämpfung, nichtlineare Optik, Vlasov-Theorie, Teilchensimulationen, Future Circular Collider



# List of Publications

The work described in this thesis has been published in the following papers:

## *Peer-reviewed publications*

- M. Schenk, X. Buffat, K. Li, and A. Maillard, “Vlasov description of the effects of nonlinear chromaticity on transverse coherent beam instabilities”, *Phys. Rev. Accel. Beams* **21**, 084402 (2018).  
(Chapter 4).
- M. Schenk, X. Buffat, L. R. Carver, R. De Maria, K. Li, and E. Métral, “Experimental stabilization of transverse collective instabilities in the LHC with second order chromaticity”, *Phys. Rev. Accel. Beams* **21**, 084401 (2018).  
(Chapter 6).
- M. Schenk, A. Grudiev, K. Li, and K. Papke, “Analysis of transverse beam stabilization with radio frequency quadrupoles”, *Phys. Rev. Accel. Beams* **20**, 104402 (2017).  
(Chapters 3 & 5).

## *Conference proceedings and internal notes*

- M. Schenk, X. Buffat, L. R. Carver, K. Li, and E. Métral, “Experiments and Theory on Beam Stabilization with Second-Order Chromaticity”, in *Proc. of ICFA Advanced Beam Dynamics Workshop on High-Intensity and High-Brightness Hadron Beams 2018 (HB’18)*, Daejeon, Korea, (June 2018), pp. 32–37.
- M. Schenk, S. Fartoukh, K. Li, L. Malina, E. Métral, and R. Tomás, *MD2190: Q” Stabilization during injection*, tech. rep. ACC-NOTE-2018-0003 (CERN, Geneva, Switzerland, Jan. 2018).
- M. Schenk, D. Amorim, N. Biancacci, X. Buffat, L. R. Carver, R. De Maria, K. Li, E. Métral, and B. Salvant, “Practical stabilisation of transverse collective instabilities with second order chromaticity in the LHC”, in *Proc. of International Particle Accelerator Conference 2017 (IPAC’17)*, Copenhagen, Denmark (May 2017), pp. 4477–4480.
- M. Schenk, X. Buffat, L. R. Carver, A. Grudiev, K. Li, A. Maillard, E. Métral, and K. Papke, “RF quadrupole structures for transverse Landau damping in circular accelerators”, in *Proc. of International Particle Accelerator Conference 2017 (IPAC’17)*, Copenhagen, Denmark (May 2017), pp. 2516–2519.

## List of Publications

---

- L. R. Carver, M. Schenk, R. De Maria et al., *MD1831: Single Bunch Instabilities with  $Q$  and Non-Linear Corrections*, tech. rep. ACC-NOTE-2017-0012 (CERN, Geneva, Switzerland, Feb. 2017).
- M. Schenk, A. Grudiev, K. Li, and K. Papke, “Use of RF Quadrupole Structures to Enhance Stability in Accelerator Rings”, in Proc. of ICFA Advanced Beam Dynamics Workshop on High-Intensity and High-Brightness Hadron Beams 2016 (HB’16), Malmö, Sweden (Aug. 2016), pp. 505–510.
- H. Bartosik, A. Oeftiger, M. Schenk, F. Schmidt, and M. Titze, “Improved Method for the Measurement and Simulation of the CERN SPS Non-linear Optics”, in Proc. of International Particle Accelerator Conference 2016 (IPAC’16), Busan, Korea (May 2016), pp. 3464–3467.
- A. Grudiev, K. Li and M. Schenk, “Radio Frequency Quadrupole for Landau Damping in Accelerators: Analytical and Numerical Studies”, in Proc. of ICFA Advanced Beam Dynamics Workshop on High-Intensity and High-Brightness Hadron Beams 2014 (HB’14), East Lansing (Michigan), USA (Apr. 2014), pp. 315–319.

Selection of additional publications that are not part of the work covered in this thesis:

- L. R. Carver, X. Buffat, K. Li, E. Métral, and M. Schenk, “Transverse beam instabilities in the presence of linear coupling in the Large Hadron Collider”, *Phys. Rev. Accel. Beams* **21**, 044401 (2018).
- B. Yee Rendon, Y. H. Chin, H. Kuboki, M. Schenk, T. Toyama, “Updated model of the resistive wall impedance for the main ring of J-PARC”, in Proc. of International Particle Accelerator Conference 2018 (IPAC’18), Vancouver (British Columbia), Canada (Apr. 2018), pp. 3204–3206.
- G. Rumolo, H. Bartosik, E. Belli, P. Dijkstal, G. Iadarola, K. Li, L. Methner, A. Romano, M. Schenk, and F. Zimmermann, “Electron cloud effects at the LHC and LHC injectors”, in Proc. of International Particle Accelerator Conference 2017 (IPAC’17), Copenhagen, Denmark (May 2017), pp. 30–36.
- H. Bartosik, B. Goddard, G. Iadarola, G. Kotzian, K. Li, L. Methner, G. Rumolo, E. Shaposhnikova, M. Schenk, and M. Taborelli, “Detailed Studies of Beam Induced Scrubbing in the CERN-SPS”, in Proc. of International Particle Accelerator Conference 2015 (IPAC’15), Newport News (Virginia), USA (Apr. 2015), pp. 3908–3910.



# Contents

<b>Acknowledgements</b>	<b>v</b>
<b>Abstract</b>	<b>vii</b>
<b>Kurzfassung</b>	<b>ix</b>
<b>List of Publications</b>	<b>xi</b>
<b>List of Figures</b>	<b>xvii</b>
<b>List of Tables</b>	<b>xxi</b>
<b>List of Symbols</b>	<b>xxiii</b>
<b>1 Introduction</b>	<b>1</b>
1.1 The CERN accelerator complex and future hadron colliders . . . . .	2
1.2 A novel approach to Landau damping . . . . .	5
1.3 Project objectives and outline . . . . .	8
<b>2 Basics of accelerator beam dynamics</b>	<b>11</b>
2.1 Single-particle dynamics . . . . .	12
2.1.1 Transverse motion . . . . .	13
2.1.2 Longitudinal motion . . . . .	20
2.2 Transverse impedance-driven single-bunch instabilities . . . . .	23
2.2.1 Wakefields and impedances . . . . .	24
2.2.2 Head-tail instabilities . . . . .	26
2.2.3 Vlasov formalism . . . . .	29
2.2.4 Circulant matrix model . . . . .	31
2.2.5 Landau damping . . . . .	33
2.3 Numerical models and computer codes . . . . .	38
2.3.1 PYHEADTAIL . . . . .	38
2.3.2 BIMBIM . . . . .	40
<b>3 Betatron detuning with longitudinal amplitude</b>	<b>41</b>
3.1 Radio-frequency quadrupole . . . . .	41
3.1.1 Description . . . . .	42
3.1.2 Working principle . . . . .	43
3.1.3 Main features . . . . .	46
	xiii

## Contents

---

3.2	Nonlinear chromaticity . . . . .	49
3.3	Existing stability diagram theory . . . . .	51
3.4	Conclusions . . . . .	52
<b>4</b>	<b>Theoretical studies: Vlasov formalism with nonlinear chromaticity</b>	<b>55</b>
4.1	Extended Vlasov equation . . . . .	55
4.2	Specific solutions . . . . .	58
4.2.1	Airbag model . . . . .	59
4.2.2	Arbitrary longitudinal distributions . . . . .	60
4.3	Benchmarks against numerical models . . . . .	61
4.3.1	Airbag model . . . . .	61
4.3.2	Gaussian beam . . . . .	64
4.4	Conclusions . . . . .	69
<b>5</b>	<b>Numerical studies: beam stabilisation with an rf quadrupole</b>	<b>71</b>
5.1	Rf quadrupole models in PYHEADTAIL . . . . .	71
5.2	Proof-of-concept . . . . .	73
5.2.1	Stabilisation through Landau octupoles . . . . .	73
5.2.2	Stabilisation through rf quadrupoles . . . . .	76
5.3	Advanced rf quadrupole schemes . . . . .	78
5.3.1	Two-family configuration . . . . .	80
5.3.2	Synergy with magnetic octupoles . . . . .	81
5.4	Rf quadrupole system for FCC-hh . . . . .	83
5.4.1	Simulation setup . . . . .	83
5.4.2	Rf quadrupole requirements . . . . .	84
5.5	Potential limitations . . . . .	85
5.5.1	Synchro-betatron resonances . . . . .	86
5.5.2	Feed-down . . . . .	90
5.5.3	Dynamic aperture . . . . .	91
5.6	Conclusions and outlook . . . . .	92
<b>6</b>	<b>Experimental studies: second-order chromaticity in the LHC</b>	<b>95</b>
6.1	Second-order chromaticity in the LHC . . . . .	95
6.1.1	Production scheme and side effects . . . . .	96
6.1.2	Measurement method . . . . .	98
6.2	Single-bunch stability at collision energy . . . . .	99
6.2.1	Without second-order chromaticity . . . . .	99
6.2.2	With second-order chromaticity . . . . .	103
6.2.3	PYHEADTAIL simulations and interpretation . . . . .	105
6.3	Conclusions . . . . .	108
<b>7</b>	<b>Experimental studies: second-order chromaticity in the SPS</b>	<b>111</b>
7.1	Design of a second-order chromaticity knob . . . . .	112
7.1.1	Basic considerations . . . . .	112
7.1.2	MAD-X/PTC predictions . . . . .	114
7.2	SPS nonlinear optics measurements . . . . .	114
7.2.1	Detuning with transverse amplitude . . . . .	115

7.2.2 Nonlinear chromaticity . . . . .	119
7.3 Beam stability studies . . . . .	121
7.3.1 Measurements in 2017 . . . . .	123
7.3.2 Measurements in 2018 . . . . .	131
7.4 Conclusions . . . . .	135
<b>8 Conclusions</b>	<b>137</b>
<b>A Vlasov theory on nonlinear chromaticity</b>	<b>143</b>
A.1 Solution for an airbag beam with linear chromaticity . . . . .	143
A.2 Equivalence of dispersion relation to existing theory . . . . .	144
<b>Bibliography</b>	<b>154</b>
<b>Acronyms</b>	<b>155</b>
<b>Curriculum Vitae</b>	<b>157</b>



# List of Figures

1.1	The CERN accelerator complex. . . . .	3
2.1	Frenet-Serret coordinate system. . . . .	12
2.2	Courant-Snyder ellipse. . . . .	16
2.3	Phase stability. . . . .	23
2.4	Circulant matrix model. . . . .	32
2.5	Stability boundary diagram theory for Landau damping. . . . .	36
3.1	Illustration of the transverse kicks in an elliptical and a four-vane quadrupole cavity. . . .	42
3.2	Electromagnetic field distributions in the elliptical and the four-vane rf quadrupole. . . .	43
3.3	Illustration of the betatron detuning introduced by an rf quadrupole . . . . .	45
3.4	Betatron tune distributions introduced by magnetic octupoles and by an rf quadrupole. .	47
3.5	Dependence of the rms tune spread on the beam energy for magnetic octupoles and an rf quadrupole. . . . .	48
3.6	Incoherent betatron tune distributions and normalised stability diagrams for detuning with longitudinal amplitude. . . . .	52
4.1	Airbag beam model in longitudinal phase space. . . . .	59
4.2	Coherent frequency shifts vs. linear chromaticity for an airbag beam obtained with BIM-BIM, PYHEADTAIL, and analytical formula. . . . .	62
4.3	Coherent frequency shifts vs. second-order chromaticity for an airbag beam obtained with BIMBIM, PYHEADTAIL, and analytical formula. . . . .	63
4.4	Comparison of betatron frequency distributions from PYHEADTAIL and analytical formula. .	65
4.5	Coherent frequency shift vs. first-order chromaticity for a narrow-band resonator obtained with PYHEADTAIL and analytical formula. . . . .	66
4.6	Dependence of the imaginary coherent frequency shift for a head-tail mode zero induced by a narrow-band resonator, as obtained with PYHEADTAIL and analytical calculations. .	67
4.7	Stability boundary diagrams as a function of second-order chromaticity with isolines on imaginary frequency shift. . . . .	68
4.8	Imaginary frequency shifts as a function of second-order chromaticity as obtained with PYHEADTAIL and stability diagram theory. . . . .	68
5.1	Incoherent betatron tune distributions for the detuning and the localised kick models of the rf quadrupole in PYHEADTAIL. . . . .	72

## List of Figures

---

5.2	PYHEADTAIL simulations of the horizontal bunch centroid evolution, frequency spectra, and the head-tail mode pattern of the LHC instability at 3.5 TeV. . . . .	74
5.3	PYHEADTAIL results of the LHC head-tail mode as a function of Landau octupole current. . . . .	75
5.4	Stability boundary diagrams for LHC Landau octupoles compared to PYHEADTAIL and BIMBIM simulations. . . . .	75
5.5	PYHEADTAIL results of the LHC head-tail mode as a function of rf quadrupole strength. . . . .	77
5.6	Approximate stability boundary diagram for an rf quadrupole compared with BIMBIM and PYHEADTAIL. . . . .	78
5.7	PYHEADTAIL simulations of the stabilising efficiency of an rf quadrupole for two operational modes. . . . .	80
5.8	Illustration of the asymmetry in the stabilising efficiency of an rf quadrupole for the two transverse planes. . . . .	80
5.9	Stabilising efficiency of an rf quadrupole in a two-family configuration. . . . .	81
5.10	HL-LHC study case demonstrating the stabilising efficiency of an rf quadrupole in combination with Landau octupoles. . . . .	82
5.11	Example of transverse instability growth rates vs. rf quadrupole strength for FCC-hh. . . . .	84
5.12	Stabilisation of the SPS head-tail mode at injection energy using a single rf quadrupole. . . . .	87
5.13	Follow-up study of the incoherent regime discovered in SPS simulations with the rf quadrupole. . . . .	88
5.14	Diffusion map in $Q_s$ vs. $Q_x$ space with a single rf quadrupole in the SPS. . . . .	89
5.15	Diffusion map in $Q_s$ vs. $Q_x$ space with a single rf quadrupole in the HL-LHC. . . . .	90
5.16	Illustration of the local closed orbit distortion from rf quadrupole feed-down. . . . .	91
6.1	MAD-X/PTC calculation of second-order chromaticity as a function of the LHC sextupole knobs. . . . .	97
6.2	MAD-X/PTC calculation of transverse amplitude detuning introduced by the LHC sextupole knobs. . . . .	97
6.3	Measured variation of the relative momentum deviation and corresponding base-band tune metre data. . . . .	100
6.4	Head-tail mode patterns from LHC measurements and PYHEADTAIL simulations for a single bunch at collision energy. . . . .	101
6.5	PYHEADTAIL simulations of single-bunch stabilisation in the LHC using Landau octupoles. . . . .	102
6.6	Horizontal bunch centroid signals as obtained with PYHEADTAIL for four different Landau octupole currents in the LHC. . . . .	103
6.7	Comparison of the two head-tail modes observed in the machine and in PYHEADTAIL simulations. . . . .	105
6.8	PYHEADTAIL studies with and without detuning with transverse amplitude showing the predicted head-tail instabilities as a function of the LHC sextupole knobs. . . . .	106
7.1	Dispersion function along the full circumference of the SPS ring in Q20 optics. . . . .	113
7.2	Horizontal beta and dispersion functions in Q20 optics for the first sector in the SPS. . . . .	113
7.3	Predictions from SPS MAD-X/PTC model on octupole strengths for the second-order chromaticity knob. . . . .	115
7.4	Measurement of horizontal amplitude detuning for the SPS LOF family. . . . .	117
7.5	Measurement of horizontal amplitude detuning for the SPS LOD family. . . . .	117
7.6	Measurement of horizontal amplitude detuning for the SPS LOEs. . . . .	117

7.7 Compensation of horizontal amplitude detuning using the SPS second-order chromaticity knob. . . . .	118
7.8 SPS measurement of nonlinear chromaticity for the bare machine with Q20 optics. . . . .	120
7.9 Contribution to nonlinear chromaticity from the LOF family. . . . .	121
7.10 Contribution to nonlinear chromaticity from the LOD family. . . . .	122
7.11 Contribution to nonlinear chromaticity from the LOEs. . . . .	122
7.12 Measurements vs. PYHEADTAIL simulations of the instability growth rate of a head-tail mode zero in the SPS as a function of first-order chromaticity. . . . .	123
7.13 Measurements vs. PYHEADTAIL simulations of the head-tail mode zero instability growth rates as a function of first-order chromaticity using various simulation scenarios. . . . .	124
7.14 Overview of the beam stability study with the second-order chromaticity knob. . . . .	126
7.15 Summary plots of the beam stability study with the second-order chromaticity knob. . . . .	127
7.16 PYHEADTAIL simulations of the effect of a second-order chromaticity knob on the instability growth rates with and without chromatic feed-down. . . . .	129
7.17 Example measurement of the horizontal closed orbit in the SPS. . . . .	130
7.18 Overview of chromaticity feed-down calculated with MAD-X/PTC from SPS orbit data acquired during the scan with the second-order chromaticity knob. . . . .	131
7.19 Overview of the dedicated feed-down study with the second-order chromaticity knob. . . . .	132
7.20 Summary plots showing the measured $Q'_x$ and $Q''_x$ as a function of the second-order chromaticity knob. . . . .	133
7.21 Dependence of first-order chromaticity on the main sextupole knob QPH in the SPS. . . . .	134
7.22 Dependence of second-order chromaticity on the main sextupole knob QPH employed to control $Q'_x$ in the SPS. . . . .	135





# List of Tables

1.1	Main beam parameters of the LHC, HL-LHC, HE-LHC, and FCC-hh at collision energy. . . . .	5
4.1	Main PYHEADTAIL and BIMBIM parameters used to benchmark the Vlasov formalism for an airbag beam. . . . .	62
4.2	Main PYHEADTAIL and BIMBIM parameters used to benchmark the Vlasov formalism for a Gaussian beam. . . . .	65
5.1	PYHEADTAIL and BIMBIM parameters used to reproduce the LHC experiment at 3.5 TeV. . . . .	74
5.2	PYHEADTAIL simulation parameters used to study the combination of rf quadrupoles and magnetic octupoles. . . . .	82
5.3	PYHEADTAIL simulation parameters used to evaluate the requirements for an rf quadrupole system for FCC-hh. . . . .	84
5.4	Summary of required rf quadrupole strengths for stable single-bunch operation for various scenarios in FCC-hh. . . . .	85
5.5	PYHEADTAIL simulation parameters used to evaluate a potential rf quadrupole prototype test in the SPS. . . . .	87
6.1	Definition of LHC sextupole powering schemes to introduce second-order chromaticity. . . . .	98
6.2	Main PYHEADTAIL parameters used to reproduce the LHC experiment at 6.5 TeV. . . . .	101
6.3	MAD-X/PTC calculations vs. measurements of second-order chromaticity introduced by the Landau octupoles. . . . .	101
6.4	MAD-X/PTC calculations vs. measurements of second-order chromaticity for both LHC beams at zero Landau octupole current. . . . .	102
6.5	Parameters of the four individual bunches during the second-order chromaticity measurements. . . . .	104
6.6	MAD-X/PTC calculations of second-order chromaticity vs. measurements with powering of the main sextupoles at zero Landau octupole current. . . . .	104
7.1	Main parameters used for all the nonlinear optics studies in the SPS. . . . .	115
7.2	Overview of amplitude detuning measurements in the SPS. . . . .	118
7.3	Nonlinear chromaticity measurement in the SPS for the bare machine. . . . .	119
7.4	Summary of nonlinear chromaticity contributions from the octupole families in the SPS. . . . .	121



# List of Symbols

$(J_x, J_y, J_s)$	Vector of horizontal, vertical, and longitudinal particle action.
$(q, \theta)$	Polar coordinates in transverse (horizontal or vertical) phase space.
$(r, \varphi)$	Polar coordinates in longitudinal phase space.
$(x, x')$	Horizontal coordinate and conjugate momentum pair.
$(y, y')$	Vertical coordinate and conjugate momentum pair.
$(z, \delta)$	Longitudinal coordinate and conjugate momentum pair.
$B_\beta$	Betatron block matrix in the circulant matrix model.
$C$	Accelerator circumference.
$D_x(s)$	Horizontal dispersion function.
$E_0$	Reference beam energy.
$E_{\text{rf}}$	Longitudinal electric field in the main rf cavities.
$G_1^l(r, \varphi)$	Azimuthal eigenmodes of the free Vlasov equation for nonlinear chromaticity with $l \in \mathbb{Z}$ .
$H_l^k(r)$	Generalised Bessel function for nonlinear chromaticity with $l, k \in \mathbb{Z}$ .
$I_{\text{oct}}$	Current in the Large Hadron Collider (LHC) magnetic octupoles.
$J_l(x)$	Bessel function of the first kind with $l \in \mathbb{Z}$ .
$M_0$	One-turn matrix in the circulant matrix model.
$N$	Bunch intensity in number of particles (here: protons).
$N_{\text{mp}}$	Number of macroparticles used in PYHEADTAIL.
$N_r$	Number of rings in the circulant matrix model.
$N_s$	Number of azimuthal slices in the circulant matrix model.
$N_{\text{turns}}$	Number of turns used in PYHEADTAIL.
$N_{\text{wake}}$	Decay time of wakefields in PYHEADTAIL.
$N_c$	Number of cells in the circulant matrix model.
$N_k$	Number of $k$ modes used for the calculation of the effective impedance.

## List of Symbols

---

$P_{N_s}$	Permutation matrix in the circulant matrix model.
$Q$	Resonator quality factor.
$Q_s, \omega_s$	Synchrotron tune and angular synchrotron frequency respectively.
$Q_x, q_x$	Full and fractional horizontal tune respectively.
$Q_y, q_y$	Full and fractional vertical tune respectively.
$Q_{(x,y),0}$	Horizontal and vertical tunes in the bare machine.
$Q_{x,y}^{(n)}$	Horizontal and vertical chromaticities of order $n$ .
$Q'_x, Q''_x, Q'''_x$	Horizontal first-, second-, and third-order chromaticities.
$Q'_y, Q''_y, Q'''_y$	Vertical first-, second-, and third-order chromaticities.
$R$	Accelerator radius.
$R_l(r)$	Radial dependence of the azimuthal mode decomposition in the Vlasov formalism with $l \in \mathbb{Z}$ .
$R_s$	Shunt impedance of a resonator.
$S_r, \tilde{S}_r$	Circulant matrix without and with chromaticity effects respectively.
$T_0$	Revolution period of the beam.
$T_s$	Synchrotron period.
$V_1, V_2$	Voltages of the first and second harmonic rf cavities.
$V_{\text{rf}}$	Amplitude of the main rf voltage.
$W_{x,y}^{\text{const}}(z)$	Horizontal and vertical constant wake functions.
$W_{x,y}^{\text{dip}}(z)$	Horizontal and vertical dipolar (driving) wake functions.
$W_{x,y}^{\text{quad}}(z)$	Horizontal and vertical quadrupolar (detuning) wake functions.
$Z_{x,y}(\omega)$	Horizontal and vertical impedance functions.
$\Delta Q_{\text{rms}}$	Betatron (horizontal or vertical) rms tune spread.
$\Delta Q_{x,y}$	Horizontal and vertical tune shifts.
$\Delta \Omega_{\text{lin}}$	Complex coherent frequency shift of a head-tail mode in absence of frequency spread (i.e. without Landau damping).
$\Delta \omega_\beta$	Horizontal or vertical (betatron) frequency distribution.
$\Delta \psi_{x,y}$	Horizontal and vertical phase advances.
$\Gamma$	Gamma function.
$\Omega^{(l)}, \Delta \Omega^{(l)}$	Absolute and relative (i.e. shift wrt. unperturbed sideband) complex coherent frequency of an azimuthal head-tail mode $l$ .
$\Psi$	Particle distribution in phase space.
$\Psi_0, \Psi_1$	Unperturbed (stationary) and perturbed particle distribution functions in phase space respectively.
$\alpha_c$	Linear momentum compaction factor.

$\alpha_{x,y}(s)$	Horizontal and vertical alpha functions (1 <sup>st</sup> Twiss parameter).
$\beta$	Relativistic beta.
$\beta_{x,y,z}(s)$	Horizontal, vertical, and longitudinal Courant-Snyder beta functions (2 <sup>nd</sup> Twiss parameter).
$\beta_{x,y}^*$	Horizontal and vertical beta functions at the interaction point.
$\delta$	Dirac delta function.
$\delta = dp/p$	Relative momentum deviation.
$\eta$	Phase slip factor.
$\gamma$	Relativistic gamma (Lorentz factor).
$\gamma_t$	Lorentz factor at transition energy.
$\gamma_{x,y}(s)$	Horizontal and vertical gamma functions (3 <sup>rd</sup> Twiss parameter).
$\hat{\delta}$	Oscillation amplitude of the longitudinal momentum deviation of a particle.
$\hat{z}$	Oscillation amplitude of the longitudinal position of a particle.
$\lambda$	Longitudinal stationary particle distribution (notation of Scott Berg and Ruggiero).
$\mathbb{I}_n$	$n \times n$ -dimensional identity matrix.
<b>B</b>	Magnetic field vector.
<b>E</b>	Electric field vector.
<b>F<sub>L</sub></b>	Lorentz force vector.
$\mathbf{p}_\perp = (p_x, p_y)$	2D vector of transverse particle momenta.
<b>v</b>	Velocity vector.
$\mathcal{D}$	Horizontal or vertical dipole moment of the perturbed distribution (dipole mode).
$\mathcal{L}$	Instantaneous luminosity of a particle collider.
<b>i</b>	Imaginary unit.
$\omega_{\text{rfq}}$	Rf quadrupole angular frequency.
$\omega_{\text{rf}}$	Angular frequency of the main rf system.
$\omega_\xi$	Chromatic angular frequency.
$\omega_\beta$	Horizontal or vertical betatron angular frequency.
$\phi_0$	Constant phase offset in the main rf cavities.
$\phi_s$	Synchronous phase.
$\rho$	Bending radius.
$\sigma_t$	rms bunch length in (s).
$\sigma_z$	rms bunch length in (m).
$\sigma_{x,y}$	Horizontal and vertical rms beam sizes.
$\sigma_{x,y}^*$	Horizontal and vertical rms beam sizes at the interaction point.
$\tau$	Rise time of a head-tail instability.
$\tau_{\text{fb}}$	Transverse feedback damping time.

## List of Symbols

---

$\varepsilon_{x,y}^{\text{geo}}$	Horizontal and vertical <i>geometric</i> emittances of the beam.
$\varepsilon_{x,y}^{\text{norm}}$	Horizontal and vertical <i>normalised</i> emittances of the beam.
$\varphi_0$	Rf quadrupole constant phase offset.
$\tilde{\rho}(\omega)$	Frequency spectrum of a particle distribution.
$\xi^{(n)}$	Horizontal and vertical chromaticities of order $n$ normalised to the tune.
$a_n$	Skew multipole coefficient of the magnetic field decomposition.
$a_{uv}$	Horizontal, vertical, and longitudinal amplitude detuning coefficients with $u, v \in \{x, y, s\}$ .
$b_n$	Normal multipole coefficient of the magnetic field decomposition.
$c$	Speed of light in vacuum.
$d_Q$	Betatron tune diffusion coefficient.
$e$	Elementary charge (here: proton charge).
$f_0, \omega_0$	Revolution frequency of the beam in (Hz) and (rad/s) respectively.
$f_r, \omega_r$	Resonator frequency in (Hz) and (rad/s) respectively.
$g_0, g_1$	Unperturbed and perturbed particle distribution functions in longitudinal phase space respectively.
$g_1^l(r, \varphi)$	Azimuthal eigenmodes of the free Vlasov equation for linear chromaticity with $l \in \mathbb{Z}$ .
$h$	Harmonic number.
$h_0(q), h_1(q)$	Unperturbed and perturbed particle distribution functions in transverse (horizontal or vertical) phase space respectively.
$k_n^{(s)}$	Normalised skew multipole coefficient of the magnetic field decomposition.
$k_{\text{LOF}}, k_{\text{LOD}}, k_{\text{LOE}}$	LHC Software Architecture (LSA) trim editor knobs for the three Super Proton Synchrotron (SPS) Landau octupole families (LOF, LOD, LOE).
$k_n$	Normalised normal multipole coefficient of the magnetic field decomposition.
$l$	Azimuthal mode number of a head-tail instability.
$m$	Radial mode number of a head-tail instability.
$m_p$	Proton mass.
$n_b$	Number of bunches per beam.
$p_0$	Momentum of the synchronous particle (reference momentum).
$p_{\parallel} = p_z$	Longitudinal particle momentum.
$s$	Orbit path length parameter.

# 1 Introduction

The Standard Model (SM) of particle physics summarises, to a large extent, our current knowledge about the elementary constituents of matter as well as their ways to interact with each other [1–3]. According to the model, matter is composed of six flavours of quarks (up, down, charm, strange, top, bottom) and six flavours of leptons (electron, muon, tau, each with its associated neutrino) with both particle types organised in three generations according to their masses. There are four known fundamental kinds of interactions: the strong, electromagnetic, weak, and gravitational forces which are mediated by messenger particles called gauge bosons. While gluons and photons are the carriers of the strong and the electromagnetic force respectively, the Z and W particles mediate the weak interaction. As the theory of quantum gravity is incomplete at present, it is the only fundamental force that is not incorporated in the SM. Its force carrier particle, the graviton, is yet hypothetical. Finally, there is a scalar boson called the Higgs particle which takes a special role within the SM as it explains why all the elementary particles, apart from gluons and photons, have a mass [4–6].

Although the underlying theories of the SM have been heavily benchmarked experimentally and were successful at predicting previously unknown particles along with their properties, they do not yet manage to explain some of the phenomena observed in our universe. This is commonly referred to as Physics Beyond the Standard Model (BSM). For example: (1) there is an imbalance between matter and antimatter (baryon asymmetry) which is not expected from the Big Bang where equal amounts of matter and antimatter should have been created; (2) the visible matter described by the SM can only explain 5 % of the mass-energy in the universe – the remaining 95 % are thought to be explained by dark matter (27 %) and dark energy (68 %), possibly through yet undiscovered particles or phenomena; (3) the SM does not provide a unified description of all four known fundamental forces which could, for example, be achieved by introducing a supersymmetrical extension to the model; (4) the hierarchy problem, i.e. why is the gravitational force  $10^{24}$  times weaker than the weak force, or, why is the Higgs boson mass that small compared to the Planck scale; and (5) the fact that neutrinos are massive and oscillate between flavours.

Exploring the fundamental structure of the universe and addressing at least some of these open questions through the study of high-energy particle collisions is the primary objective of the European Organization for Nuclear Research (CERN), located on the Franco-Swiss border near Geneva, Switzerland. The main instruments developed and employed to achieve this goal are the particle colliders

and detectors. A circular particle collider accelerates two counter-rotating beams, composed of a large number of particles, to high kinetic energies and brings them into collision at the location of the experiments installed in the machine. The experiments operate large detectors that are able to reconstruct the events that occur during and after the collision of the particles. By doing that, the theories of the SM can be validated, or new particles and physics (BSM) may potentially be discovered.

Researchers at CERN aim to advance both the intensity and the high-energy frontiers of particle physics. At the intensity frontier the goal is to increase the particle collision rate in the detectors, which is closely related to a parameter called the luminosity of a collider. This improves the sensitivity of the experiments for the discovery of rare events and processes. At the high-energy frontier, the aim is to increase the centre-of-mass (c.m.) energy of the colliding particles to enable the creation of potential new, higher mass particles. Luminosity and c.m. energy are the two main figures of merit describing the performance of a particle collider. A boost in luminosity can, for example, be achieved by producing beams with smaller transverse sizes and higher intensities, i.e. by increasing the so called beam brightness. This, however, makes the operation of the machine much more challenging. One issue of major concern is the collective behaviour of the charged beam particles which is introduced by the electromagnetic interactions among themselves and with their surroundings. Such perturbations can drive beam instabilities leading to significant particle loss and beam quality degradation. They pose a major limitation to the performance reach of the machine. An important field of study of accelerator physics is hence how to cope with these kinds of effects.

This PhD thesis focuses on a novel approach to mitigate transverse beam instabilities in future hadron colliders to breach current limitations and make new realms in either of the two frontiers accessible. This introductory chapter motivates and defines the scope and objectives of the project. CERN's present accelerator complex is described first, followed by a brief discussion of the upcoming upgrades and current plans for future colliders in Section 1.1. The main focus is put on the challenges expected in terms of transverse beam instabilities. Section 1.2 proposes a novel technique to introduce Landau damping in circular accelerators, a commonly employed, powerful stabilising mechanism and the main subject of study of this thesis. Finally, the objectives of the project are described and an outline of the thesis is given in Section 1.3.

### 1.1 The CERN accelerator complex and future hadron colliders

The CERN accelerator complex consists of a chain of different linear and circular machines where the particle beams are accelerated to their respective final energies in stages. A schematic overview is shown in Fig. 1.1. The proton chain, which also supplies the Large Hadron Collider (LHC) [7], starts at LINAC 2, a linear machine that accelerates the particles up to a kinetic energy of 50 MeV before they are injected through a transfer line into the circular Proton Synchrotron Booster (PSB). The PSB takes the particles to a kinetic energy of 1.4 GeV and feeds them into the Proton Synchrotron (PS) where their energy is further increased to 26 GeV and the final bunch structure is established. From the PS the protons are sent to the almost 7 km long Super Proton Synchrotron (SPS) where they are accelerated to 450 GeV. The SPS marks the last stage of the LHC injector chain. From there the filling of the two counter-rotating LHC beams occurs through injections of trains consisting of multiple proton bunches whose structure is prepared at an early stage in the injector chain. Once the two rings have been filled with up to 2808 bunches each, the beams are accelerated to their final energy of presently 6.5 TeV (design energy 7 TeV),



## 1.1. The CERN accelerator complex and future hadron colliders

and are eventually brought into collision. As illustrated in the figure, there are also various fixed target experiments (ISOLDE and REX/HIE served by the PSB, East Area and the neutron time-of-flight (nTOF) experiment supplied by the PS, North Area and HiRadMat with beam from the SPS), the Advanced WAKEfield Experiment (AWAKE), an anti-proton decelerator chain (AD & ELENA), and the former CLIC Test Facility (CTF3), which has recently become the CERN Linear Electron Accelerator for Research (CLEAR). Furthermore, there is an ion chain, starting at LINAC 3, going through the Low Energy Ion Ring (LEIR) to the PS, SPS, and finally into the LHC to produce ion-ion or ion-proton collisions for the study of the quark-gluon plasma that is believed to have been present in the early stage of the universe shortly after the Big Bang [8].

The LHC is CERN's current flagship accelerator. It is the world's largest particle collider with a circumference of nearly 27 km and it delivers particle collisions at a record-setting c.m. energy to its four main experiments: ATLAS (A Toroidal LHC ApparatuS), CMS (Compact Muon Solenoid), LHCb (LHC beauty experiment), and ALICE (A Large Ion Collider Experiment). The LHC started its operation in September 2008. On 4<sup>th</sup> July 2012, the discovery of the long-sought-after Higgs boson was announced by the ATLAS and CMS collaborations [10, 11]. Both groups had detected a scalar boson with a mass of about

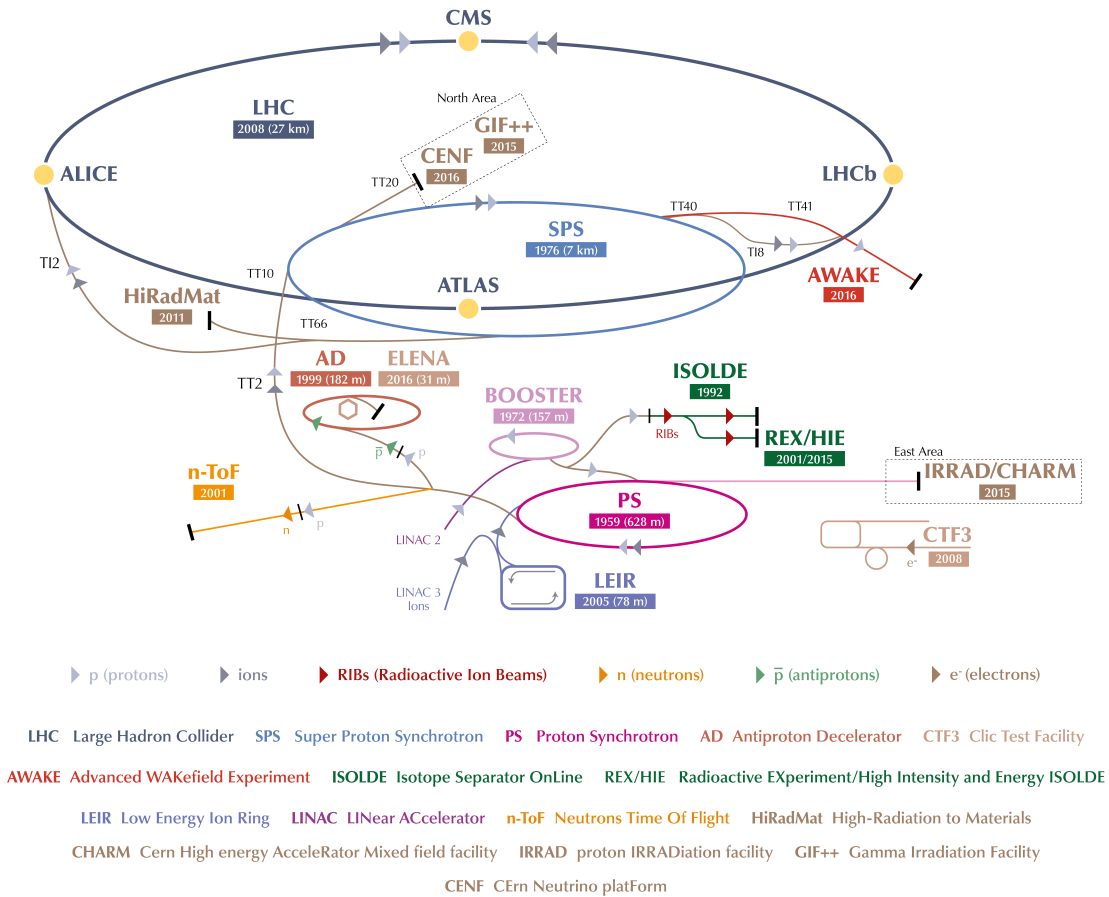


Figure 1.1: Schematic of the CERN accelerator complex (image from Ref. [9]).

125.5 GeV at a statistical significance of five standard deviations above background. The measured particle properties are consistent with the SM Higgs predicted in 1964, among others, by Higgs, Englert, and Brout [4, 5].

To exploit the full discovery potential of the LHC in the search for BSM, a number of major upgrades of the CERN accelerator complex need to be implemented, both in the injector chain (LHC Injectors Upgrade (LIU) [12, 13]) and in the LHC itself. The latter is called the High Luminosity LHC (HL-LHC) and its installation is planned to take place during the Long Shutdown 3 (LS3) lasting from 2024 to mid-2026 [14]. The ultimate goal is to significantly increase the luminosity output of the machine. This will allow to (1) push the precision of all the measurements related to the discovered Higgs boson; (2) study the rarer decay channels of the Higgs (predicted by the SM, or beyond) which are currently inaccessible; and (3) provide additional statistics to push the discovery potential for rare and low-sensitivity processes in general.

During the collision of (two) particles, a specific interaction happens with a probability called the event cross-section  $\sigma_{\text{evt}}$ , a quantity that is strongly dependent on the c.m. energy of the collision. In a particle collider, the event rate for such an interaction is given by the product  $R_{\text{evt}} = \mathcal{L} \times \sigma_{\text{evt}}$ , where the constant of proportionality  $\mathcal{L}$  is the instantaneous luminosity of the machine, typically measured in units of  $(1/\text{cm}^2 \text{ s})$ . To detect rare processes and to take high precision measurements the objective is to maximise the event rates to be able to potentially observe signals significantly above background. This is achieved by pushing the luminosity produced when colliding the two beams

$$\mathcal{L} \propto \frac{N^2 n_b f_0}{\sigma_x^* \sigma_y^*}. \quad (1.1)$$

$N$  is the bunch intensity and denotes the number of particles in each of the (typically identical) counter-rotating bunches,  $n_b$  is the number of colliding bunches,  $f_0$  is their revolution frequency, and  $\sigma_{x,y}^*$  are the rms (root mean square) beam sizes respectively in the horizontal and the vertical plane at the collision point. The latter are related to the *geometric* emittance of the beam  $\varepsilon_{x,y}^{\text{geo}} = (\sigma_{x,y}^*)^2 / \beta^*$ , a measure for the area that the beam occupies in horizontal and vertical position-momentum phase space respectively.  $\beta^*$  is the value of the beta function at the collision point, a quantity related to the transverse beam focusing strength of the machine. During particle acceleration the longitudinal momentum of the beam is increased while the transverse momenta remain constant. As a result, the transverse beam size is reduced with increasing beam energy, a kinematic effect called *adiabatic damping*. For that reason one often defines the *normalised* emittance  $\varepsilon_{x,y}^{\text{norm}} = \beta \gamma \varepsilon_{x,y}^{\text{geo}}$  which is independent of the beam energy and remains constant during acceleration.  $\beta$  denotes the particle speed in units of the speed of light  $c$ , and  $\gamma$  is the relativistic Lorentz factor. Accurate mathematical definitions of the emittance will be discussed in Chapter 2.

The LHC plans to deliver a total integrated luminosity of  $300 \text{ fb}^{-1}$  (inverse femtobarn) to its experiments during the period from 2010 to the end of 2023. HL-LHC, whose operation is planned to start in 2026, is designed to produce ten times more integrated luminosity by the year 2037 [15]. One key factor in the luminosity increase is the operation of the machine with a higher beam brightness  $N/\varepsilon_{x,y}^{\text{geo}}$  [Eq. (1.1)]. Compared to LHC design parameters, the bunch intensity will be almost doubled from  $1.15 \times 10^{11} \text{ p/b}$  to  $2.2 \times 10^{11} \text{ p/b}$  while the normalised transverse emittances will be reduced from  $3.75 \mu\text{m rad}$  to  $2.5 \mu\text{m rad}$  in both the horizontal and the vertical planes.

## 1.2. A novel approach to Landau damping

Table 1.1: Overview of the design parameters for the LHC, HL-LHC, HE-LHC, and FCC-hh [7, 16–21]. Two options are listed for the FCC-hh corresponding to two different bunch spacings (25 ns or 5 ns). All the values are for beams at collision energy.

Parameter		LHC	HL-LHC	HE-LHC	FCC-hh	
Circumference	(km)	26.7	26.7	26.7	100 (83)	
Main dipole field	(T)	8.33	8.33	16	16 (20)	
C.m. energy	(TeV)	14	14	27	100	
Bunch length rms	(cm)	7.55	7.55	7.55	8.0	
Longitudinal emittance <sup>1</sup>	(eV s)	2.5	2.5	4.0	7.0	
Bunch spacing	(ns)	25	25	25	25	5
Number of bunches		2808	2808	2808	10600	53000
Bunch intensity	( $10^{11}$ p/b)	1.15	2.20	2.20	1.00	0.20
Norm. transverse emittance	( $\mu\text{mrad}$ )	3.75	2.50	2.50	2.20	0.44
Geom. transverse emittance	(nmrad)	0.50	0.34	0.17	0.04	< 0.01
Peak luminosity	( $10^{34}/\text{cm}^2 \text{ s}$ )	1	5	25	5	< 30

<sup>1</sup> At collision energy, after the longitudinal blow-up required for longitudinal beam stability [22, 23].

The Future Circular Collider (FCC) project is an international design study launched as a result of the 2013 update of the European Strategy for Particle Physics [16, 17]. While HL-LHC will advance the intensity frontier until 2037, the main objective of the FCC study is to plan the future of particle physics beyond the HL-LHC era and to push the energy frontier by increasing the c.m. energy at collision ultimately to about 100 TeV. This would greatly extend the discovery potential for new physics beyond the SM. The study is currently in the conceptual design phase and would be realised in several stages. In the first stage, the idea would be to build an electron-positron collider (FCC-ee) that covers an energy range from 90 GeV to 350 GeV. In the second stage the machine would be replaced by a proton-proton collider (FCC-hh) which would reach c.m. energies of 100 TeV. The required circumference of the machine would be 80 km to 100 km assuming that superconducting technologies for dipole magnets will become available to reach field strengths of 16 T to 20 T. A potential alternative to FCC-hh that is also under discussion is the installation of a High Energy LHC (HE-LHC) in the existing LHC tunnel. In that scenario, the main magnets of the LHC would be replaced by FCC-hh magnet technology with 20 T dipole fields to achieve a c.m. energy of about 27 TeV.

Some of the relevant machine and beam design parameters are summarised in Table 1.1 for the LHC, HL-LHC, HE-LHC, and FCC-hh. Concerning the FCC, two options are shown for a bunch spacing of 25 ns and 5 ns respectively. The differences between the four machines are further discussed in the following section in terms of collective effects and instability mitigation techniques.

## 1.2 A novel approach to Landau damping

To successfully operate future high-luminosity and high-energy hadron colliders, transverse collective instabilities need to be studied in detail as they pose a major limitation to reaching the targeted machine performance. One important source of collective effects and instabilities is the beam-coupling impedance of the accelerator components (vacuum pipe, cavities, collimators, transitions, etc.). The

charged beam particles interact with the surrounding structure and create electromagnetic perturbations called wakefields that act back on the beam and can eventually drive it unstable, leading to beam quality degradation (emittance blow-up, particle losses, possibly beam dumps, etc.) and hence a decrease in the luminosity production. There are three main types of impedance-driven instabilities in the transverse planes: (1) coupled-bunch oscillations where two or more bunches start to move coherently, coupled by long-lived wakefields; (2) the strong (fast) single-bunch head-tail instability also known as the transverse mode coupling instability (TMCI); and (3) the weak (slow) single-bunch head-tail instability. In hadron colliders, the coupled-bunch instabilities are usually under control as they can be suppressed by means of a transverse feedback system which detects bunch-by-bunch centroid oscillations and applies a correction kick to every bunch to counter the coherent motion (active mitigation scheme). The main difference between instability types (2) and (3) is that the TMCI only appears beyond a certain intensity threshold and exhibits fast growth rates, while the weak head-tail instability is always present, independent of the intensity, but with typically much smaller growth rates. Although the TMCI is a more violent instability, effective mitigation techniques exist. Furthermore, thanks to the threshold behaviour of this type of instability, a collider can often be designed such as to operate below the intensity limit in the first place. For these reasons, instability types (1) and (2) are not part of the scope of this thesis. The focus of this study lies instead on the single-bunch weak head-tail instabilities which, since they are always excited, call for appropriate mitigation techniques.

Particles within a bunch execute transverse (betatron) and longitudinal (synchrotron) oscillations. The betatron motion is defined mainly by the quadrupole magnet arrangement and their field strengths, given by the lattice, i.e. the magnetic layout, of the machine. The synchrotron motion is a result of the longitudinal focusing provided by the radio-frequency (rf) system. The oscillations of every particle are characterised by their horizontal, vertical, and longitudinal amplitudes and frequencies. The latter are also called the betatron and synchrotron tunes. In an accelerator with perfectly linear fields, the particles would all oscillate at the same betatron frequency, called the bare machine tune. However, this is not the case in general since there are nonlinearities from various sources, such as nonlinear magnetic fields, magnet imperfections, space charge effects, beam-beam forces during bunch encounters at the collision points, etc. As a result, the transverse tunes vary slightly among the particles as they experience different frequency shifts away from the bare machine tune depending on their amplitudes of oscillation. The result of this incoherent betatron tune spread is a powerful, passive stabilising mechanism called Landau damping which can be employed against the weak head-tail instabilities [type (3) above] [24, 25]. Typically, the stabilising effect becomes stronger with increasing widths of the tune distributions. Since the aforementioned parasitic nonlinearities are often rather weak and not easily controllable, dedicated nonlinear elements, such as magnetic octupoles, are installed in the lattice for better control and efficiency of the Landau damping. In the LHC, for example, families of 84 focusing and 84 defocusing, 0.32 m long superconducting “Landau octupoles” are installed to produce a dedicated betatron frequency spread that provides Landau damping [7]. The tune shifts introduced by the magnetic octupole field are dependent on the *transverse* oscillation amplitudes of a particle. They are small for low amplitudes and large for high amplitudes. By consequence, if the transverse amplitude spread of the particles within a bunch is small, the overall tune spread is small and hence the bunch experiences little Landau damping and is more likely to become unstable in a given configuration.

The Landau octupoles are an integral part of the LHC transverse instability mitigation toolset and are extensively and successfully used for beam stabilisation during machine operation [26, 27]. However,

as explained above, their stabilising efficiency is strongly dependent on the size of the spread in the transverse oscillation amplitudes within a bunch. This quantity in turn is determined by the transverse geometric emittance  $\varepsilon_{x,y}^{\text{geo}}$  of the beam which is linearly reduced with increasing beam energy as a result of adiabatic damping. Additionally, for future operation, the transverse emittances will be shrunk further to produce brighter beams and higher luminosities. As illustrated by the values in Table 1.1,  $\varepsilon_{x,y}^{\text{geo}}$  will be up to a factor 50 lower in the FCC-hh compared to the LHC, making the Landau octupoles significantly less effective. Furthermore, the beams may suffer from more violent instabilities due to their higher bunch intensities and/or the increased overall machine impedance. To suppress potentially performance-limiting instabilities, it is hence desirable to explore and study alternative mitigation techniques that are more efficient and easier to implement than Landau octupoles.

One promising technique is to employ Landau damping from betatron detuning with the *longitudinal* rather than the transverse amplitude. The reason for the great potential of this approach is that the longitudinal amplitude spread, defined by the longitudinal bunch emittance, is orders of magnitude larger than the transverse ones. For example, for the HL-LHC, the ratio between the rms transverse and longitudinal amplitudes at a beam energy of 7 TeV is about  $10^{-4}$ . For FCC-hh, this ratio becomes another ten to 100 times smaller. This comes as a result of adiabatic damping in the transverse planes as explained above. At the same time, the longitudinal emittance is deliberately blown up during the energy ramp to keep the beams longitudinally stable [22, 23]. This blow-up has no significant impact on the luminosity. Longitudinal amplitude thus provides a larger handle to generate the betatron tune spread required for Landau damping. A basic analytical understanding of this particular stabilising mechanism has already been developed by Scott Berg and Ruggiero in 1997 as reported in Ref. [28]. With their work they demonstrate that the tune spread introduced as a function of the longitudinal amplitude can indeed improve the transverse stability of the particle beams. The underlying mechanism is similar to the Landau damping effect from magnetic octupoles, but the beam dynamics is more involved and requires a more in-depth understanding.

A superconducting rf quadrupole cavity was proposed by Grudiev in 2014 as a dedicated device to generate a betatron frequency spread as a function of longitudinal amplitude [29]. The quadrupole focusing strength of the device has a harmonic dependence on the longitudinal position of the particles in the bunch. As a result, the time-average betatron frequencies of the individual particles are shifted according to their longitudinal amplitudes. Thanks to the orders of magnitude larger spread in the longitudinal compared to the transverse amplitudes, an rf quadrupole is able to generate the betatron frequency spread more effectively than magnetic octupoles. For example, analytical calculations predict that the maximum rms betatron tune spread generated by the LHC Landau octupoles can theoretically be achieved with a less than one metre long superconducting rf device operating in a transverse quadrupolar mode [29]. This is for LHC beam and machine design parameters at collision energy (7 TeV). For comparison, the total magnetic length of the LHC Landau octupoles is about 54 m. It is worth noting, however, that the size of the tune spread alone, although indicative, does not make a full statement about the amount of Landau damping present in a bunch. The reason for that is that the stabilising mechanisms for detuning with transverse and longitudinal amplitude are not identical.

Another effect that changes the betatron frequencies of individual particles within a bunch as a function of longitudinal parameters is *chromaticity*. The longitudinal momentum distribution of the bunch has a certain finite width, meaning that the particles have slightly different longitudinal momenta. This difference is described by the momentum deviation from the reference value defined by the

main magnetic dipole field of the accelerator. As a result, every particle experiences different focusing and defocusing forces in the quadrupole magnets used to spatially confine the beams. This in turn has an impact on the transverse oscillation frequencies of every particle and hence again leads to a transverse oscillation frequency spread within the bunch. At first order in the momentum deviation, this frequency spread does not introduce Landau damping, however, since the betatron tune shifts are not amplitude-dependent and hence average out over time. It can be shown, however, that the second-order dependence of the betatron frequencies on the momentum deviation, known as the second-order chromaticity, introduces a spread that depends on the longitudinal amplitude, similarly to the rf quadrupole described above. Hence, one way to approximately mimic the stabilising effect of an rf quadrupole is to modify the beam optics of the accelerator in such a way as to gain control over the second-order chromaticity. Although this method may require significant modifications of the machine optics and is less versatile than a dedicated element like the rf quadrupole due to constraints posed by optics requirements, it can be applied without installing additional equipment in the accelerator system. This makes it a valuable tool to experimentally validate analytical and numerical models on a reasonable timescale and budget.

Additional alternatives for the stabilisation of transverse intra-bunch instabilities in future colliders are under study by other research groups. One prominent example is the electron lens which is also used to enhance Landau damping through betatron detuning with the transverse amplitudes, similarly to magnetic octupoles [30]. The electron lens promises to have a higher damping performance than Landau octupoles since it generates the largest tune shifts for the particles residing in the core of the bunch where they are most abundant. When using octupole magnets, the core particles experience almost no tune shifts and the Landau damping is provided mostly by the large amplitude particles of which there are fewer.

Another mitigation scheme for collective beam instabilities are feedback systems. Contrary to Landau damping, they belong to the class of active stabilising systems. In the transverse planes, for example, beam pick-ups detect bunch oscillations and correction kicks are applied to the bunch to counter the movement in subsequent turns. While feedback systems are, conceptually, the cleanest means to mitigate coherent oscillations, so far they did not have the bandwidth to suppress higher-order intra-bunch modes, such as weak head-tail modes, given the relatively short bunch lengths of high-energy hadron collider beams. However, the development of wideband pick-ups and kickers is under way and a prototype system installed in the SPS has already been shown to successfully resolve and damp intra-bunch motion [31, 32].

### 1.3 Project objectives and outline

This thesis reports on the work done and the results achieved during the three-year doctoral project based at CERN. The main objective of the project is to evaluate the newly proposed Landau damping approach through detuning with longitudinal amplitude. The beam dynamics is studied from the points-of-view of theory, numerical simulations using various accelerator physics models, and experiments performed in the SPS and the LHC to validate these models. The use of this method is evaluated primarily in terms of collective effects, but also the main single-particle aspects are considered as they may potentially limit the practicality of this new approach to Landau damping. Both concepts, the rf quadrupole and nonlinear chromaticity, are explored in parallel. The former can only be studied

theoretically and with simulations as there is no rf quadrupole available at present. The construction, installation, and test of a superconducting rf quadrupole system in an existing machine such as the SPS, although feasible, is costly and may only be realised on a timescale of five to ten years. Second-order chromaticity, on the other hand, can be enhanced in an existing accelerator by modifying the machine optics without engineering and installing new equipment. It makes a proof-of-principle experiment possible, for example, in the LHC. In this way, the theoretical and numerical studies can be backed up with measurement data.

The thesis is organised as follows:

First, the basics of accelerator beam dynamics relevant for the understanding of the project are re-capped and summarised in Chapter 2. The focus is put on the formation of impedance-driven weak head-tail instabilities and their mitigation through the process of Landau damping. Two different accelerator physics models, the existing Vlasov formalism for impedance-driven dipole modes and the circulant matrix model are introduced. The two main computer codes used throughout the thesis, the PYHEADTAIL macroparticle tracking model and BIMBIM, a circulant matrix solver, are briefly explained.

Chapter 3 introduces betatron detuning with longitudinal amplitude from both an rf quadrupole cavity and from second-order chromaticity. The rf quadrupole is compared to the traditionally employed octupole magnets that provide detuning with the transverse amplitudes. The main advantages and features of the new method, and the rf quadrupole in particular, are pointed out. It is also demonstrated that second-order chromaticity provides a detuning mechanism that is equivalent to that of the rf quadrupole in a first approximation. The equivalence between the two methods is fundamental as it enables the experimental validation of the numerical studies performed for the rf quadrupole. The first part of the work presented in this chapter has been published in Ref. [33].

Within the scope of this thesis, the existing Vlasov theory has been extended to include the effects of nonlinear chromaticity on the coherent beam dynamics and the main derivations are presented in Chapter 4. The description provides a fundamental theoretical understanding of the beam dynamics expected from detuning with longitudinal amplitude. The theory is benchmarked against both a particle tracking and a circulant matrix model, implemented in PYHEADTAIL and BIMBIM respectively. Results for two longitudinal beam distributions, an airbag and a Gaussian model, are compared. The two beam models allow switching on and off the Landau damping effect provided by nonlinear chromaticity. The benchmarks prove an excellent agreement and demonstrate a solid understanding of the involved dynamics. The study has been published in Ref. [34].

In Chapter 5, two models of the device implemented in PYHEADTAIL are explained and the results of benchmarks demonstrating its correct modelling are shown. The main objective of this chapter is to provide a numerical proof-of-principle study for beam stabilisation with the rf quadrupole and to analyse more generally its effect on the beam dynamics by means of PYHEADTAIL. Furthermore, an rf quadrupole system is evaluated for the FCC-hh and the corresponding requirements are highlighted. Finally, potential drawbacks of the rf quadrupole in terms of single-particle effects are pointed out. These include synchro-betatron resonances and feed-down effects expected for a beam that traverses the cavity off-axis. The majority of the work presented in this chapter has been published in Ref. [33].

The results from single-bunch experiments made in the LHC are presented in Chapter 6. The second-order chromaticity was enhanced in the machine by means of a sextupole magnet powering scheme. It is shown that both the single- and multi-particle effects observed in the LHC are well-understood and

## Chapter 1. Introduction

---

correctly modelled. The coherent beam dynamics, in particular, is accurately reproduced by PYHEADTAIL simulations and the stabilising effect expected from the Vlasov theory of nonlinear chromaticity developed in Chapter 4 is proven experimentally along with the side effects that are correctly predicted by the theory. This proves the reliability of the numerical models in PYHEADTAIL and indirectly demonstrates transverse beam stabilisation with an rf quadrupole. The work discussed in this chapter has been published in Ref. [35].

Chapter 7 summarises and discusses the results from experiments conducted in the SPS. Here, the second-order chromaticity was enhanced by means of a magnetic octupole powering scheme. The chapter first details on measurements of the nonlinear optics of the machine which were necessary to perform the delicate experiments with nonlinear chromaticity. The measurements are compared to the beam optics code MAD-X demonstrating a good agreement. However, the beam stability studies show that the sensitivity of the machine is not sufficient to make a clear statement about Landau damping from second-order chromaticity. A detailed analysis pinpointing the reasons for that is given instead.

Every chapter contains a discussion of the conclusions that can be drawn from the corresponding work that was carried out. A global perspective on the project, including the main conclusions, is taken in Chapter 8, followed by an appendix that contains additional analytical derivations made within the Vlasov framework.



## 2 Basics of accelerator beam dynamics

This chapter introduces the basics of charged single- and multi-particle dynamics in a strong-focusing proton synchrotron. The discussion is based on Refs. [25, 36–38] and is limited to the concepts required for the understanding of the work developed in this thesis.

Synchrotrons are a type of ring accelerator where the radius of the reference particle orbit remains constant as the energy of the particle beam increases. This is achieved by tuning the frequency of the main rf system, responsible for the acceleration and longitudinal focusing of the particles, such that it is synchronised with the revolution frequency of the beam. Simultaneously, the strength of the magnetic dipole bending field is increased to account for the constantly growing particle momentum along the energy ramp. This guarantees that the radius of the reference particle orbit remains constant at all times. The idea behind *strong-focusing* is to use alternating focusing and defocusing lenses (quadrupole magnets) in the two transverse planes to provide a strong horizontal and vertical confinement for the particles. This concept was developed in 1952 by Courant, Livingston, and Snyder [39], and has become the standard scheme for high-energy particle accelerators.

In a synchrotron, the beams are usually composed of many longitudinally separated particle bunches. For the machines at CERN, every proton bunch typically contains of the order of  $10^{11}$  particles. In this thesis we limit ourselves to the description of single-bunch beams and their dynamics. In Section 2.1, we first consider the particles within a bunch independent of each other and free from collective behaviour. The physics describing their individual transverse and longitudinal motion is called single-particle dynamics. In reality charged particles interact electromagnetically with each other and with the surrounding structure which leads to phenomena known as collective effects. These are particularly pronounced when operating with increased phase space densities required for future high-brightness beams. The discussion on collective phenomena, in particular the weak head-tail instabilities and their mitigation through the Landau damping mechanism, follows in Section 2.2. Last, two main computer codes employed for modelling the collective behaviour of particle beams are described in Section 2.3.

## 2.1 Single-particle dynamics

The motion of a particle in an accelerator ring is confined around a reference trajectory thanks to the Lorentz force  $\mathbf{F}_L$  induced by the applied external electric  $\mathbf{E}$  and magnetic  $\mathbf{B}$  fields

$$\mathbf{F}_L = e(\mathbf{E} + \mathbf{v} \times \mathbf{B}), \quad (2.1)$$

where  $e$  is the electric charge of the particle and  $\mathbf{v} = (v_x, v_y, v_z)$  its velocity vector. Electric fields are generated in rf cavities and are mostly employed for longitudinal acceleration of the beams. Magnetic fields, on the other hand, are used to deflect particles transversely as the magnetic force always acts perpendicularly to their direction of motion.

The arrangement of dipole and quadrupole magnets, called the machine lattice, deflects and focuses the beam to keep the particles close to a reference closed orbit of circumference  $C = 2\pi R$ , a trajectory closing onto itself after one revolution around the accelerator ring and ideally passing through the centre of all the magnets. The particle that follows this path is called the on-momentum or the synchronous particle and has a momentum  $p_0$ . The motion of any particle within a bunch is conveniently described in a curvilinear and co-moving frame  $\Sigma$  known as the Frenet-Serret system illustrated in Fig. 2.1. The local coordinate system defined by the horizontal  $\hat{x}(s)$ , vertical  $\hat{y}(s)$ , and longitudinal  $\hat{z}(s)$  axes moves along the reference orbit together with the beam. The reference orbit itself is parametrised by the path length  $s$ . The coordinates  $x(s)$ ,  $y(s)$ , and  $z(s)$  denote the horizontal, vertical, and longitudinal positions of a particle and are measured with respect to the origin of the local co-moving coordinate system.

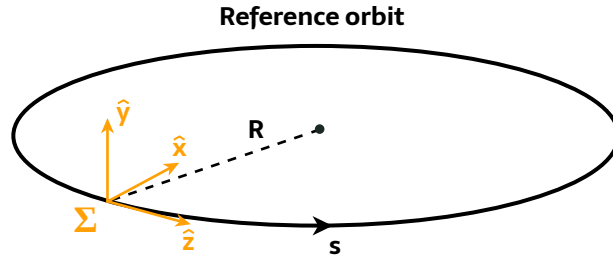


Figure 2.1: The Frenet-Serret coordinate system.

The direction of motion of the beam is mostly longitudinal as the particles have very small transverse velocities compared to the longitudinal one,  $v_{x,y} \ll v_z$ , meaning that the beam is paraxial. Furthermore, static magnets designed for accelerators aim for purely transverse magnetic fields and their effect in the longitudinal direction is hence negligible [compare Eq. (2.1)]. The magnetic fields can be expressed through a multipole expansion

$$B_y + iB_x = \sum_{n=1}^{\infty} (b_n + ia_n)(x + iy)^{n-1}, \quad (2.2)$$

where  $n$  denotes the order of the field component. The strength of the multipole field is characterised respectively by *normal* (“upright”) and *skew* (normal field rotated around the  $z$ -axis by an angle  $\pi/2n$ ) coefficients denoted by  $b_n$  and  $a_n$  and measured in units of  $(\text{T}/\text{m}^{n-1})$ . In modern accelerators, every field component of the multipole expansion is provided by a separate, dedicated magnet. The elements producing the lowest-order multipoles are called dipoles ( $n = 1$ ), quadrupoles ( $n = 2$ ), sextupoles

( $n = 3$ ), octupoles ( $n = 4$ ), etc. For an ideal, i.e. a pure, normal multipole of order  $n$  and strength  $b_n$ , for example, the coefficients are given by

$$\begin{aligned} a_k &= 0, & k \in \mathbb{N} \\ b_k &= \begin{cases} b_n \neq 0, & k = n, \\ 0, & \text{otherwise.} \end{cases} \end{aligned} \quad (2.3)$$

In this case,

$$b_n = \frac{1}{(n-1)!} \frac{\partial^{n-1} B_y}{\partial x^{n-1}} = \frac{1}{(n-1)!} \frac{\partial^{n-1} B_x}{\partial y^{n-1}} \quad (2.4)$$

Analogous equations exist for the ideal skew multipole. In accelerator physics, the multipole strengths are often normalised to  $e/p_0$ , by convention, and denoted respectively by  $k_n = b_n p_0 / e$  and  $k_n^{(s)} = a_n p_0 / e$  for the normal and the skew multipole.

Throughout this thesis, we only consider synchrotron machines that are planar in the  $x$ - $z$  plane and hence work with vertical dipole fields  $\mathbf{B}_{\text{dip}} = (0, B_0, 0)$ , such that the charged particles are deflected horizontally. One can obtain an expression for the bending radius  $\rho$  of a proton that moves under the influence of such a uniform field by equating the Lorentz force to the centrifugal force

$$e|v_z B_0| = \frac{\gamma m_p v^2}{\rho} \quad \Leftrightarrow \quad |B_0 \rho| \approx \frac{p}{e}, \quad (2.5)$$

where  $m_p$  is the proton mass,  $\gamma$  the Lorentz factor,  $v = |\mathbf{v}|$ , and  $p = \gamma m_p v = \gamma m_p \beta c$  is the particle momentum. The quantity  $|B_0 \rho|$  is also referred to as the beam rigidity. The approximation in Eq. (2.5) is a result of the assumption that the beams are paraxial, i.e.  $v \approx |v_z|$ . As explained above, satisfying Eq. (2.5), i.e. keeping a constant bending radius  $\rho$  while the particle momentum varies is one of the basic underlying principles of the synchrotron.

### 2.1.1 Transverse motion

The transverse state of a particle in coordinate-momentum space ("trace" space) is described by the position and divergence angle pair  $\mathbf{u} = (u, u')$  with  $u \in \{x, y\}$ . The angle  $u'(s) = du/ds$  is related to the transverse particle momentum. Assuming the paraxial approximation,  $u' = p_u / p_0$ .

#### Hill's equations

As explained above, dipole magnets keep the beam on a closed, curved trajectory. However, the particles generally have initial nonzero divergence angles ( $x'_0, y'_0$ ) and would hence spread out transversely, away from the reference orbit. This movement can be countered by means of quadrupole focusing magnets. Using Eq. (2.2), one calculates that the magnetic field in a normal quadrupole is given by

$$\mathbf{B}_{\text{quad}} = b_2 (y, x, 0), \quad (2.6)$$

where the quadrupole strength  $b_2$  can be either positive or negative. The force that acts on a particle

travelling along the  $z$ -axis [ $\mathbf{v} = (0, 0, v_z)$ ] is hence given by

$$\mathbf{F}_{\text{quad}} = b_2 v_z (-x, y, 0). \quad (2.7)$$

As a result, for  $b_2 > 0$ , particles with a horizontal offset experience a horizontal restoring (focusing) force, while particles that are vertically off-axis are subject to a vertical defocusing force. Quadrupoles with  $b_2 > 0$  are hence referred to as focusing quadrupoles. Contrary, quadrupoles with  $b_2 < 0$  are horizontally defocusing and vertically focusing and are called defocusing quadrupoles. In alternating-gradient synchrotrons, both families of quadrupoles are necessary to provide an overall focusing of the beam in the two transverse planes. This is achieved by arranging the quadrupole magnets periodically with alternating polarities which is called the strong-, or alternating-gradient-focusing scheme.

The betatron motion in a lattice composed of (vertical) dipoles and two families of quadrupoles is described by Hill's equations [40]

$$\begin{aligned} x''(s) + K_x(s) x(s) &= 0, & y''(s) + K_y(s) y(s) &= 0, \\ K_x(s) &= 1/\rho^2 - K_1(s), & K_y(s) &= K_1(s). \end{aligned} \quad (2.8)$$

The equations have been linearised in  $x$  and  $y$  since the betatron oscillation amplitudes are generally small. In this simplified form, we also assume that the horizontal and the vertical motions are independent, i.e. there is no coupling between the two planes. Thanks to the presence of horizontally deflecting dipole magnets there is an additional, weak, focusing term  $1/\rho^2$  in the horizontal plane which is missing in the vertical plane. The quadrupole focusing effect is described by the effective focusing function  $K_1(s)$  which is the same in both transverse planes apart from the difference in the signs. In the following, the variable  $u \in \{x, y\}$  is used to describe both the horizontal and the vertical planes.

Accelerator lattices are usually composed of several, identical periodic sectors of length  $L$ , such that the periodicity condition  $K_u(s) = K_u(s + L)$  holds. As a result, the differential equation (2.8) can be solved using Floquet's theorem [41]. The general solution is a superposition of the two linearly independent solutions

$$u(s) = a_u w_u(s) e^{i\psi_u(s)}, \quad u^*(s) = a_u w_u(s) e^{-i\psi_u(s)}, \quad (2.9)$$

with  $a_u$  a constant,  $w_u(s)$  the amplitude function, and  $\psi_u(s)$  the phase function. The latter must fulfil the betatron envelope and phase equations

$$w_u''(s) + K_u(s) w_u(s) - \frac{1}{w_u(s)^3} = 0, \quad \psi_u'(s) = \frac{1}{w_u(s)^2}, \quad (2.10)$$

since  $K_u(s)$  is real-valued. They can be solved numerically with an iterative approach once the lattice of the accelerator has been defined. The linear transverse transport of a particle from one place  $s_1$  to another  $s_2$  in a beam transport line with known solutions  $w_u(s)$  and  $\psi_u(s)$  can be conveniently described by a matrix-vector multiplication  $\mathbf{u}(s_2) = M_u(s_2|s_1) \mathbf{u}(s_1)$ , with

$$M_u(s_2|s_1) = \begin{pmatrix} \sqrt{\beta_{u,2}} & 0 \\ -\frac{\alpha_{u,2}}{\sqrt{\beta_{u,2}}} & \frac{1}{\sqrt{\beta_{u,2}}} \end{pmatrix} \begin{pmatrix} \cos \Delta\psi_u & \sin \Delta\psi_u \\ -\sin \Delta\psi_u & \cos \Delta\psi_u \end{pmatrix} \begin{pmatrix} \frac{1}{\sqrt{\beta_{u,1}}} & 0 \\ \frac{\alpha_{u,1}}{\sqrt{\beta_{u,1}}} & \sqrt{\beta_{u,1}} \end{pmatrix}. \quad (2.11)$$

The phase difference  $\Delta\psi_u = \psi_u(s_2) - \psi_u(s_1)$  denotes the phase advance between  $s_1$  and  $s_2$ , while

$\beta_{u,i} = w_u^2(s_i)$  and  $\alpha_{u,i} = -\beta'_{u,i}/2$  are two of the three Courant-Snyder (aka. Twiss) parameters at location  $s_i$ . The phase advance for one full revolution around the accelerator ring divided by  $2\pi$  is a particularly important quantity known as the betatron tune of the machine

$$Q_u = \frac{1}{2\pi} [\psi_u(s+C) - \psi_u(s)] = \frac{1}{2\pi} \oint_C \frac{1}{\beta_u(s)} ds. \quad (2.12)$$

It corresponds to the number of betatron oscillations a particle undergoes in one revolution around the accelerator. Often, the betatron tune is expressed via an angular frequency in units of (rad/s),  $\omega_{\beta,u} = 2\pi f_0 Q_u = \omega_0 Q_u$ , where  $f_0$  and  $\omega_0$  denote the revolution frequency of the beam in units of (Hz) and (rad/s) respectively.

### Courant-Snyder ellipse

The solution for the evolution of the transverse position and divergence angle can be obtained in action-angle coordinates  $(J_u, \psi_u)$  of a particle

$$u = \sqrt{2J_u\beta_u} \cos\psi_u, \quad u' = -\sqrt{\frac{2J_u}{\beta_u}} [\sin\psi_u + \alpha_u \cos\psi_u]. \quad (2.13)$$

Up to a factor  $2\pi$ , the action corresponds to the phase space area enclosed by the Courant-Snyder ellipse, which is an invariant of the motion

$$\varepsilon_u = \gamma_u u^2 + 2\alpha_u u u' + \beta_u u'^2 = \text{const.} \quad (2.14)$$

The third and last Twiss parameter  $\gamma_u = (1 + \alpha_u^2)/\beta_u$  has been introduced here.

The values of the coordinate-momentum pair of a particle at a specific location  $s$  in the machine lattice characterised by the Twiss parameters  $[\alpha_u(s), \beta_u(s), \gamma_u(s)]$  trace out the Courant-Snyder ellipse over time as illustrated in Fig. 2.2. The ellipse has a different size for every individual particle, depending on its action. The enclosed phase space area is given by  $\pi\varepsilon_u = 2\pi J_u$ , and  $\varepsilon_u$  is sometimes referred to as the single-particle emittance. At different locations in the lattice, the ellipse has a different shape defined by the local Twiss parameters as illustrated in the figure. Its area, however, is independent of  $s$  and remains constant. The maximum amplitude and divergence angle of the betatron motion at location  $s$  are given by  $\sqrt{\beta_u(s)\varepsilon_u}$  and  $\sqrt{\gamma_u(s)\varepsilon_u}$  respectively.

### Transverse emittance

The bunches in an accelerator consist of a large number of individual, charged particles which populate the transverse and longitudinal phase spaces in which they occupy a certain area called the statistical emittance of the beam. Given that the beam can be described by a normalised distribution function  $\rho(u, u')$ , i.e.  $\int \rho(u, u') du du' = 1$ , its moments are calculated according to

$$\langle u \rangle = \int u \rho(u, u') du du', \quad \langle u' \rangle = \int u' \rho(u, u') du du' \quad (2.15)$$

$$\sigma_u^2 = \int (u - \langle u \rangle)^2 \rho(u, u') du du', \quad \sigma_{u'}^2 = \int (u' - \langle u' \rangle)^2 \rho(u, u') du du', \quad (2.16)$$

$$\sigma_{uu'} = \int (u - \langle u \rangle) (u' - \langle u' \rangle) \rho(u, u') du du', \quad (2.17)$$

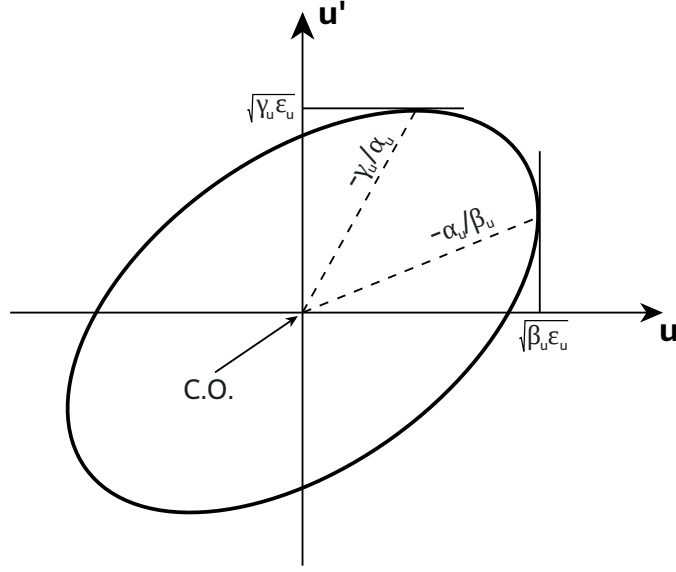


Figure 2.2: Courant-Snyder ellipse for a specific set of Twiss parameters  $[\alpha_u(s), \beta_u(s), \gamma_u(s)]$ . The closed orbit (C.O.) defines the origin of the ellipse. Note that the dependence of the Twiss parameters on  $s$  has been omitted in the figure.

where  $\sigma_u$  and  $\sigma_{u'}$  are the rms beam widths of the particle distribution in terms of the transverse coordinate and momentum variables  $u$  and  $u'$  respectively, and  $\sigma_{uu'}$  denotes the correlation between the two quantities. The *geometric* rms emittance of a particle beam is defined as

$$\epsilon_u^{\text{geo}} = \sqrt{\sigma_u^2 \sigma_{u'}^2 - \sigma_{uu'}^2}. \quad (2.18)$$

This formula is valid assuming that the expectation values for the variables  $u$  and  $u'$  are both zero. Given that an accelerator lattice is composed only of linear elements such as dipoles and quadrupoles, and if the beam is at constant energy,  $\epsilon_u^{\text{geo}}$  is an invariant quantity. It corresponds to the area enclosed by the Courant-Snyder ellipse traced out by the rms particle. The beam size  $\sigma_u(s)$ , however, is a quantity that depends on the local Twiss parameter  $\beta_u(s)$ . It is related to the geometric emittance through  $\sigma_u(s) = \sqrt{\beta_u(s) \epsilon_u^{\text{geo}}}$ .

During beam acceleration, the geometric emittance defined as a function of  $(u, u')$  in Eq. (2.18) is no longer invariant. To obtain the invariant phase space area, one needs to consider the conjugate phase space coordinates  $(u, p_u)$ , where  $p_u = p_0 u' = \gamma m_p \beta c u'$ . One can then define a *normalised* emittance  $\epsilon_u^{\text{norm}} = \beta \gamma \epsilon_u^{\text{geo}}$  which is also invariant during acceleration. Given that  $\epsilon_u^{\text{norm}} = \text{const.}$ , the geometric emittance decreases with  $1/\beta\gamma$ , a process called *adiabatic damping*. The reason is that during acceleration, the transverse velocities  $v_u$  of the particles remain constant, while their divergence angles  $u' = p_u/p_0$  decrease with increasing  $p_0$ , leading to a smaller area occupied by the beam in trace space.

### Off-momentum effects

Until now the particle momenta were assumed to correspond to the reference value  $p_0$  of the synchronous particle. In a beam, however, there is a momentum spread meaning that the particle momenta are distributed around  $p_0$ . We define the relative momentum deviation of a particle as

$$\delta = \frac{\Delta p}{p_0} = \frac{p - p_0}{p_0}. \quad (2.19)$$

Particles with a nonzero momentum deviation experience magnetic deflecting forces different from those of the synchronous particle. This has various consequences, two of which are explained below to first order in  $\delta$ .

In dipole magnets, for example, a momentum deviation leads to dispersion effects. A particle with  $\delta < 0$  has a lower magnetic rigidity and is hence deflected more strongly by the magnets. On the other hand, a particle with  $\delta > 0$  experiences a reduced bending force in the dipoles. By consequence, off-momentum particles travel on a closed orbit that deviates from the reference orbit of the synchronous particle. Since we assume purely vertical dipole fields here, such dispersion effects appear only in the horizontal plane. In mathematical terms, the consequence is that the horizontal Hill's equation [Eq. (2.8)] becomes inhomogeneous and dependent on longitudinal beam parameters

$$x''(s) + K_x(s) x(s) = \frac{1}{\rho(s)} \frac{\Delta p}{p_0}. \quad (2.20)$$

The off-momentum, called chromatic, effects coming from the quadrupole gradient errors have been neglected here as they are discussed separately below. The general solution to the inhomogeneous differential equation is expressed as a linear superposition of the solution  $x_\beta(s)$  to the homogeneous equation (2.13) and a particular solution:  $x(s) = x_\beta(s) + D_x(s)\delta$ .  $D_x(s)$  is referred to as the dispersion function and accounts for the difference of the off-momentum closed orbit with respect to the reference trajectory followed by the synchronous particle. For Gaussian particle distributions in the longitudinal and transverse phase spaces, dispersion increases the local rms beam size to  $\sigma_x^2(s) = \beta_x(s) \epsilon_x^{\text{geo}} + D_x(s)^2 \delta_{\text{rms}}^2$  as a result of this closed orbit distortion.

In quadrupole magnets, particles with  $\delta > 0$  experience a weaker effective focusing strength due to their larger magnetic rigidity. The situation is inverse for particles with  $\delta < 0$ . The difference in focusing strength with respect to the reference particle is reflected in the quadrupole gradient errors

$$\Delta K_x = \left[ -\frac{2}{\rho^2} + K_1 \right] \delta + \mathcal{O}(\delta^2) \approx -K_x \delta, \quad (2.21)$$

$$\Delta K_y = -K_1 \delta + \mathcal{O}(\delta^2) \approx -K_y \delta. \quad (2.22)$$

These errors lead to chromatic aberration of which chromaticity is one main effect. As a result of the stronger (weaker) focusing, off-momentum particles have a higher (lower) betatron oscillation frequency than the on-momentum particle. The chromaticity of a machine describes the dependence of the betatron tunes on the momentum deviation of every particle. At first order in  $\delta$  it is defined as

$$Q'_u = \left. \frac{\partial Q_u}{\partial \delta} \right|_{\delta=0}, \quad (2.23)$$

and the betatron tune shift, measured with respect to the tune of the on-momentum particle, is given by

$$\Delta Q_u(\delta) = Q'_u \delta. \quad (2.24)$$

Chromaticity is often normalised to the betatron tune of the reference particle  $Q_{u,0}$ . At first order,  $\xi_u^{(1)} = Q'_u / Q_{u,0}$ .

Since the particles differ in their momentum deviation, they experience different betatron tune shifts from the quadrupole gradient errors. This leads to an *incoherent* tune shift

$$\Delta Q_u \approx \left( -\frac{1}{4\pi} \oint_C \beta_u K_u ds \right) \delta. \quad (2.25)$$

The term in brackets denotes the natural linear chromaticity of a machine lattice and is negative. This can be intuitively understood: a particle with a positive (negative) momentum deviation experiences weaker (stronger) focusing and hence oscillates at a lower (higher) tune than the synchronous one.

The natural chromaticity needs to be corrected in order to suppress undesired single-particle (resonances) and multi-particle (coherent instabilities) effects that could lead to beam loss. Sextupole magnets can be used to compensate and control the natural linear chromaticity, but they can also introduce nonlinear chromatic terms. The same applies to octupole magnets located in regions of nonzero dispersion. The potential use of nonlinear chromaticity from sextupole and octupole magnets is one of the main subjects of this thesis and will be discussed further in subsequent chapters.

### Lattice imperfections

Up to now we have assumed that the closed orbit of the beam passes perfectly through the centre of all the magnetic elements in the lattice. However, in general, there are geometric imperfections, such as transverse misalignments of the magnets for example. A beam passing through a magnetic element with a transverse offset experiences, apart from the primary multipole field, perturbations from all the lower orders of the multipole. This effect is called feed-down.

Let us consider, for instance, an ideal normal quadrupole. If the particle passes through the centre of the magnet, it experiences a pure quadrupole field as given in Eq. (2.6). However, in case of, for example, a horizontal misalignment of the element by  $\Delta x$  from the reference position, the particle will traverse the magnet with an offset, such that  $x \rightarrow x - \Delta x$ . In this case, one finds that

$$\begin{aligned} \mathbf{B}_{\text{quad}} &= b_2(y, x - \Delta x, 0) \\ &= b_2[(y, x, 0) - (0, \Delta x, 0)]. \end{aligned} \quad (2.26)$$

The first term in the square bracket is the same quadrupole field as in a perfectly aligned magnet. However, there is a second term which introduces a dipole kick leading to a distortion of the closed orbit of the beam at the location of the element.

As a second example, a horizontally misaligned normal sextupole introduces a normal quadrupole (tune shift) as well as a normal dipole (closed orbit distortion) feed-down component at first and second order respectively. In the event that it is vertically misaligned, it introduces a skew quadrupole component (linear coupling) at first order, and again a normal dipole kick at second order.



In general, the feed-down chain of a horizontally ( $\Delta x$ ) and/or vertically ( $\Delta y$ ) misaligned multipole can be expressed as

$$\begin{array}{ccccccc}
 & & \xrightarrow{\quad |\Delta x| \quad} & & & & \\
 & a_n & \rightarrow & a_{n-1} & \rightarrow & a_{n-2} & \cdots \\
 & \downarrow & & \downarrow & & \downarrow & \\
 |\Delta y| \downarrow & b_{n-1} & \rightarrow & b_{n-2} & \rightarrow & \cdots & \\
 & \downarrow & & \downarrow & & & \\
 & a_{n-2} & \rightarrow & \cdots & & & \\
 & \downarrow & & & & & \\
 & \cdots & & & & & 
 \end{array} \tag{2.27}$$

Feed-down effects from an rf quadrupole and from octupole magnets will be discussed further in Chapters 5 and 7 respectively.

Magnets typically also have rotational misalignments which introduces a mixture of normal and skew fields. And, in addition to geometric errors, there are magnetic field imperfections, i.e. magnets are never ideal multipoles of a specific order. A treatment of these effects is out of the scope of this thesis, but can be found, e.g., in Ref. [42].

### Resonances

The linear and nonlinear fields present in an accelerator introduce perturbations of the single-particle motion which may add up coherently over time and drive single particles unstable. This happens when the recurrent perturbing kick fulfils a certain synchronicity condition with respect to the betatron and/or synchrotron oscillation frequencies. If a particle is on-resonance, its amplitude of oscillation, or action, grows over time and the particle is eventually lost from the stable beam as it hits the aperture of the machine. Resonances lead to single-particle losses and hence reduce the beam lifetime. In storage rings, such as the LHC, where beams are routinely stored for ten hours or more, the effect of resonances must be minimised. This is mostly achieved by a careful selection of the working point, i.e. the betatron tunes of the machine, away from most prominent resonance lines, as well as by keeping the incoherent tune spread as small as possible.

Resonances that are purely transverse are not part of the scope of this thesis, but are discussed in detail in Refs. [36, 37, 42]. Here, the focus lies on a different type of resonance called the *synchro-betatron resonance* (SBR). Other than purely transverse resonances, SBR rely on a specific synchronicity condition between the longitudinal *and* transverse oscillation frequencies of the particles. These resonances can be driven when there is a coupling mechanism between the transverse and longitudinal planes, such as dispersion in sextupoles and rf cavities, transverse fields in rf cavities, and beam-beam interactions with a crossing angle as explained in Ref. [43]. Given that such a perturbation exists, a particle  $i$  is said to be on-SBR when it fulfils the relation

$$j Q_{x,i} + k Q_{y,i} + l Q_{s,i} = n, \tag{2.28}$$

with  $j, k, l, n \in \mathbb{Z}$ .  $Q_{x,i}$  and  $Q_{y,i}$  are the betatron tunes and  $Q_{s,i}$  denotes the synchrotron tune of the particle. The latter will be introduced in the following section.

### 2.1.2 Longitudinal motion

In synchrotrons, the acceleration of particles is achieved by means of the longitudinal electric field provided by the main rf cavities

$$E_{\text{rf}}(t) = E_z \sin(\omega_{\text{rf}} t + \phi_0), \quad (2.29)$$

where  $E_z$  is the field amplitude and  $\phi_0$  is a constant phase offset. The rf system operates at a frequency  $\omega_{\text{rf}}$  which is an integer multiple of the angular revolution frequency  $\omega_0$  of the synchronous particle, such that  $\omega_{\text{rf}} = h\omega_0$ . This guarantees that the synchronous particle arrives at the main rf cavities with the same phase turn after turn.  $h$  is called the harmonic number and corresponds to the number of rf periods that fit in the machine circumference. It defines how many rf buckets there are and hence it specifies the maximum number of bunches that can in principle be placed in the accelerator ring.

#### First equation of motion

Since the particles take a finite amount of time to traverse an rf cavity, the electric field changes during their passage. This is accounted for by the transit-time factor  $T$ . It is convenient to define an effective, reduced, rf voltage amplitude seen by the particles,  $V_0 = gTE_z$ , where  $g$  denotes the cavity gap width. Given that the momentum spread in a bunch is small and since we are considering ultra-relativistic beams, the transit-time factor is assumed to be identical for all the particles. The effective rf voltage is hence given by

$$V_{\text{rf}}(t) = V_0 \sin \phi(t), \quad (2.30)$$

where  $\phi(t)$  denotes the longitudinal coordinate of the particles within the bunch. It is related to the longitudinal position  $z(t)$  through  $\phi(t) = -h z(t)/R$ .  $z$  and  $\phi$  are equivalent descriptions of the longitudinal coordinate.

The synchronous particle being perfectly synchronised with the frequency of the rf system arrives at the cavities always with the same phase  $\phi(t) = \phi_s$ . As a result, its energy  $E_0$  changes by the amount  $eV_0 \sin \phi_s$  with every passage through the cavities. The rate of energy gain or loss can now be expressed as

$$\frac{dE_0}{dt} = \frac{\omega_0}{2\pi} eV_0 \sin \phi_s, \quad (2.31)$$

using the approximation that the energy change occurs continuously over time. For  $\phi_s = 0$  or  $\phi_s = \pi$ , the beam energy remains constant. For any other value of  $\phi_s$ , the cavities are in accelerating (decelerating) mode. In order to provide longitudinal focusing it is important that the phase is set correctly. The concept of longitudinal focusing will be discussed below.

Off-momentum particles with an energy  $E = E_0 + \Delta E$  arrive with a different, time-dependent phase  $\phi(t) \neq \phi_s$  at the rf system (earlier or later) than the synchronous one and hence experience a different energy gain (loss) during their passage through the cavity

$$\frac{dE}{dt} = \frac{\omega_0}{2\pi} eV_0 \sin \phi(t). \quad (2.32)$$

By combining Eqs. (2.31) and (2.32), we can derive the first longitudinal equation of motion describing

the time evolution of the energy error  $\Delta E = E - E_0$  of a particle

$$\frac{d(\Delta E)}{dt} = \frac{\omega_0}{2\pi} e V_0 (\sin \phi - \sin \phi_s). \quad (2.33)$$

$\Delta E$  is related to the relative momentum deviation defined in Eq. (2.19) through

$$\delta = \frac{\Delta p}{p_0} = \frac{\Delta E}{\beta^2 E_0}. \quad (2.34)$$

$\delta$  and  $\Delta E$  are equivalent descriptions of the longitudinal conjugate momentum variable.

### Phase slippage

There are two important dispersion effects in the longitudinal plane. First, particles with positive (negative)  $\delta$  travel at higher (lower) velocity than the synchronous particle. At low energies, this velocity dependence on  $\delta$  is very important. As described by the theory of special relativity, however, once  $\beta \rightarrow 1$ , the dependence of the velocity on  $\delta$  becomes negligible. Second, particles with positive (negative)  $\delta$  are more (less) rigid and hence are deflected differently by the dipole magnets. As a result, a high (low) momentum particle travels on a longer (shorter) orbit. It is intuitively clear that these two effects are counteracting. Depending on the beam energy and optics configuration of a machine, one or the other effect dominates.

Analytically, the two effects are identified by considering the dependencies of the relative revolution frequency  $\omega = \beta c/R$  of the beam. The revolution frequency varies with velocity error  $d\beta$  and orbit error  $d(\Delta R)$

$$\frac{d\omega}{\omega} = \frac{d\beta}{\beta} - \frac{d(\Delta R)}{R}. \quad (2.35)$$

At this point, we define the linear momentum compaction factor

$$\alpha_c = \frac{1}{C} \frac{d(\Delta C)}{dp/p}, \quad \text{with } \Delta C = \left[ \oint \frac{D_x(s)}{\rho} ds \right] \delta. \quad (2.36)$$

It describes the relative change of the orbit path length with respect to the momentum deviation. As illustrated by Eq. (2.36), the change in path length  $\Delta C$  can be expressed as an integral of the dispersion function over the full circumference of the accelerator.  $\alpha_c$  is hence a parameter that depends on the machine optics.

Using  $p = \gamma m_p \beta c$ , it follows that  $dp/p = \gamma^2 d\beta/\beta$ . Since  $d(\Delta R)/R = d(\Delta C)/C$ , Eq. (2.35) can now be expressed as

$$\frac{d\omega}{\omega} = \left( \frac{1}{\gamma^2} - \alpha_c \right) \frac{dp}{p} = \eta \frac{dp}{p}, \quad (2.37)$$

where we have defined the first-order phase slippage factor  $\eta$ . The terms in brackets describe the two competing effects. The first term corresponds to the dependence of velocity on the momentum deviation while the second one represents the relative change of orbit length with respect to the momentum deviation. At relatively low beam energies, the first term dominates over the second one, while at ultra-relativistic energies the situation is inverse. This is because for  $\beta \rightarrow 1$ , the dependence of velocity on the momentum becomes insignificant. Naturally, there is an intermediate beam energy where the two effects cancel each other out. This energy is called transition energy and one defines the

relativistic transition gamma  $\gamma_t$ , according to

$$\eta = \frac{1}{\gamma_t^2} - \alpha_c = 0 \Leftrightarrow \gamma_t = \frac{1}{\sqrt{\alpha_c}}. \quad (2.38)$$

### Second equation of motion

To complete the description of longitudinal particle motion in a synchrotron, a second equation is needed that describes the time evolution of the phase  $\phi(t)$ . It can be obtained by considering the relative difference between the revolution times of an arbitrary particle with respect to the synchronous one

$$\Delta t = T - T_0 = 2\pi \left( \frac{1}{\omega} - \frac{1}{\omega_0} \right) = -\frac{2\pi}{\omega_0} \frac{\Delta\omega}{\omega}. \quad (2.39)$$

The difference in the phase is calculated as  $\Delta\phi = \omega_{\text{rf}} \Delta t$ . Combining Eqs. (2.34), (2.37), and (2.39), we can derive the second equation of motion

$$\frac{d(\Delta\phi)}{dt} = \frac{h\omega_0\eta}{\beta^2 E_0} \Delta E. \quad (2.40)$$

### Synchrotron motion and phase stability

Despite their asynchronous arrival times, off-momentum particles do not move away from the synchronous particle, given that the phase of the rf system is correctly adjusted. They oscillate about the phase of the synchronous particle and remain longitudinally focused. This effect, called longitudinal focusing, is explained by the concept of phase stability discovered independently by McMillan and Veksler [44–46]. The longitudinal oscillation called synchrotron motion is described by the second-order differential equation obtained when combining Eqs. (2.33) and (2.40)

$$\frac{d^2(\Delta\phi)}{dt^2} = \frac{\eta h\omega_0^2 e V_0}{2\pi\beta^2 E_0} (\sin\phi - \sin\phi_s). \quad (2.41)$$

For  $\Delta\phi \ll 1$ , one can use the approximation  $\sin\phi - \sin\phi_s \approx \Delta\phi \cos\phi_s$  and hence the differential equation for the *small-amplitude* phase oscillations reads

$$\frac{d^2(\Delta\phi)}{dt^2} \approx \frac{\eta h\omega_0^2 e V_0 \cos\phi_s}{2\pi\beta^2 E_0} \Delta\phi = \omega_s^2 \Delta\phi, \quad (2.42)$$

where the constant factors have been combined in  $\omega_s$ . Equation (2.42) describes a harmonic oscillator with angular frequency

$$\omega_s = \omega_0 \sqrt{\frac{h e V_0 |\eta \cos\phi_s|}{2\pi\beta^2 E_0}}, \quad (2.43)$$

called the (small-amplitude) synchrotron frequency. Often, one normalises the synchrotron frequency to the revolution frequency to obtain the synchrotron *tune*  $Q_s = \omega_s/\omega_0$ . The small-amplitude oscillation is sometimes also referred to as linear synchrotron motion. In reality, however, i.e. for the actual rf bucket,  $\omega_s$  is dependent on the longitudinal action  $J_s$ .

The phase stability condition is given by  $\eta \cos\phi_s < 0$ . During acceleration, if  $\gamma < \gamma_t$  (below transition),

or  $\eta < 0$ , phase stability is guaranteed for  $0 \leq \phi_s \leq \pi/2$ . For  $\gamma > \gamma_t$  (above transition), or  $\eta > 0$ , instead phase stability is given if  $\pi/2 \leq \phi_s \leq \pi$ . A machine that accelerates a beam through transition requires hence, along with other manipulations, a change of the rf phase (phase jump), to restore longitudinal focusing of the beam. In the stationary case, i.e. without acceleration, the synchronous phase must be adjusted to  $\phi_s = 0$  below transition, and to  $\phi_s = \pi$  above transition.

The concept of phase stability is illustrated in Fig. 2.3. For example, above transition energy  $\eta > 0$  and in case of proton acceleration, phase stability is guaranteed for  $\pi/2 \leq \phi_s \leq \pi$ . The graph shows the synchronous particle ( $\delta = 0$ , red), as well as two off-momentum particles, one with a momentum respectively larger ( $\delta > 0$ , orange) or smaller ( $\delta < 0$ , green) than that of the synchronous one. Above transition, the change of orbit length with momentum is more important than the change of particle velocity. Hence, a higher (lower) momentum particle takes longer (shorter) to complete one revolution than the synchronous one. By consequence, the higher (lower) momentum particle arrives late (early) at the rf cavities compared to the synchronous one. As illustrated in the figure, when  $\phi_s$  is set between  $\pi/2$  and  $\pi$ , the late arriving, higher momentum particle receives less energy during the passage through the cavity than the synchronous one. As a result, it will take a shorter amount of time to complete the next revolution and will hence move closer to the synchronous particle as indicated by the small grey arrow. The situation is inverse for the lower momentum particle.

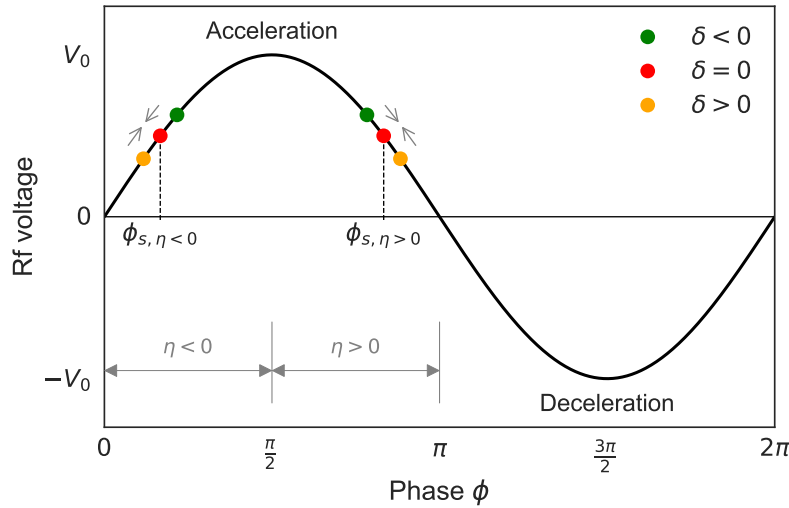


Figure 2.3: Illustration of phase stability in the longitudinal plane below and above transition energy.

## 2.2 Transverse impedance-driven single-bunch instabilities

Up to now we have only discussed single-particle dynamics which means that the particles were considered independent of each other. The only electromagnetic fields included in the description were the externally applied fields generated by the (perfect) multipole magnets (dipoles, quadrupoles, sextupoles, etc.) and the rf cavities. However, the particles are electrically charged and hence are sources of additional electromagnetic fields themselves. Hence, the particles within a beam cannot be considered independent. They influence each other and can develop collective behaviour. In accelerator physics, collective effects are summarised as a class of phenomena for which the evolution

of the beam depends on both the external and the additional electromagnetic fields generated by the presence of other charged particles. These effects generally lead to beam quality degradation which can be inferred from macroscopic quantities such as the beam intensity (particle losses), the centroid of oscillation, the emittances, the beam size and its profiles (moments). There is a clear distinction between *incoherent* and *coherent* effects. The group of incoherent effects includes all the phenomena that affect individual particles, but not the entity of the beam. By consequence, incoherent effects cannot be observed on the beam centroid for instance. One example of incoherent effects are single particles that start oscillating resonantly until their amplitude grows so large that they hit the surrounding structure. Typically, such effects lead to (slow) particle losses and hence a poor beam lifetime, emittance growth, as well as halo/tail formation. Coherent effects, on the other hand, affect the beam as an entity and the particles exhibit collective behaviour. Here, typically an exponential growth of the centroid amplitude of oscillation (or of another, higher-order moment of the particle distribution) can be observed as well as fast particle losses and emittance blow-up.

Collective effects start playing a major role in high-brightness and high-intensity machines where the particles are squeezed into a small amount of phase space. They can strongly limit the luminosity reach of a particle collider which is its main performance figure of merit. It is of great importance to have a thorough understanding of the impact of collective effects on the performance of the machine, the underlying mechanisms, and possible mitigation techniques. Sessler summarised this challenging task as follows [47]:

*“At the heart of our problem – and I mean the problem of the accelerator physicist – is the pernicious self-destructive behavior of particle beams. What inherent flaw makes beams destroy themselves?”*

Although there are plenty of different collective phenomena, such as space charge, electron/ion clouds, beam-beam effects, etc., this thesis focuses on those driven by the beam-coupling impedance and we shall hence limit ourselves to their description.

### 2.2.1 Wakefields and impedances

Charged particles travelling inside an accelerator environment interact with their surroundings, such as the resistive vacuum pipe walls, rf cavities, beam collimators, bellows, etc. The result of these interactions are electromagnetic perturbations, called wakefields, which act back on the beam and hence have an important impact on its dynamics. The evolution of the beam is thus determined not only by the external, applied, but also by internal, self-induced electric and magnetic fields. Wakefields are created in all the structures that are not perfect electric conductors (PEC), or at geometric discontinuities in general. The origin of the wakefields are delayed currents in the structure walls induced by the travelling particles. The delay is caused by the finite conductivity of the materials or by the geometric discontinuities of the vacuum pipe or other structures.

Since wakefields introduce collective behaviour among the particles in a beam, they can lead to coherent instabilities. Each particle acts as a *source* of wakefields which in turn affect all the other particles in the beam, called *witnesses*. Electromagnetic waves propagate at the speed of light. Hence, for ultra-relativistic beams, the wakefield created by a source particle can only act upon trailing particles, meaning that there is no “wake-in-front”. Multi-turn effects may still need to be considered, though, as

## 2.2. Transverse impedance-driven single-bunch instabilities

a source can also act upon itself in subsequent turns. For all the studies presented in this thesis, the ultra-relativistic limit is a valid approximation and the wake-in-front can hence be safely neglected. Multi-turn wakefields will be included whenever they have a significant impact on the beam dynamics.

To make a mathematical description of the wakefield concept let us consider two particles travelling at the speed of light, a source of charge  $q_s$ , and a witness  $q_w$  following the source at a constant distance  $\Delta z$  through an accelerator structure of length  $L$ . The two charges can be represented by Dirac delta functions  $q_s \delta(s - ct)$  and  $q_w \delta(s - ct - \Delta z)$ . As a result of the interaction of the source with the surrounding structure, a wakefield  $W(z)$  is excited with horizontal, vertical, and longitudinal components. The wakefields in the transverse and longitudinal planes can be treated separately when studying impedance-driven instabilities. It is hence sufficient to consider only the transverse components  $W_{x,y}(z)$  when determining the unstable modes in the transverse planes. A wakefield can, furthermore, be broken down into its multipole components by expanding it into a Taylor series. The effect of the transverse wakefields on the witness particles are transverse kicks, i.e. changes of their transverse momenta. To linear order, the kicks can be expressed as

$$\begin{aligned}\Delta x' &= \int_0^L F_x(s, \Delta z, \Delta x_s, \Delta x_w) ds \approx -q_s q_w \left[ W_x^{\text{const}}(\Delta z) + W_x^{\text{dip}}(\Delta z) \Delta x_s + W_x^{\text{quad}}(\Delta z) \Delta x_w \right], \\ \Delta y' &= \int_0^L F_y(s, \Delta z, \Delta y_s, \Delta y_w) ds \approx -q_s q_w \left[ W_y^{\text{const}}(\Delta z) + W_y^{\text{dip}}(\Delta z) \Delta y_s + W_y^{\text{quad}}(\Delta z) \Delta y_w \right],\end{aligned}\tag{2.44}$$

where  $F_{x,y}$  denotes the transverse force exerted by the wakefield over the length  $L$  of the structure.  $W_{x,y}^{\text{const}}(z)$ ,  $W_{x,y}^{\text{dip}}(z)$ , and  $W_{x,y}^{\text{quad}}(z)$  are the transverse *constant*, *dipole* (driving), and *quadrupole* (detuning) wakefields respectively.  $(\Delta x_s, \Delta y_s)$  and  $(\Delta x_w, \Delta y_w)$  denote the transverse offsets of the source and witness particles. In case of top/bottom or left/right symmetry of the accelerator structure under consideration, the constant wakefield is zero. Since only first-order terms are considered here, the coupling wakes between the horizontal and vertical planes have been neglected.

Wakefields are a time domain description of the interaction of the beam with its surroundings. A beam circulating in an accelerator can also be perceived as a current flowing in an equivalent electric circuit with a specific impedance. The *beam-coupling impedance* of the accelerator structure corresponds to the frequency spectrum of the wakefield. The descriptions in terms of wakefields (time domain) or impedances (frequency domain) are equivalent. Wakes and impedances can be converted between each other by means of the Fourier transform

$$\begin{aligned}W_{x,y}(z) &= -\frac{i}{2\pi} \int_{-\infty}^{\infty} Z_{x,y}(\omega) e^{i\omega z/c} d\omega, \\ Z_{x,y}(\omega) &= \frac{i}{c} \int_{-\infty}^{\infty} W_{x,y}(z) e^{-i\omega z/c} dz.\end{aligned}\tag{2.45}$$

Since wakefields are real-valued functions, an important property of the transverse impedance can be deduced from Eq. (2.45)

$$-\overline{Z}_{x,y}(\omega) = Z_{x,y}(-\omega),\tag{2.46}$$

where the overline denotes the complex conjugate. In other words, the imaginary and real parts of the transverse impedance are respectively even and odd functions of  $\omega$ .

One particular impedance that is used in this thesis to benchmark numerical models against analytical

calculations is that of a resonator. Its transverse components are given by [25]

$$Z_{\perp}(\omega) = \frac{c}{\omega} \frac{R_s}{1 + iQ \left( \frac{\omega_r}{\omega} - \frac{\omega}{\omega_r} \right)}, \quad (2.47)$$

where  $R_s$  is the shunt impedance,  $\omega_r$  the resonant angular frequency, and  $Q$  the quality factor. The corresponding wakefield reads

$$W_{\perp}(z) = \frac{cR_s\omega_r}{Q\bar{\omega}} e^{\alpha z/c} \sin\left(\frac{\bar{\omega}z}{c}\right), \quad (2.48)$$

where  $\alpha = \omega_r/2Q$  and  $\bar{\omega} = \sqrt{\omega_r^2 - \alpha^2}$ . In time domain the quality factor describes the decay time of the wakefield. A narrow-band resonator (high  $Q$  factor) generates a wakefield that rings for a long time and can introduce multi-turn wakefield effects. In that case, the source particles see their own wakefield after one or even after several revolutions around the accelerator. A broad-band resonator with  $Q = 1$ , on the other hand, generates a fast-decaying wakefield. In frequency domain, a narrow-band resonator is characterised by a sharp, narrow peak in the frequency spectrum, while a broad-band resonator extends over a larger range of frequencies.

A simplified impedance or wakefield model of an entire accelerator consists usually of a combination of a resistive wall model, a broad-band resonator, and several narrow-band resonators [25, 48]. The resistive wall describes the impedance of the beam pipe which has a finite conductivity. It typically decays fast and hence affects mostly the particles that are following the source at a close distance. It can, however, also decay slowly and thus lead to multi-turn or coupled-bunch effects. The resonators represent rf cavities or beam pipe transitions for example. They can be slowly-decaying (narrow-band), or fast-decaying (broad-band) wakes. By consequence, they can affect particles within the same bunch, but also couple multiple bunches or introduce multi-turn effects.

A detailed wakefield or impedance model of an accelerator is usually obtained by a combination of bench measurements and electromagnetic computations (e.g. analytical or finite-element solvers) of all the individual elements installed in the lattice. Another way to benchmark and validate an existing impedance model is to perform beam-based measurements, such as the intensity-dependent tune shift, which is introduced by the presence of the impedance, or by measuring growth rates of coherent instabilities, as well as bunch lengthening effects.

### 2.2.2 Head-tail instabilities

The goal of this section is to give a rough phenomenological description of the transverse *strong* and *weak* single-bunch head-tail instabilities. These types of instabilities can evolve given the synchronicity between the synchrotron and betatron motion, and the wakefield kicks of the particles within a bunch. A detailed mathematical formulation of the dynamics within the Vlasov framework follows in Section 2.2.3.

#### Strong head-tail instability

The strong head-tail instability, also known as the transverse mode coupling instability (TMCI), can be understood as the synchrotron analogue to the dipole beam break-up instability observed in linacs. It can be explained by considering a two-particle model where particle 1 represents the head of a bunch



## 2.2. Transverse impedance-driven single-bunch instabilities

and particle 2 its tail. In a linac, the longitudinal positions of the two particles are frozen. Particle 1 at the head oscillates freely and excites a dipole wakefield that kicks the trailing particle 2 resonantly. As a result, the betatron amplitude of the trailing particle grows over time and the bunch, or more precisely its tail, is driven unstable. The dynamics of the strong head-tail instability in a synchrotron is similar. The trailing particle experiences the wakefield kicks excited by the head of the bunch and hence its betatron oscillation grows in amplitude. However, in a synchrotron, the longitudinal positions of the two particles are no longer fixed. Thanks to synchrotron motion, the two particles have exchanged positions after half a synchrotron period (continuous process). Particle 1 now takes the role of the trailing particle and receives wakefield kicks excited by particle 2 located at the head of the bunch and oscillating freely. This mixing has a stabilising effect and, to a certain extent, “washes away” the amplitude growth that the trailing particle has experienced in the previous half of the synchrotron period. This is the reason why the strong head-tail instability in synchrotrons exhibits an intensity threshold behaviour. In the event that the bunch intensity is below the threshold  $N_{\text{thr}}$ , the instability is not observed.

For a qualitative understanding of the main dependencies of the intensity threshold one can analyse the eigenvalues of the two-particle system and finds that [25]

$$N_{\text{thr}} \propto \gamma \omega_s \frac{C}{\beta_{\perp} W_0}, \quad (2.49)$$

where  $W_0$  denotes the strength of the wakefield, assuming a constant dipole wake, and  $\beta_{\perp}$  is the transverse beta function at the location of the impedance. The equation shows that a faster synchrotron motion increases the threshold. This is intuitively clear: a faster mixing between head and tail allows less time for the trailing particle to suffer from amplitude growth.  $W_0/C$  corresponds to the strength of the wakefield per unit length: a larger integrated wakefield strength lowers the intensity threshold linearly. Furthermore, a larger beta function  $\beta_{\perp}$  at the location of the wakefield source enhances the kicks and thus also leads to a lower threshold. Finally,  $N_{\text{thr}} \propto \gamma$  indicates that higher-energy beams are intrinsically more stable due to their increased rigidity. Apart from the threshold behaviour, another main feature of the TMCI is that its growth rate is a steep function of intensity beyond the instability threshold. This means that the TMCI is typically a fast instability, even for intensities not far above threshold. In this regime, the amplitude of the centroid motion grows exponentially with short rise times and the beam can be lost within a fraction of a synchrotron period. Furthermore, the instability mechanism relies on the chromaticity being (close to) zero.

When computing the eigenmodes of the system (of which there are only two in the two-particle model), one also discovers that their eigenfrequencies shift towards one another depending on the bunch intensity. These frequency shifts are caused by the impedance and become larger with increasing intensity. They are discussed further below as they are an important means to characterise the eigenmodes of a bunch, not only for the strong, but also for the weak head-tail instability. For the strong head-tail instability, it is exactly at the threshold intensity  $N_{\text{thr}}$  where the two frequencies become equal, and the modes “couple” such that the beam is unstable. In an actual bunch with billions of particles, there are equally more eigenmodes. Although usually the lowest-order modes, 0 and  $-1$  are the most likely modes to couple and lead to a TMCI, it is also possible to have a coupling between modes  $-2$  and  $-3$ , such as, for example, in the SPS at CERN [49]. This actually depends on the relationship between bunch length and the main contributing frequencies in the impedance spectrum.

A common mitigation technique against the TMCI is to operate the accelerator with slightly positive or negative first-order chromaticity, depending on whether the system is above or below transition energy. This, however, usually results in slow particle losses. Despite its fast growth rates, the TMCI is often not of concern during machine operation, but still a very important intensity-limiting mechanism to be considered already during the design phase of a machine.

### Weak head-tail instability

The driving force of the weak head-tail instability is the dipole wakefield excited by the particles at the head of a bunch. Other than the TMCI, the development of the weak head-tail instability relies on a more subtle mechanism that involves nonzero (first-order) chromaticity. With chromaticity, every particle oscillates at a different betatron frequency depending on the momentum deviation as explained in Section 2.1.1. This introduces an amplitude growth term that does not wash out over the synchrotron period any longer [25]. Instead, the growth may accumulate slowly over time. As a result, the weak head-tail instability does not show any threshold behaviour, but appears at any bunch intensity if the right synchronicity conditions are met. The rise times, however, are typically much longer than those of the TMCI and can reach several synchrotron periods. Since first-order chromaticity is the main player when dealing with weak head-tail instabilities, it has to be well controlled. This is achieved by means of sextupole magnets installed in dispersive regions of the machine lattice.

The weak head-tail modes are standing waves, equivalently to the eigenmodes of the vibrations observed on a drumhead. The mode pattern is given by the transverse motion of the bunch as a function of the 2D longitudinal phase space  $(z, \delta)$ . By consequence, a mode is fully described through a pair of numbers, called the azimuthal  $l$  and the radial  $m$  mode numbers. For example, the fundamental mode has azimuthal and radial numbers  $(0, 0)$  – all the particles in the bunch execute transverse oscillations in phase. In an actual accelerator, one typically only considers the projection of the mode onto the  $z$ -axis, which can be measured by means of head-tail monitors, which are essentially fast oscilloscopes (see, e.g., Ref. [50] for the LHC). The number of nodes seen on the standing wave head-tail pattern corresponds to the radial mode number. The azimuthal number can be obtained from the frequency spectrum of the bunch centroid, identifying the growing synchrotron sideband that corresponds to the instability.

### Impedance-induced frequency shifts

Head-tail modes introduce an exponential dependence of the bunch centroid amplitude

$$x(t) \propto e^{i(\Omega_0^{(l)} + \Delta\Omega^{(l)})t} = e^{i(\Omega_0^{(l)} + \Delta\Omega_{\text{re}}^{(l)})t} e^{-\Delta\Omega_{\text{im}}^{(l)}t}, \quad (2.50)$$

where  $\Omega_0^{(l)}$  is the real-valued, unperturbed frequency associated with a particular mode (here the azimuthal mode  $l$ ), and  $\Delta\Omega^{(l)} = \Delta\Omega_{\text{re}}^{(l)} + i\Delta\Omega_{\text{im}}^{(l)}$  is the complex coherent frequency shift introduced by the beam-coupling impedance discussed briefly above. From Eq. (2.50) it is clear that the real part  $\Delta\Omega_{\text{re}}^{(l)}$  modifies the oscillation frequency. This can be observed, for example, by looking at the Fourier spectrum of the bunch centroid and comparing the measured frequency with the unperturbed tune (in absence of impedance) of the synchrotron sideband of the mode under consideration. The shift grows with increasing intensity. Beam-based measurements can be performed where the shift is measured as a function of bunch intensity to obtain information about the imaginary part of the machine impedance. The second term  $e^{-\Delta\Omega_{\text{im}}^{(l)}t}$  illustrates that the amplitude of the motion grows for  $\Delta\Omega_{\text{im}}^{(l)} < 0$  (unstable

bunch) and is damped for  $\Delta\Omega_{\text{im}}^{(l)} > 0$  (stable bunch). The imaginary coherent frequency shift is hence directly related to the instability growth rate through  $1/\tau^{(l)} = -\Delta\Omega_{\text{im}}^{(l)}$  and reveals information about the real part of the machine impedance.

### 2.2.3 Vlasov formalism

This section summarises the Vlasov formalism for transverse collective single-bunch head-tail modes in a machine with purely linear chromaticity. The derivations are based on Ref. [25] and are valid in the ultra-relativistic limit, i.e. for  $\beta = 1$ .

Let  $\Psi = \Psi(s, u, p_u, z, \delta)$  be the particle distribution of the bunch in 4D phase space, considering the longitudinal (2D) and only one transverse plane (2D), either the horizontal ( $u = x$ ) or the vertical one ( $u = y$ ). The parameter  $s$  denotes the longitudinal position of the bunch along the accelerator and is equivalent to the time  $t$  through  $s = ct$ . The variable pairs  $(u, p_u)$  and  $(z, \delta)$  correspond respectively to the transverse and longitudinal coordinates and conjugate momenta. These four phase space variables are all implicitly dependent on  $s$ . The Vlasov equation hence reads

$$\frac{d\Psi}{ds} = (\partial_s + u'\partial_u + p'_u\partial_{p_u} + z'\partial_z + \delta'\partial_\delta)\Psi = 0, \quad (2.51)$$

where  $u'$ ,  $p'_u$ ,  $z'$ , and  $\delta'$  denote the first derivatives with respect to  $s$ . The derivatives are known from the transverse and longitudinal equations of motion describing the single-particle beam dynamics

$$\begin{aligned} u' &= p_u, \\ p'_u &= -\left(\frac{\omega_{\beta,0}}{c}\right)^2 u + \frac{1}{E_0} F_u(z, s), \end{aligned} \quad (2.52)$$

$$\begin{aligned} z' &= -\eta\delta, \\ \delta' &= \frac{1}{\eta}\left(\frac{\omega_s}{c}\right)^2 + \frac{u}{E_0} \frac{\partial F_u}{\partial z}(z, s), \end{aligned} \quad (2.53)$$

where  $\omega_{\beta,0}$  denotes the unperturbed angular betatron frequency in the transverse plane under consideration, and  $E_0 = \gamma m_p c^2$  is the total energy of the protons.  $F_u$  describes the transverse force and represents the effect of transverse dipolar wakefields on the beam here. It is defined by the convolution of the transverse wake with the longitudinal bunch profile, or, equivalently, by the overlap sum of the transverse impedance with the frequency spectrum of the bunch, called the effective impedance. As in Ref. [25], the longitudinal kick introduced by the transverse wakefield in Eq. (2.53) can be neglected since it has an insignificant impact on our studies. This is a valid approximation as long as synchro-betatron resonance conditions are avoided and given that the transverse beam sizes remain small enough [43].

The Vlasov equation can be simplified using polar coordinates in the transverse and longitudinal planes

$$\begin{aligned} (u, p_u) &= (q \cos \theta, -\frac{\omega_{\beta,0}}{c} q \sin \theta), \\ (z, \delta) &= (r \cos \varphi, \frac{1}{\beta_z} r \sin \varphi), \end{aligned} \quad (2.54)$$

where  $\beta_z = \eta c / \omega_s$  is the longitudinal equivalent to the transverse Courant-Snyder beta function. Linear synchrotron motion is assumed throughout. The subscript  $u$  denoting the transverse plane will be omitted in the following. The Vlasov equation in polar coordinates reads

$$\left[ \partial_s + \frac{\omega_{\beta,0}}{c} (1 + \xi^{(1)} \delta) \partial_\theta + \frac{\omega_s}{c} \partial_\varphi - \frac{c}{\omega_{\beta,0}} \frac{F}{E_0} \left( \sin \theta \partial_q + \frac{\cos \theta}{q} \partial_\theta \right) \right] \Psi = 0. \quad (2.55)$$

The betatron frequency is  $\omega_\beta(\delta) = (1 + \xi^{(1)} \delta) \omega_{\beta,0}$ , and  $\xi^{(1)} = \omega_{\beta,0}^{-1} (\partial \omega_\beta / \partial \delta)|_{\delta=0}$  denotes the first-order chromaticity as introduced earlier in this chapter. The solutions  $\Psi$  to Eq. (2.55) are the collective transverse dipole modes. They can be described by a sum of a stationary solution and a perturbation term  $\Psi = \Psi_0 + \Psi_1$ , with

$$\begin{aligned} \Psi_0 &= g_0(r) h_0(q), \\ \Psi_1 &= g_1(r, \varphi) h_1(q, \theta) e^{-i\Omega s/c}. \end{aligned} \quad (2.56)$$

The longitudinal  $g_0(r)$  and transverse  $h_0(q)$  distributions being stationary can only have a radial dependence. The two planes are furthermore assumed to be fully decoupled which is why  $\Psi_0$  can be expressed as a product of two independent functions. The perturbative distributions  $g_1(r, \varphi)$  and  $h_1(q, \theta)$  represent respectively the longitudinal and transverse structures of the coherent mode. The exponential term describes its time evolution where  $\Omega$  is the complex coherent frequency associated with the mode. The transverse instabilities under study are of dipolar nature and hence their transverse structure can be anticipated  $h_1(q, \theta) = -\mathcal{D} h'_0(q) e^{i\theta}$ .  $\mathcal{D}$  is the dipole moment of the perturbed distribution and  $h'_0(q)$  is the first derivative of  $h_0(q)$  with respect to  $q$ .

To further simplify the Vlasov equation, the wakefield force term is expressed in frequency domain using the transverse dipolar impedance  $Z_\perp(\omega)$  and the frequency spectrum  $\tilde{\rho}_1(\omega)$  of the bunch. The latter is given by the Fourier transform of  $\Psi_1$  projected onto the  $z$ -axis

$$\tilde{\rho}_1(\omega) = \frac{\omega_s}{\eta c} \int_0^\infty \int_0^{2\pi} r e^{-\frac{i\omega}{c} r \cos \varphi} g_1(r, \varphi) d\varphi dr. \quad (2.57)$$

The wakefield force, including multi-turn effects, is expressed as

$$F = i \frac{\mathcal{D} e^2 \omega_0^2}{4\pi^2 c} e^{-i\Omega s/c} \sum_{k=-\infty}^\infty \tilde{\rho}_1(\omega') Z_\perp(\omega') e^{i\omega' z/c}, \quad (2.58)$$

where  $\omega' = k\omega_0 + \Omega$ . Equations (2.57) and (2.58) are inserted into Eq. (2.55) and all the partial derivatives, apart from  $\partial_\varphi$  can be evaluated. After linearisation in the perturbation  $\Psi_1$ , the Vlasov equation reads

$$\begin{aligned} i [\Omega - \omega_{\beta,0}(1 + \xi^{(1)} \delta) - \omega_s \partial_\varphi] g_1(r, \varphi) &= \frac{e^2 \omega_s}{2\omega_{\beta,0} T_0^2 E_0 \eta} g_0(r) \\ &\times \sum_{k=-\infty}^\infty Z_\perp(\omega') \int_0^\infty \int_0^{2\pi} \tilde{r} e^{\frac{i\omega'}{c} (r \cos \varphi - \tilde{r} \cos \tilde{\varphi})} g_1(\tilde{r}, \tilde{\varphi}) d\tilde{\varphi} d\tilde{r}. \end{aligned} \quad (2.59)$$

To integrate the equation over  $\varphi$ ,  $g_1(r, \varphi)$  is decomposed into a series of azimuthal modes  $g_1^l(r, \varphi)$

$$g_1(r, \varphi) = \sum_{l'=-\infty}^\infty R_{l'}(r) e^{il'\varphi} e^{i\xi^{(1)} \frac{\omega_{\beta,0}}{\eta c} r \cos \varphi}, \quad (2.60)$$

using the fact that  $g_1(r, \varphi)$  has a  $2\pi$ -periodicity in  $\varphi$ . It can be verified that the functions  $g_1^l(r, \varphi)$  are the eigenmodes of the *free* ( $Z_\perp \equiv 0$ ) Vlasov equation (2.59), where  $l$  denotes the azimuthal mode number. The corresponding eigenvalues are given by  $\Omega^{(l)} = \omega_{\beta,0} + l\omega_s$ , for  $l \in \mathbb{Z}$ . Plugging the decomposed  $g_1(r, \varphi)$  into Eq. (2.59) and after multiplying both sides with  $e^{-il\varphi}$ , one can perform the integration over  $\varphi$  and obtains an “infinite” set of equations

$$\begin{aligned} \left( \Omega^{(l)} - \omega_{\beta,0} - l\omega_s \right) R_l(r) = iK g_0(r) \sum_{l', k=-\infty}^{\infty} \int_0^\infty r' R_{l'}(r') i^{l-l'} \\ \times Z_\perp(\omega') J_l \left( \frac{\omega' - \omega_\xi}{c} r \right) J_{l'} \left( \frac{\omega' - \omega_\xi}{c} r' \right) dr', \text{ for } l \in \mathbb{Z}. \end{aligned} \quad (2.61)$$

$J_l(x)$  denotes the Bessel functions of the first kind. Furthermore, the definitions  $\omega_\xi = \xi^{(1)} \omega_{\beta,0} / \eta$  and  $K = \pi e^2 \omega_s / \omega_{\beta,0} T_0^2 E_0 \eta$  have been introduced. Finally, using the above expression for  $\Omega^{(l)}$  one obtains  $\omega' = k\omega_0 + \omega_{\beta,0} + l\omega_s$ . The result in Eq. (2.61) is equivalent to Chao's Eq. (6.179) in Ref. [25]. The impedance-induced frequency shift  $\Delta\Omega$  described in Section 2.2.2 is related to  $\Omega^{(l)}$  through  $\Delta\Omega^{(l)} = \Omega^{(l)} - \omega_{\beta,0} - l\omega_s$ , i.e. the shift is measured with respect to the unperturbed frequency of the unstable synchrotron sideband associated with the mode.

#### 2.2.4 Circulant matrix model

The circulant matrix model (CMM) is a powerful description of many beam dynamics aspects in synchrotrons [51–53]. In the CMM, the longitudinal phase space  $(z, \delta)$  of a bunch is discretised radially and azimuthally as illustrated in Fig. 2.4. The discretisation is characterised by the number of rings  $N_r$  and slices  $N_s$ , and the total number of cells is given by the product  $N_c = N_r \times N_s$ . Each cell  $i$  has two corresponding transverse coordinates and momenta  $(u_i, u'_i)$ , again with  $u \in \{x, y\}$ , but the formalism can also be extended to the full four-dimensional transverse phase space. By assigning appropriate weights to every cell, one can model different particle distributions. The transverse state of the bunch at turn  $j$  is described by a vector

$$\mathbf{u}_j = \begin{pmatrix} u_{1,j} \\ u'_{1,j} \\ \vdots \\ u_{N_c,j} \\ u'_{N_c,j} \end{pmatrix}. \quad (2.62)$$

The goal is to first define the unperturbed one-turn matrix  $M_0$  describing the synchrotron and betatron motion of the beam, such that  $\mathbf{u}_{j+1} = M_0 \mathbf{u}_j$ , and then to include the effects of the beam-coupling impedance. By diagonalising the full one-turn matrix one calculates the eigenfrequencies and eigenmodes of the beam and can hence assess the stability of the system. Although the model is ideally suited to describe multi-bunch beams, only single bunches are considered here. Furthermore, purely the effects of the beam-coupling impedance are included in this discussion and we limit ourselves to the key points that characterise the model. A thorough description including beam-beam effects can be found, e.g., in Refs. [51–54].

The unperturbed one-turn synchro-betatron matrix for a single bunch executing linear synchrotron

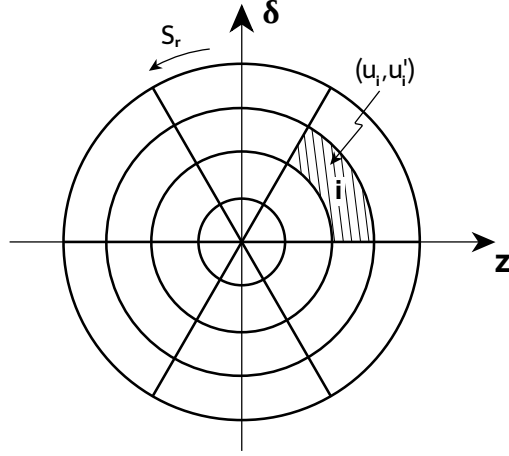


Figure 2.4: Longitudinal phase space discretisation for the CMM.

and betatron motion can be described by

$$M_0 = \frac{1}{N_r N_s} \mathbb{1}_{N_r} \otimes S_r \otimes B_\beta, \quad (2.63)$$

where  $\otimes$  denotes the Kronecker product,  $\mathbb{1}_n$  is the  $n \times n$ -dimensional identity matrix, and  $B_\beta$  is the betatron block matrix composed of submatrices

$$B_{u,\beta} = \begin{pmatrix} \cos(2\pi Q_u) & \beta_u \sin(2\pi Q_u) \\ -\frac{1}{\beta_u} \sin(2\pi Q_u) & \cos(2\pi Q_u) \end{pmatrix}, \quad (2.64)$$

each representing the betatron motion for one of the cells.  $S_r = (P_{N_s})^{N_s Q_s}$  is the circulant matrix which describes the synchrotron motion through a permutation matrix which rotates all the cells in longitudinal phase space as illustrated in Fig. 2.4. The pure permutation matrix is given by

$$P_{N_s} = \begin{pmatrix} 0 & 1 & 0 & \cdots & 0 \\ 0 & 0 & 1 & \ddots & 0 \\ \vdots & \vdots & \ddots & \ddots & \vdots \\ 0 & 0 & \cdots & 0 & 1 \\ 1 & 0 & \cdots & 0 & 0 \end{pmatrix}, \quad (2.65)$$

and does not include chromaticity effects. To add first-order chromaticity, for example, it can be extended with a multiplication of a diagonal phase matrix from the right

$$\tilde{S}_r = \left[ P_{N_s} \cdot \begin{pmatrix} e^{-ik\delta_1} & \cdots & 0 \\ \vdots & \ddots & \vdots \\ 0 & \cdots & e^{-ik\delta_{N_s}} \end{pmatrix} \right]^{N_s Q_s}, \quad (2.66)$$

with  $k = \frac{2\pi Q'_u}{N_s Q_s}$  [54]. The identity matrix  $\mathbb{1}_n$  corresponds to the assumption that all the rings have the

same synchrotron tune (linear synchrotron motion). It is possible to replace the identity matrix such that every ring has its own specific synchrotron tune to better approximate the dynamics of the rf bucket (amplitude-dependent synchrotron tune).

Finally, the wakefield effect on slice  $i$  is modelled as a kick of the form

$$\Delta u'_i = \mathcal{C} \sum_j W_u^{\text{dip}}(z_j - z_i) u_j, \quad z_j > z_i, \quad (2.67)$$

taking into account all the contributions of source cells  $j$  that are ahead of target cell  $i$ , assuming again the ultra-relativistic limit.  $W_u^{\text{dip}}(z)$  denotes the dipole wakefield in the transverse plane  $u$  and  $\mathcal{C}$  is a constant that is defined by the machine and beam parameters. The wakefield matrix has to be multiplied to the synchro-betatron matrix  $M_0$  defined in Eq. (2.63) to obtain the full circulant matrix system. To compute the coherent tune shifts of all the allowed head-tail modes, given by the number of slices and rings, one diagonalises the full one-turn matrix. This can be done numerically, for example, using the BMBIM code [52]. A significant limitation of the circulant matrix model is that multi-turn wakefields cannot be described within this framework.

### 2.2.5 Landau damping

In its original form, Landau damping describes the collisionless damping of collective oscillations (Langmuir waves) in plasmas. It was first discovered by Landau in 1946 and was published in Ref. [24]. A similar damping effect is observed for the particle beams in accelerators where coherent intra-bunch modes may be stabilised thanks to a spread in the betatron frequencies among the particles within a bunch [25, 55]. The goal of this section is to outline the mathematical derivation by providing an overview of the key pillars: the dispersion relation, stability boundary diagrams, and the betatron frequency spread.

#### Dispersion relation

We start from a harmonic oscillator of natural frequency  $\omega$ , driven by an oscillating force of frequency  $\Omega$  and amplitude  $A$  starting at time  $t = 0$ . It is convenient to write the equations in complex notation, considering that only the real parts are meaningful

$$\ddot{x}(t) + \omega^2 x(t) = A e^{-i\Omega t}, \quad (2.68)$$

with initial conditions  $x(0) = 0$  and  $\dot{x}(0) = 0$ . Assuming that a system is composed of  $N$  such oscillators with a frequency distribution  $\rho(\omega)$  one can write down the equation for the centroid response to the external excitation

$$\langle x \rangle(t) = \int_{-\infty}^{\infty} x(t) \rho(\omega) d\omega. \quad (2.69)$$

It can be shown that the ensemble of oscillators considered here has an *asymptotic*<sup>1</sup> ( $t \rightarrow \infty$ ) complex response [see Ref. [25], Eqs. (5.10) and (5.36)]

$$\langle x \rangle(t) = \frac{A}{2\omega_\beta} e^{-i\Omega t} \int_{-\infty}^{\infty} \frac{\rho(\omega)}{\omega - \Omega} d\omega. \quad (2.70)$$

<sup>1</sup>We are not interested in the transient effects at the onset of the driving force at  $t = 0$ .

Here, we have assumed a narrow frequency spectrum  $\rho(\omega)$  around the frequency  $\omega_\beta$  and that  $\Omega \approx \omega_\beta$ . To avoid the singularity at  $\omega = \Omega$  while performing the integral over  $\omega$ , one makes use of the Landau bypass rule. The idea is to define an integration path in the complex plane of  $\omega$ . One integrates along the real axis of  $\omega$  except for the pole at  $\omega = \Omega$  which is circumvented by an integration along a semicircle (see Fig. 5.4 in Ref. [25]). The first part of the integration corresponds to the Cauchy principal value (P. V.), while the second one leads to the pole contribution  $i\pi\rho(\Omega)$ , such that

$$\langle x \rangle(t) = \frac{A}{2\omega_\beta} e^{-i\Omega t} \left[ \text{P. V.} \int \frac{\rho(\omega)}{\omega - \Omega} d\omega + i\pi\rho(\Omega) \right]. \quad (2.71)$$

Alternatively, one can bypass the pole by shifting the integration path by a (positive or negative) infinitesimal, imaginary, amount  $i\varepsilon$ , i.e.  $(\omega - \Omega) \rightarrow (\omega - \Omega - i\varepsilon)$ , such that

$$\langle x \rangle(t) = \frac{A}{2\omega_\beta} e^{-i\Omega t} \int_{-\infty}^{\infty} \frac{\rho(\omega)}{\omega - \Omega - i\varepsilon} d\omega. \quad (2.72)$$

Using the definitions

$$\begin{aligned} f(u) &= \Delta\omega \text{ P. V.} \int \frac{\rho(\omega)}{\omega - \Omega} d\omega, \\ g(u) &= \pi \Delta\omega \rho(\omega_\beta - u \Delta\omega), \end{aligned} \quad (2.73)$$

with  $u = (\omega_\beta - \Omega)/\Delta\omega$ , and  $\Delta\omega$  the frequency spread of the beam spectrum, the asymptotic beam response can be expressed as

$$\langle x \rangle(t) = \frac{A}{2\omega_\beta \Delta\omega} e^{-i\Omega t} [f(u) + ig(u)]. \quad (2.74)$$

The response of a beam to a sinusoidal driving force is hence mostly defined by the dimensionless term  $f(u) + ig(u)$ , also known as the beam transfer function (BTF). The BTF is an important quantity since it can be measured in an actual machine. It can reveal direct information about the amount of Landau damping present in the system.

We now apply the results obtained above to a bunch composed of  $N$  particles. Every particle oscillates at its own betatron frequency  $\omega$  such that the bunch possesses a natural frequency spread. Each individual particle fulfils the equation of motion

$$u''(s) + \left(\frac{\omega}{c}\right)^2 u(s) = -\frac{Ne^2}{C\gamma m_p c^2} \sum_{j=1}^{\infty} \langle u \rangle(s - jC) W_u^{\text{dip}}(-jC), \quad (2.75)$$

where  $u \in \{x, y\}$  is the transverse coordinate of the particle and we have again assumed the ultra-relativistic limit ( $\beta = 1$ ). Here, the driving force on the right hand side of the equation is given by a dipolar wakefield. The sum over  $j$  accounts for multi-turn effects. As explained in Section 2.2.2, in the event of an instability the bunch centroid amplitude evolves according to an exponential function

$$\langle u \rangle(s) = B e^{-i\Omega s/c}, \quad (2.76)$$



## 2.2. Transverse impedance-driven single-bunch instabilities

where  $B$  is the initial ( $s = 0$ ) amplitude of the oscillation. Substituting Eq. (2.76) into Eq. (2.75) yields

$$u''(s) + \left(\frac{\omega}{c}\right)^2 u(s) = -\frac{BNe^2}{C\gamma m_p c^2} \mathcal{W} e^{-i\Omega s/c}, \quad (2.77)$$

where  $\mathcal{W} = \sum_{j=1}^{\infty} W_u^{\text{dip}}(-jC) e^{i\omega_\beta j T_0}$ ,  $T_0 = C/c$ , and we have assumed that the mode frequency shift is small such that  $\Omega \approx \omega_\beta$  with  $\omega_\beta$  the centre of the frequency spectrum of the bunch. Equation (2.77) shows that the bunch is driven by an oscillatory force of the form  $Ae^{-i\Omega s/c}$  of which we already know the solution from Eq. (2.72) [alternatively Eqs. (2.71) or (2.74)]

$$\langle u \rangle(s) = -\frac{BNe^2 \mathcal{W}}{2C\gamma m_p c^2 \omega_\beta} e^{-i\Omega s/c} \int_{-\infty}^{\infty} \frac{\rho(\omega)}{\omega - \Omega - i\varepsilon} d\omega. \quad (2.78)$$

However, we have assumed above that the collective motion of the bunch  $\langle u \rangle(s)$  follows Eq. (2.76). As a result, given that the beam motion is non-trivial ( $B \neq 0$ ) the mode frequency  $\Omega$  must obey a self-consistency condition called the *dispersion relation*

$$1 = -\frac{Ne^2 \mathcal{W}}{2C\gamma m_p c^2 \omega_\beta} \int_{-\infty}^{\infty} \frac{\rho(\omega)}{\omega - \Omega - i\varepsilon} d\omega. \quad (2.79)$$

It can be shown that the impedance-induced *unperturbed* frequency shift  $\Delta\Omega_{\text{lin}} = (\Omega - \omega_\beta)_{\text{lin}}$  of the mode, i.e. in absence of frequency spread and Landau damping (linear lattice), corresponds to [25]

$$\Delta\Omega_{\text{lin}} = \frac{Ne^2 \mathcal{W}}{2C\gamma m_p c^2 \omega_\beta}, \quad (2.80)$$

and the dispersion relation becomes

$$-\frac{1}{\Delta\Omega_{\text{lin}}} = \int_{-\infty}^{\infty} \frac{\rho(\omega)}{\omega - \Omega - i\varepsilon} d\omega. \quad (2.81)$$

This equation contains all the information about the Landau damping present in the system under consideration. It can be solved, for example, through numerical integration which yields the *stability boundary diagrams* discussed in the next paragraph. The frequency distribution  $\rho(\omega)$  can usually be replaced by a term that depends explicitly on the transverse or longitudinal amplitudes of the particles as discussed below. The frequency distribution depends on the method used to introduce the spread. For example, with magnetic octupoles or from beam-beam interactions,  $\rho(\omega) \rightarrow \Delta\omega = \Delta\omega(J_x, J_y)$ . The dispersion relation for this case can be found, for instance, in Ref. [28]. This thesis, however, focuses on detuning with longitudinal amplitude, i.e.  $\rho(\omega) \rightarrow \Delta\omega = \Delta\omega(J_s)$ . The dispersion relation for the latter will be derived and explained in Chapter 4 by extending Vlasov's formalism.

### Stability boundary diagrams

A practical approach to illustrate and assess the Landau damping generated by an incoherent frequency spread in accelerators is to use stability diagram theory [28]. Figure 2.5 illustrates the concept based on the example of betatron detuning with transverse amplitude  $\Delta\omega(J_x, J_y)$ , e.g. introduced by octupole magnets [28, 56]. The figure shows the complex frequency space  $\text{Re}\Delta\Omega$  vs.  $-\text{Im}\Delta\Omega$ , centred about the unperturbed coherent frequency of the mode under consideration. Every head-tail instability can be characterised by its unperturbed coherent tune shift  $\Delta\Omega_{\text{lin}}$  which is represented by a point in the

complex plane (e.g. the blue cross). The stability boundary diagram separates the plane into regions of stable (below the boundary) and unstable (above the boundary) modes. For example, if there is no frequency spread and hence no Landau damping, the stability boundary is given by the red line shown in the figure. In that case, only the head-tail modes with  $-\text{Im} \Delta\Omega < 0$  are stable, a result that was already obtained in Section 2.2.2. By introducing a frequency spread, the stability boundary gets distorted and starts to reach into the upper half of the complex plane (orange line), making the system more stable. Every mode whose unperturbed frequency shift has become part of the area underneath the curve is now stable thanks to the tune spread and the Landau damping mechanism. In the figure, the specific mode represented by the blue cross would still be unstable in case of moderate Landau damping, however, with a slower rise time. With an even larger frequency spread and hence more Landau damping, the mode is eventually included in the stable region (green line). The available Landau damping is typically defined by the amount of frequency spread that can be produced among the particles within a bunch. A larger frequency spread can be obtained, for example, by introducing higher integrated octupolar field strengths, or by using alternative, more effective detuning mechanisms as explained below. The large frequency spread usually has a negative impact on the beam lifetime, however, due to resonance lines that are driven by imperfections in the accelerator lattice.

Stability boundary diagrams are computed from the dispersion relation which has the form of Eq. (2.81). The idea is to determine how the real axis ( $\text{Im} \Delta\Omega = 0$ ) in presence of frequency spread, maps onto the unperturbed frequency shifts  $\Delta\Omega_{\text{lin}}$ . Or, in other words, the objective is to figure out all the (unperturbed) frequency shifts that are just at the limit of stability once the frequency spread is introduced. This is achieved by (numerically) performing the integral over  $d\omega$  for real-valued  $\Omega$ , and for  $\varepsilon \rightarrow 0$ .

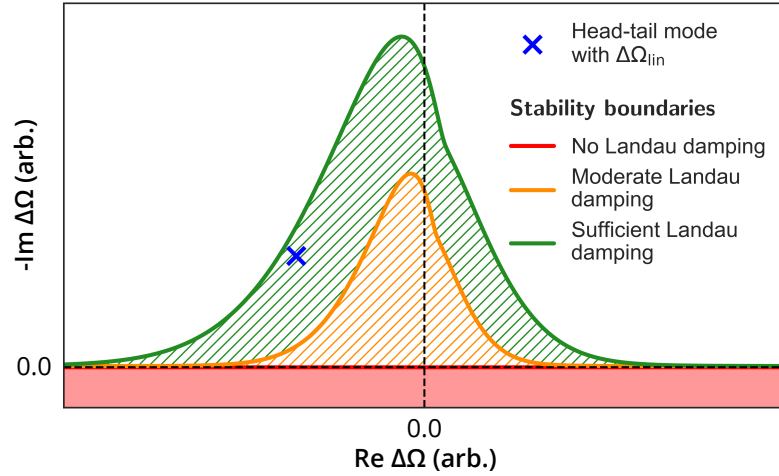


Figure 2.5: Illustration of stability boundary diagrams for Landau damping.

### Incoherent tune spread

The incoherent tune spread required for Landau damping is introduced partially by the nonlinear magnetic fields, magnet imperfections, space charge, beam-beam forces during collision, etc. Some of these parasitic sources, however, are small in modern colliders due to the high accuracy of the nonlinear optics corrections. And, although the tune spread provided by the beam-beam interaction, for example, is a very strong source of Landau damping, it is not present during the first stages of the machine cycle

## 2.2. Transverse impedance-driven single-bunch instabilities

where the beams are not yet in collision. In these early phases of the cycle, it is hence necessary to have dedicated nonlinear elements at hand that can provide betatron detuning in a controlled manner to stabilise the beams.

Traditionally, magnetic octupoles are used for that purpose. They introduce a betatron detuning depending on the transverse action  $J_{u,i}$ ,  $u \in \{x, y\}$ , of a particle  $i$  (first-order amplitude detuning). This can be derived assuming a single octupole magnet installed in an otherwise linear machine lattice, e.g. described in Ref. [38]. The horizontal angular kick on particle  $i$  from a (thin) octupole magnet is given by  $\Delta x'_i = g(3x_i y_i^2 - x_i^3)$ , where  $g$  is proportional to the magnetic field strength of the octupole element. In the following, the only term of interest to us is  $-gx_i^3$  since it is the contribution that introduces detuning with amplitude. Using trigonometry and the known solutions of the betatron motion, one can demonstrate that this single kick introduces an additional incoherent phase advance of  $\Delta\phi_{x,i} = ga_{x,i}^2 \sin^4(\phi_{x,i})$ , where  $a_{x,i}$  is the transverse amplitude of the given particle and  $a_{x,i}^2 = 2J_{x,i}$ . The betatron phase of the particle evolves over time as  $\phi_{x,i}(t) = 2\pi\omega_0 Q_{x,0}t + \phi_{i,0}$  neglecting the additional phase advance from the octupole kicks. Given that  $\phi_{x,i}(t)$  (modulo  $2\pi$ ) is evenly distributed in the interval  $[0, 2\pi)$  as  $t \rightarrow \infty$ , which is true if the bare tune  $Q_{x,0}$  is not a rational fraction, the average additional phase advance per turn generated by the octupole kick on particle  $i$  reads

$$\langle \Delta\phi_{x,i} \rangle = ga_{x,i}^2 \langle \sin^4(\phi_{x,i}) \rangle = \frac{3}{8}ga_{x,i}^2, \quad (2.82)$$

which translates into a tune change of  $\Delta Q_{x,i} = 3gJ_{x,i}/8\pi$  demonstrating betatron detuning with transverse amplitude. It can be analogously shown that detuning with amplitude is introduced also in the vertical plane.

Multipoles with even orders in the exponent of the kick (e.g. sextupoles, decapoles, etc.) do not produce detuning with amplitude to *first order* in  $g$ , because  $\langle \sin^{2m+1}(\phi_{x,i}) \rangle = 0$ ,  $m \in \mathbb{N}_0$ . This is, however, no longer true for instance for sextupole magnets at second order as explained in Ref. [57] and discussed in Chapter 6. Some multipoles, such as octupole magnets also introduce a second-order detuning with amplitude  $\partial^2 Q_x / \partial (2J_x)^2$  as a second-order contribution [58]. Additionally, when placed in dispersive regions, i.e.  $x_i \rightarrow x_i + D_x \delta_i$ , it can be demonstrated that an octupole kick introduces second-order chromatic effects [59]. This will be discussed further in Chapter 7.

In general, the octupole kicks are distributed along the lattice and it is common that two families of octupole magnets are installed, one focusing (at high  $\beta_x$ , low  $\beta_y$ ) and one defocusing (at low  $\beta_x$ , high  $\beta_y$ ), to optimise the shape of the incoherent tune spread to provide an equal amount of Landau damping in both transverse planes (see, e.g., Ref. [60]). The general linear detuning formulae for magnetic octupoles can be expressed as

$$\begin{aligned} \Delta Q_x(J_x, J_y) &= a_{xx}2J_x + a_{xy}2J_y, \\ \Delta Q_y(J_x, J_y) &= a_{yy}2J_y + a_{yx}2J_x, \end{aligned} \quad (2.83)$$

where the particle index has been omitted. The parameters  $a_{uv}$ , with  $u, v \in \{x, y\}$  are called anharmonicities or detuning coefficients. They depend on the one-turn integrated octupole field strengths weighted with the beta functions at the location of the magnets and are inversely proportional to the magnetic rigidity of the beam [60]. The two cross-detuning coefficients are identical, i.e.  $a_{xy} = a_{yx}$ . Equation (2.83) shows that for a fixed beam energy, machine optics, and octupole strengths, the amount of tune spread, and hence in a first approximation the amount of Landau damping, depends on the

spreads in the transverse actions, defined by the geometric transverse emittances  $\epsilon_{x,y}^{\text{geo}}$  of the beam. Since  $a_{uv} \propto 1/\gamma$  and  $\epsilon_{x,y}^{\text{geo}} \propto 1/\gamma$ , the tune spreads are reduced as  $\Delta Q_{x,y} \propto 1/\gamma^2$ . Thus, for future, high-energy, low-emittance beams, Landau octupoles may no longer be the most suitable solution to provide the tune spreads.

In view of the new Landau damping approach studied in this thesis, where the betatron tunes become dependent on the longitudinal oscillation amplitude, a more general description of detuning with amplitude is desirable. We limit ourselves to a linear dependence of the betatron and synchrotron tunes ( $Q_x, Q_y, Q_s$ ) on the particle actions ( $J_x, J_y, J_s$ ). In this frame, the dependence of the tunes can be expressed through a  $3 \times 3$  matrix equation

$$\begin{pmatrix} Q_x \\ Q_y \\ Q_s \end{pmatrix} = \begin{pmatrix} Q_{0,x} \\ Q_{0,y} \\ Q_{0,s} \end{pmatrix} + \begin{pmatrix} a_{xx} & a_{xy} & a_{xs} \\ a_{yx} & a_{yy} & a_{ys} \\ a_{sx} & a_{sy} & a_{ss} \end{pmatrix} \begin{pmatrix} 2J_x \\ 2J_y \\ 2J_s \end{pmatrix}, \quad (2.84)$$

The vector  $(Q_{x,0}, Q_{y,0}, Q_{s,0})$  contains the unperturbed (bare) machine tunes. The transverse and longitudinal detuning coefficients have been combined in the  $3 \times 3$  matrix. For completeness, the amplitude dependence of the synchrotron tune  $Q_s$  is also included. The synchrotron tune spread can introduce Landau damping in the longitudinal plane.

## 2.3 Numerical models and computer codes

This section introduces the two main accelerator physics codes that are used throughout this thesis to study impedance-driven collective effects. The first model is a macroparticle tracking code and the second one is a circulant matrix solver.

### 2.3.1 PYHEADTAIL

PYHEADTAIL is a 6D macroparticle tracking code under development at CERN and is the successor of the HEADTAIL program [61, 62]. The purpose of the software is to accurately and effectively model the formation of collective instabilities in synchrotrons to make the study of the involved mechanisms possible, and to develop and evaluate appropriate mitigation techniques.

The basic PYHEADTAIL model represents a particle bunch as a collection of macroparticles, each of which is described by a mass, an electric charge, and its generalised coordinates and canonically conjugate momenta with two longitudinal and four transverse dimensions. Depending on the scenario (type of machine, its impedance, beam parameters), typically of the order of  $10^6$  macroparticles are required for an accurate representation of a proton bunch. There are various transverse and longitudinal initial distributions available, such as Gaussian, waterbag, or airbag models. It is also possible to match a longitudinal distribution to a multi-harmonic rf bucket. The accelerator ring is divided into a number of segments. At the end of every segment there is an interaction point where the macroparticles experience collective effects (wakefields, space charge, etc.), kicks from a specific accelerator component such as a transverse feedback system, or pass through an aperture element allowing to identify particles that leak out of the rf bucket longitudinally or hit the vacuum pipe transversely. The betatron motion between two consecutive interaction points is modelled with linear

maps which take into account the Twiss parameters and the dispersion at the start and at the end of the connecting segment. Nonlinear tracking features such as chromaticity, up to arbitrary orders, are modelled as a change in the phase advance of each individual macroparticle in the beam. The betatron detuning with transverse amplitude introduced by magnetic octupoles, for example, is parametrised by the effective machine anharmonicities  $a_{uv}$ , with  $u, v \in \{x, y\}$ , and is implemented in the same manner. The synchrotron motion is either linear or nonlinear with the possibility to include particle acceleration and the effects of multi-harmonic rf systems. Depending on the problem at hand, between  $10^5$  to several  $10^6$  turns are usually required for the simulations. This number determines the slowest possible instability growth rates that can still be resolved.

The effect of the beam-coupling impedance is implemented in time domain in the form of wakefield kicks. Usually, the total machine impedance is lumped in one location of the ring and its effect is applied only there (one segment, smooth approximation). To further improve the computational efficiency, the bunch is divided longitudinally into a specific number of (uniform) slices and the wakefield kicks are calculated on a slice-by-slice basis where each slice acts as both a wakefield source and witness. The longitudinal slicing extends usually between two to four rms bunch lengths in both directions. The particles located outside of the slicing region do not generate or receive wakefield kicks, but are still tracked through the accelerator ring. The kicks are computed using a convolution of the wake function with respectively the zeroth (for constant and quadrupole wakes), or first (for dipole wakes) moments of each slice. Typically, dipole and quadrupole wakefields are considered, also including the wake-in-front for low-beta machines if needed. In addition, PYHEADTAIL offers the possibility to account for multi-bunch and multi-turn wakefield effects. The wake function of the machine, or a particular element, can be defined either as a combination of a resistive wall and broad- and narrow-band resonators (analytical formulae), or imported from a table. The latter option is normally chosen as it allows the input of a specific, detailed impedance model of a machine created with dedicated electromagnetic finite-element solvers (see, e.g., Ref. [63]).

PYHEADTAIL being a macroparticle tracking code does not directly compute and output the coherent frequency shifts of the head-tail modes. Instead, the user chooses to save bunch-, slice-, or particle-specific data using the bunch, slice, or particle monitors respectively. Often, for the analysis of head-tail instabilities, the light-weight bunch monitor is sufficient. It stores, for example, the bunch centroid evolution in time domain. In the event of an instability, the amplitude of the bunch centroid oscillation rises exponentially. After a certain latency time, which depends, among others, on the initial particle distribution that determines the “seeding” of the instability, there is usually one dominant (aka. most unstable) mode that establishes and is responsible for the amplitude growth. The growth rate of the exponential hence corresponds to the imaginary part of the coherent frequency shift of the most unstable mode. The other head-tail modes that are present, but possibly stable or at least have a much slower rise time, cannot be accessed through time domain analysis. One method to obtain the imaginary frequency shifts of individual azimuthal modes is to analyse the growth rates of each synchrotron sideband in the frequency domain using a sliding-window Fourier transform. With this technique, stable modes can in principle also be assessed by exciting them and measuring their rate of decay. For the studies presented in this thesis, both time- and frequency domain analysis methods have been employed for comparison, and an excellent agreement was always found on the growth rate of the most unstable mode. To obtain the real part of the coherent frequency shift, a frequency analysis of the centroid motion is performed, either employing a Fast Fourier Transform (FFT) or the SUSSIX algorithm [64]. The shift is typically measured with respect to the unperturbed synchrotron sideband.

### 2.3.2 BIMBIM

BIMBIM is an accelerator physics code developed at CERN and its main purpose is to model beam-beam and wakefield effects [52, 53]. The underlying scheme is the CMM described in Section 2.2.4. BIMBIM solves the circulant matrix and outputs directly the complex coherent frequency shifts of all the allowed (stable and unstable) modes. Naturally, the chosen number of slices and rings for the discretisation of the longitudinal phase space puts a limit on the maximum order of the unstable mode that can be described by the model. Since the formalism is based on matrices, it only accounts for linear dependencies on the transverse phase space variables, and hence it cannot model, for instance, detuning with transverse amplitude as introduced by Landau octupoles. In the longitudinal plane, however, nonlinear dependencies are correctly described and hence arbitrary orders of chromaticity can be included. Another important limitation of the code is that it assumes the wakefield to decay within one turn. While this is a valid approximation for broad-band resonator impedances, it is no longer fulfilled for narrow-band resonators with large quality factors. For the latter, the wakefields typically keep ringing for several turns. The two limitations are the main differences with respect to PYHEADTAIL concerning the scenarios studied throughout this thesis.

## 3 Betatron detuning with longitudinal amplitude

Landau damping is present when there is an amplitude-dependent spread in the betatron frequencies of the particles within a bunch. Traditionally, the frequency spread is purposely introduced by means of magnetic octupoles. The underlying mechanism is referred to as betatron detuning with *transverse* amplitude and has already been explained in Section 2.2.5. An alternative approach studied in this thesis is to introduce betatron detuning with *longitudinal* amplitude. From theoretical considerations, the latter promises to be much more effective than the former, particularly in future hadron colliders. The reason is that the spread in actions, i.e. the beam emittances, is orders of magnitude larger in the longitudinal compared to the transverse planes, for instance for the beams of HL-LHC, HE-LHC, or FCC-hh.

This chapter discusses two different methods to generate detuning with longitudinal amplitude. First, it introduces the rf quadrupole cavity, originally proposed by Grudiev at CERN [29], in Section 3.1. The design and working principle of this device are explained as well as its main features. It is, furthermore, compared to the traditional Landau damping approach which employs magnetic octupoles. Thereafter, nonlinear chromaticity is discussed in Section 3.2 as an alternative method to provide a betatron tune spread that depends on the longitudinal amplitude of the particles. It is demonstrated that both the rf quadrupole and the even orders of chromaticity, in particular the second order, share the same underlying mechanisms and hence influence the beam dynamics in an equivalent manner. Finally, in Section 3.3, the existing stability diagram theory for betatron detuning with longitudinal amplitude is briefly recapitulated. The chapter is partially based on the work published in Refs. [33, 65–67].

### 3.1 Radio-frequency quadrupole

This section gives a brief overview on the main aspects of an rf quadrupole. It discusses first two cavity designs explaining the main differences between the two geometries as well as the relevant parameters that have been optimised [29, 68]. Subsequently, the basic working principle of the device is explained by deriving an analytical formula for the incoherent betatron detuning that it generates. Finally, the features and potential advantages over conventional stabilising methods are discussed in more detail in terms of the mitigation of collective instabilities.

### 3.1.1 Description

The purpose of an rf quadrupole cavity is to generate transverse quadrupole kicks on the particles within a bunch with a strength that depends on their longitudinal position. Every particle is subject to a different focusing (defocusing) force as it passes through the device and hence experiences a change in the betatron tunes depending on its longitudinal position. This results in an incoherent betatron tune spread along the bunch which can provide Landau damping of transverse collective instabilities.

The frequency of the rf quadrupole described in this study is chosen to be 800 MHz for two reasons. First, the bunches of HL-LHC, HE-LHC, and FCC-hh are foreseen to have lengths in the order of  $\sigma_z \approx 0.1$  m [18, 69] (compare also Table 1.1). An rf quadrupole operating at 800 MHz thus has an rf wave length that is comparable to the bunch length and provides the best beam stabilising efficiency according to numerical simulations. Second, for practical reasons, the rf quadrupole frequency is limited to harmonics of the main rf system (400 MHz) of the aforementioned machines. Numerical evaluations with other frequencies have been performed for the HL-LHC during this thesis and are reported in Ref. [70].

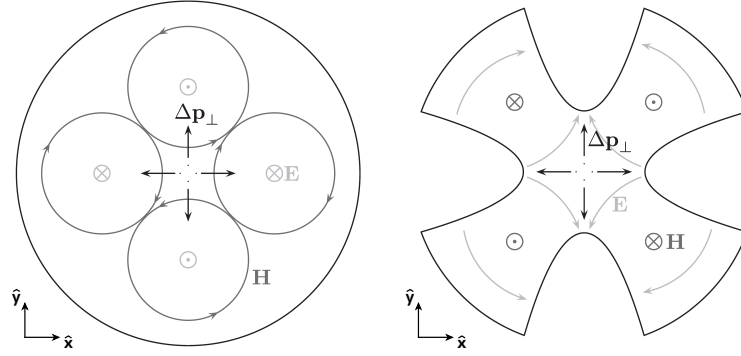


Figure 3.1: Qualitative description of the electromagnetic quadrupole fields leading to transverse kicks on charged particles (cross-section). The directions of the momentum changes  $\Delta \mathbf{p}_\perp$  are indicated for a positively charged particle. *Left*: Elliptical cavity type operating in a TM mode. *Right*: Four-vane cavity operating in a TE mode (images from Ref. [68]).

Reference [68] proposes two different cavity designs for a superconducting rf quadrupole. The two types have been thoroughly optimised primarily for quadrupolar field strength  $b_2$ , but also in terms of transverse and longitudinal beam-coupling impedance, and peak electric  $E_{pk}$  and magnetic  $B_{pk}$  surface fields. While the first type is an elliptical cavity operating in a transverse magnetic (TM) quadrupolar mode, the second one is a four-vane cavity operating in a transverse electric (TE) quadrupolar mode. The geometry of the latter was motivated by the rf quadrupole (RFQ) linac [71]. Its design was chosen to reach higher quadrupole field strengths at smaller cavity size. A cross-section of the quadrupole fields for the two cavity types is given in Fig. 3.1. The directions of the transverse kicks  $\Delta \mathbf{p}_\perp$  on a positively charged particle passing the device off-axis at a specific moment in time are indicated by the black arrows.

The goal of the cavity optimisation procedure was primarily to determine a geometry that provides the largest quadrupole field strength at the lowest surface fields and impedance. For the elliptical cavity, the  $\text{TM}_{210}$  mode is the best choice for that purpose. An illustration of the normalised magnetic (left)



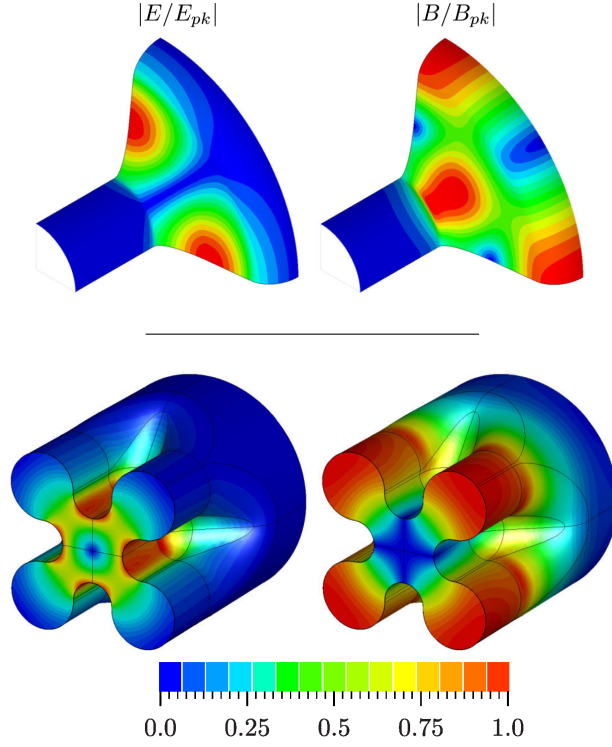


Figure 3.2: Normalised electric (left) and magnetic (right) fields for an octant of the elliptical (top) and for half of the four-vane (bottom) cavity respectively (images from Ref. [68]).

and electric (right) field distributions for this particular mode is given in the upper part of Fig. 3.2 showing one octant of the elliptical cavity. The geometry and the corresponding field distributions of the four-vane cavity are depicted in the lower part of the figure. The main advantages of the four-vane cavity compared to an elliptical one are: (1) the quadrupole field strength per cavity is up to two to five times larger than that of the elliptical one, given that the aperture has a radius  $< 50$  mm; and (2) the four-vane cavity is more compact and requires hence smaller cryomodules and less cooling power. As a result, the number of cavities can be reduced and therewith the overall impedance and cost of the system.

The final results of the cavity optimisation study are described in detail in Ref. [68]. The aperture (iris) of the cavity has a major impact on the impedance of the cavity as well as on the achievable maximum quadrupole strength. The increase in maximum quadrupole strength at smaller apertures comes at the expense of higher impedances. The two cavity designs are also very different in terms of performance. For example, the four-vane (4V) and the elliptical (El) cavity reach quadrupole strengths of respectively  $b_2^{4V, \max} = 0.35 \text{ Tm/m}$  and  $b_2^{\text{El}, \max} = 0.16 \text{ Tm/m}$  at a 30 mm iris radius.

### 3.1.2 Working principle

In the thin-lens approximation, an ultra-relativistic particle of index  $i$ , electric charge  $e$ , and momentum  $p$  traversing an rf quadrupole on-axis along the  $z$  direction experiences both transverse and longitudinal

kicks (Panofsky-Wenzel theorem [72])

$$\Delta \mathbf{p}_{\perp,i} = p k_2 (y_i \hat{\mathbf{y}} - x_i \hat{\mathbf{x}}) \cos(\omega_{\text{rfq}} t_i + \varphi_0), \quad (3.1)$$

$$\Delta p_{\parallel,i} = -\frac{\omega_{\text{rfq}}}{2\beta c} p k_2 (x_i^2 - y_i^2) \sin(\omega_{\text{rfq}} t_i + \varphi_0), \quad (3.2)$$

where  $\omega_{\text{rfq}}$  denotes the rf quadrupole angular frequency,  $\hat{\mathbf{x}}$  and  $\hat{\mathbf{y}}$  are the unit vectors along the  $x$  and  $y$  coordinates respectively,  $\varphi_0$  is a constant phase offset that determines the mode of operation of the cavity, and  $t_i$  is the time when the particle traverses the device. The latter is defined with respect to the particle which is at the zero-crossing of the rf quadrupole voltage, and  $t_i = 0$  coincides with the bunch centre. The substitution  $t_i = z_i / \beta c$  gives the longitudinal dependence of the quadrupole kick strength along the particle bunch. The parameter  $k_2$  refers to the amplitude of the normalised integrated quadrupole gradient, including the transit-time factor,

$$k_2 = \frac{e}{\pi \tilde{r} p c} \int_0^{2\pi} \left\| \int_0^L (E_x - c B_y) e^{i\omega_{\text{rfq}} z/c} dz \right\| \cos \tilde{\varphi} d\tilde{\varphi}, \quad (3.3)$$

where  $L$  is the length of the rf quadrupole cavity, and  $[\tilde{r}, \tilde{\varphi}, z]$  are the cylindrical coordinates. As explained in Section 2.1,  $k_2$  can be expressed in magnetic units (Tm/m) using  $b_2 = |B_0 \rho| k_2$ . Depending on their longitudinal position, particles traversing the rf quadrupole experience a different quadrupolar focusing force and hence a change in their betatron tunes

$$\Delta Q_{x,y}^i = \pm \beta_{x,y} \frac{b_2}{4\pi B_0 \rho} \cos\left(\frac{\omega_{\text{rfq}} z_i}{\beta c} + \varphi_0\right), \quad (3.4)$$

where  $\beta_{x,y}$  are the transverse beta functions at the location of the quadrupole kicks. Equation (3.4) describes the detuning that a particle  $i$  experiences from a single passage through the rf quadrupole according to its current longitudinal position  $z_i$  in the bunch. It is equivalent to a tune change introduced by a  $z$ -dependent quadrupole field error. As the particle undergoes synchrotron motion its longitudinal position changes turn after turn and  $z_i$  is hence implicitly dependent on  $t$ . Thus, every time it passes through the device the particle experiences a different kick and a different betatron detuning. Given enough time, the longitudinal turn-by-turn position of the particle will be evenly distributed in the interval  $[-\hat{z}_i, \hat{z}_i]$ , where  $\hat{z}_i$  is its maximum synchrotron oscillation amplitude. This is true as long as the synchrotron tune is not a rational number. Figure 3.3 illustrates the situation for two different rf quadrupole phase offsets  $\varphi_0 = 0$  (top) and  $\varphi_0 = -\pi/2$  (bottom). The grey background represents the particle distribution (Gaussian) in the longitudinal plane. One particle (red) is observed over time as it passes through the rf quadrupole (orange) turn after turn. At every passage it experiences a detuning kick according to its current longitudinal position. The black dashed line corresponds to the interval  $[-\hat{z}_i, \hat{z}_i]$  that the particle eventually traces out as it passes through the rf quadrupole for many turns, i.e. considering a long enough time (several synchrotron periods). The situation is analogous for detuning with transverse amplitude, such as from magnetic octupoles as explained in Section 2.2.5 and in Ref. [38]. The only difference is that for an rf quadrupole, the synchrotron rather than the betatron period is the relevant timescale over which the averaging of the betatron tune shift occurs.

It is clear from Fig. 3.3 that for  $\varphi_0 = 0$  the average detuning of the particles is nonzero which corresponds to a non-vanishing incoherent tune spread. For  $\varphi_0 = -\pi/2$ , however, the average detuning vanishes for all the particles and there is no net tune spread. Hence, to maximise the achievable tune spread

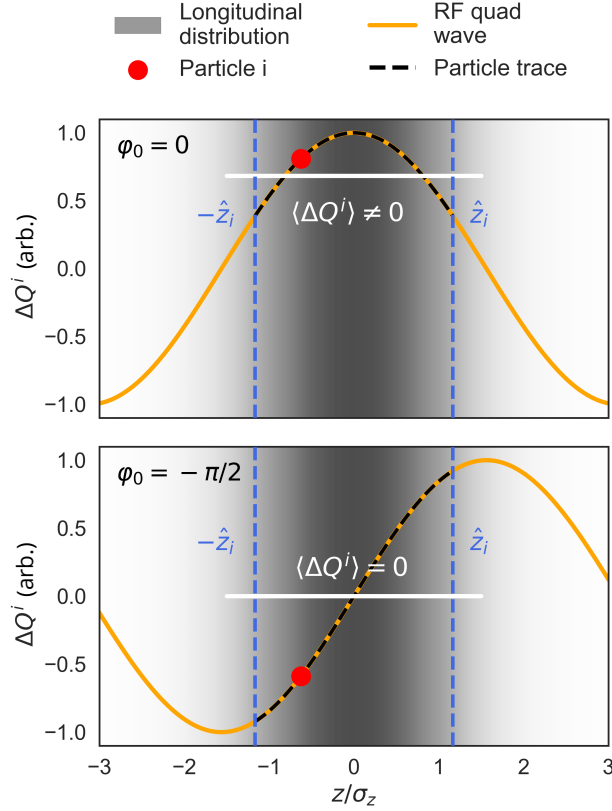


Figure 3.3: Illustration of the betatron detuning that a particle (red) experiences as it passes through the rf quadrupole (orange) turn after turn. Given enough time, the longitudinal position of the particle will be evenly distributed over the interval  $[-\hat{z}_i, \hat{z}_i]$  due to the synchrotron motion. It will hence experience a changing tune shift every time it passes through the device (black dashed curve). If the rf quadrupole phase is  $\varphi_0 = 0$  (top), the average detuning will not vanish and there is a finite incoherent tune spread. For  $\varphi_0 = -\pi/2$ , on the other hand there will be no effective tune spread.

and to prevent it from averaging out over time, the rf quadrupole is operated with a phase of  $\varphi_0 = 0$  or  $\varphi_0 = \pi$ . This is an essential requirement for the Landau damping mechanism to work against the slow head-tail instabilities which typically develop over timescales of many synchrotron periods. Selecting  $\varphi_0 = 0$  means that the device is focusing (defocusing) in the horizontal (vertical) plane for particles in the centre of the bunch  $z_i = 0$ . The situation is inverse for  $\varphi_0 = \pi$ . Equivalently, operating the cavity in one of these two modes means that particles located in the bunch centre enter the device (anti-) on-crest of the rf wave. This is different from earlier studies where an rf quadrupole was proposed to increase the threshold of the TMCI [73, 74]. In that case, the cavity would have to be operated at the zero-crossing of the rf voltage, i.e. with  $\varphi_0 = \pm\pi/2$ .

In the following we set  $\varphi_0 = 0$ . Equation (3.4) can be expanded into a Taylor series in  $z_i$

$$\Delta Q_{x,y}^i = \pm \beta_{x,y} \frac{b_2}{4\pi B_0 \rho} \left[ 1 - \frac{1}{2} \left( \frac{\omega_{\text{rfq}}}{\beta c} \right)^2 z_i^2(t) + \mathcal{O}(z_i^4(t)) \right]. \quad (3.5)$$

Given that the rf wave length is much longer than the bunch, i.e.  $\omega_{\text{rfq}}\sigma_z/\beta c \ll 1$ , the higher-order terms  $\mathcal{O}(z_i^4)$  can be neglected. The constant quadrupolar detuning term in Eq. (3.5) does not contribute to the effective tune spread as it affects all the particles in the same manner. It is hence irrelevant for the assessment of the Landau damping dynamics and can be neglected in the following. With linear synchrotron motion, the longitudinal coordinate of the particle changes as

$$z_i(t) = \hat{z}_i \sin(\omega_s t + \phi_i), \quad (3.6)$$

where  $\phi_i$  the constant synchrotron phase offset of the particle. The effective detuning with amplitude is obtained by averaging Eq. (3.5) for  $t \rightarrow \infty$ . This is analogous to the derivations made for Landau damping from magnetic octupoles. If  $\omega_s$  is not a rational number, this is equivalent to taking the average over one synchrotron period  $T_s = 2\pi/\omega_s$ . One obtains

$$\begin{aligned} \langle \Delta Q_{x,y}^i \rangle &\approx \mp \beta_{x,y} \frac{b_2}{8\pi B_0 \rho} \left( \frac{\omega_{\text{rfq}} \hat{z}_i}{\beta c} \right)^2 \frac{1}{T_s} \int_0^{T_s} \sin^2(\omega_s t + \phi_i) dt \\ &= \mp \beta_{x,y} \frac{b_2}{16\pi B_0 \rho} \left( \frac{\omega_{\text{rfq}} \hat{z}_i}{\beta c} \right)^2. \end{aligned} \quad (3.7)$$

The synchrotron oscillation amplitude  $\hat{z}_i^2$  of a particle can be rewritten in terms of its longitudinal action  $J_s^i$ ,  $\hat{z}_i^2 = 2\beta_z J_s^i$ . Hence,

$$\begin{aligned} \Delta Q_{x,y}(J_s) &\approx \mp \beta_{x,y} \frac{b_2}{16\pi B_0 \rho} \left( \frac{\omega_{\text{rfq}}}{\beta c} \right)^2 \beta_z 2J_s \\ &= \mp a_{s(x,y)} 2J_s, \end{aligned} \quad (3.8)$$

where the particle index has been dropped. All the constants can be combined in the longitudinal detuning coefficient

$$a_{s(x,y)} = \beta_{x,y} \beta_z \frac{b_2}{16\pi B_0 \rho} \left( \frac{\omega_{\text{rfq}}}{\beta c} \right)^2, \quad (3.9)$$

introduced conceptually in Section 2.2.5. The approximation is valid as long as  $\omega_{\text{rfq}}\sigma_z/\beta c \ll 1$ . Furthermore, it assumes that the rf quadrupole is operating with a phase  $\varphi_0 = 0$ . By changing the phase to  $\varphi_0 = \pi$ , the signs are flipped, meaning that the tune spreads between the two transverse planes are swapped.

The longitudinal kick in Eq. (3.2), in a similar manner, leads to an incoherent synchrotron tune shift that introduces Landau damping in the longitudinal plane. This effect, however, is negligible here given the parameters of the particle colliders under consideration as explained in Ref. [29].

### 3.1.3 Main features

Figure 3.4 compares two different incoherent betatron tune distributions in the transverse tune space  $Q_x$  vs.  $Q_y$ , averaged over several synchrotron periods. First, from magnetic octupoles [blue, Eq. (2.83)], and second, from a single rf quadrupole with  $\varphi_0 = 0$  [red, Eq. (3.8)]. Here, the magnetic octupoles are powered in a two-family scheme with both focusing and defocusing elements. This scheme is applied, for example, in the LHC to optimise the beam stabilising efficiency in both transverse planes [60]. When powered in such a way, magnetic octupoles produce a two-dimensional tune footprint in  $(Q_x, Q_y)$ -

space as illustrated in Fig. 3.4. The distribution is obtained assuming negative (positive) polarity of the focusing (defocusing) family, but equal absolute field strengths. The projection of the tune distribution onto the  $Q_x$ - ( $Q_y$ -)axis is nearly symmetric with respect to the bare machine tunes  $Q_{x,0}$ , and  $Q_{y,0}$  indicated by the green lines.

For the rf quadrupole, the tune changes in  $Q_x$  and  $Q_y$  are fully correlated. This is explained by the fact that the detuning is dependent on only one variable  $J_s$ . The tilt of the distribution generated by the rf quadrupole is determined by the ratio of  $\beta_x$  vs.  $\beta_y$  at the location of the device [see Eq. (3.8)]. Here, the transverse beta functions are assumed to be identical. The plot shows that the tune projections for a single rf quadrupole are strongly asymmetric. This has important consequences for the stabilising mechanism in the two transverse planes as discussed in more detail in Section 3.3 and Chapters 4 and 5. As already mentioned above, in addition to the incoherent tune spread, the rf quadrupole also introduces a constant, quadrupole tune shift which is the same for all the particles. This is understood formally from the presence of the zeroth-order term in Eq. (3.5). Such an effect can be compensated with a dedicated quadrupole magnet if needed.

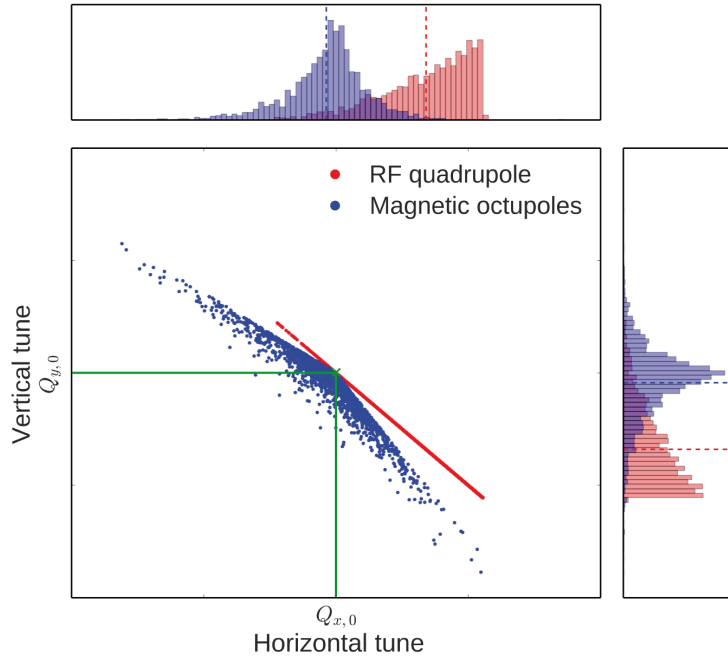


Figure 3.4: Comparison of incoherent betatron tune distributions in the  $(Q_x, Q_y)$ -space introduced by magnetic octupoles (blue) powered in a two-family scheme with negative (positive) polarity in the focusing (defocusing) family, and a single rf quadrupole (red). The lines and the cross in green mark the bare machine tunes  $(Q_{x,0}, Q_{y,0})$ . Histograms on the top and on the side show the projections of the tune distributions onto the  $Q_x$ - and the  $Q_y$ -axis respectively.

Figure 3.5 compares the transverse rms tune spreads  $\Delta Q_{\text{rms}}$  produced by an rf quadrupole (red) and the LHC Landau octupoles (blue) as a function of the beam energy for LHC design parameters [7, 60]. The comparison is made using an 800 MHz rf quadrupole installed at a location with  $\beta_{x,y} = 200\text{m}$ . The strength is fixed to  $b_2 = 0.22\text{Tm/m}$  and is chosen in such a way as to provide the same rms tune spread as the LHC Landau octupoles powered at their maximum current of 550A at LHC collision

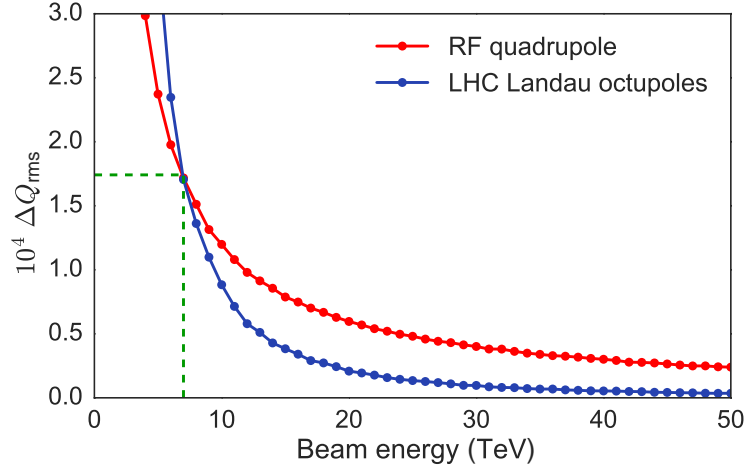


Figure 3.5: Dependence of the rms tune spread  $\Delta Q_{rms}$  on the beam energy for both LHC magnetic octupoles at maximum strength (blue) and for an rf quadrupole (red), designed in such a way as to produce the same rms tune spread at 7 TeV (green dashed line).

energy (7 TeV, green dashed line). The strengths of both the rf quadrupole and the magnetic octupoles are held constant as a function of the beam energy. While the LHC Landau octupoles have a total active length of 54 m, the equivalent rf quadrupole strength can theoretically be achieved with just *one* four-vane cavity with a total active length of 0.2 m to 0.3 m [68]. For this particular case, the active length of the rf quadrupole compared to magnetic octupoles is hence shorter by a factor 180 to 280. The reason behind the much larger efficiency of an rf quadrupole in terms of the tune shifts is the fact that the spread in  $J_s$  is several orders of magnitude larger than that in  $(J_x, J_y)$ . This is generally true for the beams of high-energy hadron colliders like LHC, HL-LHC, or FCC-hh. Specifically, for LHC design beam parameters at the energy of 7 TeV there is roughly a factor  $10^4$  difference in the transverse and the longitudinal action spreads. The main reason why the difference in active lengths between the rf quadrupole and magnetic octupoles does not reach a factor  $10^4$ , but rather is limited to 180 to 280 at 7 TeV, is that the transverse deflecting kicks in an rf cavity are much smaller than those in a superconducting magnetic octupole. This becomes evident when comparing the detuning coefficients of an rf quadrupole with those of magnetic octupoles. In this particular case and for the given beam energy, the former is  $a_{s(x,y)} \approx 16 \text{ m}^{-1}$ , while the latter are of the order of  $10^5 \text{ m}^{-1}$  for the LHC Landau octupoles at maximum strength [75]. The ratio between the two detuning coefficients amounts to a factor  $\approx 10^4$  which, as expected, corresponds to the difference in the action spreads between the longitudinal and the transverse planes.

The advantages of producing a betatron tune spread with an rf quadrupole rather than with magnetic octupoles become more evident when the beam energy increases as demonstrated by Fig. 3.5. Two effects play an important role here. First, due to the increased beam rigidity accounted for by the detuning coefficients, the effect of the kicks from both magnetic octupoles and the rf quadrupole is reduced by  $1/\gamma$ . This directly translates into a reduction of the rms tune spread by the same factor. Second, the spreads in respectively the transverse and the longitudinal actions exhibit a different dependence on the beam energy. The longitudinal beam stability in a machine like the LHC heavily relies on Landau damping in the longitudinal plane [22, 23]. During the energy ramp, the longitudinal

emittance needs to be kept large in order to keep enough stability margin longitudinally. For this reason, it is artificially blown up during acceleration. As a result, the longitudinal action spread is roughly held constant as the beam energy is increased. On the other hand, the transverse action spreads suffer from adiabatic damping and decrease as  $1/\gamma$ . To summarise, the rms tune spread produced by the rf quadrupole is only reduced as  $1/\gamma$  (beam rigidity) while the one introduced by magnetic octupoles decreases as  $1/\gamma^2$  (beam rigidity *and* adiabatic damping). These considerations are based on the assumption that the machine optics remain unchanged during the energy ramp. In addition to the improved detuning efficiency compared to magnetic octupoles, the performance of the rf quadrupole also remains unaffected by beam manipulations in the transverse planes, such as beam halo cleaning through collimation. During this process, the large transverse amplitude particles are removed from the beam in a controlled manner for reasons of machine protection [7, 18].

The rf quadrupole finds a potential application predominantly in future, high-energy hadron colliders, such as HL-LHC, HE-LHC, or FCC-hh, where the differences between the transverse and longitudinal emittances are significant. Due to the small transverse emittances of the beams foreseen for these machines, the number of magnetic octupoles required to provide the tune spread for sufficient Landau damping is large and a solution relying only on magnetic octupoles may be less cost-effective than an rf quadrupole or a combination of the two technologies. However, it is worth pointing out that the size of the incoherent betatron tune spread alone does not make a complete statement about the effectiveness of the Landau damping. This will be addressed in Chapter 5.

## 3.2 Nonlinear chromaticity

The purpose of this section is to introduce nonlinear chromaticity and to show that the incoherent betatron tune shifts produced by the second-order chromaticity depend on the longitudinal action of the particles. Finally, it will be demonstrated that the tune spread from second-order chromaticity is equivalent to that of an rf quadrupole in a first approximation.

### General description

The betatron tune shift introduced by nonlinear chromaticity, including up to order  $m$ , is given by

$$\Delta Q_{x,y}(\delta) = \sum_{n=1}^m \frac{1}{n!} Q_{x,y}^{(n)} \delta^n, \quad (3.10)$$

where the chromaticities of order  $n$  are defined as

$$Q_{x,y}^{(n)} = \left. \frac{\partial^n Q_{x,y}}{\partial \delta^n} \right|_{\delta=0}, \quad n \in \mathbb{N}. \quad (3.11)$$

Often the first-, second-, and third-order chromaticities are alternatively denoted  $Q'_{x,y}$ ,  $Q''_{x,y}$ , and  $Q'''_{x,y}$  respectively.

### Second-order chromaticity

Given a machine lattice with first- and second-order chromaticities  $Q'_{x,y}$  and  $Q''_{x,y}$ , a particle  $i$  with a

### Chapter 3. Betatron detuning with longitudinal amplitude

relative momentum deviation  $\delta_i$  experiences a betatron tune shift

$$\Delta Q_{x,y}^i(\delta_i) = Q'_{x,y} \delta_i + \frac{Q''_{x,y}}{2} \delta_i^2. \quad (3.12)$$

Since the particle undergoes synchrotron motion, its momentum deviation varies over time and takes on values in the interval  $[-\hat{\delta}_i, \hat{\delta}_i]$ , where  $\hat{\delta}_i$  is the maximum momentum deviation amplitude of the synchrotron oscillation. By consequence,  $\Delta Q_{x,y}^i$  has an implicit time dependence and the effective incoherent detuning of the particle is given by the time-average  $\langle \Delta Q_{x,y}^i[\delta_i(t)] \rangle_{t \rightarrow \infty}$ , analogous to Section 3.1.2. Assuming again linear synchrotron motion

$$\delta_i(t) = \hat{\delta}_i \cos(\omega_s t + \phi_i), \quad (3.13)$$

the calculation of the effective detuning becomes straightforward

$$\langle \Delta Q_{x,y}^i \rangle = \frac{Q''_{x,y} \hat{\delta}_i^2}{2} \frac{1}{T_s} \int_0^{T_s} \cos^2(\omega_s t + \phi_i) dt = \frac{Q''_{x,y} \hat{\delta}_i^2}{4}. \quad (3.14)$$

Integrating over one synchrotron period is again equivalent to averaging for  $t \rightarrow \infty$ , given that  $\omega_s$  is not a rational number.  $\hat{\delta}_i^2$  can be rewritten in terms of the longitudinal action  $J_s^i$  of the particle as  $\hat{\delta}_i^2 = 2J_s^i Q_s / \eta R$ . This leads to the final expression

$$\langle \Delta Q_{x,y}^i \rangle = \frac{Q''_{x,y}}{4} \frac{Q_s}{\eta R} 2J_s^i = a_{s(x,y)} 2J_s^i, \quad (3.15)$$

where

$$a_{s(x,y)} = \frac{\partial \langle \Delta Q_{x,y}^i \rangle}{\partial (2J_s^i)} = \frac{Q''_{x,y} Q_s}{4\eta R} \quad (3.16)$$

is the longitudinal detuning coefficient, defined in analogy to detuning with transverse amplitude.

Equations (3.8) and (3.15) manifestly demonstrate the equivalence of  $Q''$  and the rf quadrupole given the approximation  $\omega_{rfq} \sigma_z / \beta c \ll 1$ . Therefore, the betatron tune shifts introduced respectively by  $Q''$  and an rf quadrupole are generated according to the same mechanism and the effects on the beam dynamics are directly comparable. It will be shown later that  $Q''$  is hence a suitable tool for a first, cost-effective, experimental validation of the stabilising effect from an rf quadrupole. Furthermore, it also makes benchmarks of the numerical models with beam measurements possible as reported in Chapters 6 and 7. It can be shown that the effect of the rf quadrupole cavity can be identically mimicked when including all the even orders of nonlinear chromaticity.

The average detuning in Eq. (3.14) contains only the term with  $Q''_{x,y}$ . The first-order chromaticity does not contribute to the effective tune spread and hence does not introduce Landau damping. It does, however, change the effective impedance and can modify the head-tail instability mechanism and, be used to raise the transverse mode coupling instability threshold [25]. A similar change of the effective impedance is also observed for  $Q''_{x,y}$ . This effect often plays an important role in addition to the Landau damping when dealing with nonlinear chromaticity. A detailed treatment of the effects of nonlinear chromaticity on the coherent beam dynamics is provided in Chapter 4.



### 3.3 Existing stability diagram theory

An approximate dispersion relation for betatron detuning with longitudinal amplitude has been derived by Scott Berg and Ruggiero in 1996 [28]. Their work shows that the incoherent tune spread leads to an increase of the stable region in the complex frequency space  $\text{Re } \Delta\Omega$  vs.  $-\text{Im } \Delta\Omega$  similarly to Landau damping from magnetic octupoles. The dispersion relation reads

$$\begin{aligned}\Delta\Omega_{\text{lin}}^{-1} &= \frac{1}{\mathcal{N}} \int_0^\infty \frac{J_s^{|l|} \lambda(J_s)}{\omega - \omega_\beta(J_s) - l\omega_s} dJ_s, \\ \mathcal{N} &= \int_0^\infty J_s^{|l|} \lambda(J_s) dJ_s.\end{aligned}\tag{3.17}$$

The letter  $l$  denotes the azimuthal mode number of the instability under consideration and  $\lambda$  represents the unperturbed, stationary particle distribution in the longitudinal phase space.  $\omega_\beta(J_s) = \omega_{\beta,0} + \Delta\omega_\beta(J_s)$  describes the betatron frequency dependence on the longitudinal action. As explained in Section 2.2.5, a small imaginary component ( $-\epsilon$ ) is added to the denominator to perform the integration (Landau bypass rule).

Example stability diagrams are shown in the bottom plot of Fig. 3.6 for the corresponding tune distributions displayed in the top plot for different signs of the detuning coefficient  $a_{s(x,y)}$ . A Gaussian particle distribution and an azimuthal mode  $l = 0$  head-tail instability were assumed in this example here to solve the dispersion relation. The asymmetry of the tune spreads is reflected in the shape of the stability boundary diagrams. The plots are equally valid for second-order chromaticity and the rf quadrupole. For second-order chromaticity,  $a_{s(x,y)} \propto Q''_{x,y}$ , i.e. if the real coherent tune shift of a head-tail mode is negative which is typically the case for a dipolar impedance, negative  $Q''_{x,y}$  is favourable in terms of stabilising efficiency in both transverse planes. For an rf quadrupole, however, Eq. (3.8) demonstrates that the directions of the detuning are opposite in the two transverse planes. This is a result of the quadrupolar nature of the device. By consequence, the stability diagrams are mirrored in the two transverse planes which means that one plane can be stabilised more easily than the other, assuming that the real coherent tune shift of a mode has the same sign in both planes. This asymmetry can be resolved by means of a two-family rf quadrupole scheme discussed and evaluated in Chapter 5.

The dispersion relation in Eq. (3.17) is based on two main assumptions and does hence not describe all the beam dynamics aspects in presence of nonlinear chromaticity or an rf quadrupole. First, in the general case it would depend on the specific impedance of the machine under consideration. In the derivation made by Scott Berg and Ruggiero, this dependency has been neglected under the assumption that the frequency range of the impedance is small compared to the frequency spectrum of the beam [28]. This condition holds for instance for a strongly peaked impedance, i.e. a narrow-band resonator with a very high quality factor. However, for the impedance model and the beam parameters of a hadron collider like the LHC, for example, it is no longer valid. One reason is that several machine components have an impedance that extends over a large range of frequencies [75]. Second, nonlinear chromaticity or an rf quadrupole act on the betatron tunes as a function of the longitudinal coordinate and thus introduce a correlation between the betatron and the synchrotron motion. By consequence, they directly affect the interaction between the beam and the impedance with the result that the effective impedance changes. This effect is similar to a first-order chromaticity which can be accounted for by the head-tail phase parameter describing the frequency shift of the beam spectrum with respect to the impedance. A change of the effective impedance leads to a modification of the complex coherent

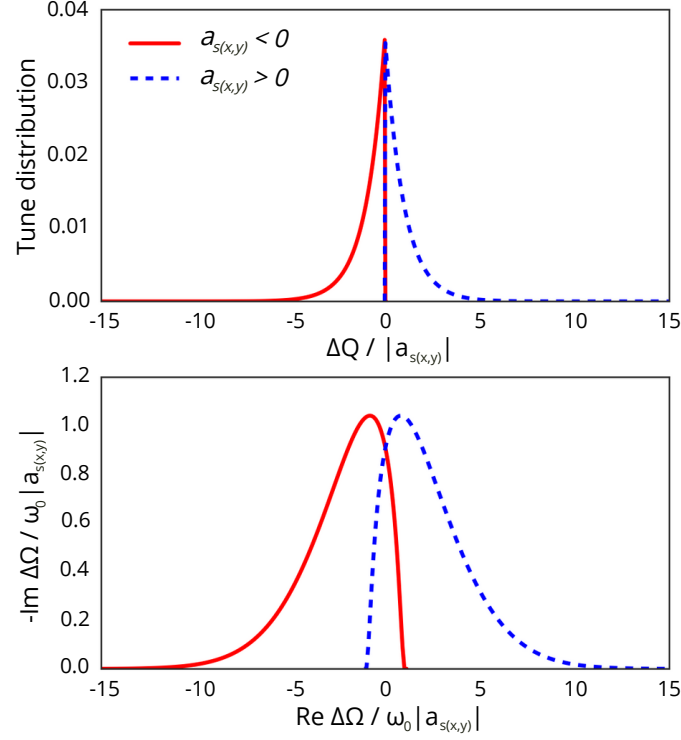


Figure 3.6: Incoherent betatron tune distributions (top) and normalised stability diagrams (bottom) for detuning with longitudinal amplitude for  $a_{s(x,y)} < 0$  (red, solid) or  $a_{s(x,y)} > 0$  (blue, dashed) respectively, computed using the dispersion relation in Eq. (3.17).

tune shift of the instability under consideration. This manifests itself, for example, as a change of the instability rise time which can become faster or slower depending on the impedance of the machine and the respective unstable head-tail mode. At large enough detuning strengths it is even possible that a mode is excited on a different synchrotron sideband (change of the azimuthal mode number). These effects are discussed analytically and numerically in Chapter 4 and are demonstrated with experimental measurements in the LHC in Chapter 6.

### 3.4 Conclusions

The concept of an rf quadrupole for Landau damping was introduced discussing two different cavity geometries in terms of their achievable quadrupole strength and explaining the working principle of the device. The comparison with magnetic octupoles, traditionally employed for beam stabilisation in the transverse planes, demonstrates that the betatron frequency spread for Landau damping can be produced more efficiently with an rf quadrupole. This is explained by the larger spread in the longitudinal compared to the transverse oscillation amplitudes of the beam particles which is particularly true for future colliders. At higher beam energies, the rms tune spread from magnetic octupoles decreases as  $1/\gamma^2$  while that from an rf quadrupole is reduced only by a factor  $1/\gamma$  as a result of the longitudinal blow-up necessary for longitudinal stability during the energy ramp.

Nonlinear chromaticity or an rf quadrupole cavity are two possible ways to introduce a betatron tune spread as a function of longitudinal action and it was shown analytically that the two mechanisms are equivalent. Specifically, the second-order chromaticity has the advantage that it can, in principle, be introduced in a machine like the LHC by using the existing hardware and tweaking the optics of the accelerator. This is of fundamental importance for this PhD project since it makes it possible to validate the underlying beam stabilising mechanism from an rf quadrupole as well as to benchmark the numerical models with experimental data.



## 4 Theoretical studies: Vlasov formalism with nonlinear chromaticity

The basics of the existing Vlasov theory for transverse coherent beam instabilities with first-order chromaticity have been recapitulated in Section 2.2.3. Here, we extend this theory to account for the beam dynamics effects introduced by nonlinear chromaticity. The chapter contains the work published in Refs. [34, 76].

The derivation of the new Vlasov theory is presented in Section 4.1 and is based on the existing formalism discussed in Section 2.2.3. It will be shown that nonlinear chromaticity has two effects on the beam dynamics: (1) it changes the effective impedance which results in a modification of the coherent frequencies of the head-tail modes; and (2) it introduces Landau damping of transverse modes through betatron detuning with longitudinal action. In general, the two effects are interlinked and hence difficult to study separately, especially in particle tracking simulations. Based on the new formalism, however, the two mechanisms can be identified and isolated by studying them analytically with both an airbag and a Gaussian beam in Section 4.2. Finally, the theory is successfully benchmarked against the circulant matrix solver BMBIM as well as the PYHEADTAIL macroparticle tracking code in Section 4.3. The main conclusions of the study are drawn in Section 4.4.

It is worth pointing out that the beam dynamics effects of second-order chromaticity are equivalent to those of an rf quadrupole in a first approximation (compare Section 3.2). The analytical understanding gained here of the effects of nonlinear chromaticity is hence directly applicable to the rf quadrupole.

### 4.1 Extended Vlasov equation

The goal of this section is to extend the existing Vlasov formalism, briefly reviewed in Section 2.2.3, by introducing a general variation  $\Delta\omega_\beta(\delta)$  of the betatron frequency with arbitrary orders of chromaticity  $\xi^{(n)} = Q^{(n)}/Q_0$

$$\Delta\omega_\beta(\delta) = \omega_{\beta,0} \sum_{n=1}^m \frac{\xi^{(n)}}{n!} \delta^n, \quad (4.1)$$

with

$$\xi^{(n)} = \frac{1}{\omega_{\beta,0}} \left. \frac{\partial^n \omega_\beta}{\partial \delta^n} \right|_{\delta=0}, \quad (4.2)$$

and to evaluate the transverse stability in that case. The following formalism can analogously be developed for an rf quadrupole by introducing instead a general variation of the betatron frequency with the longitudinal position  $\Delta\omega_\beta(z)$ . Note that as in Section 2.2.3 we are again considering only one of the two transverse planes. The derivations explained in Eqs. (2.51) to (2.59) are analogous even for an arbitrary chromatic change of the betatron frequency. A dependency on higher-order chromaticity can hence be introduced simply by replacing

$$\omega_{\beta,0} (1 + \xi^{(1)} \delta) \rightarrow \omega_{\beta,0} + \Delta\omega_\beta(\delta), \quad (4.3)$$

on the left hand side of Eq. (2.59). However, the eigenmode decomposition in Eq. (2.60) cannot be used anymore as an ansatz and needs to be replaced by a different one. It is convenient to define

$$G_1(r, \varphi) = e^{\frac{i}{\omega_s} \int_0^\varphi \Delta\omega_\beta(\delta(r, u)) du} g_1(r, \varphi), \quad (4.4)$$

such that the Vlasov equation can be expressed as

$$\begin{aligned} [\Omega - \omega_{\beta,0} + i\omega_s \partial_\varphi] G_1(r, \varphi) = & -iK g_0(r) \sum_{k=-\infty}^{\infty} Z_\perp(\omega') \\ & \times \int_0^\infty \int_0^{2\pi} \tilde{r} e^{i\frac{\omega'}{c}(r \cos \varphi - \tilde{r} \cos \tilde{\varphi})} e^{\frac{i}{\omega_s} A(r, \varphi, \tilde{r}, \tilde{\varphi})} G_1(\tilde{r}, \tilde{\varphi}) d\tilde{\varphi} d\tilde{r}, \end{aligned} \quad (4.5)$$

with

$$A(r, \varphi, \tilde{r}, \tilde{\varphi}) = \int_0^\varphi \Delta\omega_\beta(\delta(r, u)) du - \int_0^{\tilde{\varphi}} \Delta\omega_\beta(\delta(\tilde{r}, u)) du, \quad (4.6)$$

and

$$K = \frac{\pi e^2 \omega_s}{\omega_{\beta,0} T_0^2 E_0 \eta}. \quad (4.7)$$

It is straightforward to show that Eq. (4.5) reduces to Eq. (2.59) when assuming a purely linear chromaticity  $\Delta\omega_\beta(\delta) = \omega_{\beta,0} \xi^{(1)} \delta$ .

In analogy to Section 2.2.3, the decomposition of  $G_1(r, \varphi)$  is chosen such that the functions  $G_1^l(r, \varphi)$  are the azimuthal eigenmodes of the free ( $Z_\perp \equiv 0$ ) Vlasov equation

$$[\Omega - \omega_{\beta,0} + i\omega_s \partial_\varphi] G_1^l(r, \varphi) = 0. \quad (4.8)$$

By imposing again the  $2\pi$ -periodicity in  $\varphi$  for  $G_1(r, \varphi)$ , one finds the free eigenvalues and eigenmodes

$$\begin{aligned} \Omega^{(l)} &= \omega_{\beta,0} + l\omega_s + \langle \Delta\omega_\beta \rangle_\varphi, \\ G_1^l(r, \varphi) &= R_l(r) e^{i\left(l + \frac{\langle \Delta\omega_\beta \rangle_\varphi}{\omega_s}\right)\varphi}, \text{ for } l \in \mathbb{Z}. \end{aligned} \quad (4.9)$$

Note that the  $R_l(r)$  are, in general, different functions than in the case of first-order chromaticity described in Section 2.2.3. The term  $\langle \Delta\omega_\beta \rangle_\varphi$  denotes the average betatron frequency shift with respect to  $\varphi$  and is, in general, dependent on the longitudinal amplitude  $r$  of every particle

$$\langle \Delta\omega_\beta \rangle_\varphi(r) = \frac{1}{2\pi} \int_0^{2\pi} \Delta\omega_\beta[\delta(r, \varphi)] d\varphi. \quad (4.10)$$

It describes the betatron frequency spread introduced through detuning with longitudinal amplitude. It will become clear in the following that this term leads to Landau damping. It should be noted, though, that for odd orders of chromaticity  $\xi^{(2n+1)}$ ,  $n \in \mathbb{N}_0$ , the average frequency spread vanishes  $\langle \Delta\omega_\beta \rangle_\varphi(r) \equiv 0$ . This result is independent of the longitudinal particle distribution. Hence, odd orders of chromaticity do not introduce Landau damping, at least for instabilities on the timescale of several synchrotron periods where the frequency spread averages to zero<sup>1</sup>. On the other hand, even orders  $\xi^{(2n)}$ ,  $n \in \mathbb{N}$ , of chromaticity introduce a betatron frequency spread with longitudinal amplitude that does not average out over time which leads to Landau damping, similarly to an rf quadrupole operating (anti-) on-crest with  $\varphi_0 = 0$  or  $\varphi_0 = \pi$ . In either case, though, both odd and even orders of chromaticity introduce a change of the effective impedance and modify the coherent frequencies of the modes. Both effects will be discussed in Section 4.2.2.

Using a series of the free eigenmodes [Eq. (4.9)] as an ansatz for  $G_1(r, \varphi)$  in Eq. (4.5), one obtains

$$\begin{aligned} \sum_{l''=-\infty}^{\infty} R_{l''}(r) [\Omega - \omega_{\beta,0} - l''\omega_s - \langle \Delta\omega_\beta \rangle_\varphi(r)] e^{il''\varphi} = -iKg_0(r) \sum_{l', k=-\infty}^{\infty} Z_\perp(\omega') \\ \times \int_0^\infty \int_0^{2\pi} \tilde{r} e^{\frac{i\omega'}{c}[r \cos \varphi - \tilde{r} \cos \tilde{\varphi}]} R_{l'}(\tilde{r}) e^{il'\tilde{\varphi}} e^{\frac{i}{\omega_s}[B(r, \varphi) - B(\tilde{r}, \tilde{\varphi})]} d\tilde{\varphi} d\tilde{r}, \end{aligned} \quad (4.11)$$

where

$$B(r, \varphi) = \int_0^\varphi [\Delta\omega_\beta[\delta(r, u)] - \langle \Delta\omega_\beta \rangle_\varphi(r)] du. \quad (4.12)$$

The next step is to multiply both sides with  $e^{-il\varphi}$  and to perform the integration over  $\varphi$  from 0 to  $2\pi$

$$\begin{aligned} [\Omega^{(l)} - \omega_{\beta,0} - l\omega_s - \langle \Delta\omega_\beta \rangle_\varphi(r)] R_l(r) = -i2\pi Kg_0(r) \\ \times \sum_{l', k'=-\infty}^{\infty} Z_\perp(\omega') \int_0^\infty \tilde{r} R_{l'}(\tilde{r}) \overline{H_l^{k'}(r)} H_l^{k'}(\tilde{r}) d\tilde{r}, \text{ for } l \in \mathbb{Z}, \end{aligned} \quad (4.13)$$

where

$$H_l^k(r) = \frac{1}{2\pi} \int_0^{2\pi} e^{il\varphi} e^{-\frac{i\omega'}{c}r \cos \varphi} e^{-\frac{i}{\omega_s}B(r, \varphi)} d\varphi, \quad (4.14)$$

with  $l, k \in \mathbb{Z}$ .  $H_l^k(r)$  can be perceived as a generalised Bessel function. It is easy to show that in the event of a purely linear chromaticity,  $H_l^k(r)$  reduces to the Bessel function of the first kind (see Appendix A.1). The phase terms  $e^{-iB(r, \varphi)/\omega_s}$  describe the alteration of the interaction of the beam with the impedance caused by arbitrary orders of chromaticity. The result is that the overlap sum over index  $k'$  in Eq. (4.13) between the  $H_l^{k'}(r)$  functions and the impedance  $Z_\perp(\omega')$  changes. In time domain the chromatic phase terms can be understood as a change of the synchronicity between wake kicks, betatron, and synchrotron motion of the particles. This causes a change of the coherent frequency  $\Omega$ , both for the real and imaginary components, for all the modes and is studied in more detail in Sections 4.2 and 4.3 for specific beam models. The mechanism can mimic the “stabilisation” of a given coherent mode if the change of effective impedance induced by a change of chromaticity is such that the growth rate of the particular mode is reduced. However, the modification of the effective impedance does not introduce a frequency spread and there is no increase of the area of stability in the complex frequency space. Thus,

<sup>1</sup>This is analogous to an rf quadrupole operated with a phase offset of  $\varphi_0 = \pm\pi/2$  studied in Refs. [73, 74] to increase the TMCI threshold.

this effect is not related to Landau damping. Nevertheless, Landau damping is still part of the beam dynamics with higher-order chromaticity. It is introduced through  $\langle \Delta\omega_\beta \rangle_\varphi(r) \neq 0$  from even orders of chromaticity. This term leads to a dispersion integral and to an increase of the area of stability in the complex frequency space as demonstrated in the following. To summarise, Eq. (4.13) clearly decouples the two beam dynamics effects introduced by higher-order chromaticity, i.e. Landau damping and the change of the effective impedance.

To further simplify Eq. (4.13), it can be multiplied with  $r H_l^k(r)$  and integrated over  $r$  from 0 to  $\infty$

$$\sigma_{lk} = -iK \sum_{l', k'=-\infty}^{\infty} \sigma_{l'k'} Z_\perp \left( k' \omega_0 + \Omega^{(l)} \right) \int_0^\infty \frac{r g_0(r) \overline{H_l^{k'}}(r) H_l^k(r)}{\Omega^{(l)} - \omega_{\beta,0} - l\omega_s - \langle \Delta\omega_\beta \rangle_\varphi(r)} dr, \quad (4.15)$$

where

$$\sigma_{lk} = \int_0^\infty r R_l(r) H_l^k(r) dr. \quad (4.16)$$

When neglecting azimuthal mode interactions, the summation on  $l'$  can be ignored and one obtains an infinite set of separate equations, one for each azimuthal mode. The dispersion integral on the right hand side of Eq. (4.15) proves that the term  $\langle \Delta\omega_\beta \rangle_\varphi(r)$  in the denominator indeed introduces Landau damping. A dispersion relation that makes the computation of stability boundary diagrams with nonlinear chromaticity possible is derived in Section 4.2.2 and numerical solutions are given in Section 4.3.

## 4.2 Specific solutions

In this section, solutions of the previously derived Vlasov equation (4.15) are determined for two different types of longitudinal particle distributions. The first type is an airbag beam for which all the particles have exactly the same longitudinal amplitude. As a result, there can be no net betatron frequency spread from chromaticity of any order ( $\langle \Delta\omega_\beta \rangle_\varphi(r) \equiv 0$ ) and hence there is no Landau damping. For that case, an exact solution of Eq. (4.15) is determined for arbitrary orders of chromaticity. The second type of longitudinal distributions is general as it accounts for a spread in the longitudinal action of the particles, such as Gaussian and waterbag beams, for example. In that case, Eq. (4.15) cannot be solved exactly. Instead, the analytical solution is determined with strict assumptions on the shape of the transverse dipolar impedance using a narrow-band resonator.

The two types of distributions are chosen to decouple the two beam dynamics effects that have been identified above. Nonlinear chromaticity cannot introduce Landau damping for an airbag beam, but it does cause a change of effective impedance. Hence, for an airbag model, the latter mechanism can be studied independently of the Landau damping which facilitates the understanding of the beam dynamics in presence of higher-order chromaticity in general. With the second type of beam distributions, on the other hand, there is an interplay of both mechanisms as illustrated by Eq. (4.13). The analytical results derived and presented here are benchmarked numerically with two different accelerator physics models in Section 4.3.



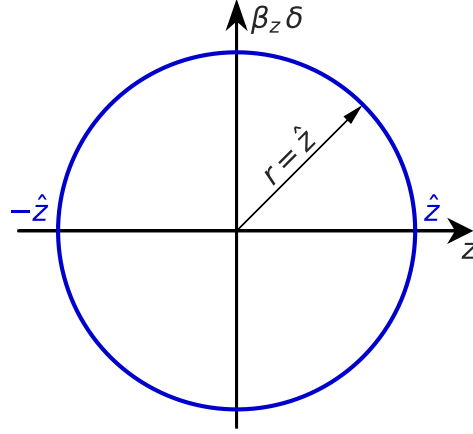


Figure 4.1: Illustration of the airbag model in the normalised longitudinal phase space. The particles populate a circle of radius  $r = \hat{z}$ .

#### 4.2.1 Airbag model

In the airbag model, the beam particles are assumed to populate an infinitesimally thin elliptical shell in longitudinal phase space. Such a distribution is also known as a hollow beam model. It is described by the distribution function

$$g_0(r) = \frac{N\eta c}{2\pi\omega_s \hat{z}} \delta(r - \hat{z}), \quad (4.17)$$

where  $N$  is the bunch intensity in number of particles,  $\hat{z}$  defines the radius of the distribution in the normalised longitudinal phase space  $(z, \beta_z \delta)$ , and  $\delta$  is the Dirac delta function. For the airbag beam, all the particles have the same longitudinal action  $J_s = \hat{z}^2/2\beta_z$ . An illustration of the longitudinal particle distribution is given in Fig. 4.1.

In the weak-wake approximation considered here, azimuthal mode coupling can be neglected, meaning that the summation over index  $l'$  can be ignored in Eq. (4.15). Instead, one can solve the equations for all the azimuthal modes independently of one another. Using the airbag distribution the integration over  $r$  can be easily performed which leads to

$$\sigma_{lk} = -i \frac{Ne^2 c}{2\omega_{\beta,0} T_0^2 E_0} \sum_{k'=-\infty}^{\infty} \sigma_{lk'} Z_{\perp}(\omega') \frac{\overline{H_l^{k'}}(\hat{z}) H_l^k(\hat{z})}{\Omega^{(l)} - \omega_{\beta,0} - l\omega_s - \langle \Delta\omega_{\beta} \rangle_{\varphi}(\hat{z})}. \quad (4.18)$$

The detuning term  $\langle \Delta\omega_{\beta} \rangle_{\varphi}(\hat{z}) = \text{const.}$  is now independent of the longitudinal amplitude  $r$  and is identical for all the particles. As expected, the dispersion integral has disappeared from the equation which can be interpreted as the absence of Landau damping.

The eigenvalue problem in Eq. (4.18) can be analytically solved and the solution reads

$$\Omega^{(l)} - \omega_{\beta,0} - l\omega_s - \langle \Delta\omega_{\beta} \rangle_{\varphi}(\hat{z}) = -i \frac{Ne^2 c}{2\omega_{\beta,0} T_0^2 E_0} \sum_{k=-\infty}^{\infty} Z_{\perp}(k\omega_0 + \omega_{\beta,0} + l\omega_s) \left| H_l^k(\hat{z}) \right|^2, \quad (4.19)$$

where  $\omega' \approx k\omega_0 + \omega_{\beta,0} + l\omega_s$  and  $l \in \mathbb{Z}$ . We have obtained an explicit expression for the coherent

frequency shift of each azimuthal mode  $l$ . One feature that is discussed further in Section 4.3 is that the average detuning term  $\langle \Delta\omega_\beta \rangle_\varphi(\hat{z})$  only affects the real part of  $\Omega^{(l)}$  and is identical for all the azimuthal modes.

Equation (4.19) is a generalisation of Chao's Eq. (6.188) derived in Ref. [25] and is valid for arbitrary orders of chromaticity. It reduces to Chao's equation for a purely linear chromaticity as shown in Appendix A.1.

## 4.2.2 Arbitrary longitudinal distributions

The goal is now to study the eigenvalue problem in Eq. (4.15) for arbitrary longitudinal distributions  $g_0(r)$ , for which, in general, there is a spread in amplitudes  $r$ , or longitudinal action  $J_s$ , for the particles in the beam. In combination with even orders of chromaticity, the finite distribution in the particle action translates into a betatron frequency spread and Landau damping. This can be seen from the dispersion integral on the right hand side of Eq. (4.15). Indeed, Landau damping is a result of the  $\langle \Delta\omega_\beta \rangle_\varphi(r)$  term which describes detuning with longitudinal amplitude. This is similar to a dispersion integral for detuning with transverse amplitude introduced for instance by magnetic octupoles.

The eigenvalue problem for arbitrary distributions is difficult to solve, even numerically. Hence, to obtain an analytical solution where the dispersion relation and Landau damping become even more apparent, and can be benchmarked against numerical models, constraints are imposed on the shape of the impedance. Here, a highly narrow-band resonator impedance is considered, such that effectively

$$Z_\perp(\omega') = \begin{cases} Z_{k_0} \neq 0, & k = k_0, \\ 0, & \text{otherwise.} \end{cases} \quad (4.20)$$

For this type of impedance, Eq. (4.15) simplifies to

$$1 = -iKZ_{k_0} \int_0^\infty \frac{r g_0(r) |H_l^{k_0}(r)|^2}{\Omega^{(l)} - \omega_\beta(r) - l\omega_s} dr, \quad (4.21)$$

where  $\omega_\beta(r) = \omega_{\beta,0} + \langle \Delta\omega_\beta \rangle_\varphi$ . Equation (4.21) is a dispersion relation. To obtain the stability boundary diagram, one considers the coherent frequency  $\Omega_{\text{lin}}^{(l)}$  in absence of Landau damping (*linear lattice*). This can be achieved by ignoring the frequency spread, i.e. by setting  $\langle \Delta\omega_\beta \rangle_\varphi(r) = 0$  in Eq. (4.21)

$$1 = -i \frac{KZ_{k_0}}{\Omega_{\text{lin}}^{(l)} - \omega_{\beta,0} - l\omega_s} \int_0^\infty r g_0(r) |H_l^{k_0}(r)|^2 dr. \quad (4.22)$$

The integral over  $r$  can be performed numerically. Combining Eqs. (4.21) and (4.22), one reveals the formula to determine the stability boundary diagrams

$$\begin{aligned} \frac{1}{\Delta\Omega_{\text{lin}}^{(l)}} &= \frac{1}{\mathcal{N}} \int_0^\infty \frac{r g_0(r) |H_l^{k_0}(r)|^2}{\Omega^{(l)} - \omega_\beta(r) - l\omega_s} dr, \\ \mathcal{N} &= \int_0^\infty r g_0(r) |H_l^{k_0}(r)|^2 dr, \end{aligned} \quad (4.23)$$

where  $\Delta\Omega_{\text{lin}}^{(l)} = \Omega_{\text{lin}}^{(l)} - \omega_{\beta,0} - l\omega_s$ . The stability boundary diagram is obtained by numerically computing the frequency shifts  $\Delta\Omega_{\text{lin}}^{(l)}$  for different values of  $\Omega^{(l)}$  as explained in Section 2.2.5. Again, according to the Landau bypass rule, a small complex part  $-i\varepsilon$  is added to the denominator of Eq. (4.23) to perform the integration. An example for Gaussian beams is discussed in Section 4.3.

By making additional assumptions on the beam spectrum and impedance, it can be shown that the dispersion relation derived here is equivalent to the results found by Scott Berg and Ruggiero, originally presented in Ref. [28]. The proof is shown in Appendix A.2.

## 4.3 Benchmarks against numerical models

This section summarises the benchmarks that were made to validate the new formalism. Two different accelerator physics models are used: the circulant matrix solver BIMBIM and the PYHEADTAIL tracking code. For simplicity, the tests only include up to order two in chromaticity, but they could be easily extended to arbitrary orders. The new Vlasov formalism is tested first for an airbag model without Landau damping, and subsequently for a Gaussian beam which also experiences Landau damping.

### 4.3.1 Airbag model

#### Linear chromaticity scan

To ensure that the new formalism produces correct results, it is first benchmarked against the well-known case of an airbag model assuming a purely linear chromaticity. In this scenario,

$$\begin{aligned} \langle \Delta\omega_\beta \rangle_\varphi(r) &= 0, \\ B(r, \varphi) &= \xi^{(1)} \frac{\omega_{\beta,0} r}{\beta_z} (1 - \cos \varphi), \end{aligned} \tag{4.24}$$

and Eq. (4.19) reduces to Chao's Eq. (6.188) in Ref. [25] as proven in Appendix A.1. The expression in Eq. (4.19) allows to analytically compute the complex coherent frequency shifts of each azimuthal mode. The infinite sum over index  $k$  is approximated numerically by a sum extending from  $k = -10^5$  to  $10^5$ . This was found to be enough to reach convergence for the specific scenarios discussed here.

Equation (4.19) is benchmarked against BIMBIM and PYHEADTAIL using the machine and beam parameters listed in Table 4.1. The values are loosely based on the CERN SPS at injection energy. The machine impedance has been replaced by a broad-band ( $Q = 1$ ) resonator. For BIMBIM, using one ring for the discretisation of the longitudinal phase space is what is required to model an airbag beam. Furthermore, 90 azimuthal slices were found to be enough for the results to converge, given the relatively low orders of the modes under consideration here. For PYHEADTAIL, on the other hand,  $N_{\text{mp}} = 5 \times 10^5$  macroparticles were tracked over  $N_{\text{turns}} = 10^5$  turns. The results are summarised in Fig. 4.2. The analytical calculations are given by the coloured lines and represent the real (upper plot) and imaginary (lower plot) coherent frequency shifts of the six lowest-order azimuthal modes as a function of linear chromaticity  $\xi^{(1)}$ . The real part is measured with respect to the respective unstable synchrotron sideband  $l$ , i.e.  $\text{Re } \Delta\Omega^{(l)} = \text{Re } (\Omega^{(l)} - \omega_{\beta,0} - l\omega_s)$ , to improve the readability of the plot. It can be seen that the azimuthal modes are degenerate. The modes for a specific positive and negative azimuthal number are identical. This will no longer be the case when introducing second-order chromaticity as described below. As

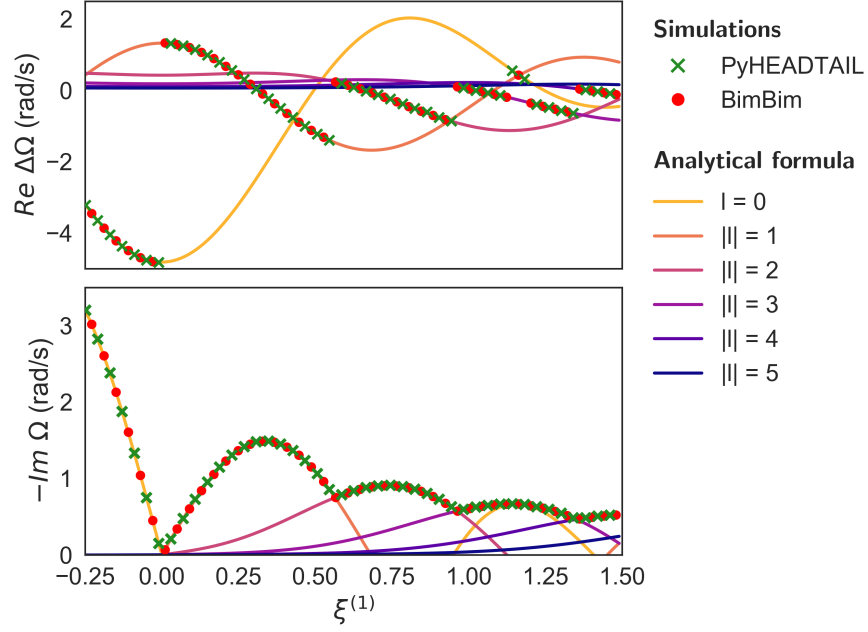


Figure 4.2: Real (top) and imaginary (bottom) coherent frequency shifts as a function of purely linear chromaticity  $\xi^{(1)}$  for an airbag model with machine and beam parameters listed in Table 4.1. Results from the circulant matrix solver BIMBIM (red circles), PYHEADTAIL simulations analysed with SUSSIX (green crosses), and analytical calculations (solid lines) are shown.

Table 4.1: Main PYHEADTAIL and BIMBIM parameters used to benchmark the Vlasov formalism for an airbag beam. The parameters  $N_{\text{mp}}$  and  $N_{\text{turns}}$  are relevant exclusively for the PYHEADTAIL simulations, while  $N_r$  and  $N_s$  are valid solely for the calculations with BIMBIM.

Parameter		Value
Relativistic gamma	$\gamma$	27.7
Bunch intensity	$N$	$10^9$ p
Longitudinal action	$J_s$	$3 \times 10^{-4}$ m
Synchrotron tune	$Q_s$	0.017
Longitudinal beta function	$\beta_z$	115 m
Resonator shunt impedance	$R_s$	$10^7 \Omega/\text{m}$
Resonator frequency	$f_r$	0.8 GHz
Resonator quality factor	$Q$	1
Wake decay time	$N_{\text{wake}}$	1 turn
Number of $k$ modes	$N_k$	$2 \times 10^5$
Number of macroparticles	$N_{\text{mp}}$	$5 \times 10^5$
Number of turns	$N_{\text{turns}}$	$10^5$ turns
Number of rings	$N_r$	1
Number of azimuthal slices	$N_s$	90

expected, for  $\xi^{(1)} < 0$  the most unstable mode is a head-tail mode zero. For increasing  $\xi^{(1)} > 0$ , the most unstable mode changes from azimuthal mode one through five given the limited range of chromaticity. The locations of the transitions between the modes depend on the choice of beam and impedance parameters. The outputs from BIMBIM (red dots) and PYHEADTAIL (green crosses) after post-processing are shown on top of the analytical results and prove an excellent agreement with the most unstable mode at each value of chromaticity. Not only is the mode number the same, but both the real and imaginary parts are in perfect agreement between the three approaches. The fact that two different numerical accelerator physics models confirm the theory to that degree of accuracy is very satisfying and demonstrates that the analytical description works well for the basic linear chromaticity case.

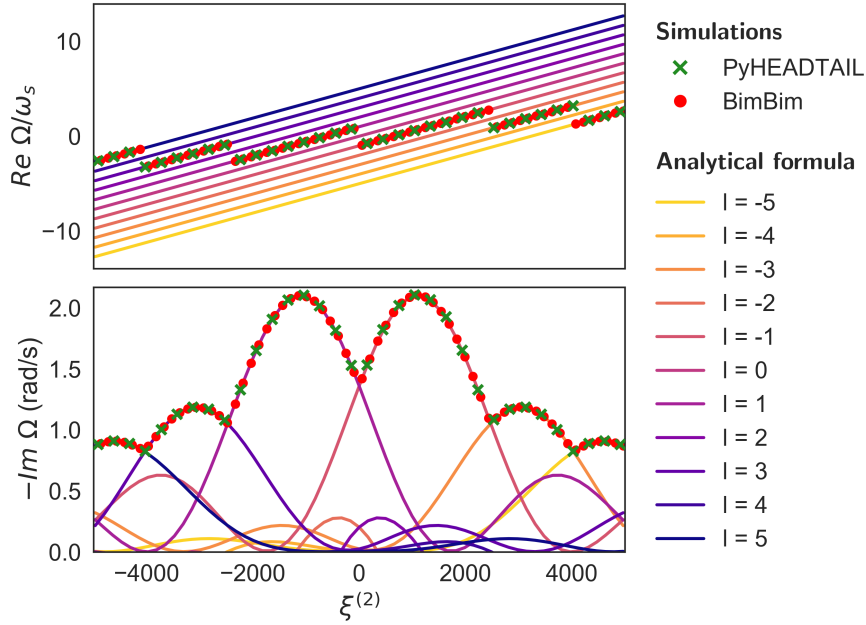


Figure 4.3: Real (top) and imaginary (bottom) coherent frequency shifts as a function of second-order chromaticity  $\xi^{(2)}$  at fixed  $\xi^{(1)} = 0.25$  for an airbag model with machine and beam parameters listed in Table 4.1. Results from the circulant matrix solver BIMBIM (red circles), PYHEADTAIL simulations analysed with SUSSIX (green crosses), and analytical calculations (solid lines) are shown.

### Second-order chromaticity scan

In the following, nonzero first- and second-order chromaticities are assumed. In that case, the change of betatron frequency is given by  $\Delta\omega_\beta = \omega_{\beta,0}(\xi^{(1)}\delta + \xi^{(2)}\delta^2/2)$ . Hence,

$$\begin{aligned} \langle \Delta\omega_\beta \rangle_\varphi(r) &= \xi^{(2)} \frac{\omega_{\beta,0} r^2}{4\beta_z^2}, \\ B(r, \varphi) &= \xi^{(1)} \frac{\omega_{\beta,0} r}{\beta_z} (1 - \cos \varphi) - \xi^{(2)} \frac{\omega_{\beta,0} r^2}{4\beta_z^2} \sin \varphi \cos \varphi. \end{aligned} \quad (4.25)$$

Combining Eqs. (4.19) and (4.25), one obtains again an explicit expression for the coherent frequency shifts of each azimuthal mode. The same number of  $k$  modes is used to guarantee the convergence of the overlap sum. Analytical results for the same machine and beam parameters as above (Table 4.1)

are plotted in Fig. 4.3 and are represented by the coloured lines. The first azimuthal modes up to order five are shown. Note that in this figure the real part is given as an absolute value normalised to the synchrotron frequency and the vertical axis hence corresponds to the azimuthal mode number. Indeed,  $\xi^{(2)}$  changes the effective impedance, and eventually, transitions to other, now more unstable, azimuthal modes occur. This is very similar to the case with first-order chromaticity. A major difference with respect to Fig. 4.2, however, is that the degeneracy in the azimuthal mode number is lifted. For a certain absolute value of the mode number  $l$ , the modes with the two opposite signs are no longer identical. Another observation is that only every other mode is excited. Additionally, the real part of the coherent frequency shift is dominated by the constant and real-valued  $\langle \Delta\omega_\beta \rangle_\varphi(\hat{z})$  which is the same for all the azimuthal modes as illustrated in Fig. 4.3 (top). This is specific to the airbag beam, and is again a result of the absence of a spread in longitudinal amplitude. For PYHEADTAIL and BMBIM again only the most unstable modes are shown with their real and imaginary parts for each value of  $\xi^{(2)}$ . As in the linear chromaticity case, the theoretical predictions are in perfect agreement with both the tracking and circulant matrix models which confirms that the formalism developed above is indeed valid for the airbag beam.

To summarise, the new theory describes the change of effective impedance from nonlinear chromaticity very accurately and gives satisfying results for the airbag model. The next step is to introduce a particle distribution that has a spread in longitudinal amplitudes to validate the theory also in presence of Landau damping.

### 4.3.2 Gaussian beam

To study the effect of Landau damping, a Gaussian beam is used for the comparison between the theory and the tracking model

$$g_0(r) = \frac{N\eta c}{2\pi\sigma_z^2\omega_s} e^{-r^2/2\sigma_z^2}, \quad (4.26)$$

where  $\sigma_z$  denotes the one-sigma bunch length.

#### Incoherent frequency distribution

For the first part of the validation procedure, the betatron frequency distributions introduced by a specific amount of  $\xi^{(2)}$  (at  $\xi^{(1)} = 0$ ) are compared between analytical formula and PYHEADTAIL. Figure 4.4 summarises the results. The blue histogram corresponds to the output from the tracking simulations of  $3 \times 10^4$  macroparticles over ten synchrotron periods using the machine parameters listed in Table 4.2 and neglecting the effect of the wakefields. The betatron frequencies of every particle were analysed with SUSSIX. The red dashed bar diagram corresponds to the analytical calculation obtained from the formula for detuning with longitudinal amplitude  $\langle \Delta\omega_\beta \rangle_\varphi(r)$  and using  $g_0(r)$  from Eq. (4.26). The agreement between the tracking model and the analytical formula is excellent and confirms the correct implementation of the second-order chromaticity detuning in PYHEADTAIL.

#### Single-peak approximation

Based on this result, the next step is to design a study case which fulfils the approximations and assumptions made to derive the dispersion relation in Eq. (4.23). The main one was to use a highly narrow-band resonator impedance as defined in Eq. (4.20), such that there would be only one dominant term in the sum over index  $k$  in Eq. (4.15). This can be achieved by tuning the quality factor and the

### 4.3. Benchmarks against numerical models

Table 4.2: Main PYHEADTAIL and BIMBIM parameters used to benchmark the Vlasov formalism for a Gaussian beam. The resonator impedance is highly narrow-band and its frequency has been tuned well to ensure that the overlap with the beam spectrum is largest at one specific  $k$  mode and negligible everywhere else.

Parameter		Value
Relativistic gamma	$\gamma$	27.7
Bunch intensity	$N$	$10^9$ p
Bunch length	$\sigma_z$	0.21 m
Synchrotron tune	$Q_s$	0.017
Longitudinal beta function	$\beta_z$	115 m
Resonator shunt impedance	$R_s$	$5 \times 10^{12} \Omega/\text{m}$
Resonator frequency	$f_r$	0.7993 GHz
Resonator quality factor	$Q$	$5 \times 10^4$
Wake decay time	$N_{\text{wake}}$	80 turns
Number of $k$ modes	$N_k$	1
Number of macroparticles	$N_{\text{mp}}$	$5 \times 10^5$
Number of turns	$N_{\text{turns}}$	$10^5$ turns

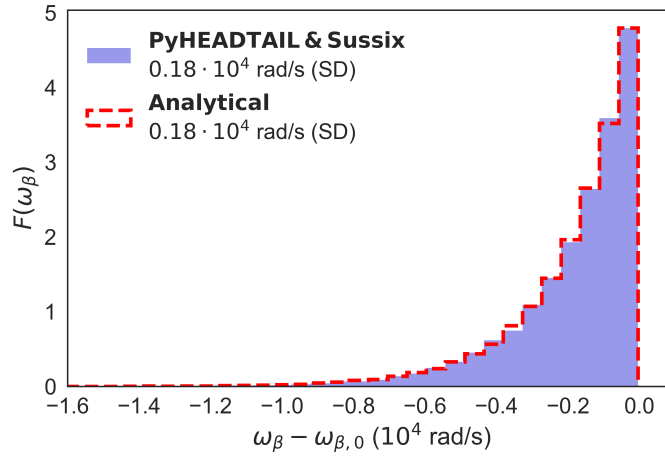


Figure 4.4: Betatron frequency distributions obtained using analytical formula (red dashed bars) and PYHEADTAIL in combination with a SUSSIX frequency analysis (blue area). The standard deviations (SD) are also listed for both cases.

frequency of the resonator accordingly. The optimisation was done by looking at the overlap area between the impedance and the bunch spectra ( $H_l^k(r)$  functions) for the main lowest-order modes. The resonator frequency and quality factor were tuned to match the spectral maximum of the azimuthal mode zero while remaining small for all the other modes. The final values are listed in Table 4.2.

To verify that the single-peak approximation is indeed valid for the chosen impedance, a scan in linear chromaticity was made first. Because of the large quality factor of the chosen resonator impedance, and therewith the slow decay time of the wakefield, PYHEADTAIL was set up to use the multi-turn

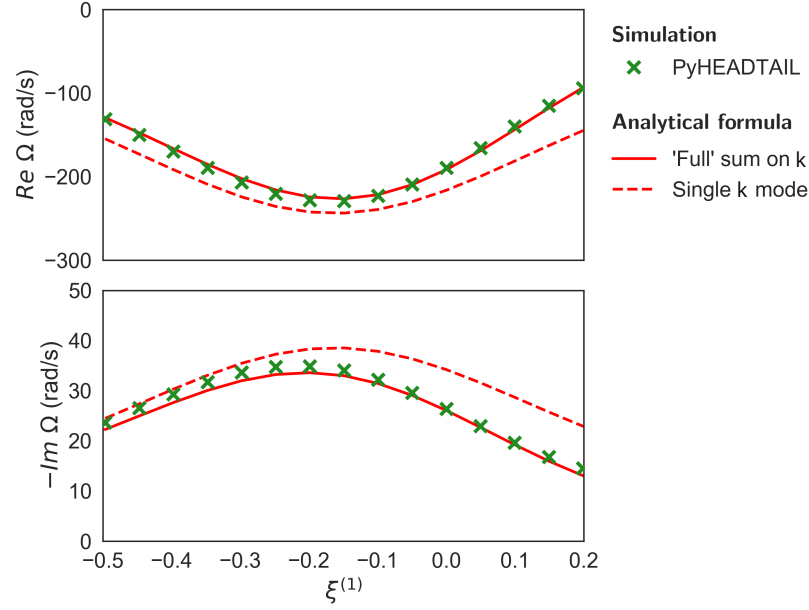


Figure 4.5: Real (top) and imaginary (bottom) coherent frequency shifts of the azimuthal mode zero as a function of  $\xi^{(1)}$  (with  $\xi^{(2)} = 0$ ) for the bunch and machine parameters in Table 4.2. PYHEADTAIL results (green crosses) are compared against analytical calculations. The latter are obtained using either the full overlap sum on index  $k$  (solid lines), or only the dominant term  $k_0$  (dashed lines).

wake feature. The number of turns for the multi-turn wakefield was set to  $N_{\text{wake}} = 80$  turns which was determined from a convergence study. Figure 4.5 summarises the results. It displays the real (top) and imaginary (bottom) frequency shifts for the most unstable mode which is by design an azimuthal mode zero, in the scanned range of  $\xi^{(1)}$ . PYHEADTAIL (green crosses) are shown on top of analytical predictions, once including the “full” overlap sum on index  $k$  (solid lines), summing up terms from  $k = -10^5$  to  $10^5$ , and once only considering the most dominant value  $k_0$  (dashed lines). It can be clearly seen that the full sum shows a very good agreement with the tracking simulations on the full range of  $\xi^{(1)}$ . The single-peak approximation is still reasonably close to PYHEADTAIL with a discrepancy of less than ten percent in both real and imaginary parts for  $-0.4 < \xi^{(1)} < -0.2$ . It becomes, however, as large as 50 percent in the imaginary part for  $\xi^{(1)} > 0.1$ . For that reason, the scan in second-order chromaticity will be performed at  $\xi^{(1)} = -0.3$  where the approximation works best for both the real and imaginary parts. This is to limit the error on the results of the scan in  $\xi^{(2)}$  originating from the single-peak approximation.

#### Second-order chromaticity scan

The PYHEADTAIL results of the scan in  $\xi^{(2)}$  are displayed in Fig. 4.6. The plot shows the dependence of the imaginary coherent frequency shift, or the instability growth rate, on the second-order chromaticity as obtained from tracking (green) when including the betatron frequency spread from  $\xi^{(2)}$ . Clearly, the stabilisation of the mode zero is achieved by introducing a small amount of negative  $\xi^{(2)}$  of about  $-10$  units, or a slightly larger amount of positive  $\xi^{(2)}$  (about 150 units). Beyond these values, there are no other modes that become unstable given that the scan was performed up to  $|\xi^{(2)}| = 1000$ . It will be demonstrated in the following with a detailed analysis that the stabilisation occurs indeed through



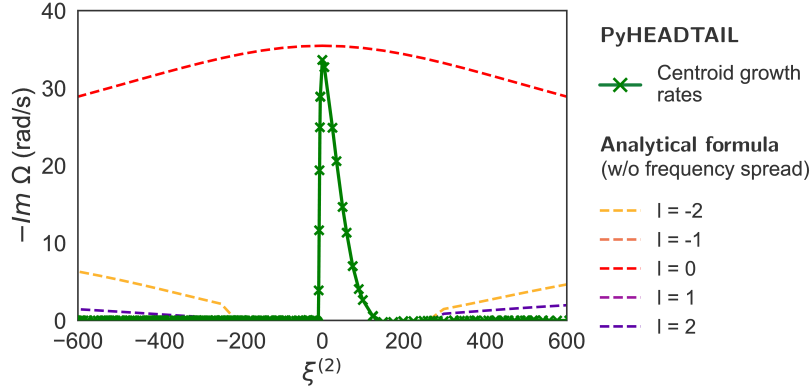


Figure 4.6: Dependence of the imaginary coherent frequency shift (growth rate) of the azimuthal mode zero on  $\xi^{(2)}$  using the bunch and machine parameters in Table 4.2 and  $\xi^{(1)} = -0.3$ . PYHEADTAIL results (green) include the frequency spread and Landau damping from  $\xi^{(2)}$  while analytical calculations (dashed lines) intentionally neglect it to model only the change of effective impedance for comparison.

the Landau damping mechanism. The reason why a larger amount of second-order chromaticity is required when using a positive sign has already been discussed previously. It is due to the fact that the specific azimuthal mode has a negative real coherent frequency shift combined with the one-sided frequency spreads and stability boundaries that are introduced by  $\xi^{(2)}$  as illustrated, e.g. in Fig. 4.4. In that case,  $\xi^{(2)} < 0$  provides much more effective Landau damping. Analytical solutions (dashed lines) are shown alongside the tracking results. They deliberately exclude the frequency spread from  $\xi^{(2)}$  to remove the effect of Landau damping and to illustrate solely the implications of a change of effective impedance. Unfortunately, this decoupling of the two effects cannot be achieved in a macroparticle tracking code as Landau damping is intrinsically included in the model once nonlinear chromaticity is added. At  $\xi^{(2)} = 0$ , PYHEADTAIL and the analytical prediction are expected to be identical. The small difference is due to the single-peak approximation as already discussed in Fig. 4.5 (at  $\xi^{(1)} = -0.3$ ). The red dashed line indicates that with  $\xi^{(2)}$  the growth rate of the mode zero instability is also decreased, but at a much smaller rate compared to PYHEADTAIL. This difference is due to the wilful neglect of the frequency spread and Landau damping. Additionally, there are two other modes ( $l = -2$  and  $l = 2$ ) that appear according to the Vlasov formalism with a much slower rise time than the mode zero. These modes are also suppressed in PYHEADTAIL. Although not displayed in the figure, the frequency spectra obtained from tracking simulations indicate that the dominant frequency component is always the mode zero which is in agreement with analytical predictions.

In the following, the Vlasov formalism is applied including the betatron frequency spread to make a detailed comparison with the tracking output possible. This is achieved by numerically solving the dispersion relation in Eq. (4.23) which gives the stability boundary diagram in complex frequency space. The results are only presented for  $\xi^{(2)} < 0$  here since negative second-order chromaticity provides more effective Landau damping. Stabilisation for  $\xi^{(2)} > 0$  can be shown analogously. The numerical solutions of the dispersion relation are displayed in Fig. 4.7 for six different values of  $\xi^{(2)} < 0$ , increasing in absolute value from top left to bottom right. The plots illustrate the increase of the stability boundary (black line,  $-\text{Im } \Omega = 0$ ) and hence of the stable area (blue hatched region,  $-\text{Im } \Omega \leq 0$ ) in complex frequency space. The instability under consideration is again the head-tail mode zero from Fig. 4.5

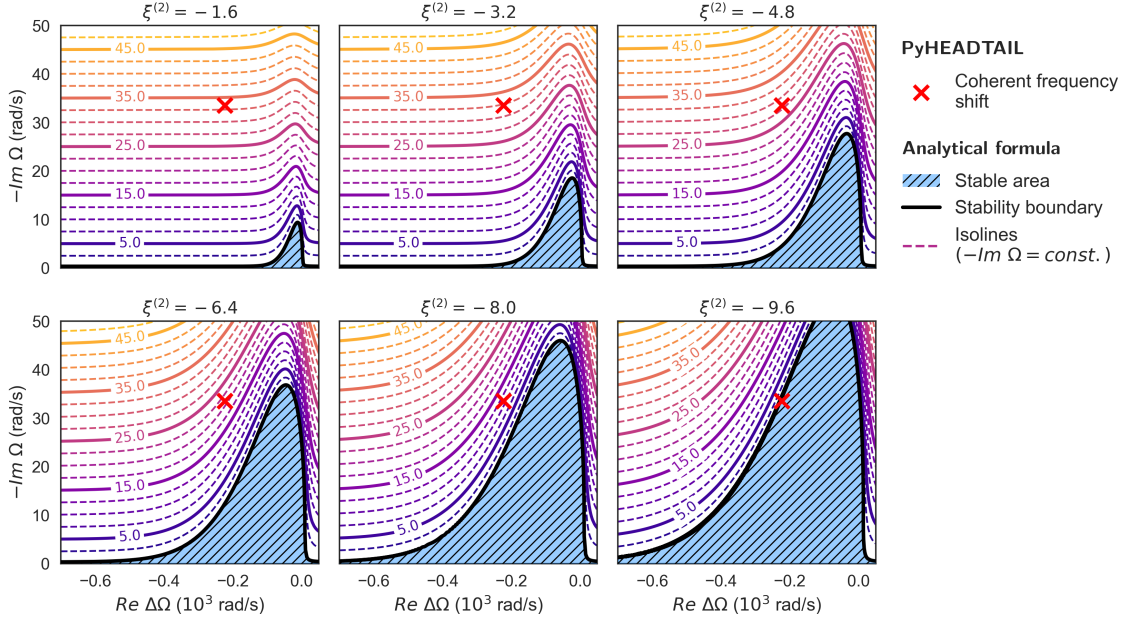


Figure 4.7: Stability boundary diagrams in complex frequency space obtained using Eq. (4.23) are shown for six different values of second-order chromaticity with  $|\xi^{(2)}|$  increasing from top left to bottom right. The unstable mode under consideration is marked with the red cross. The stability boundary is given by the black solid line and the area where  $-\text{Im } \Omega < 0$  is represented by the blue hatched region. The coloured lines show a selection of isolines  $-\text{Im } \Omega = \text{const.}$  and illustrate the distortion of the complex frequency space which becomes stronger with increasing frequency spread from  $\xi^{(2)}$ .

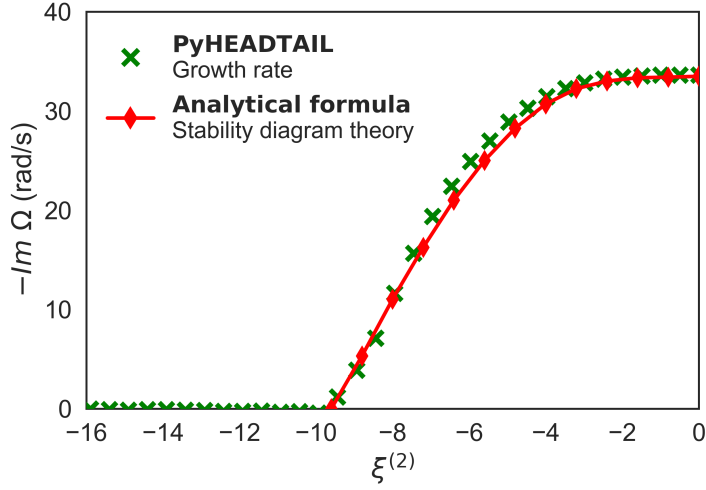


Figure 4.8: Stabilisation of the head-tail mode zero as a function of second-order chromaticity for a Gaussian beam. PYHEADTAIL simulations (green crosses) are shown together with analytical predictions computed by means of stability diagram theory (red diamonds). The latter are obtained from Fig. 4.7.

at  $\xi^{(1)} = -0.3$ . Its coherent frequency shift (red cross) is obtained from PYHEADTAIL simulations. As demonstrated by Fig. 4.6, the change of the effective impedance introduced by  $\xi^{(2)}$  is negligible for  $|\xi^{(2)}| \leq 200$  for this specific instability, and Landau damping is clearly the dominant effect. As a result, the unperturbed coherent frequency can be assumed to be independent of  $\xi^{(2)}$ . The coloured lines in the figure refer to constant values of imaginary frequency shift ( $-\text{Im } \Omega = \text{const.}$ ) and follow the distortion of the frequency space caused by the spread introduced by second-order chromaticity. It can be seen that for real frequency shifts far away from the extent of the spread, the frequency space remains undistorted and the isolines coincide with the ticks shown on the vertical axis.

Using the isolines in Fig. 4.7, one can read off the effective change (here: a decrease) of the imaginary frequency shift of the unstable mode as a function of frequency spread, or  $\xi^{(2)}$ . This illustrates the damping process: as the spread increases, the imaginary part of the unstable mode is effectively reduced, meaning that the growth rate of the instability decreases. For  $\xi^{(2)} \leq -9.6$ , the area of stability becomes large enough as to fully include the unstable mode. At this point the mode is Landau damped. A comparison of the growth rates of the instability between stability diagram theory and PYHEADTAIL tracking simulations is displayed in Fig. 4.8. The values read off from the stability diagrams and isolines in Fig. 4.7 are given in red. The growth rates obtained with PYHEADTAIL tracking simulations are represented by the green crosses and demonstrate an excellent agreement with theoretical predictions. Not only the stabilising threshold for the amount of  $\xi^{(2)}$  matches, but also the intermediate stages of  $\xi^{(2)}$  show a remarkable agreement on the imaginary frequency shift. This proves that the theory works successfully and that second-order chromaticity indeed provides Landau damping.

## 4.4 Conclusions

The existing Vlasov theory on transverse dipole modes has been extended to include the effects of nonlinear chromaticity up to arbitrary orders. This new formalism made it possible to confirm the hypothesis that nonlinear chromaticity has two effects on the beam dynamics of transverse coherent modes: (1) it leads to a change of effective impedance; and (2) it introduces Landau damping thanks to the incoherent betatron frequency spread with longitudinal amplitude which is present for even orders of chromaticity only. Indeed, the two mechanisms have been identified and studied separately using analytical formulae.

In addition, the theory has been successfully benchmarked up to second-order chromaticity for an airbag model and a Gaussian beam. In the first case, there is no Landau damping due to the missing frequency spread from detuning with longitudinal amplitude. Analytical results have been validated both with a tracking model and a circulant matrix solver which revealed an outstanding agreement. For the Gaussian beam it has been demonstrated that, given the assumption of a strongly peaked impedance, analytical predictions from stability diagram theory are in excellent agreement with tracking simulations. This proves that detuning with longitudinal amplitude indeed provides Landau damping. The frequency spread can be introduced, for example, by second-order chromaticity, or, similarly, by an rf quadrupole. This is in accordance with experiments and simulations that were carried out on the rf quadrupole and on second-order chromaticity in the LHC, discussed in Chapters 5 and 6, and provides the foundation for the interpretation of these results. All the theory derived for nonlinear chromaticity here can be directly applied to the rf quadrupole.

#### **Chapter 4. Theoretical studies: Vlasov formalism with nonlinear chromaticity**

---

The study also demonstrates, however, that the stabilisation with the rf quadrupole or second-order chromaticity is not easily evaluated analytically for arbitrary impedances. Macroparticle tracking simulations are hence still the most accurate way to study these effects which is the subject of the following chapter.

## 5 Numerical studies: beam stabilisation with an rf quadrupole

The basic working principle of an rf quadrupole for Landau damping was introduced in Chapter 3, and the theory of its effects on the beam dynamics was developed in Chapter 4. Here, the objective is to benchmark and confirm the stabilising effect predicted by Vlasov theory by means of numerical tracking simulations with PYHEADTAIL. This is achieved based on a single-bunch head-tail instability, observed in the LHC during commissioning in 2010 [77]. More advanced schemes of rf quadrupole systems will also be proposed and applied to HL-LHC and FCC-hh operational scenarios. Finally, potential downsides of the device will be pointed out and discussed briefly. The first part of the chapter is based on the work published in Refs. [33, 65–67].

The chapter is structured as follows: Section 5.1 introduces two complementary numerical models of the rf quadrupole and discusses their implementation in PYHEADTAIL, including basic benchmarks against theoretical calculations. In Section 5.2, the models are applied to an experimentally observed, slow LHC head-tail instability to demonstrate that the rf quadrupole can indeed provide beam stabilisation, similarly to magnetic octupoles. Thereafter, Section 5.3 proposes advanced usage schemes of rf quadrupoles, such as a two-family scheme, partially motivated by Vlasov theory, or the synergy of the device with magnetic octupoles. Their advantages are pointed out and backed with PYHEADTAIL simulations. In Section 5.4, an rf quadrupole system for the FCC-hh is evaluated in terms of single-bunch stabilisation, both at injection and collision energies. Stability thresholds as well as the minimum number of cavities required are provided for various likely operational scenarios. Section 5.5 briefly touches on potential downsides of an rf quadrupole which are mostly linked to single-particle (incoherent) effects and will require dedicated studies in the future. Finally, the main findings are summarised in Section 5.6.

### 5.1 Rf quadrupole models in PYHEADTAIL

To study the stabilising mechanism of an rf quadrupole with numerical simulations, the device was implemented in PYHEADTAIL with two different models: (1) as a detuning element; and (2) as localised kicks. The first model directly applies Eq. (3.4). It is implemented equivalently to the other effective nonlinear tracking features in PYHEADTAIL, such as chromaticity and magnetic octupoles: every macroparticle experiences a change in its phase advance depending on its longitudinal position in the

bunch. In the second, more accurate localised kick model, every macroparticle receives kicks to its transverse and longitudinal momenta computed according to the thin-lens approximation defined by Eqs. (3.1) and (3.2). Betatron detuning then follows naturally as a result after transverse tracking. The use of the thin-lens approximation is justified as the focal length of the rf quadrupole is much larger than the length of the element itself. For example, the quadrupole strength  $b_2$  required to stabilise the most unstable head-tail mode in the HL-LHC at 7 TeV is of the order of 0.3 Tm/m (see Section 5.3.2). This translates into a focal length  $> 7.7 \times 10^4$  m which is orders of magnitude larger than the length of the device ( $< 1$  m).

Both the detuning and the localised kick model of the rf quadrupole account for the constant phase offset  $\varphi_0$  introduced in Chapter 3. This way, different operational modes of the device can be studied. In terms of collective effects and Landau damping in particular, the two models are expected to produce identical results. The main difference is that the detuning model does not apply kicks to the particle momenta meaning that the transverse and longitudinal actions of each individual macroparticle remain unchanged. By consequence, resonances potentially introduced by the rf quadrupole (see Section 5.5.1) are not excited in this model, but must instead be analysed using the localised kick implementation. The two models are hence particularly useful when coherent and incoherent effects are to be studied separately.

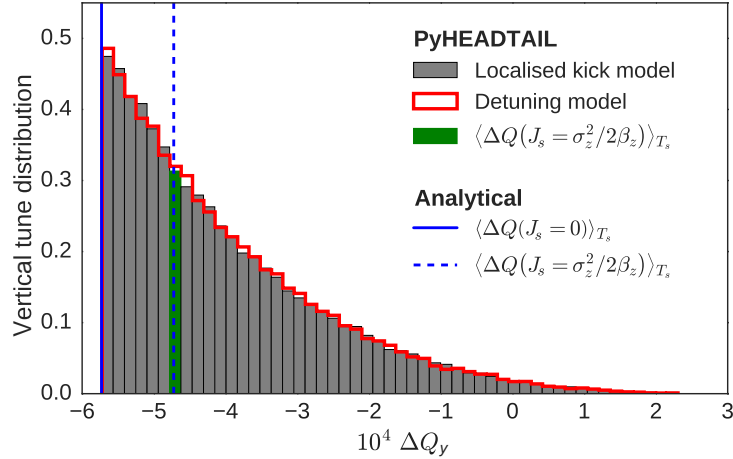


Figure 5.1: Comparison of the incoherent betatron tune distributions introduced by an rf quadrupole for the detuning (red) and the localised kick (grey) model implemented in PYHEADTAIL. Both models produce consistent results. Furthermore, the betatron detuning obtained from PYHEADTAIL for particles with respectively  $J_s = \sigma_z^2 / 2\beta_z$  (green) and  $J_s = 0$  is in good agreement with analytical calculations (blue).

The results of a benchmark comparing the two rf quadrupole models in PYHEADTAIL are displayed in Fig. 5.1. The rf quadrupole phase is set to  $\varphi_0 = 0$ . The two histograms show the incoherent vertical tune distributions established after tracking a 6D Gaussian bunch with  $N_{\text{mp}} = 5 \times 10^4$  macroparticles over five synchrotron periods assuming linear synchrotron motion. The frequency analysis is performed by means of the SUSSIX code. The two models yield consistent results within expectations given the limited number of macroparticles. The bin coloured in green represents particles with a longitudinal action of  $J_s = \sigma_z^2 / 2\beta_z$ . The blue dashed line marks the corresponding detuning expected from analytical calculations [Eq. (3.7)] and shows an excellent agreement with both tracking models. The approximation of

Eq. (3.7) holds as the beam and rf quadrupole parameters are chosen such that  $\omega\sigma_z/\beta c \ll 1$ . The blue solid line marks the average betatron detuning determined analytically for particles at  $J_s = 0$ , i.e. the particles residing in the centre of the longitudinal phase space. As expected, it coincides with the lower bound of the distribution. Since for these particles  $z$  remains zero over time, the (average) detuning is given simply by the constant quadrupole term  $-\beta_y b_2/4\pi B_0\rho$ . This result is exact, independent of whether or not the condition  $\omega\sigma_z/\beta c \ll 1$  holds.

## 5.2 Proof-of-concept

The numerical validation of the stabilising effect of an rf quadrupole is based on a horizontal single-bunch instability originally observed in the LHC at 3.5 TeV during machine commissioning in 2010 [77]. The analysis of the experimental data demonstrates that the particular instability can be characterised as a slow head-tail mode with an azimuthal number  $l = -1$ . In the same reference, it is shown experimentally that the instability can be suppressed by means of the Landau damping mechanism introduced by powering the Landau octupoles installed in the machine. The LHC octupole magnets are subdivided into a focusing and a defocusing family, depending on whether they are installed near the focusing or defocusing quadrupoles respectively. During machine operation, both families are powered with the same absolute current, but opposite polarities. The symbol  $I_{\text{oct}}$  denotes the current in the focusing family throughout this chapter. The threshold current in the Landau octupoles required to damp the head-tail mode under consideration was measured to be  $I_{\text{oct}}^{\text{meas}} = -15 \pm 5$  A. The corresponding instability rise time was found to be  $\tau \approx 9.8$  s at  $I_{\text{oct}} = -10$  A. The rise time at  $I_{\text{oct}} = 0$  A is expected to be significantly shorter, but was not studied experimentally.

### 5.2.1 Stabilisation through Landau octupoles

To confirm the validity of the numerical models attempts are made to reproduce the experimental observations made in the LHC employing two different accelerator physics codes. First, the macroparticle tracking code PYHEADTAIL, and second, the circulant matrix solver BIMBIM, both introduced in Section 2.3. PYHEADTAIL employs the detuning implementation of the octupole magnets where every particle receives, instead of transverse kicks, amplitude-dependent changes to its phase advances in order to model the incoherent tune shifts. The main input for the two codes is an accurate impedance (wakefield) model of the LHC as well as the beam and machine parameters at the time of the measurement. The latter are summarised in Table 5.1.

The output from PYHEADTAIL simulations makes a full characterisation of the observed unstable mode possible. The main results are summarised in Fig. 5.2 where  $N_{\text{mp}} = 10^6$  macroparticles were tracked over  $N_{\text{turns}} = 3 \times 10^5$  turns. The first plot (left) displays the time evolution of the horizontal bunch centroid in absence of incoherent tune spread, i.e. at zero octupole current. The amplitude growth is fitted with an exponential function to obtain the rise time  $\tau_0^{\text{sim}} = 3.7$  s of the unstable mode. For comparison with the aforementioned experimental measurements, the rise times from simulations are also determined for two different nonzero Landau octupole currents. At  $I_{\text{oct}} = -10$  A the rise time is  $\tau_{10}^{\text{sim}} = 4.5$  s and at  $I_{\text{oct}} = -15$  A it is  $\tau_{15}^{\text{sim}} = 12.8$  s. The values are consistent with the experiments  $\tau_{10}^{\text{meas}} = 9.8$  s, given the uncertainties of the model and the measurements (bunch intensity, sources of non-linearities other than octupole magnets not included in PYHEADTAIL, uncertainties in the impedance model). A spectral

Table 5.1: Main parameters used in PYHEADTAIL and BIMBIM to reproduce the LHC experimental machine setup at 3.5 TeV [77]. The parameters  $N_{\text{mp}}$  and  $N_{\text{turns}}$  are relevant exclusively for the PYHEADTAIL simulations, while  $N_r$  and  $N_s$  are valid solely for the calculations with BIMBIM.

Parameter		Value
Beam energy	$E_0$	3.5 TeV
Bunch intensity	$N$	$1.0 \times 10^{11}$ p
First-order chromaticity	$Q'_{x,y}$	6
Norm. transverse emittance	$\varepsilon_{x,y}^{\text{norm}}$	$3.75 \mu\text{m rad}$
Bunch length	$\sigma_z$	0.06 m
Number of macroparticles	$N_{\text{mp}}$	$10^6$
Number of turns	$N_{\text{turns}}$	$3 \times 10^5$ turns
Number of azimuthal slices	$N_s$	100
Number of rings	$N_r$	19

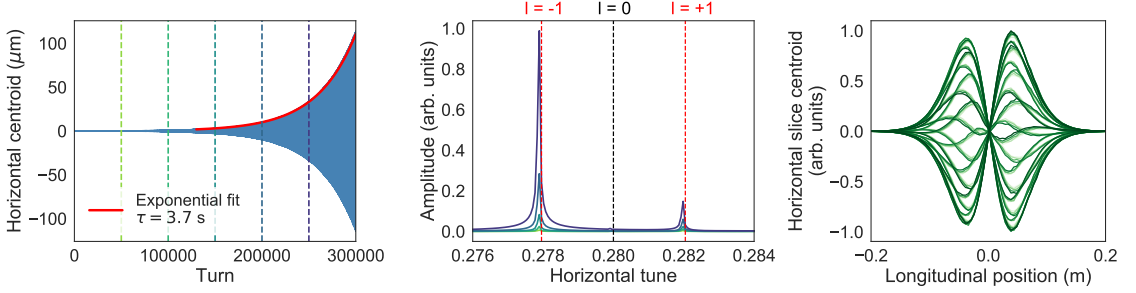


Figure 5.2: PYHEADTAIL simulation of the LHC instability observed at 3.5 TeV. *Left*: Horizontal bunch centroid evolution over time with an exponential fit of the rise time (red). *Middle*: Frequency spectra of the bunch centroid at different times during the simulation (see coloured, dashed lines in the left plot). *Right*: Horizontal slice centroid vs. longitudinal position for 80 consecutive turns. The head-tail motion is characterised by one node located at the centre of the bunch.

analysis of the bunch centroid oscillation at different times during the evolution of the instability is shown in the middle plot. The spectral curves correspond to the vertical dashed lines in the first plot and are obtained from a sliding-window FFT. The spectra clearly demonstrate that the azimuthal mode  $l = -1$  is the fastest growing mode which is again consistent with experimental observations [77]. The corresponding head-tail mode pattern is a standing wave with a single node in the bunch centre (right plot) indicating a radial mode number  $m = 1$ . The characterisation of the head-tail instability at hand is completed by the complex coherent tune shift of the *unperturbed* mode. The real part is obtained from spectral analysis (SUSSIX) and the imaginary component is calculated from the instability rise time fit  $\tau_0^{\text{sim}}$ . The results are

$$\begin{aligned} \text{Re}(\Delta\Omega_{\text{lin}}^{\text{PyHT}}/\omega_0) &= -3.6 \times 10^{-6}, \\ -\text{Im}(\Delta\Omega_{\text{lin}}^{\text{PyHT}}/\omega_0) &= 9.2 \times 10^{-5}. \end{aligned} \tag{5.1}$$



To determine the amount of Landau damping required to suppress this particular mode, the LHC Landau octupoles are added to the PYHEADTAIL tracking model and a scan in  $I_{\text{oct}}$  is performed with a stepsize of 5 A. A selection of the results is presented in Fig. 5.3. The instability is suppressed with a Landau octupole current of  $I_{\text{oct}}^{\text{PyHT}} = -17.5 \pm 2.5 \text{ A}$  which is consistent with experimental measurements.

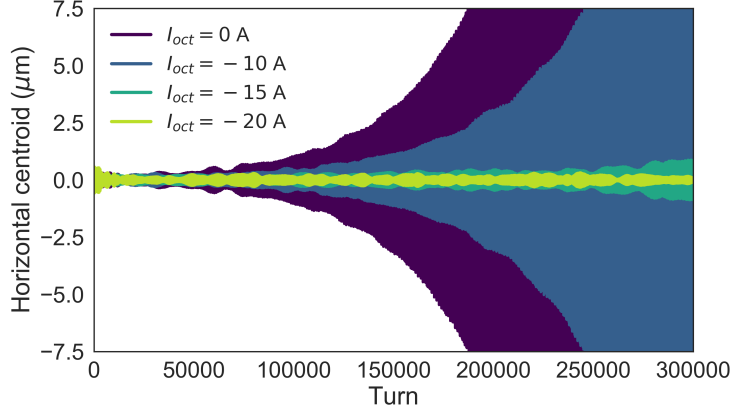


Figure 5.3: PYHEADTAIL results of the bunch centroid motion are displayed for different values of the Landau octupole current using the simulation parameters in Table 5.1.

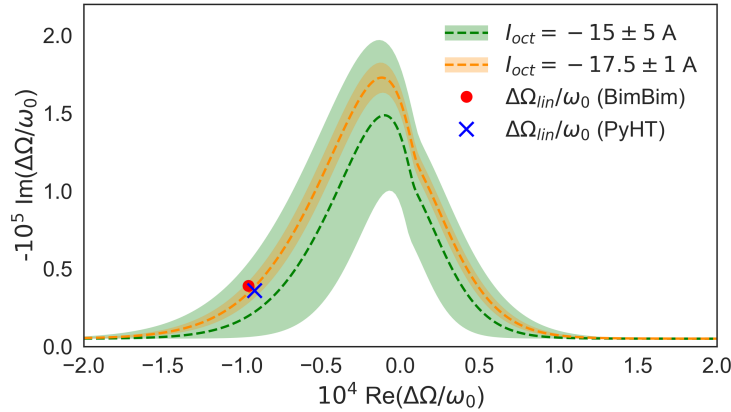


Figure 5.4: The dashed lines are stability diagrams obtained with the PYSSD code for two different Landau octupole currents  $I_{\text{oct}} = -15 \pm 5 \text{ A}$  (green) and  $I_{\text{oct}} = -17.5 \pm 1 \text{ A}$  (orange). The coloured areas are the corresponding uncertainties. The former corresponds to the values obtained experimentally, while the latter is determined from the unperturbed complex coherent tune shifts (red circle: BimBim, blue cross: PYHEADTAIL).

Complementary to the studies carried out with PYHEADTAIL, the second accelerator physics model used here is the CMM implemented in the BimBim code. It includes, among others, the effects of impedance and chromaticity, but neglects for instance multi-turn wakefields and Landau damping from magnetic octupoles. The former is a valid approximation for the LHC model as the relevant wakefields decay on timescales faster than the revolution period [75]. The absence of Landau damping in the CMM is a consequence of the linearisation of the system in the transverse planes. This approximation excludes the possibility to account for the nonlinear effects required to model detuning with transverse

amplitude. For the LHC instability, the most unstable mode in BIMBIM is again the azimuthal mode  $l = -1$  with a coherent tune shift of

$$\begin{aligned} \operatorname{Re}(\Delta\Omega_{\text{lin}}^{\text{CMM}}/\omega_0) &= -3.9 \times 10^{-6}, \\ -\operatorname{Im}(\Delta\Omega_{\text{lin}}^{\text{CMM}}/\omega_0) &= 9.6 \times 10^{-5}. \end{aligned} \quad (5.2)$$

The values are in good agreement with PYHEADTAIL tracking simulations (Eq. (5.1)).

As the CMM cannot model Landau damping from magnetic octupoles, stability diagram theory is used to determine the stabilising current  $I_{\text{oct}}$ . The Python Solver for Stability Diagrams (PYSSD) is employed here for that purpose [52, 56]. The results are shown in Fig. 5.4 in the complex tune space  $\operatorname{Re}(\Delta\Omega/\omega_0)$  vs.  $-\operatorname{Im}(\Delta\Omega/\omega_0)$  for two different Landau octupole currents,  $I_{\text{oct}} = -15 \pm 5 \text{ A}$  (green), and  $I_{\text{oct}} = -17.5 \pm 1 \text{ A}$  (orange). The coloured areas are respectively the corresponding uncertainties or the resolution of the scan in the Landau octupole current. The values of the unperturbed coherent tune shifts obtained from BIMBIM and PYHEADTAIL are given by the red and blue markers respectively. For this particular case, the theory predicts stability from the Landau octupoles at  $I_{\text{oct}}^{\text{SDT}} = -17.5 \pm 1 \text{ A}$  as illustrated by the orange dashed line and area. This is again fully consistent with tracking simulations and experiments (green line and area).

The studies presented above clearly demonstrate that the impedance model of the LHC used for the simulations with PYHEADTAIL and BIMBIM is reliable. Both accelerator physics models produce the same outcome and reproduce the observations made in the machine to a high degree of accuracy. The observed head-tail mode is Landau damped in experiments, tracking simulations, and in theory with fully consistent results on the required Landau octupole current. The fact that stability diagram theory predicts the same Landau octupole current as obtained from experiments and tracking studies underlines that the stabilisation of this mode is indeed a result of Landau damping. Furthermore, the Landau damping mechanism is accurately modelled in PYHEADTAIL and this forms the basis for the numerical proof-of-concept of the stabilising effect from an rf quadrupole discussed in the following.

### 5.2.2 Stabilisation through rf quadrupoles

The PYHEADTAIL study presented above is repeated with now an rf quadrupole (localised kick model) instead of the LHC Landau octupoles. A scan is performed in the integrated quadrupole field strength  $b_2$  with the Landau octupoles switched off. The results of the scan are summarised in Fig. 5.5. They show a picture that is very similar to Fig. 5.3. With increasing quadrupole strength, and hence increasing tune spread, the growth rate of the unstable mode is reduced and eventually it is suppressed entirely. The stability threshold is at  $b_2 = 0.105 \pm 0.005 \text{ Tm/m}$  for this particular case. Although not displayed here, an identical result is obtained with the detuning model of the rf quadrupole in PYHEADTAIL. The studies confirm the effect expected from the theory and demonstrate that an rf quadrupole for beam stabilisation can work conceptually. According to preliminary cavity design studies, the required stabilising quadrupole strength could be achieved with a single cavity with an equivalent active length of about 0.3 m (see Ref. [68]). For comparison, to stabilise the same mode with the LHC Landau octupoles an equivalent active length of about 1.5 m is required. This is assuming that they are powered at their maximum current of 550 A. The ratio of active lengths required for stabilisation between the rf quadrupole and octupole magnets is hence a factor five here. However, this value is strongly dependent on the beam energy as explained in Section 3.1.2. The differences in efficiency between

Landau octupoles and rf quadrupoles will thus become much more important for machines such as HL-LHC, HE-LHC, or FCC-hh.

In analogy to the analysis performed above for the Landau octupoles, the stabilising strength of an rf quadrupole is evaluated also by means of stability diagram theory. For that purpose, the approximate dispersion relation in Eq. (3.17) is solved numerically for the parameters of the PYHEADTAIL simulation. The outcome is presented in Fig. 5.6. The red and blue markers are again the unperturbed complex coherent tune shifts obtained with BIMBIM and PYHEADTAIL respectively. The dashed line marks the stability diagram for an rf quadrupole strength of  $b_2 = 0.0235 \pm 0.0010$  Tm/m. The coloured area corresponds to the resolution of the scan in  $b_2$ . There is a clear discrepancy of a factor four in the required stabilising strength between theory and PYHEADTAIL tracking simulations. The main reason for this difference is that the dispersion relation does not take into account the impedance model of the LHC, as explained in Section 3.3 and Chapter 4. It assumes instead that there is only a single peak in the impedance spectrum that is responsible for driving the given instability. Clearly, this is not the case here: (1) the LHC impedance has several broad-band components; and (2) the overlap between the bunch spectrum and the impedance determines the coherent tune shift (and growth rate) of the instability [25, 75]. Furthermore, the tracking simulation takes into account the full cosine dependence of the detuning from the rf quadrupole while the analytical formula considers only the first-order term in  $J_s$ . For the given rf quadrupole frequency and bunch length, the detuning of the particles at large longitudinal amplitudes and thus the overall tune spread and the Landau damping are overestimated by the theory compared to tracking simulations.

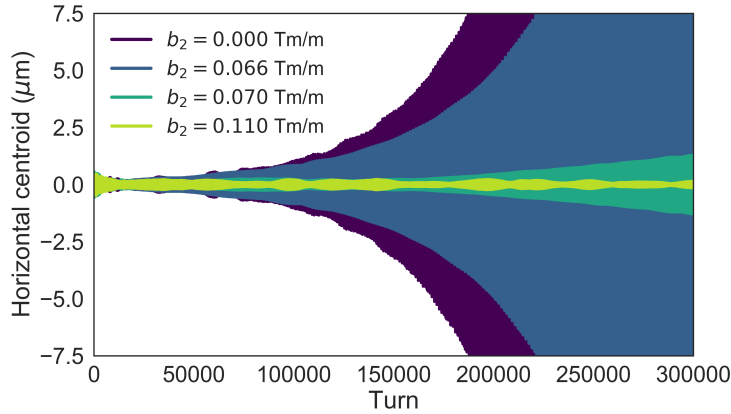


Figure 5.5: PYHEADTAIL results of the bunch centroid motion for different values of the rf quadrupole strength  $b_2$  and simulation parameters in Table 5.1.

Comparing the amounts of rms tune spread required for beam stability from magnetic octupoles and the rf quadrupole helps estimate the Landau damping efficiency for the two mitigation techniques. The rms tune spreads  $\Delta Q_{\text{rms}}$  required to suppress slow head-tail instabilities are typically much smaller than the synchrotron tune since  $\text{Re}(\Delta\Omega_{\text{lin}}/\omega_0) \ll Q_s$ . For the unstable mode studied here, they are (from PYHEADTAIL)

$$\begin{aligned}\Delta Q_{\text{rms}}^{\text{oct}} &= (2.4 \pm 0.3) \times 10^{-5} \approx 0.012 Q_s, \\ \Delta Q_{\text{rms}}^{\text{rfq}} &= (3.4 \pm 0.5) \times 10^{-5} \approx 0.017 Q_s,\end{aligned}\tag{5.3}$$

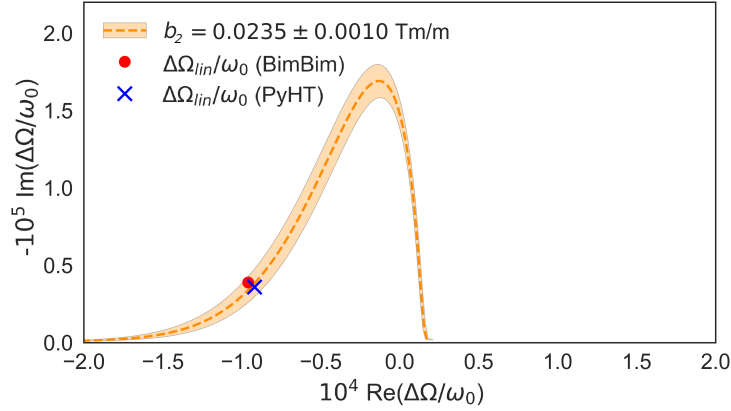


Figure 5.6: Stability diagram obtained by numerically solving the approximate dispersion relation for an rf quadrupole with  $b_2 = 0.0235 \pm 0.0010$  Tm/m. The coloured area corresponds to the resolution of the scan in  $b_2$ . The unperturbed complex coherent tune shifts from BimBim (red circle) and from PyHEADTAIL (blue cross) are shown as well.

with  $Q_s \approx 2 \times 10^{-3}$ . Although the two values are of a similar order of magnitude, the discrepancy is significant and emphasises that the amount of incoherent tune spread alone does not give the whole picture about whether an unstable mode is Landau damped or not. The imaginary part of the unperturbed coherent tune shift as well as the shape of the stability diagram are both essential ingredients to address this question. This becomes clear by comparing Figs. 5.4 and 5.6. The reason for the difference of the required tune spreads is a consequence mainly of the way the Landau damping mechanism works for detuning with transverse and longitudinal amplitude respectively. The dispersion integral equations for the two approaches differ significantly from each other as explained earlier in the thesis. As a result, the corresponding stability diagrams have a different shape and the tune spreads required to suppress a particular instability will in general be different as well. It should also be taken into account that the size of the stability diagram for detuning with longitudinal amplitude depends on the azimuthal mode number. Given a specific tune spread, the area of stability is larger for higher-order modes and they can hence be suppressed more easily. This is not the case for Landau damping from magnetic octupoles [78].

### 5.3 Advanced rf quadrupole schemes

Stability diagram theory for detuning with longitudinal amplitude predicts, among others, a strong asymmetry in the stabilising efficiencies between the two transverse planes. This has been discussed in Chapter 4 and is studied in the following by qualitatively comparing theory against tracking simulations. To overcome the asymmetry, a two-family scheme for rf quadrupoles is proposed and the performance is evaluated with tracking simulations. The idea is motivated by the two-family scheme employed for beam stabilisation with magnetic octupoles [60]. Finally, the synergy between rf quadrupoles and magnetic octupoles is studied in terms of stabilising efficiency for an HL-LHC machine setup.

The horizontal and the vertical complex coherent frequency shifts of the unstable head-tail modes are typically very similar for a hadron collider like the LHC, i.e.  $\Delta\Omega_{\text{lin}}^x \approx \Delta\Omega_{\text{lin}}^y$ . For LHC operational

beam and machine parameters, for instance, the most unstable impedance-driven head-tail modes are characterised by  $\text{Re}(\Delta\Omega_{\text{lin}}^{x,y}/\omega_0) < 0$ . For a single rf quadrupole, the stability diagrams in Fig. 3.6 illustrate that the stable regions in the two transverse planes are mirrored about the vertical axis with respect to each other. Given that  $\text{Re}(\Delta\Omega_{\text{lin}}^{x,y}/\omega_0) < 0$ , one plane (here: horizontal) is expected to exhibit a much better stabilising efficiency than the other one for an rf quadrupole with a phase of  $\varphi_0 = 0$ . The situation is inverse when the device is operated with  $\varphi_0 = \pi$ . This asymmetry has first been observed in PYHEADTAIL simulations for the LHC instability at an energy of 3.5 TeV, introduced in the previous section. For this particular case, by changing the phase  $\varphi_0$  from 0 to  $\pi$ , the stabilising quadrupole strength increases roughly by a factor three from  $b_{2,0} = 0.105 \pm 0.005 \text{ Tm/m}$  to  $b_{2,\pi} = 0.35 \pm 0.02 \text{ Tm/m}$ .

The asymmetric nature of the rf quadrupole kicks is impractical and a systematic study is made with PYHEADTAIL to further examine this particular observation and to find possible solutions to circumvent it. To simplify the simulation setup, a pure dipolar analytical broad-band resonator impedance is used with identical components in the horizontal and the vertical planes [see Eq. (2.47)]. For further simplification of the setup the first-order chromaticity is set to  $Q' < 0$  to induce a weak azimuthal mode  $l = 0$  head-tail instability (note that the study is done above transition energy). This has no impact on the underlying stabilising mechanism described by stability diagram theory. Both the real and the imaginary components of the coherent tune shift are controlled by varying the beam intensity. With increasing intensity the coherent tune shift becomes larger due to the stronger interaction of the beam with the impedance. It is hence expected from theory that more rf quadrupole strength will be required to achieve stabilisation. The two transverse planes are affected equivalently by the intensity increase. However, theory predicts that the stabilising rf quadrupole strength must be different in the two planes due to the strong asymmetry of the stability diagrams.

The results of the simulation studies are summarised in Fig. 5.7.  $N_{\text{mp}} = 8 \times 10^4$  macroparticles were tracked over  $N_{\text{turns}} = 10^5$  turns and a scan in  $b_2$  was performed for every beam intensity. The top plot corresponds to an rf quadrupole with  $\varphi_0 = 0$  and clearly represents the asymmetry expected from the theory. The horizontal plane becomes stable already at much lower quadrupole strengths than the vertical one. By changing  $\varphi_0$  from 0 to  $\pi$ , the behaviour in the two planes is swapped (bottom plot), again in accordance with expectations given the quadrupole nature of the device. At the maximum beam intensity, the difference between the threshold quadrupole strengths in the two planes reaches almost a factor five for this particular case.

Figure 5.8 underlines the qualitative agreement between tracking simulations and theory and provides an explanation for the observations made. The plot shows the complex tune space with the dependence of the unperturbed tune shift on the beam intensity, represented by the coloured markers. They are normalised to the absolute value of the maximum real coherent tune shift measured at the highest intensity of the scan. The real and the imaginary parts depend approximately linearly on the beam intensity. Furthermore,  $\text{Re}(\Delta\Omega_{\text{lin}}^{x,y}/\omega_0) \leq 0$ . Stability diagrams for two different quadrupole strengths of an rf quadrupole operated with  $\varphi_0 = 0$  are overlaid for the horizontal (solid lines) and the vertical plane (dashed lines). It is obvious that the stabilising behaviour in the horizontal plane is expected to be significantly better than in the vertical one. Additionally, comparing the stability diagrams for the two quadrupole strengths, the area of stability grows much faster in the horizontal compared to the vertical plane. This explains the increase in the difference between the stability thresholds as a function of beam intensity observed in Fig. 5.7.

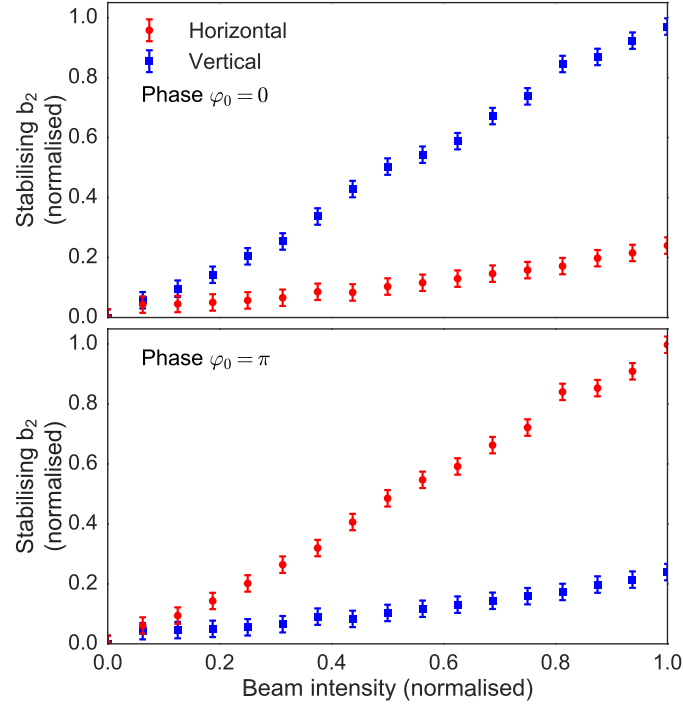


Figure 5.7: PYHEADTAIL tracking simulations illustrating the stabilising efficiency in the horizontal (red) and the vertical (blue) planes with an rf quadrupole with  $\varphi_0 = 0$  (top) and  $\varphi_0 = \pi$  (bottom) respectively.

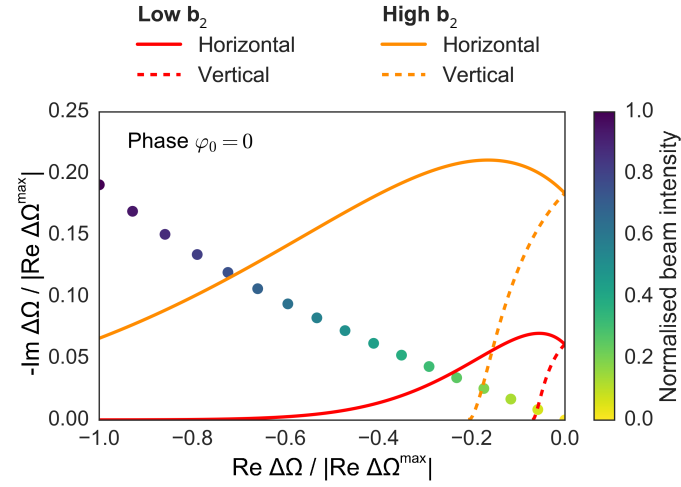


Figure 5.8: Evolution of the unperturbed coherent tune shift in the complex tune space as a function of beam intensity. Stability diagrams for the horizontal (solid lines) and the vertical (dashed lines) planes are overlaid for two different strengths for an rf quadrupole operated with  $\varphi_0 = 0$ .

### 5.3.1 Two-family configuration

The asymmetric stabilising behaviour in the two transverse planes can be overcome by installing two independent rf quadrupole families that operate with opposite phases and are placed at two different

locations in the machine lattice. One of them is placed at high  $\beta_x$ , low  $\beta_y$  to improve beam stability mainly in the horizontal plane while the other one is installed at a location with low  $\beta_x$  and high  $\beta_y$  for stability mainly in the vertical plane. Naturally, the difference between the local beta functions must be as large as possible to avoid significant compensation of the detuning effects between the two families.

Figure 5.9 illustrates the stabilising efficiency in the two transverse planes for the two-family rf quadrupole scheme for the broad-band resonator driven instability introduced in the previous section. For illustrative purposes, values of ten have been assumed for respectively the ratio  $\beta_x/\beta_y$  and  $\beta_y/\beta_x$  at the two locations. The vertical axis represents the *total* quadrupole strength, i.e. the sum of the strengths of the two families, to allow a better comparison with the one-family schemes depicted in Fig. 5.7. The two families are powered with identical strengths. The new scheme offers two main advantages. First, the strong asymmetry between the two planes is removed and the required stabilising strength is equalised in both planes. Second, the total quadrupole strength to achieve stability in the two planes is significantly lower overall. However, since the two families counteract each other to a small amount, the stabilising strength in the two-family scheme cannot reach the values of the respective favoured plane in the one-family scheme. The effect of compensation between the families is minimised by maximising the ratio of the beta functions in the two transverse planes at the locations of the rf quadrupole cavities.

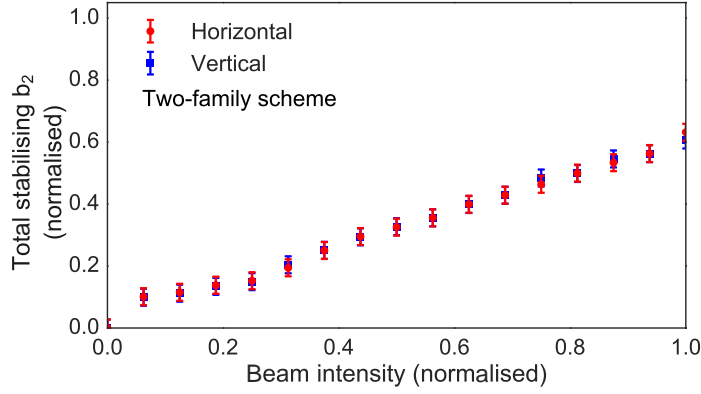


Figure 5.9: PYHEADTAIL tracking simulations illustrating the stabilising efficiency in the horizontal (red) and the vertical (blue) planes with the two-family rf quadrupole scheme.

### 5.3.2 Synergy with magnetic octupoles

To understand the practicality and usefulness of an rf quadrupole in a future hadron collider, such as the HL-LHC, it is important to assess its interplay with magnetic octupoles. The reason is that for the HL-LHC, the octupole magnets currently installed in the LHC will remain an essential part of the instability mitigation toolset. The stabilising performance of an ensemble of 800 MHz superconducting rf quadrupole cavities (single-family scheme) is evaluated in presence of the LHC Landau octupoles. A single-bunch instability driven by the dipolar accelerator impedance for foreseen operational beam and machine parameters serves as a study case. The main values of the machine setup are summarised in Table 5.2. An idealised, transverse bunch-by-bunch feedback system with a damping time of  $\tau_{fb} = 50$  turns is also included in the simulation model. At a first-order chromaticity of  $Q'_{x,y} = 10$ , the

most unstable mode is a slow head-tail instability with azimuthal and radial mode numbers  $l = 0$  and  $m = 2$  respectively. This is consistent with experimental observations made in the LHC at 6.5 TeV [26] (see also Chapter 6).

Table 5.2: Main machine and PYHEADTAIL simulation parameters used for the HL-LHC case to study the combination of rf quadrupoles and magnetic octupoles.

Parameter		Value
Beam energy	$E_0$	7 TeV
Bunch intensity	$N$	$2.2 \times 10^{11}$ p
First-order chromaticity	$Q'_{x,y}$	10
Norm. transverse emittance	$\epsilon_{x,y}^{\text{norm}}$	$2.5 \mu\text{m rad}$
Bunch length	$\sigma_z$	0.082 m
Transverse feedback	$\tau_{\text{fb}}$	50 turns
Number of macroparticles	$N_{\text{mp}}$	$8 \times 10^5$
Number of turns	$N_{\text{turns}}$	$6 \times 10^5$ turns

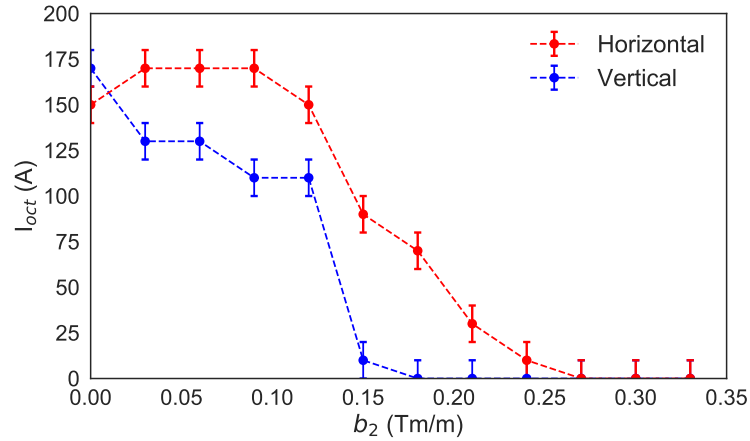


Figure 5.10: PYHEADTAIL tracking simulations illustrating the combined stabilising effect from LHC Landau octupoles and an rf quadrupole in the HL-LHC for machine and beam parameters in Table 5.2.

PYHEADTAIL simulations with  $N_{\text{mp}} = 8 \times 10^5$  macroparticles tracked over  $N_{\text{turns}} = 6 \times 10^5$  turns predict that beam stability from LHC Landau octupoles alone is guaranteed for  $I_{\text{oct}} = 170 \pm 10$  A or higher. This is about one third of the maximum reachable current. By adding an rf quadrupole to the simulation model the stabilising current in the Landau octupoles can be significantly lowered as demonstrated in Fig. 5.10. The beta functions at a potential location of the rf quadrupole in the HL-LHC lattice are set to a conservative  $\beta_{x,y} = 200$  m. Although there is a minor effect on the threshold current  $I_{\text{oct}}$  up to a cavity strength of about  $b_2 = 0.1$  Tm/m, the simulations predict that already for  $b_2 \geq 0.27$  Tm/m the Landau octupoles are no longer required to mitigate the instability. Given the possible cavity designs, the latter strength could in principle be provided with one rf cavity of the four-vane type (see Ref. [68] and Chapter 3).



## 5.4 Rf quadrupole system for FCC-hh

As explained in Chapter 1, the FCC-hh project is planning to reach a c.m. energy of 100 TeV for protons (50 TeV per beam) and aims at producing a peak luminosity of up to  $\mathcal{L} = 30 \times 10^{34} \text{ cm}^{-2} \text{ s}^{-1}$ . This can be achieved, among others, by colliding beams with small transverse emittances. Indeed, according to the preliminary collider design, the transverse geometric emittances could reach values of  $\varepsilon_{x,y}^{\text{geo}} < 0.01 \text{ nm rad}$  at 50 TeV, compared to  $\varepsilon_{x,y}^{\text{geo}} = 0.50 \text{ nm rad}$  for the LHC beams (7 TeV). The bunch length, on the other hand, would remain comparable to that of the LHC beams. At collision energy, the longitudinal action spreads in the bunches of the FCC-hh would hence be up to six orders of magnitude larger than the transverse ones. As a result, the number of magnetic octupoles required to provide the tune spread for sufficient Landau damping of an LHC-equivalent head-tail instability at collision energy could reach up to about 3,500 LHC-type magnets (total active length of approximately 1.1 km) as calculated in Ref. [78]. In the same reference, a scenario is drawn up assuming advanced magnet technology with a 3.5 times higher octupole strength and twice the active length per magnet compared to LHC octupoles. In that case, one could lower the number of required magnets to about 500. However, it is arguable whether an increase in the kick strength per octupole magnet is favourable. Typically, strong localised kicks can have a detrimental impact on the beam lifetime and detailed simulation studies will hence be required. Furthermore, even with advanced magnet technology, a total active length of approximately 325 m of magnetic octupoles would be necessary to provide an amount of Landau damping equivalent to that in the LHC. For comparison, the total active length of the Landau octupoles in the LHC is about 54 m. This is why an rf quadrupole system could potentially be an attractive solution for the FCC-hh.

The advantages of the two-family scheme for rf quadrupoles were demonstrated in Section 5.3. It was shown that the asymmetry in the quadrupole field strengths required to provide stability in the two transverse planes is removed and that the total strength can be lowered overall. This scheme is hence highly recommended for the FCC-hh and the studies presented in the following were conducted in this configuration. The proposed locations for the two families in the FCC-hh lattice and the corresponding values of the beta functions are also discussed below.

### 5.4.1 Simulation setup

PYHEADTAIL simulations were performed to study the transverse single-bunch instabilities expected for the FCC-hh at injection (3.3 TeV) and collision (50 TeV) energies. The latest transverse dipolar wakefield model (as of November 2017) of the machine was used with the wake strengths *multiplied by a factor three* to account for uncertainties as well as additional contributions from elements that may be included in the machine lattice in the future. The rf quadrupole effect is applied as a thin-lens kick, according to the model described in Section 5.1. The desired operating point for the FCC-hh lies at a first-order chromaticity close to zero, but various scenarios are currently under study. Here, the simulations are carried out with  $Q'_{x,y}$  set to 0, 5, and 10, respectively, and with an idealised transverse bunch-by-bunch feedback system with a damping time of  $\tau_{\text{fb}} = 60$  turns at injection energy, and respectively 300 turns or 600 turns at collision energy. For each of these settings, a scan in integrated rf quadrupole field gradient  $b_2$  is made to determine the number of cavities required for beam stabilisation for each operational scenario.

The simulation setup uses the FCC-hh machine and beam design parameters summarised in Ta-

ble 5.3 [16, 17]. The bunch is modelled as a collection of  $N_{\text{mp}} = 4 \times 10^5$  macroparticles which are tracked over  $N_{\text{turns}} = 6 \times 10^5$  turns. Two rf quadrupole families operating with a phase difference of  $\Delta\varphi_0 = \pi$  are installed in locations with  $\beta_{x,\pi} = 80 \text{ m} / \beta_{y,\pi} = 360 \text{ m}$  and  $\beta_{x,0} = 360 \text{ m} / \beta_{y,0} = 80 \text{ m}$  respectively. The values for the beta functions originate from a preliminary lattice calculation with MAD-X and refer to locations  $s_\pi = 54,000 \text{ m}$  and  $s_0 = 54,820 \text{ m}$  respectively, in the main rf straight section [79]. They may be subject to further optimisations of which the rf quadrupole performance could benefit as the number of cavities is inversely proportional to the values of the beta functions. In addition, by further optimising the ratio of  $\beta_x$  and  $\beta_y$  at the locations of the two families, the mutual partial compensation of respectively the horizontal or the vertical tune spreads could be minimised.

Table 5.3: Main machine and PYHEADTAIL simulation parameters used for different FCC-hh operational scenarios to define the requirements for an rf quadrupole system.

Parameter		Value
Beam energies	$E_0$	{3.3, 50.0} TeV
Bunch intensity	$N$	$10^{11} \text{ p}$
First-order chromaticities	$Q'_{x,y}$	{0, 5, 10}
Norm. transverse emittance	$\epsilon_{x,y}^{\text{norm}}$	$2.2 \mu\text{m rad}$
Bunch length	$\sigma_z$	$0.08 \text{ m}$
Transverse feedback	$\tau_{\text{fb}}$	{60, 300, 600} turns
Number of macroparticles	$N_{\text{mp}}$	$4 \times 10^5$
Number of turns	$N_{\text{turns}}$	$6 \times 10^5 \text{ turns}$

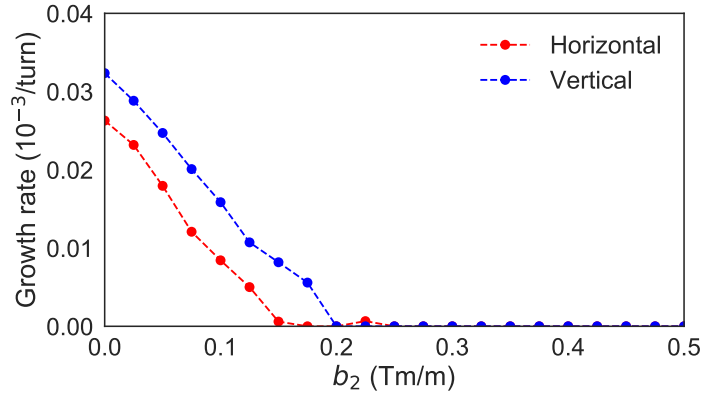


Figure 5.11: Example of horizontal (red) and vertical (blue) instability growth rates vs. total rf quadrupole strength for FCC-hh at injection energy. The result is for  $Q'_{x,y} = 5$  and a transverse feedback damping time of  $\tau_{\text{fb}} = 60$  turns.

#### 5.4.2 Rf quadrupole requirements

An example outcome from the rf quadrupole scans in  $b_2$  is displayed in Fig. 5.11 for FCC-hh at injection energy, assuming a first-order chromaticity of  $Q'_{x,y} = 5$  and a transverse feedback damping time of  $\tau_{\text{fb}} = 60$  turns. Without the rf quadrupole, the model predicts that the bunch is unstable in both

transverse planes. The observed head-tail instability is an azimuthal mode  $l = 1$ . The plot illustrates the reduction of the instability growth rates in the two transverse planes with increasing rf quadrupole strength. The stabilising strengths  $b_2^{\text{stable}}$  are approximately the same for both planes. This is thanks to the two-family scheme and also a result of similar dipolar beam-coupling impedances in the horizontal and vertical planes of the FCC-hh.

Table 5.4: Summary of required rf quadrupole strengths for stable single-bunch operation for various scenarios using the latest impedance model of the machine (as of November 2017) multiplied by a factor of three (safety margin). The number of cavities is assuming the four-vane cavity design with an aperture radius of 30 mm and the lowest taper angle (per cavity strength of  $b_2^{\text{cavity}} = 0.35 \text{ Tm/m}$  with an active length of about 0.3 m).

Scenario	$Q'_{x,y}$ $\tau_{\text{fb}}$ (turns)		Mode	$b_2^{\text{stable}}$ (Tm/m)		# cavities (per family)	Total active length (m)
			(Azim.)	Horizontal	Vertical		
Injection	0	60	-1	$0.45 \pm 0.05$	$0.45 \pm 0.05$	2	1.2
	5	60	1	$0.15 \pm 0.03$	$0.20 \pm 0.03$	1	0.6
	10	60	0	$0.1 \pm 0.1$	$0.4 \pm 0.1$	2	1.2
Collision	0	300	-1	$8.6 \pm 0.4$	$6.8 \pm 0.4$	25	15.0
	5	300	-1	$8.6 \pm 0.4$	$6.4 \pm 0.4$	25	15.0
	10	300	2	$1.9 \pm 0.1$	$1.9 \pm 0.1$	6	3.6
	0	600	0	$7.1 \pm 0.4$	$5.6 \pm 0.4$	21	12.6
	5	600	-1	$7.9 \pm 0.4$	$6.4 \pm 0.4$	23	13.8
	10	600	-1	$6.4 \pm 0.4$	$7.1 \pm 0.4$	23	13.8

The same type of simulations was performed for a selection of potential FCC-hh operational scenarios. Table 5.4 shows a summary of the rf quadrupole requirements for each of them, with the required values of  $b_2$  given per family. At injection energy, the number of cavities required is relatively low. This is mainly thanks to the low beam rigidity and thus the stronger effect of the quadrupole kicks. At collision energy, the strength required for stable single-bunch operation is up to a factor 20 larger. This is roughly in agreement with the ratio of the Lorentz factors at collision (*coll*) and injection (*inj*) energies,  $\gamma_{\text{coll}}/\gamma_{\text{inj}} \approx 15$  and illustrates that the efficiency of the rf quadrupole scales roughly with  $1/\gamma$  as a result of the increased beam rigidity as described in Chapter 3. The slight discrepancy can be explained by the difference in the wakefields at injection and collision energies as well as the different damping times of the feedback system used for the two scenarios. The total active length, accounting for the two families, is given in the last column of the table. It is to be compared to the abovementioned total active length of the Landau octupoles (325 m in the best case). As explained above, a reduction of the number of cavities can be achieved by optimising the beta functions at the locations of the rf quadrupole system. With fewer cavities, the longitudinal impedance of the rf quadrupole system can also be linearly reduced. In addition, by decreasing the number of cavities, the number of cryogenic modules will be smaller as well which will greatly reduce the cost of the entire system.

## 5.5 Potential limitations

In terms of collective effects, numerical simulations demonstrate that the rf quadrupole can indeed be successfully used to mitigate single-bunch instabilities through Landau damping. However, the impact

of the device on the single-particle dynamics is yet to be studied in detail. Here, we will briefly discuss three of the effects that need to be thoroughly evaluated before moving on to building a prototype cavity for a proof-of-principle experiment. First, it has been observed that the rf quadrupole can drive synchro-betatron resonances under certain conditions and a summary of these observations is discussed here. Second, like multipole magnets, the rf quadrupole introduces feed-down effects. For example, if the beam passes through the cavity with a transverse offset, it is subject to an additional rf dipole field. Finally, the importance of dynamic aperture studies is pointed out and first estimates of the impact of an rf quadrupole are made using the results from HL-LHC “crab cavity” simulations [80]. We provide here a qualitative description of the above items.

### 5.5.1 Synchro-betatron resonances

The rf quadrupole produces, among others, a horizontal kick on a particle  $i$  as a function of its longitudinal coordinate

$$\Delta p_{x,i}(t) = -e b_2 x_i(t) \cos\left(\omega \frac{z_i(t)}{\beta c}\right). \quad (5.4)$$

Hence, if a synchronicity condition between the longitudinal and the transverse motion is fulfilled, i.e. a specific relation between the transverse and longitudinal tunes [see Eq. (5.5) below], the rf quadrupole kicks may add up coherently over time and drive a resonance (similarly in the vertical plane). The transverse kicks in rf cavities thus typically drive resonances of the synchro-betatron type (SBR) since they introduce a coupling between the longitudinal and transverse oscillations of the particles. The concept has been briefly explained in Section 2.1.1. An rf quadrupole also drives SBR, but the device does not couple the horizontal and the vertical motion at first order, and hence the SBR condition [Eq. (2.28)] can be simplified. For the horizontal plane ( $k = 0$ )

$$j Q_{x,i} + l Q_{s,i} = n, \quad (5.5)$$

with  $j, l, n \in \mathbb{Z}$ . A similar condition can be obtained for the vertical plane by setting instead  $j = 0$  in Eq. (2.28).

SBR excited by an rf quadrupole have already been brought up as a potential downside of the device in Refs. [73, 74] where the authors assessed the use of such cavities to raise the TMCI threshold. They have demonstrated analytically and numerically that an rf quadrupole operating at the zero-crossing of the rf wave ( $\varphi_0 = \pm\pi/2$ ) can indeed be employed to increase the TMCI threshold. To have an impact on the TMCI, however, the necessary amount of detuning must be of the order of the synchrotron tune or higher<sup>1</sup>, requiring large quadrupole strengths. In combination with the strong betatron detuning that the device creates, the beam lifetime may suffer due to single-particle losses caused by resonances. As a result, the idea was not pursued any further.

The operational mode of the cavity for the mitigation of the TMCI is different from the rf quadrupole for Landau damping studied in this thesis, as also discussed briefly in Chapter 3. Weak head-tail modes typically have (real) coherent tune shifts that are much smaller than the synchrotron tune. To suppress these modes, a tune spread that has the width of a fraction of the synchrotron tune is hence usually sufficient, translating into relatively small quadrupole strengths.

<sup>1</sup>This “spread” is *not* amplitude dependent, but instead similar to the odd orders of chromaticity and hence averages out over the synchrotron period. It does not provide Landau damping for the slow head-tail modes.

Table 5.5: Main machine and PYHEADTAIL simulation parameters used to study scenarios for a potential rf quadrupole prototype test in the SPS.

Parameter		Value
Beam energy (total)	$E_0$	26 GeV
Bunch intensity	$N$	$2.5 \times 10^{10}$ p
Norm. transverse emittance	$\varepsilon_{x,y}^{\text{norm}}$	2.0 $\mu\text{m}$ rad
Bunch length	$\sigma_z$	0.23 m
Betatron tunes	$Q_x, Q_y$	20.13, 20.18
First-order chromaticity	$Q'_x, Q'_y$	5, -2
(Linear) synchrotron tune	$Q_s$	0.0169
Circular aperture (radius)		0.05 m
Number of macroparticles	$N_{\text{mp}}$	$1.3 \times 10^6$
Number of turns	$N_{\text{turns}}$	$10^5$ turns

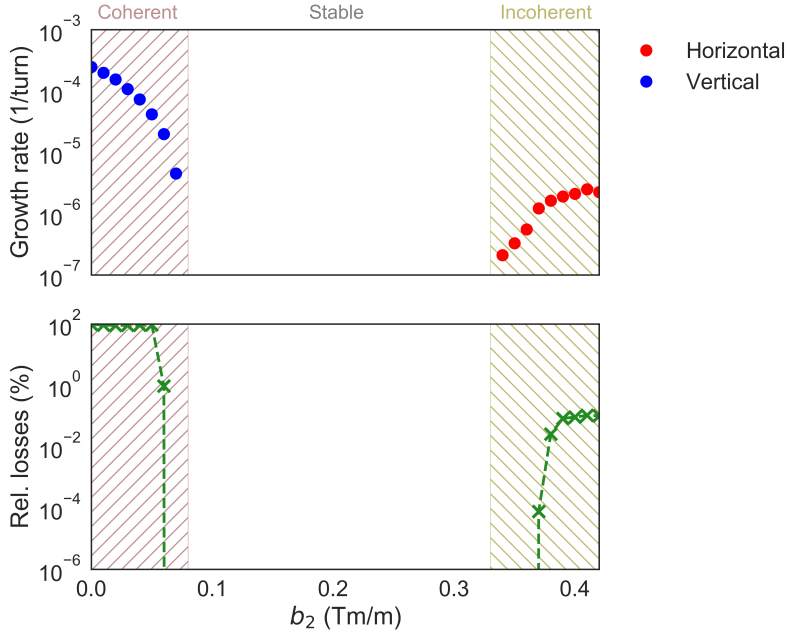


Figure 5.12: Stabilisation of the head-tail mode zero in the SPS at injection energy using a single rf quadrupole. Three regimes can be identified: (1) vertical *coherent* losses at low  $b_2$ ; (2) stable beam at intermediate  $b_2$ ; and (3) horizontal *incoherent* losses at high  $b_2$ .

Despite the lower strengths, SBR were observed when studying scenarios for a potential future prototype test of the rf quadrupole in the SPS. Figure 5.12 displays the results from PYHEADTAIL simulations illustrating the effect of the rf quadrupole on a vertical head-tail mode zero in the SPS, excited by running the machine at negative first-order chromaticity. The centroid growth rate (top) as well as the fraction of lost particles (bottom) over the simulation period are shown. The main beam and machine parameters are summarised in Table 5.5. Up to an rf quadrupole strength of  $b_2 = 0.08$  Tm/m, the bunch

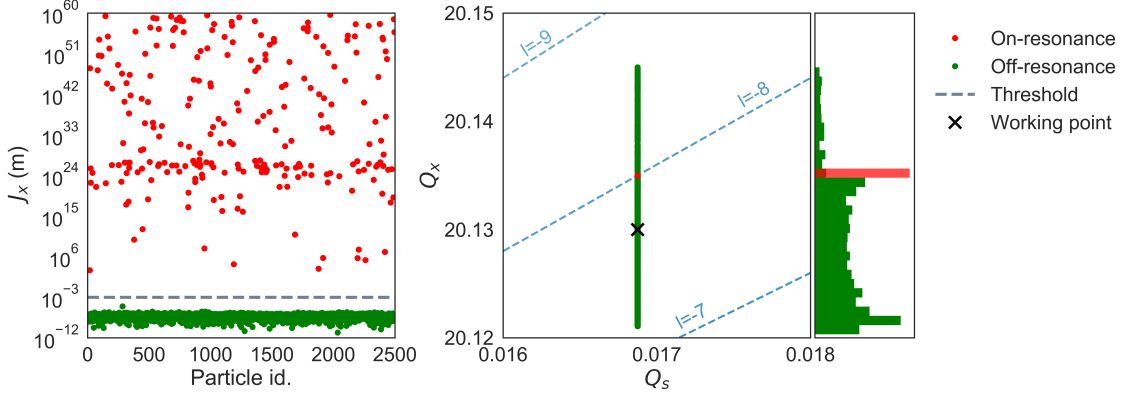


Figure 5.13: Follow-up study of the incoherent regime discovered during simulations with the rf quadrupole in the SPS (Fig. 5.12). *Left*: Distribution of horizontal action at the end of the simulation. *Right*: Tune analysis of the high (red) and low (green) amplitude particles. SBR lines from analytical calculations are overlaid (blue, dashed).

is coherently unstable and thus most of the particles are lost over the course of the simulation (typically more than 90 %). In the intermediate regime, with  $b_2$  between 0.08 Tm/m and 0.33 Tm/m, the beam is stabilised by the rf quadrupole and no losses are observed over the simulation period. This is the region where one would operate the device. When increasing the rf quadrupole strength further, particle losses appear again, although they are strongly reduced ( $\leq 0.1$  %) compared to the amounts observed in the coherent regime. In addition, they appear in the horizontal plane, while the original coherent instability was a vertical one. In this regime, looking at the evolution of the single-particle motion over time reveals that the bunch remains stable as a whole. However, some individual particles exhibit a strong growth in their horizontal amplitudes indicating that the beam dynamics is governed by incoherent effects, such as resonances.

To confirm that the losses observed in the incoherent regime would indeed stem from SBR, a follow-up simulation was performed, tracking 2,500 macroparticles over 50 synchrotron periods with a single rf quadrupole (kick model) powered with  $b_2 = 0.4$  Tm/m. The chromaticity was set to zero and wakefield effects were excluded to study the impact solely of the rf quadrupole kicks on the beam. The left plot in Fig. 5.13 shows the distribution of the horizontal action for all the particles at the end of the simulation. The majority of the particles in the bunch (green) remained at their initial action. However, there are particles that have undergone a large growth in their amplitudes (red), presumably because they were on a (SBR) resonance excited by the rf quadrupole. The plot on the right in Fig. 5.13 shows the SUSSIX tune analysis of the high and low amplitude particles. The black cross marks the SPS working point (bare tune). The tune spread is a result of detuning with longitudinal amplitude introduced by the rf quadrupole. The tune analysis reveals that all the particles suffering from a strong growth in amplitude have the same pair of synchrotron and betatron tunes. They also lie exactly on the SBR line (blue, dashed) calculated using Eq. (5.5), with  $j = 1$ ,  $l = -8$ , and  $n = 20$ .

### Frequency map analysis

The frequency map analysis (FMA) is a numerical tool developed by Laskar to study the dynamics of quasi-periodic systems and the stability of orbits in celestial mechanics [81]. This technique is

equally applicable to the trajectories in particle accelerators to examine, for example, the resonances introduced by the rf quadrupole more systematically. The way to perform an FMA is to first track a large number of individual particles, generated with different initial conditions, through an accelerator lattice to obtain their turn-by-turn trajectories. This can be achieved by means of a tracking code, such as SIXTRACK [82, 83]. In a second step, one computes the *tune diffusion* for every particle between two equally long time intervals from the tracking data

$$d_Q = \sqrt{(Q_{x,1} - Q_{x,2})^2 + (Q_{y,1} - Q_{y,2})^2}. \quad (5.6)$$

$Q_{x,1}$  ( $Q_{y,1}$ ) and  $Q_{x,2}$  ( $Q_{y,2}$ ) are the horizontal (vertical) tunes of a particle obtained in the first and the second time interval respectively. The tune diffusion is directly linked to the stability of a particle trajectory. For regular, i.e. stable, trajectories the tune diffusion remains small. On the other hand, a particle that follows a chaotic, unstable, trajectory will have a large diffusion. As a result, by plotting the diffusion in the tune space (here  $Q_s$  vs.  $Q_x$ ), one can visualise regions of unstable and stable single-particle motion.

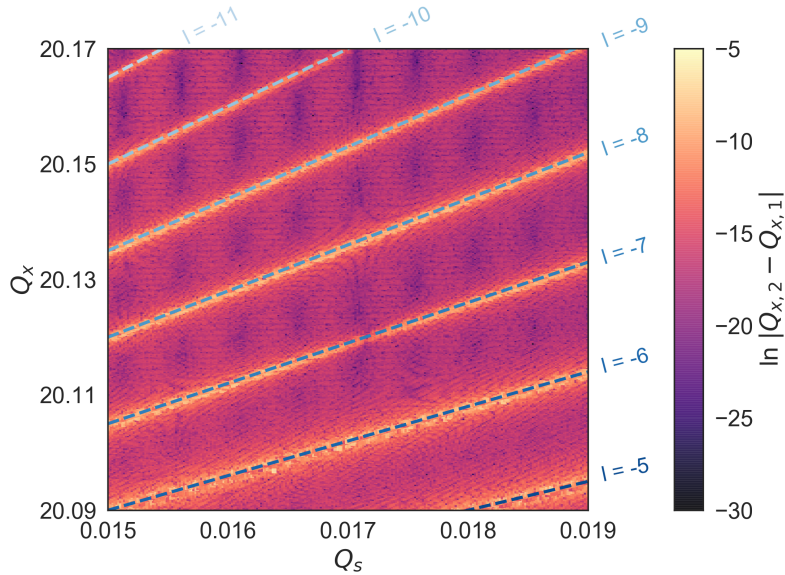


Figure 5.14: Diffusion map in  $Q_s$  vs.  $Q_x$  space for a single rf quadrupole kick per turn in the SPS at injection energy. SBR lines expected from the theory [Eq. (5.5),  $j = 1$ ,  $n = 20$ ] are overlaid and the corresponding orders  $l$  are indicated by the numbers along the plot (blue, dashed).

An FMA was performed for the previously introduced SPS case with one rf quadrupole installed in the lattice. Tracking simulations, here with PYHEADTAIL rather than SIXTRACK, were run for 120,000 particles, each with different initial conditions (i.e. betatron and synchrotron tunes), over 300 synchrotron periods. From the tracking data, the tune diffusion between the first and the last 1024 turns was calculated for every particle. Figure 5.14 displays the results of the study. Distinct lines appear in the  $Q_s$  vs.  $Q_x$  tune space where the tune diffusion is much larger than elsewhere. They correspond to the SBR lines that are again expected from Eq. (5.5), using  $j = 1$ ,  $n = 20$ , and  $l \in [-11, -5]$  (blue, dashed). Since the resonances are of relatively low order, they are strongly pronounced. The reason why they are low-order resonances is that the fractional betatron tune is relatively close to zero ( $q_x \in [0.09, 0.17]$ ),

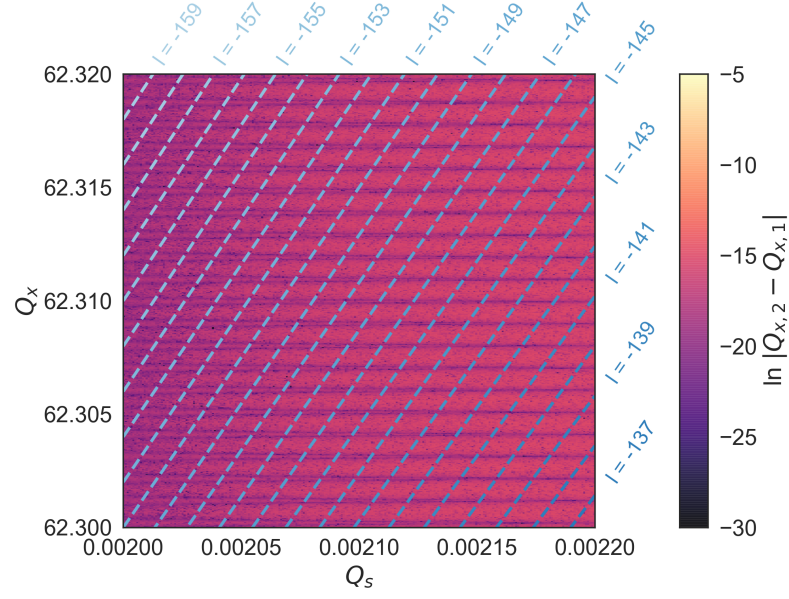


Figure 5.15: Diffusion map in  $Q_s$  vs.  $Q_x$  space for a single rf quadrupole kick per turn in the HL-LHC at collision energy. SBR lines expected from the theory [Eq. (5.5),  $j = 1$ ,  $n = 62$ ] are overlaid and the corresponding orders  $l$  are indicated by the numbers along the plot (blue, dashed).

while at the same time the synchrotron tune is rather large ( $Q_s \in [0.015, 0.019]$ ). The strong dependence of the SBR on the synchrotron tune has also been observed at the Large Electron Positron collider (LEP) at CERN which was operating at high synchrotron tunes [84, 85]. One can also recognise that the higher the order of the SBR, the weaker the tune diffusion and hence the strength of the resonance.

A first evaluation of SBR from an rf quadrupole was also done for the HL-LHC at collision energy (7 TeV) with a single rf quadrupole kick of the same relative strength as in the SPS case ( $b_2 = 0.5 \text{ Tm/m}$ ). The design betatron tunes at collision energy are  $Q_x = 62.31$  and  $Q_y = 60.32$  respectively. The linear synchrotron tune is at  $Q_s = 0.0021$ . Compared to the SPS, the fractional betatron tune is hence much larger, while the synchrotron tune is a factor ten smaller. By consequence, we expect that the SBR lines close to the HL-LHC working point are of high orders and hence less likely to cause beam degradation. This is confirmed by the results from the FMA given in Fig. 5.15. The PYHEADTAIL simulations did not reveal any excitation of SBR over the simulated time period. Analytical predictions indicate that the expected SBR would be of orders  $l \in [137, 159]$ .

Although these preliminary studies indicate that SBR are less likely an issue for HL-LHC parameters, detailed follow-up studies on this subject are required, for example using the SIXTRACK code with a complete machine lattice and tracking over longer time periods.

### 5.5.2 Feed-down

As explained in Section 2.1.1, a bunch passing through a normal magnetic quadrupole with a transverse offset also experiences a dipole kick from feed-down which introduces a distortion of its closed orbit.



For the rf quadrupole the magnetic field is rf-modulated, meaning that a bunch traversing the device with a transverse offset will be subject to an rf dipole feed-down kick.

Producing rf dipole kicks is the main purpose of a “crab cavity”, currently being tested in the SPS and to be installed during 2021 in the LHC as part of the high-luminosity upgrade [80]. Crab cavity kicks introduce a transverse tilt of the bunches from head to tail at the interaction points of the collider to increase the overlap of the particle distributions during the collision. The goal is to counteract the luminosity decrease introduced by the crossing-angle. To understand the consequences of feed-down effects from the rf quadrupole, one can hence infer information from the crab cavity studies, in particular from the global crabbing scheme [86]. The closed orbit distortion introduced by the rf dipole kicks is a function of the longitudinal coordinate. The result is that, depending on the chosen rf phase, the bunch will be curved or tilted and oscillate about the unperturbed closed orbit all around the accelerator ring. This puts additional constraints on the collimation system of a machine, for example [80]. The oscillation amplitude depends on the strength of the rf dipole kick and hence on the magnitude of the transverse offset of the bunch. A qualitative example of the effect is shown in Fig. 5.16 for FCC-hh parameters at injection energy (see Table 5.3) assuming a horizontal offset of  $-2 \times 10^{-3}$  m of the bunch at the location of the rf quadrupole kick, with  $\varphi_0 = 0$  and a strength of  $b_2 = 0.5$  Tm/m (compare Table 5.4, worst case scenario at injection energy requires  $b_2 = 0.45 \pm 0.05$  Tm/m). The cavity voltage has been ramped up adiabatically over 50 turns. The red arrow marks the amplitude of the closed orbit distortion. It is linearly dependent on the offset of the beam and on the rf quadrupole strength.

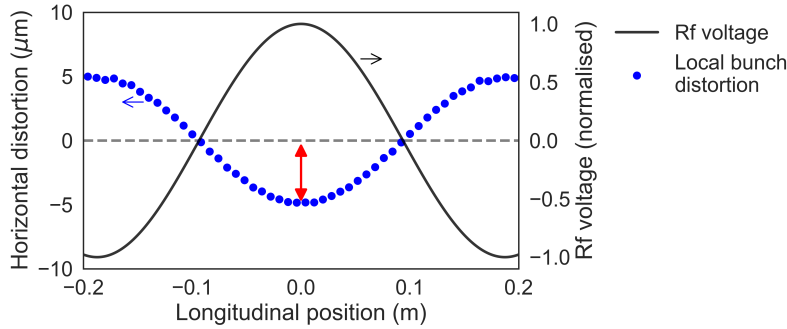


Figure 5.16: Illustration of local closed orbit distortion (blue) from rf quadrupole feed-down.

Depending on the parameters of the collider where the rf quadrupole system would be installed, studies will be required to assess whether the feed-down introduces issues for the operation of the machine. The studies will provide an answer to whether orbit corrector dipoles are required around the location of the rf quadrupole to ensure that the beam passes as close through the centre of the device as possible.

### 5.5.3 Dynamic aperture

A particle travelling in a storage ring may experience an increase in its amplitude of oscillation over time due to various beam dynamics effects, such as resonances. The dynamic aperture (DA) is defined as the maximum oscillation amplitude for which the particle motion still remains stable. It is hence a quantity that describes the acceptance of a machine, including many aspects of, mostly single-particle, but also some multi-particle (e.g. beam-beam, space charge), beam dynamics. A particle situated

outside of the DA is in the regime of chaotic motion and will eventually be lost from the beam. The DA is hence correlated with the beam lifetime. If, for example, the beam size is large compared to the DA, the lifetime will be poor.

The DA is also related to the size of the footprint of a beam in the tune space. A beam with a large tune footprint is more likely to contain particles that coincide with resonance lines that are driven by errors in the machine lattice. From a single-particle dynamics point-of-view, it is hence desirable to limit the amount of incoherent detuning, e.g. introduced by chromaticity, to keep the tune footprint as small as possible. On the other hand, one also tries to avoid strong excitement (drivers) of resonances. In the same manner, an amplitude-dependent tune spread required for Landau damping can have an important impact on the DA. In fact, introducing a tune spread for Landau damping usually comes at the expense of a reduced DA. The effect of the Landau octupoles on the DA, for example in the LHC, has been studied in Refs. [87–89] and demonstrates their detrimental impact on the beam lifetime, especially in combination with linear coupling. For similar reasons, also the rf quadrupole is expected to reduce the DA. It is, however, potentially possible to find operational modes where the octupole magnets (and possibly the rf quadrupole) can also have a positive impact on the DA, e.g. when partially compensating the beam-beam tune spread.

Assessing the effect of an rf quadrupole on the DA was not within the scope of this thesis. To complete the evaluation of the practicality of such a device, however, detailed single-particle simulations are, at present, the main missing piece of the puzzle and will be required in the future. The DA studies carried out for the crab cavities to be installed in the HL-LHC give first indications that an rf quadrupole may significantly affect the DA [80]. Reference [90] reports, for example, on the impact of the higher-order rf multipoles introduced by the crab cavities. Concerning the quadrupole error  $b_2$ , the minimum DA (60 seeds, tracking over  $10^5$  turns) is reduced from  $11.5\sigma_{x,y}$  to about  $7\sigma_{x,y}$  assuming that the cavities introduce a quadrupole component of  $b_2 = 0.15 \text{ Tm/m}$ . This is about half the quadrupole strength that would be required for an rf quadrupole for the HL-LHC to stabilise the beams at 7 TeV (compare Fig. 5.10). These numbers will also need to be compared to the FCC-hh Landau octupole scheme for a fair performance assessment of the two technologies potentially used in the FCC-hh.

## 5.6 Conclusions and outlook

Two models of the rf quadrupole have been implemented in PYHEADTAIL and were successfully benchmarked against each other and against analytical calculations. The full validation of the PYHEADTAIL model, i.e. the formation of impedance-driven instabilities as well as the Landau damping mechanism, was based on a slow head-tail mode observed experimentally at 3.5 TeV in the LHC. The comparison of the LHC Landau octupole current required to stabilise the beam revealed an excellent agreement between experiment, numerical simulations from particle tracking and the circulant matrix model, and stability diagram theory. In a second step, the Landau octupoles were replaced with an rf quadrupole to prove that such a device can provide stability in a similar manner. This is the first numerical proof-of-principle study made for an rf quadrupole for Landau damping.

Due to the quadrupole nature of the device, the stabilising efficiency in the two transverse planes is strongly asymmetric. This is predicted by stability diagram theory and was confirmed by tracking simulations. Based on these results, a two-family scheme for rf quadrupoles was proposed and tested

in tracking simulations. Not only could the asymmetry be cleared away, but also the overall quadrupole strength required for beam stability in the two transverse planes was reduced. Based on an HL-LHC operational scenario, the combined stabilising effect from magnetic octupoles and an rf quadrupole was studied as well and shown to be successful.

An rf quadrupole system with two families was evaluated for the current version of the FCC-hh. The simulations demonstrate that the system can indeed be used to counter the single-bunch head-tail instabilities faced at injection and at collision energy. The number of cavities required for stabilisation reaches from one to 25 per family, depending on the operational scenario and on the beam energy. The total active length can be up to 15 m which is to be compared to 325 m of magnetic octupoles (advanced magnet technology), or even up to 1.1 km (LHC octupole technology). These numbers depend, among others, on the optics, but also on the overall impedance of the machine. For example, by optimising the horizontal and vertical beta functions at the locations of the two rf quadrupole families one could reduce the number of elements further.

Finally, potential downsides of the rf quadrupole were briefly discussed, such as resonances, feed-down, and its impact on the dynamic aperture. A first assessment was made using PYHEADTAIL to get a qualitative understanding. It was found that synchro-betatron resonances can indeed be excited, but they are less likely to cause issues for colliders like HL-LHC or FCC-hh, since these machines operate with relatively high betatron tunes and rather low synchrotron tunes. Feed-down leads to a closed orbit distortion that depends on the longitudinal coordinate of the bunch. The crab cavity studies currently being made at the SPS can provide further insight into the potential consequences of this effect. To minimise the closed orbit distortion, orbit corrector dipoles may need to be installed at the location of the rf quadrupole to make sure that the bunch passes through its centre. Whether or not such a correction will be required depends on the parameters of the machine and the rf quadrupole system. A potential reduction of the dynamic aperture from the rf quadrupole was also discussed qualitatively. Judging from crab cavity simulations analysing the impact of multipole errors on the dynamic aperture, in particular the quadrupole term, it is clear that a suitable simulation code such as SIXTRACK, which can include the full machine lattice, must be employed to make a detailed assessment of the reduction of dynamic aperture due to an rf quadrupole.

Overall, the rf quadrupole promises to be an efficient means for stabilisation of coherent instabilities driven by the beam-coupling impedance. It has been successfully validated numerically in terms of collective effects which was one of the main objectives of this thesis. Concerning single-particle dynamics, however, additional work is required to make a definite statement about the practicality of the device for a future hadron collider. In particular, its impact on the dynamic aperture, also compared to magnetic octupoles, is the main open question at this stage.



## 6 Experimental studies: second-order chromaticity in the LHC

Based on the theoretical and numerical studies of Landau damping from detuning with longitudinal amplitude developed previously in this thesis, experiments were performed in the LHC to benchmark the models and to confirm the analytical predictions. In particular, the idea was to observe the two distinct beam dynamics effects introduced by nonlinear chromaticity that were identified analytically: the change of the effective impedance and hence of the associated coherent mode frequencies, and beam stabilisation through Landau damping. This chapter discusses the stabilisation of single bunches with second-order chromaticity in the LHC. The study demonstrates that second-order chromaticity can be introduced and well controlled in the machine by employing its main sextupole magnets. The experimental methods and the machine setup are described and the observations made are compared to detailed PYHEADTAIL tracking simulations also taking into account a thorough optics model of the accelerator. The chapter is composed of the work published in Refs. [35, 91, 92].

Section 6.1 describes the production scheme for second-order chromaticity in the LHC using two dedicated knobs defined to power the main sextupole magnets in a specific configuration. This includes numerical calculations as well as an analysis of undesired side effects introduced by the knobs. Section 6.2 discusses the stability of single bunches in the LHC at collision energy (6.5 TeV), without and with second-order chromaticity. The analysis is done using both experimental data and results from PYHEADTAIL. It demonstrates that the simulations successfully reproduce the beam dynamics in the machine from both the single- and multi-particle points-of-view. Among others, the differences between stabilising a single bunch with Landau octupoles compared to second-order chromaticity become evident. Conclusions drawn from the experiments, taking into account also the analytical predictions made in Chapter 4, are discussed in Section 6.3.

### 6.1 Second-order chromaticity in the LHC

This section is split into two parts and discusses how second-order chromaticity can be produced and measured in the LHC. First, the sextupole powering scheme employed to generate second-order chromaticity is analysed by means of the LHC MAD-X model. The detuning with transverse amplitude introduced by the sextupole magnets, a major side effect of creating second-order chromaticity in this manner, is discussed and compared to the detuning coefficients generated by the LHC Landau

octupoles. Second, the nonlinear chromaticity measurement method is explained and illustrated with example data.

### 6.1.1 Production scheme and side effects

The second-order chromaticity is an energy-dependent aberration that is defined primarily by the integral of the terms  $\beta'_{x,y}(\delta)k_2$ ,  $\beta'_{x,y}(\delta)D_x k_3$ , and  $D_x^2 k_4$  around the machine lattice [93, 94].  $k_2$ ,  $k_3$ , and  $k_4$  are the quadrupole, sextupole, and octupole strengths respectively,  $\beta'_{x,y} = \partial\beta_{x,y}/\partial\delta$  is the first derivative of the beta function with respect to the relative momentum deviation, and  $D_x$  denotes the horizontal dispersion function. In the LHC, the main sextupoles (MS) are grouped into focusing (SF) and defocusing (SD) families, installed respectively at focusing and defocusing quadrupoles in the lattice. SF and SD are further divided into two interleaved sub-families separated by a phase advance of approximately  $\pi$ . They are called  $(F_1, F_2)$  and  $(D_1, D_2)$  respectively. Each of the four families can be individually powered for each of the eight sectors of the LHC. With this sextupole scheme,  $\beta'_{x,y}(\delta)$  can be enhanced to correct, or introduce,  $Q''_{x,y}$  without affecting the first-order chromaticity  $Q'_{x,y}$ . This is achieved by varying the strengths of the two sub-families with opposite signs for both SF and SD separately in all the eight sectors  $u \in \{12, 23, \dots, 78, 81\}$  of the machine

$$\begin{aligned} \text{SF: } \quad \Delta k_{2,F_1}^u &= +w_F^u \Delta_F, & \Delta k_{2,F_2}^u &= -w_F^u \Delta_F, \\ \text{SD: } \quad \Delta k_{2,D_1}^u &= +w_D^u \Delta_D, & \Delta k_{2,D_2}^u &= -w_D^u \Delta_D. \end{aligned} \tag{6.1}$$

The absolute change of the sextupole strength  $\Delta_{F(D)}$  is the same for all the SF (SD) in the lattice, but the families in each sector are powered with different signs denoted by  $w_{F(D)}^u$ . With the definitions in Eq. (6.1), the absolute value of second-order chromaticity depends quadratically on the sextupole strength, i.e.  $|Q''_{x,y}| \propto \Delta_{F,D}^2$  [93, 94]. By choosing the signs  $w_{F,D}^u$  carefully for each sector, one can define a set of almost orthogonal knobs to change  $Q''$  towards positive or negative values in the two beams and for both planes independently. For the experiment in the LHC, the goal was to define a sextupole scheme that produces a large negative second-order chromaticity in both transverse planes. The choice is based on the fact that the real part of the coherent tune shifts for the most unstable head-tail modes in the LHC is negative [33]. This is a result of the inductive nature of the collimator impedances which are the main contributors to the effective impedance at collision energy [75]. The stability diagrams that have been discussed in Chapter 3 (Fig. 3.6) demonstrate that, in this case, negative provides more effective Landau damping than positive  $Q''$ .

The best powering scheme to generate a significant amount of negative second-order chromaticity for the LHC optics configuration used at collision energy has been determined by means of MAD-X/PTC [7, 79, 95]. The final results are listed in Table 6.1. The two sextupole knobs are called QPPF and QPPD for the focusing and the defocusing sextupole families respectively. The maximum possible variation in the sextupole strengths is given by  $\Delta_{F,D}^{\max}$  together with the corresponding amounts of  $Q''_x$  and  $Q''_y$  expected from MAD-X/PTC calculations for both beam 1 and beam 2. The values illustrate that the QPPF and QPPD knobs mainly produce  $Q''$  in the horizontal and the vertical planes respectively. The quadratic dependence of the second-order chromaticity on the strength of the knobs is further illustrated in Fig. 6.1 for both beams and the two transverse planes. The plots also clearly demonstrate that  $Q''$  in the horizontal and the vertical planes can be controlled independently. The differences between the two beams, particularly pronounced in the vertical plane, are a result of how the knobs are defined.

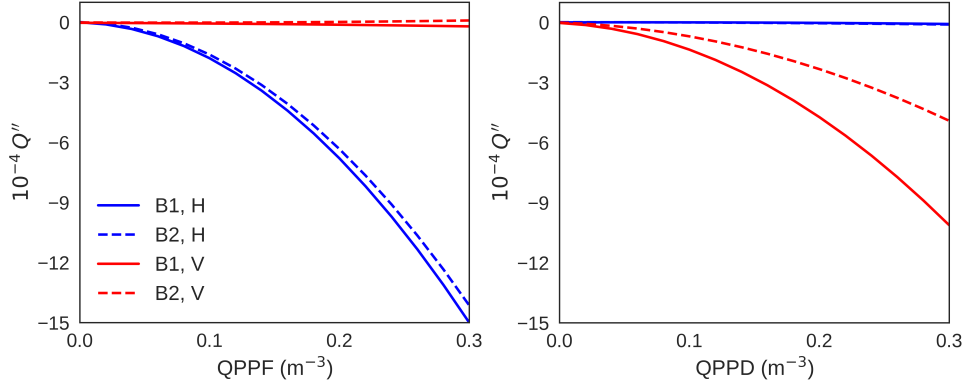


Figure 6.1:  $Q''$  predicted by MAD-X/PTC for the two beams (B1 and B2) for the horizontal (H) and the vertical (V) planes as a function of the QPPF (left) and QPPD (right) sextupole knobs respectively.

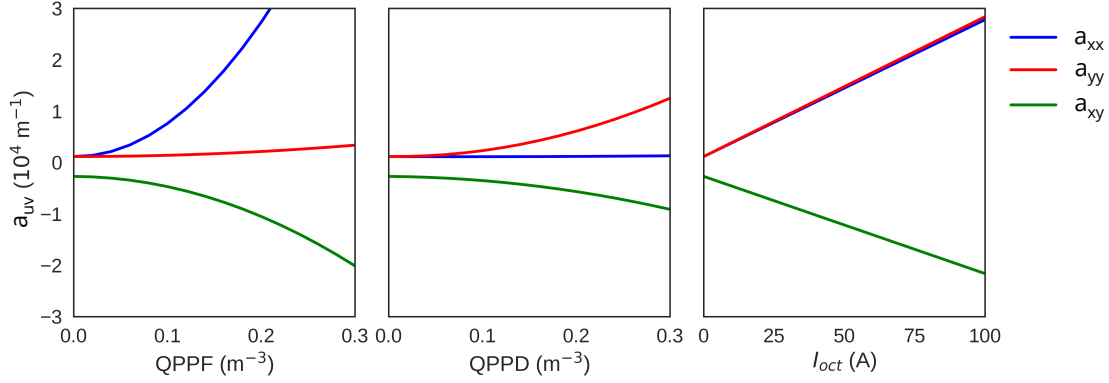


Figure 6.2: MAD-X/PTC calculation of the three transverse amplitude detuning coefficients in beam 1 introduced by the two sextupole knobs QPPF (left) and QPPD (middle), and, for comparison, by the LHC Landau octupoles (right).

Table 6.1 demonstrates that the polarities of the sextupole families, given by  $w_{FD}^u$ , are different for beam 1 and beam 2. The chosen configuration also determines the maximum achievable amount of  $Q''$ .

Powering the main sextupoles with the scheme described above does not only introduce  $Q''$ , but also creates non-negligible transverse amplitude detuning coefficients  $a_{uv}$ , with  $u, v \in \{x, y\}$ . They give rise to detuning with *transverse* amplitude and hence Landau damping in the same manner as from magnetic octupoles (see Section 2.2.5). For the studies presented here, the additional detuning with transverse amplitude is an undesired side effect. After all, the goal is to show that the beam stabilisation occurs as a result predominantly of detuning with longitudinal amplitude. The additional transverse amplitude detuning coefficients complicate the process of determining the actual origin of the Landau damping, i.e. whether it is mostly a result of detuning with transverse or longitudinal amplitude. However, as long as the amount of transverse amplitude detuning from the sextupole magnets is small enough, and given that the optics model of the machine is reliable, the two effects can be clearly disentangled by means of tracking simulations as will be demonstrated in Section 6.2.3.

Table 6.1: Definition of the sextupole powering schemes used to introduce  $Q''_{x,y} < 0$  in the LHC at collision energy. For each of the two knobs QPPF and QPPD, the maximum strengths are listed together with the corresponding amounts of  $Q''$  predicted by MAD-X/PTC in the two beams and planes.

Knob	Beam	$w_{F,D}^{(12,23,\dots,78,81)}$	$\Delta_{F,D}^{\max} \text{ (m}^{-3}\text{)}$	$10^{-4} Q''_x$	$10^{-4} Q''_y$
QPPF	1	++-+-+--	0.30	-15.0	-0.2
	2	-+-+----	0.30	-14.1	0.1
QPPD	1	-+++----	0.28	-0.1	-8.9
	2	---+--+-	0.28	-0.1	-4.3

Figure 6.2 illustrates the amount of detuning with transverse amplitude introduced by the two sextupole knobs QPPF (left) and QPPD (middle) respectively, predicted by means of MAD-X/PTC calculations. Here, only the results for beam 1 are displayed, but they are similar for beam 2. Clearly, QPPF introduces mainly  $a_{xx}$  and  $a_{xy}$ , while QPPD gives rise mostly to  $a_{yy}$ . For comparison, the detuning coefficients introduced by the LHC Landau octupoles are also plotted in the figure (right). The two LHC octupole families are again powered with opposite polarities, but identical absolute currents. The results in Fig. 6.2 were obtained using positive (negative) polarity in the focusing (defocusing) family. The symbol  $I_{\text{oct}}$  corresponds to the current in the focusing family.

### 6.1.2 Measurement method

To measure the nonlinear chromaticity in the LHC, a sinusoidal frequency modulation is applied to the main rf system of the machine. This results in a variation of the momentum deviation  $dp/p$  of the beam as illustrated in the top plot in Fig. 6.3. Because of chromaticity, such a modulation translates into time-varying betatron tunes  $Q_{x,y}(t)$  which can be determined from the base-band tune metre (BBQ) measurement [96]. The middle plot in Fig. 6.3 shows an example of horizontal BBQ spectral data. The fractional tune values  $q_x$  are obtained from the BBQ turn-by-turn measurement with a sliding window frequency analysis using SUSSIX. Several synchrotron sidebands as well as some noise lines can be seen (yellow). To eliminate systematic errors in the measurement of  $Q''$ , one synchrotron sideband must be selected consistently throughout the modulation period as illustrated by the overlaid red markers. To extract the first- and second-order chromaticities the selected tune values are binned with respect to  $dp/p$  and a weighted second-order polynomial fit of  $Q$  vs.  $dp/p$  is applied. The result is given in the bottom plot of Fig. 6.3. The error bars correspond to the error of the mean calculated during the binning process.

The main reason for choosing this method is that it provides a fast measurement of the nonlinear chromaticity. Modulation windows of about 60s contain enough data to obtain a satisfying result. While usually optics measurements at the LHC are performed with a bunch of only  $10^{10}$  p, here the measurement had to be done with bunches of ten times higher intensities, because of time constraints. As a result of the larger bunch charge, the reach in  $dp/p$  was limited to about  $\pm 3 \times 10^{-4}$  (losses at aperture), implying a reduced accuracy of the measurement. At these values of  $dp/p$ , the sensitivity of the betatron tunes to the higher orders of chromaticity is relatively low. Hence, in particular for values of  $Q''$  close to zero, the relative error on the second-order chromaticity measurement is significant. Furthermore, the widths of the peaks in the frequency spectra, which are particularly large in presence



of the tune spread created by a strong powering of the Landau octupoles, contribute to the uncertainty of the fits as do the noise lines. The noise as well is a result mostly of the large bunch intensity used during the measurement.

To improve the accuracy of the chromaticity measurement, a DC change of the main rf frequency can be applied such that the betatron tunes for a specific  $dp/p$  setting can be measured and averaged over a longer period of time. By performing such a measurement of the tunes for different settings of  $dp/p$ , one obtains a very accurate assessment of the amount of nonlinear chromaticity in the machine. However, this method is time intensive and was hence not a valid option for the experiments shown here. It will be discussed in Chapter 7 as part of the studies carried out in the SPS.

## 6.2 Single-bunch stability at collision energy

This section discusses the single-bunch stability in the LHC at 6.5 TeV. The most unstable head-tail mode at collision energy is characterised and its mitigation with the Landau octupoles is explained both using experimental data and PYHEADTAIL simulations.

### 6.2.1 Without second-order chromaticity

In 2016 a campaign was launched in the LHC to measure the single-bunch stability thresholds at different first-order chromaticities [26, 97]. At an energy of 6.5 TeV, with design bunch parameters,  $Q'_{x,y}$  between 11 and 14 units, and in presence of the transverse feedback system with a damping time of  $\tau_{fb} \approx 100$  turns, the most prominent transverse instability was found to be a horizontal head-tail mode with azimuthal and radial numbers  $l = 0$  and  $m = 2$  respectively. The upper plot in Fig. 6.4 displays the corresponding head-tail mode pattern acquired with the LHC Head-Tail Monitor during the measurement [50]. Using a detailed impedance model of the LHC [75] and a simplified model of the transverse feedback system, macroparticle tracking simulations with PYHEADTAIL predict the same instability as observed in the machine with the correct azimuthal and radial mode numbers. The associated head-tail mode pattern is given in the lower plot of Fig. 6.4 and is in good agreement with the pattern observed during the measurement. The main beam, machine, and simulation parameters used for the study are summarised in Table 6.2.

During LHC routine operation this instability is mitigated by means of the Landau octupoles. As part of the measurement campaign, the minimum Landau octupole current required to suppress the instability was determined to  $I_{oct}^{meas} = 96_{-9}^{+29}$  A for the beam and machine parameters listed in Table 6.2 [26]. The upper error corresponds to the step size used for the scan in Landau octupole current which was performed from high to low. The lower error originates from the uncertainty in the transverse emittance measurement.

The Landau damping from the octupole magnets in the LHC is mainly due to the incoherent tune spread from detuning with transverse amplitude. However, there is also an indirect contribution of detuning with longitudinal amplitude from these magnets. As explained in Section 6.1.1, second-order chromaticity has a contribution, among others, from the integral of  $D_x^2 k_4$  around the accelerator ring. By consequence, the LHC Landau octupoles located in dispersive regions will introduce second-order chromaticity with an amount that depends linearly on the octupole strength  $k_4$ . For this reason, the

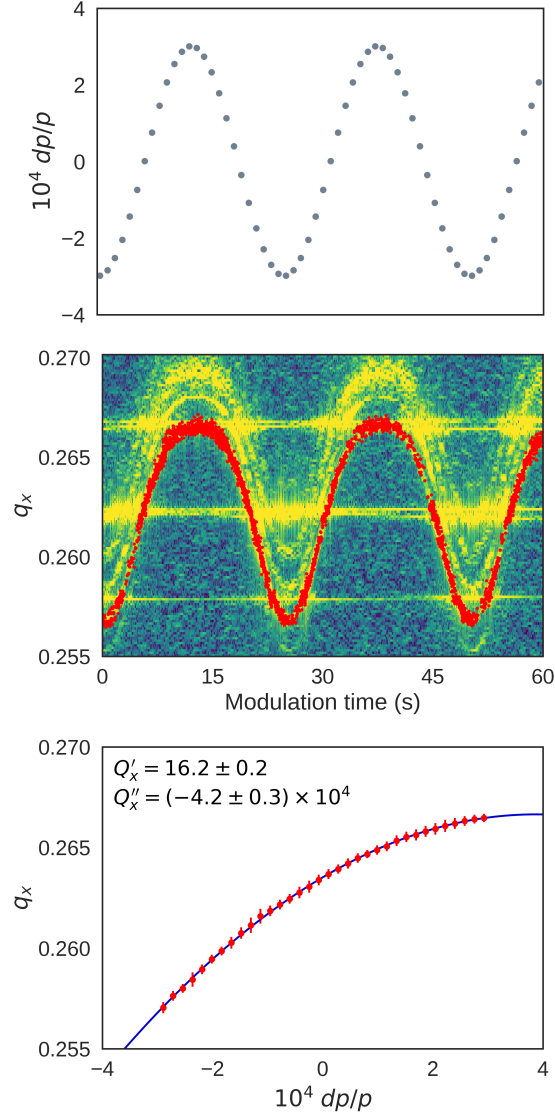


Figure 6.3: *Top*: Variation of the momentum deviation of the beam as a result of the rf frequency modulation. *Middle*: Horizontal BBQ spectral data acquired during the modulation period, overlaid with the selected SUSIX tune peaks (red markers). *Bottom*: Weighted second-order polynomial fit (blue line) to data (red).

$Q''$  contribution from the Landau octupoles was both measured and simulated for the given machine configuration. For the measurement, the change of  $Q''$  was determined when increasing the Landau octupole current from  $I_{\text{oct}} = 40 \text{ A}$  to  $I_{\text{oct}} = 320 \text{ A}$ . The measured amounts of  $Q''$  introduced per current are summarised in Table 6.3 alongside MAD-X/PTC predictions. The values obtained from the model are consistent with the measurements, although the latter have rather large uncertainties due to the limited sensitivity of the measurement method, as explained in Section 6.1.2. It is worth noting that in absence of the Landau octupoles, the  $Q''_{x,y}$  in the LHC is practically zero, both in measurements and in

## 6.2. Single-bunch stability at collision energy

Table 6.2: Main parameters used in PYHEADTAIL to reproduce the LHC experimental machine setup at 6.5 TeV and to study the single-bunch instability.

Parameter		Value
Beam energy	$E_0$	6.5 TeV
Bunch intensity	$N$	$1.2 \times 10^{11}$ p
First-order chromaticity	$Q'_{x,y}$	13
Norm. transverse emittance	$\epsilon_{x,y}^{\text{norm}}$	$2.0 \mu\text{m rad}$
Bunch length	$4\sigma_t$	1.20 ns
Transverse feedback	$\tau_{\text{fb}}$	100 turns
Number of macroparticles	$N_{\text{mp}}$	$10^6$
Number of turns	$N_{\text{turns}}$	$5 \times 10^5$ turns

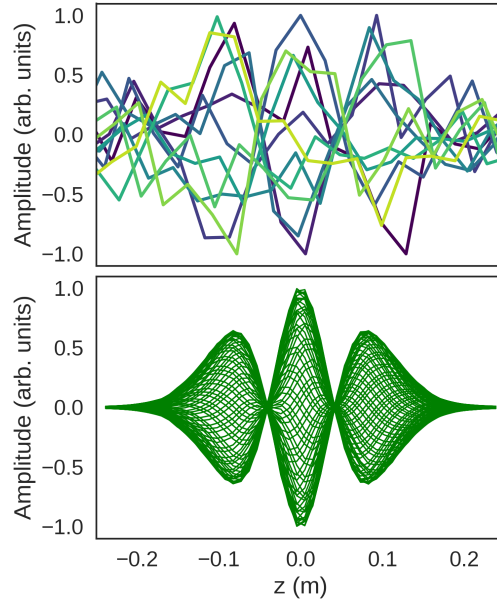


Figure 6.4: Head-tail mode patterns from LHC measurements (top) and PYHEADTAIL simulations (bottom) for a single bunch at collision energy (6.5 TeV), with beam and machine parameters listed in Table 6.2.

Table 6.3: MAD-X/PTC calculations vs. measurements of second-order chromaticity introduced by the Landau octupoles per current for the two LHC beams.

Beam	$\Delta Q_x'' / \Delta I_{\text{oct}} (1/\text{A})$		$\Delta Q_y'' / \Delta I_{\text{oct}} (1/\text{A})$	
	Simulated	Measured	Simulated	Measured
1	49	$57 \pm 20$	-23	$2 \pm 27$
2	48	$43 \pm 22$	-21	$-7 \pm 28$

Table 6.4: MAD-X/PTC calculations vs. measurements of second-order chromaticity at 6.5 TeV for the two LHC beams at zero Landau octupole current for operational machine settings.

Beam	$10^{-4} Q''_x$		$10^{-4} Q''_y$	
	Simulated	Measured	Simulated	Measured
1	0.0	$0.0 \pm 0.2$	0.0	$0.0 \pm 0.2$
2	0.0	$0.0 \pm 0.2$	0.0	$0.0 \pm 0.2$

MAD-X/PTC calculations. A comparison is shown in Table 6.4. The contribution from octupole magnets to second-order chromaticity will be discussed further in Chapter 7.

To compare the measured stabilising Landau octupole current with model predictions, a scan in  $I_{\text{oct}}$  was performed in PYHEADTAIL, again using the parameters in Table 6.2. The contribution from the Landau octupoles to the second-order chromaticity has also been included according to the values quoted in Table 6.3. The final results are summarised in Fig. 6.5. The plot shows the instability growth rates in the horizontal (blue) and the vertical (red) planes as a function of the Landau octupole current. They were extracted from an exponential fit to the bunch centroid motion. Clearly, with increasing current, i.e. more tune spread and hence more Landau damping, the growth rates are reduced and the instability is completely suppressed. The grey hatched area marks the region where the beam is stable over the entire simulation period of  $N_{\text{turns}} = 5 \times 10^5$  turns. This is further illustrated in Fig. 6.6 where the bunch centroid motion is shown over the full simulation period for four different currents in the Landau octupoles. The stabilising current lies at  $I_{\text{oct}}^{\text{sim}} = 107.5 \pm 2.5 \text{ A}$ . At this value the Landau octupoles contribute to the second-order chromaticity with  $\Delta Q''_x \approx 5 \times 10^3$  and  $\Delta Q''_y \approx -2.4 \times 10^3$  respectively.

The model predicts a threshold current that is consistent with the measurement in the machine which demonstrates that the main beam dynamics effects are accurately modelled in PYHEADTAIL.

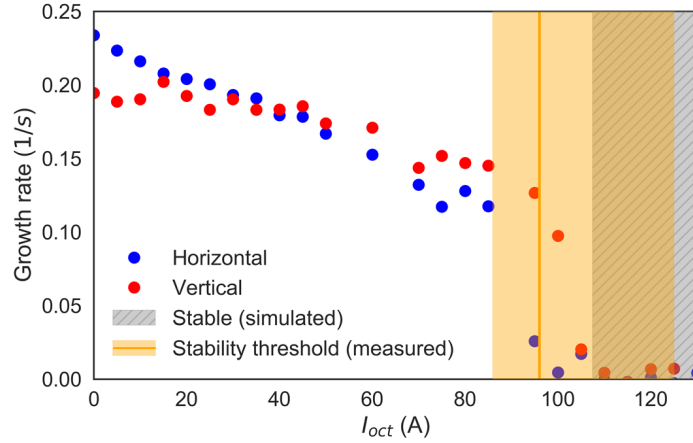


Figure 6.5: PYHEADTAIL simulations demonstrating the stabilisation of a single bunch with Landau octupoles in the LHC at 6.5 TeV. Centroid growth rates vs. Landau octupole current are shown with the grey hatched area indicating the cases that were stable over  $N_{\text{turns}} = 5 \times 10^5$  turns (compare Fig. 6.6). The measured threshold is represented by the orange line and its uncertainty by the orange area.

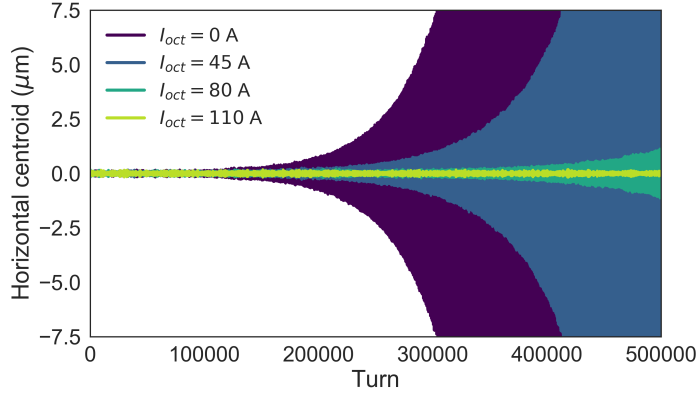


Figure 6.6: Horizontal bunch centroid signals over the full PYHEADTAIL simulation period for a selection of four different Landau octupole currents for the single-bunch head-tail instability observed in the LHC at 6.5 TeV.

In particular, the reliability of the LHC impedance model for single-bunch instabilities is confirmed for the operational machine configuration at 6.5 TeV which will also be used in the following for the stability studies with second-order chromaticity.

### 6.2.2 With second-order chromaticity

This section presents the experiments and simulations carried out with second-order chromaticity in the LHC. The experimental procedure and the observed phenomena are explained and interpreted by means of PYHEADTAIL simulations. The aim of the section is to demonstrate stabilisation of single bunches through Landau damping, which is achieved predominantly from detuning with longitudinal rather than transverse amplitude, both in experiments and simulations. The results are also discussed based on the analytical derivations made in Chapter 4.

The experiment was performed with two bunches in each of the two LHC beams at an energy of 6.5 TeV. The main parameters of the four individual bunches, i.e. the bucket number (Bkt), bunch intensity ( $N$ ), four-sigma bunch length ( $4\sigma_t$ ), and the normalised transverse emittances, are listed in Table 6.5. Due to the presence of the transverse bunch-by-bunch feedback system and the large longitudinal separation of the two bunches in each beam, coupled-bunch wakefield effects can be neglected. At the beginning of the experiment, the Landau octupoles were powered with a current of  $I_{\text{oct}} = 320$  A to guarantee beam stability. To test stabilisation with  $Q''$ , the aim was to set QPPF and QPPD such that  $Q''_{x,y} \approx -4 \times 10^4$  units in both beams once the current in the Landau octupoles would be reduced to zero. Due to the relatively high currents, the additional contribution to the second-order chromaticity from the Landau octupoles in dispersive regions was significant and hence had to be taken into account during the  $Q''$  adjustment process. At the initial current of  $I_{\text{oct}} = 320$  A, for example, they were  $\Delta Q''_x \approx 1.5 \times 10^4$  and  $\Delta Q''_y \approx -0.7 \times 10^4$  according to Table 6.3. To introduce the desired amount of second-order chromaticity, several iterations were made by varying the sextupole knobs QPPF and QPPD, re-measuring  $Q''$ , and comparing the results to MAD-X/PTC calculations.

Once the targeted sextupole settings were reached, the current in the Landau octupoles was reduced

Table 6.5: Initial bunch parameters of the four individual bunches in the two beams residing in different buckets (Bkt) while performing the experiments with second-order chromaticity.

Beam	Bkt	N ( $10^{11}$ p)	$4\sigma_t$ (ns)	$\epsilon_x^{\text{norm}}$ ( $\mu\text{m rad}$ )	$\epsilon_y^{\text{norm}}$ ( $\mu\text{m rad}$ )
1	0	$0.91 \pm 0.01$	$1.04 \pm 0.02$	$1.5 \pm 0.2$	$1.8 \pm 0.2$
	700	$1.08 \pm 0.01$	$1.06 \pm 0.02$	$1.9 \pm 0.1$	$1.7 \pm 0.1$
2	30	$0.92 \pm 0.01$	$1.04 \pm 0.02$	$1.2 \pm 0.1$	$1.5 \pm 0.1$
	740	$1.14 \pm 0.01$	$1.06 \pm 0.02$	$1.2 \pm 0.1$	$1.3 \pm 0.1$

Table 6.6:  $Q''$  MAD-X/PTC calculations vs. measurements for the two LHC beams with powering of the MS at zero Landau octupole current after the  $Q''$  adjustment procedure targeting an amount of  $Q''_{x,y} = -4 \times 10^4$  units in both beams.

Beam	MS ( $\text{m}^{-3}$ )		$10^{-4} Q''_x$		$10^{-4} Q''_y$	
	QPPF	QPPD	Simulated	Measured	Simulated	Measured
1	0.15	0.19	-3.8	$-4.4 \pm 0.6$	-3.9	$-4.0 \pm 0.6$
2	0.15	0.26	-3.7	$-3.1 \pm 0.5$	-3.7	$-3.7 \pm 0.6$

in steps of 40A from 320A down to 0A. At  $I_{\text{oct}} = 40\text{A}$  all four bunches were still stable. This already indicated a successful stabilising effect from  $Q''_{x,y}$ , recalling that  $I_{\text{oct}}^{\text{meas}} = 96^{+29}_{-9}$  A was necessary to control the instability *without* second-order chromaticity. At this point, a chromaticity measurement was performed since the effect from the Landau octupoles was small enough to allow for an accurate assessment of  $Q''$ . The obtained values are summarised in Table 6.6 and compared to MAD-X/PTC calculations after subtraction of the remaining contribution from the Landau octupoles ( $\Delta Q''_x \approx 1.9 \times 10^3$  and  $\Delta Q''_y \approx -0.9 \times 10^3$ ). They demonstrate a reasonable agreement and a successful adjustment procedure for  $Q''$  in the machine. The amount of second-order chromaticity was consistent with the targeted  $-4 \times 10^4$  units in three out of four planes, while it was, in absolute terms, slightly lower than expected in the horizontal plane of beam 2.

When the Landau octupole current was reduced further, from 40A to 0A, a horizontal instability occurred in beam 1 for the bunch residing in bucket 700, while the other three bunches remained stable. The reasons will be discussed in Section 6.2.3. For the unstable bunch, the observed head-tail instability was an azimuthal mode  $l = -1$ . The top right plot in Fig. 6.7 displays the turn-by-turn traces acquired with the LHC Head-Tail Monitor for the unstable bunch. It shows a pattern with three nodes indicating a radial mode  $m = 3$ . The characteristics of this instability are clearly different from those described in Section 6.2.1, where an azimuthal mode  $l = 0$  with two nodes in the head-tail pattern ( $m = 2$ ) was recorded (Fig. 6.7, top left). The main difference with respect to the situation in the previous section was the large amount of  $Q''_{x,y}$  that had now been present in the machine. The reasons for the change of the head-tail mode are explained using PYHEADTAIL simulations in the following Section 6.2.3.

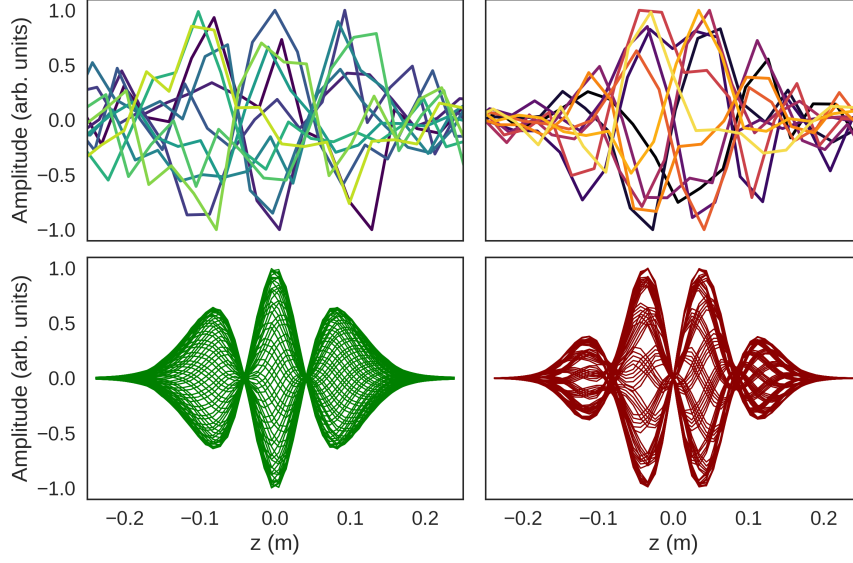


Figure 6.7: Comparison of the two modes observed in the machine (top) and in PYHEADTAIL simulations (bottom) without (left) and with (right) the effects of second-order chromaticity. The two cases correspond to the working points labelled (a) and (b) respectively in Fig. 6.8.

### 6.2.3 PYHEADTAIL simulations and interpretation

This section summarises the PYHEADTAIL studies that were performed, using the optics input from MAD-X/PTC, to reproduce the experimental observations made in the LHC. There are three main questions to be answered by means of tracking simulations: (1) Is the stabilisation of three out of four bunches indeed a result of mostly detuning with longitudinal amplitude, or could stability have been provided by the transverse amplitude detuning coefficients introduced parasitically by the QPPF and QPPD knobs? (2) Why did one of the four bunches become unstable? (3) Why is the observed head-tail mode with nonzero  $Q''$  knobs now an azimuthal mode  $l = -1$  rather than an  $l = 0$  as originally observed (Section 6.2.1).

At the experimental working point of  $QPPF = 0.15 \text{ m}^{-3}$  and  $QPPD = 0.19 \text{ m}^{-3}$  (beam 1), the transverse amplitude detuning coefficients generated by the sextupoles are comparable to LHC Landau octupole currents of  $I_{\text{oct}} \approx 50 \text{ A}$  ( $a_{xx}$ ),  $I_{\text{oct}} \approx 20 \text{ A}$  ( $a_{yy}$ ) and  $I_{\text{oct}} \approx 30 \text{ A}$  ( $a_{xy}$ ) respectively (compare Fig. 6.2). They are all well below the abovementioned single-bunch stability threshold of  $I_{\text{oct}}^{\text{meas}} = 96_{-9}^{+29} \text{ A}$  which indicates that an important contribution to beam stability must have been provided by second-order chromaticity. To understand the horizontal instability observed in one of the bunches, however, simulation studies were required. Optics results from MAD-X/PTC, among them the dependencies of  $Q''_{x,y}$  and the transverse amplitude detuning coefficients on the QPPF and QPPD knobs, displayed in Figs. 6.1 and 6.2, were also included in PYHEADTAIL, such that both the stabilising effects from detuning with transverse and longitudinal amplitudes would be modelled. In all the studies, the Landau octupoles were switched off to reproduce the situation of the experiment at  $I_{\text{oct}} = 0 \text{ A}$  where the bunch became unstable. The parameters were taken from the measurements in Table 6.5 for the bunch in beam 1, bucket 700.  $N_{\text{mp}} = 4 \times 10^5$  macroparticles were tracked over  $N_{\text{turns}} = 1.8 \times 10^6$  turns using again the same impedance model of the LHC.

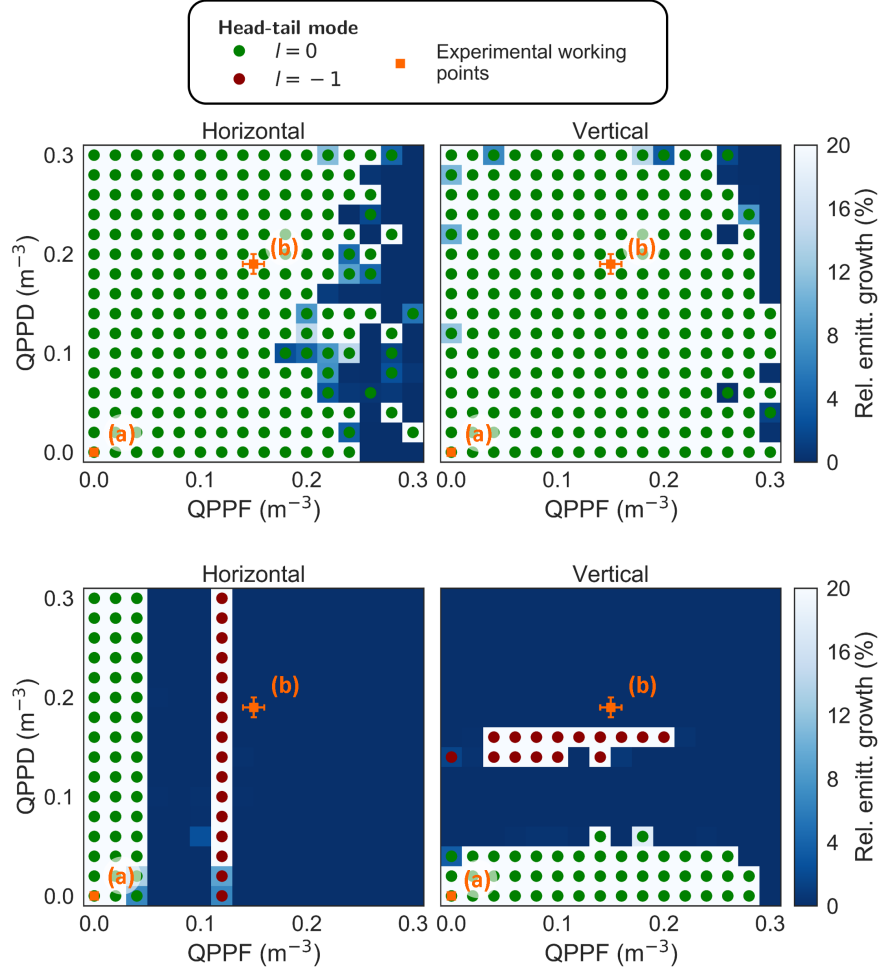


Figure 6.8: Two PYHEADTAIL studies displaying the predicted head-tail instabilities as a function of the sextupole knobs QPPF and QPPD. Labels (a) and (b) mark the two working points used during the experiments. *Top*: Results obtained *without*  $Q''_{x,y}$  effects, but including the transverse amplitude detuning coefficients from the sextupole knobs. *Bottom*: Results obtained including also the  $Q''_{x,y}$  effects.

In a first set of simulations, the tune spread from second-order chromaticity was deliberately *excluded*. This was to assess whether the spread from the transverse amplitude detuning coefficients alone, which is introduced parasitically by the QPPF and QPPD knobs, would be enough to provide stability at the working point for beam 1 ( $QPPF = 0.15 \text{ m}^{-3}$ ,  $QPPD = 0.19 \text{ m}^{-3}$ ). The results are summarised in the upper plots of Fig. 6.8 for the horizontal (left) and the vertical (right) planes. The colour code corresponds to the relative emittance growth over the simulation period (in %) where “blue” means stable and “white” means unstable. The dots represent the azimuthal mode number of the instability predicted for each setting of (QPPF, QPPD) in case the bunch was found to be unstable in the simulation. The two working points labelled (a) and (b) illustrate the situation with and without the  $Q''$  knobs and correspond to the experimental machine configuration described in Sections 6.2.1 and 6.2.2 respectively. For the latter,



the error bars correspond to the uncertainty in the  $Q''_{x,y}$  listed in Table 6.6. Most of the area is unstable, in particular the working point (b) where the  $Q''$  measurements were carried out. This demonstrates that the transverse amplitude detuning coefficients from the sextupole knobs indeed do not provide sufficient Landau damping. The experiment showed that three out of four bunches remained stable while the model predicts instability for all the bunches with a high level of significance<sup>1</sup>. Furthermore, the instability predicted by the model is an azimuthal mode  $l = 0$  (green dots) with two nodes in the head-tail pattern which is not consistent with the experimental observations made in the machine at the working point (b). Rather, an azimuthal mode  $l = -1$  with three nodes was observed experimentally (Fig. 6.7, right).

The second set of simulations is displayed in the two lower plots of Fig. 6.8. This simulation now also includes the effects of detuning with longitudinal amplitude as introduced by the second-order chromaticity. Two main observations can be made. First, large regions of stability (blue) are created in the QPPF vs. QPPD plane. The two main stable areas are separated by an unstable band in both the horizontal and the vertical planes which shows a different head-tail mode with an azimuthal number  $l = -1$  (red dots). The reason is that second-order chromaticity changes the effective impedance, similarly to a first-order chromaticity. As such, it modifies the complex coherent frequencies associated with the head-tail modes and can even completely change the nature of the modes. This effect is correctly predicted by the Vlasov formalism developed in Chapter 4. The bottom plots in Fig. 6.8 are hence a combination of a change in effective impedance and Landau damping, both introduced by second-order chromaticity. The first unstable band observed at low values of QPPF (QPPD) is the azimuthal mode zero (green dots), consistent with the experimental measurements described in Section 6.2.1. The stable region between the two unstable bands  $l = 0$  and  $l = -1$  arises from sufficient Landau damping of both modes. The further increase of QPPF (or QPPD), however, leads to a change of the effective impedance in a way that Landau damping is lost for the  $l = -1$  mode. For even larger amounts of  $Q''$ , however, all the instabilities can be suppressed. The second observation is that the working point (b), although essentially stable, lies very close to the unstable band of the  $l = -1$  mode. Indeed, the experimental data clearly revealed the observed horizontal instability to be of mode  $l = -1$ . The LHC Head-Tail Monitor signal is in good agreement with the predictions from simulations. Both of them feature a three-node coherent oscillation pattern along the bunch as shown in Fig. 6.7 on the right. It has been verified that experiment and simulation agree both in the azimuthal and radial mode numbers of the excited instability.

The simulation model cannot make a definite statement about why only one of the four bunches became unstable during the experiment. This is mostly due to the measurement uncertainties in bunch length, intensity, and emittance, and to some extent also due to the limited accuracy of the impedance model and therefore the uncertainty on the beam stability predictions from PYHEADTAIL. A number of considerations can be made, however, to better understand and explain the experimental observations: (1) the bunches in beam 1 and beam 2 do not experience the same amount of Landau damping due to different settings in  $Q''_{x,y}$  for the two beams (Table 6.6). While this may explain why beam 1 and beam 2 behave differently, it does not answer the question why the two bunches in beam 1 exhibit a different behaviour. After all, they are both subject to the same amount of second-order chromaticity. (2) The major differences between the two bunches in beam 1 are their transverse emittances and intensities listed in Table 6.5. The unstable bunch residing in bucket 700 had a slightly larger horizontal emittance compared to the stable one located in bucket 0 ( $1.9 \pm 0.1 \mu\text{m rad}$  vs.  $1.5 \pm 0.2 \mu\text{m rad}$ ). The vertical

<sup>1</sup>Note that the amount of  $Q''_{x,y}$  increases quadratically with the knobs as explained in Section 6.1.1.

emittances, on the other hand, were identical within the errors ( $1.7 \pm 0.1 \mu\text{m rad}$  vs.  $1.8 \pm 0.2 \mu\text{m rad}$ ). As a result of the larger horizontal emittance, the Landau damping introduced by the parasitic transverse amplitude detuning coefficient  $a_{xx}$  in the horizontal plane is actually larger for the unstable bunch compared to the stable one. However, the difference between the emittances is minor, and, more importantly, the transverse amplitude detuning coefficient is very small. It is clear from the upper plots in Fig. 6.8 that the Landau damping from detuning with transverse amplitude is indeed insignificant for the instability under consideration. The bunch intensities, on the other hand, are the most likely explanation for the differences observed in terms of stability. The stable bunch had an intensity of  $(0.91 \pm 0.01) \times 10^{11}$  p compared to  $(1.08 \pm 0.01) \times 10^{11}$  p for the unstable one. An impedance-driven instability is more difficult to be stabilised for a bunch of higher intensity since its complex coherent tune shift is larger and more likely to lie outside of the stability diagram for a given amount of Landau damping. This can become a crucial aspect especially within a configuration just at the border of stability as suggested by Fig. 6.8 (bottom).

To summarise, the experiments can only be reproduced in simulations when including all the effects of second-order chromaticity in PYHEADTAIL. This concerns both the Landau damping effect as well as the change of the effective impedance which manifests as a change of the azimuthal and radial mode numbers. When including the effects of the second-order chromaticity in the model, the observed head-tail modes are consistent with simulations at both working points (a) and (b). Moreover, the second-order chromaticity is the main stabilising effect while the contribution from detuning with transverse amplitude introduced by the sextupole knobs plays a minor role here. The reason why one of the four bunches went unstable during the experiment can be explained by the differences in bunch intensities as well as in the second-order chromaticities in the two beams.

### 6.3 Conclusions

Second-order chromaticity or an rf quadrupole cavity are two possible ways to introduce a betatron tune spread as a function of longitudinal action and it was proven analytically in Chapter 3 that the two mechanisms are equivalent in a first-order approximation. The second-order chromaticity has the advantage that it can be introduced in a machine like the LHC by using the existing hardware and tweaking the optics of the accelerator. In that way, it can be used to experimentally study stabilisation from betatron detuning with longitudinal amplitude in a cost-effective manner and to benchmark the numerical and analytical models. The LHC represents an ideal accelerator environment for such a proof-of-principle experiment as it is a well-studied machine, both in terms of optics and collective effects. Here, a sextupole powering scheme was employed to control  $Q''$  in both beams and the two transverse planes independently. Beam measurements and MAD-X/PTC calculations indicate a good agreement and demonstrate a thorough control of the second-order chromaticity in the LHC.

The single-bunch stability at 6.5 TeV has been recapped and the stabilising Landau octupole currents for the most unstable head-tail mode were proven to be consistent between experiments and PYHEADTAIL simulations. Based on the same machine configuration, experiments were performed to assess the stabilisation of single bunches with second-order chromaticity. Beam dynamics simulations clarify that detuning from transverse amplitude alone, introduced parasitically by the sextupole knobs, cannot explain the observations made in the machine. Clearly,  $Q''$  makes a strong contribution to the beam stability as demonstrated by the combined analysis of the data and PYHEADTAIL simulations. Fur-

thermore, it was experimentally confirmed that second-order chromaticity introduces a change of the head-tail mode as expected from the Vlasov theory for nonlinear chromaticity developed in Chapter 4, and also consistently observed in simulations. This demonstrates that the numerical and analytical models of the stabilising mechanism are correct and that the involved beam dynamics mechanisms are well understood both from the single- and multi-particle effects points-of-view. The results also serve as a first, cost-effective, experimental validation of the rf quadrupole for Landau damping.

Future studies will, among others, assess the effect of  $Q''$  on the dynamic aperture (beam lifetime), its potential for stabilisation of, for example, electron cloud driven instabilities, and the evaluation of various  $Q''$  production schemes. A step in that direction has been made with another machine development session in the LHC to address the aforementioned questions. However, the employed scheme created a large off-momentum beta-beating around the ring and hence was not machine-safe for multi-bunch operation. The offline analysis also revealed, though, that the issue of machine safety may potentially be overcome by a change of the off-momentum collimation scheme. A detailed summary of the findings can be found in Ref. [98]. The experiment performed with second-order chromaticity can be interpreted as an indication of why an rf quadrupole may be a better choice for Landau damping from detuning with longitudinal amplitude. Other than nonlinear chromaticity, it does not depend on optics constraints, but works instead as an independent device. The advantages and disadvantages of both methods, however, would need to be further evaluated, especially in terms of single-particle effects, such as dynamic aperture and resonances.



## 7 Experimental studies: second-order chromaticity in the SPS

Although the experiments with second-order chromaticity in the LHC discussed in the previous chapter showed conclusive results and demonstrated a detailed understanding of the involved beam dynamics, further tests were planned and carried out in the SPS at CERN. The goal was to use a different scheme to enhance the second-order chromaticity in the machine. The reason is that other than in the LHC, the sextupole magnets in the SPS are not effective in generating a second-order chromaticity. Instead, one can use a powering scheme for the magnetic Landau octupoles installed in the lattice.

As demonstrated in Chapter 2, magnetic octupoles primarily generate betatron detuning with transverse amplitude and it is well known that this leads to Landau damping in the transverse planes (see, e.g., Refs. [60, 77]). In this chapter, however, the objective is to show that betatron detuning with longitudinal amplitude *alone*, such as from nonlinear chromaticity, can provide beam stability in a similar fashion. By consequence, the detuning with transverse amplitude introduced by the octupole powering scheme needs to be cancelled out. This can be achieved by simultaneously employing the three different families of Landau octupoles available in the SPS and powering them in a specific configuration. Due to the complexity of the setup, mostly because of the required accurate knowledge and correction of the machine optics, it was unclear at the planning stage of the experiments whether the machine would be sensitive enough as to allow for a conclusive outcome of the study.

First, the basic theory for a second-order chromaticity knob with the SPS octupole magnets free of detuning with transverse amplitude is introduced in Section 7.1. This will also clarify why the experimental studies are split into two parts. First, the nonlinear optics model of the SPS is characterised experimentally to validate the MAD-X/PTC model of the machine as well as the second-order chromaticity knob. This preparatory work described in Section 7.2 is essential for the second part of the study where a horizontal head-tail mode zero is excited using negative horizontal first-order chromaticity, and attempted to be stabilised with the knob. The reason for exciting an azimuthal mode zero was that this type of instability is easy to observe and well-reproducible in the SPS. The analysis of 2017 measurements on beam stabilisation with the knob is discussed first, alongside PYHEADTAIL simulations in Section 7.3. This is followed by a more in-depth analysis of all the available data and additional measurements taken in 2018 to explain the discrepancies between the model and the experiments. Finally, the main conclusions from the experiments are summarised in Section 7.4.

## 7.1 Design of a second-order chromaticity knob

The SPS has a super periodicity of six and the lattice is composed of an alternating-gradient scheme with 108 cells [99]. The machine can operate with three different optics named Q20, Q22, and Q26, where the number denotes the integer part of the betatron tunes for each configuration. Q26 is the original SPS optics, while Q20 and Q22 were designed at a later stage to increase the intensity threshold of the TMCI in view of the LIU required to deliver the beams to the HL-LHC [12, 99–101]. The increase of the TMCI threshold is achieved by lowering the transition gamma  $\gamma_t$  and therewith increasing the slip factor  $\eta$  of the machine and consequently the synchrotron tune  $Q_s$ . The Q20 optics was chosen for this study for reasons discussed in the following subsections. It will also be explained why the knob was designed for the horizontal rather than the vertical plane.

### 7.1.1 Basic considerations

As explained in Section 2.2.5, an octupole kick  $\Delta x'_i = g(3xy^2 - x^3)$  [resp.  $\Delta y'_i = g(3yx^2 - y^3)$ ] introduces detuning with transverse amplitude which, at first order, can effectively be described by the transverse amplitude detuning coefficients  $a_{uv}$  with  $u, v \in \{x, y\}$ . In case an octupole magnet is located in a dispersive region, the closed orbit of the beam is distorted at the location of the kicks, such that  $x_i \rightarrow x_i + D_x \delta_i$ . It can be shown analytically that octupole magnets placed in dispersive regions hence contribute to the second-order chromaticity. For example, a single octupole magnet of length  $L$  powered with a strength  $k_4$  at beta function  $\beta_x$  and dispersion function  $D_x$  produces a horizontal second-order chromaticity of (see, e.g., Ref. [59])

$$Q_x'' = \frac{1}{4\pi} k_4 L \beta_x^2 D_x^2. \quad (7.1)$$

The SPS has three families of octupole magnets: LOF, LOD, and LOE. While *LO* stands for *Landau octupole*, *F*, *D*, and *E* stand for *focusing*, *defocusing*, and *extraction* respectively, indicating where the magnets of each family are located in the lattice. Figure 7.1 gives an overview of the SPS horizontal dispersion function in Q20 optics together with the locations of the focusing (blue) and defocusing (green) families as well as the two extraction octupoles (red) selected for the study for the full circumference of the machine. LOFs are installed near the focusing quadrupoles and are hence at locations of maximum  $\beta_x$  and minimum  $\beta_y$ . They produce mostly horizontal detuning with horizontal amplitude ( $a_{xx}$ ). The situation is inverse for the LODs which generate predominantly  $a_{yy}$ . Figure 7.2 displays a zoomed view of the first sector of the SPS including the horizontal beta function to illustrate the situation.

The LOFs are installed in high dispersion regions and can be employed to enhance  $Q_x''$ . The sign of  $Q_x''$  is determined by the polarity of the LOFs. Negative (positive) polarity produces negative (positive)  $Q_x''$ . However, as explained above, they also introduce a horizontal amplitude detuning coefficient  $a_{xx}$  which needs to be cancelled out for the studies performed here. This is achieved by means of the LOE magnets located in very low dispersion regions. The LOEs, powered with opposite polarity than the LOFs can compensate the detuning coefficient without significantly affecting  $Q_x''$ . Two elements of the extraction family, named *LOE12002* and *LOE33002*, were selected. While there are more than just these two LOEs installed in the SPS, these magnets are currently not used during routine operation and hence not all of them are equipped with a power converter. The two selected magnets were the most suitable elements for the experiments since they are located in minimum dispersion regions as illustrated by the red bars in Figs. 7.1 and 7.2. Naturally, creating the compensation of  $a_{xx}$  with only two elements of the

### 7.1. Design of a second-order chromaticity knob

LOE family rather than with a distributed scheme can be problematic since the magnets can introduce strongly localised kicks (negative impact on dynamic aperture and beam lifetime). This ultimately limits the reach of the  $Q_x''$  knob. Finally, the LODs are employed to also cancel out the cross-detuning coefficient  $a_{xy}$ .

One important constraint for the measurements, which were carried out over a period of several weeks, were the remanent fields of the multipole magnets due to the magnetic hysteresis when these elements are cycled [102, 103]. Naturally, the remanent fields depend on the preceding magnetic cycle. The sextupole and octupole fields, among others, can hence be different for a following cycle, affecting, for example, the linear and nonlinear chromaticity as well as the amount of detuning with transverse amplitude. For all of the studies presented here, it was essential that the SPS supercycle would always have the same structure, i.e. that the machine development cycle was always placed directly after the North Area Fixed Target physics cycle. This was to guarantee the same measurement conditions.

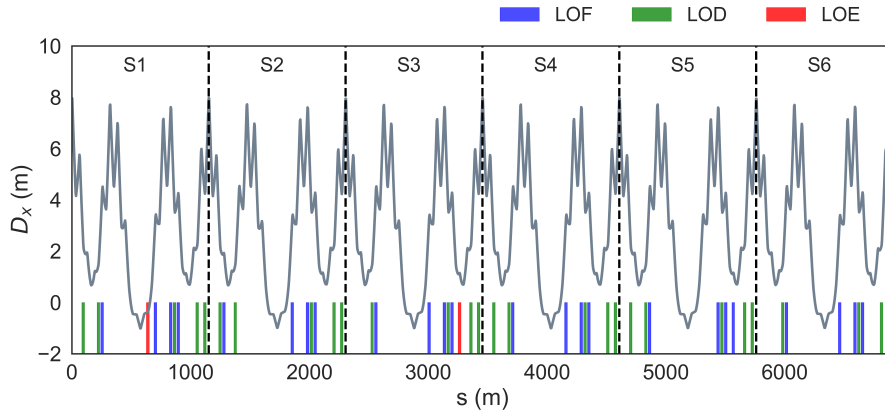


Figure 7.1: Dispersion function (slate grey) along the full circumference of the SPS ring in Q20 optics and locations of the three different families of octupole magnets (coloured bars).

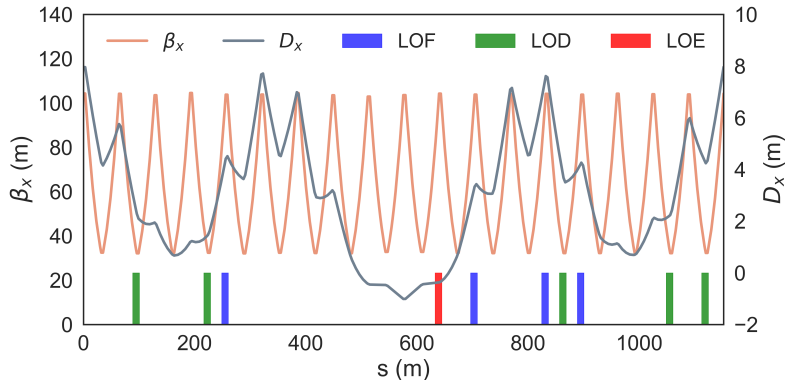


Figure 7.2: Horizontal beta (salmon) and dispersion (slate grey) functions in Q20 optics for the first sector in the SPS and locations of the three different families of octupole magnets (coloured bars).

### 7.1.2 MAD-X/PTC predictions

MAD-X/PTC scripts were used to validate the idea of employing the three octupole families to create a  $Q_x''$  knob free of detuning with transverse amplitude. Preparatory PYHEADTAIL simulations that will be discussed in Section 7.3 showed that at least a few thousand units of second-order chromaticity would be required to achieve stabilisation of the head-tail mode zero that was planned to be excited. To include a large safety margin, the knob was designed with the aim to reach up to  $Q_x'' = \pm 1.5 \times 10^4$  units. In the following, the required octupole strengths in the three families  $k_{\text{LOF}}$ ,  $k_{\text{LOD}}$ , and  $k_{\text{LOE}}$  respectively, are given in units of the LHC Software Architecture (LSA) trim editor knobs of the SPS [104].

First, the three optics Q20, Q22, and Q26 were evaluated in terms of suitability for the study. The most important ingredient for the decision is the dispersion function at the locations of the octupole magnets. A high dispersion function at the LOFs is desirable while it should be as close to zero as possible at the selected LOEs. This will guarantee that  $Q_x''$  can be efficiently created by the LOFs such that they can be powered with low strengths well within hardware limitations and without having a strong impact on the dynamic aperture. Furthermore, if the current in the LOFs can be kept low, they also introduce a smaller transverse amplitude detuning coefficient which can be compensated more easily by the LOEs. The reason why the dispersion should be close to zero at the LOEs, on the other hand, is to avoid that they compromise the  $Q_x''$  generated by the LOFs. If  $D_x$  is zero and  $\beta_x$  is large at the location of the LOEs, they will not affect  $Q_x''$ , but cancel out  $a_{xx}$  efficiently. It is of particular importance to keep the kick strengths in the LOE magnets as small as possible since only two elements could be used for the study (strongly localised kicks). When comparing the three optics configurations available in the SPS, it becomes clear that in Q20, the dispersion function is largest at the LOFs, about a factor three higher than in Q26. At the same time, it is very low at the location of the two available LOEs. This has important consequences. For example, to introduce  $Q_x'' = 5 \times 10^3$  units,  $k_{\text{LOF}}^{Q26} = -48.0$  and  $k_{\text{LOF}}^{Q20} = 1.8$ . Furthermore,  $k_{\text{LOE}}^{Q26} = 409.0$  and  $k_{\text{LOE}}^{Q20} = -14.9$ . The required octupole strengths in Q26 are by factors larger than in Q20 for a specific setting of  $Q_x''$ . For the given example, they are actually beyond hardware limitations. The Q26 configuration could hence not be used for the study. In terms of suitability, the Q22 optics is situated in between the other two configurations and Q20 hence remained as the best possible choice. Similarly, for reasons of efficiency of the knob in producing  $Q_x''$  and compensating the detuning with transverse amplitude, the horizontal instead of the vertical plane was selected for the experiments. Figure 7.3 displays the strengths required in the three octupole families as a function of the  $Q_x''$  knob according to MAD-X/PTC calculations. The values are given within the targeted range of  $Q_x'' = \pm 1.5 \times 10^4$  for Q20 optics. The strengths in the LOEs have been scaled by a factor 0.1 for better readability of the plot. The strength required in the LODs is small ( $k_{\text{LOD}} = -0.35$ ) and remains roughly constant over the full range of the  $Q_x''$  knob.

## 7.2 SPS nonlinear optics measurements

A detailed knowledge of the nonlinear optics is essential to improve the modelling and the performance of a machine, both in terms of incoherent and collective effects. Nonlinear optics measurements, such as to obtain amplitude detuning and nonlinear chromaticity, have been performed in the SPS on several occasions since the year 2000 (see, e.g., Refs. [105–107]). However, a full systematic study to assess the nonlinear optics contributions from the three octupole families in Q20 optics, available since 2012, has yet been missing.



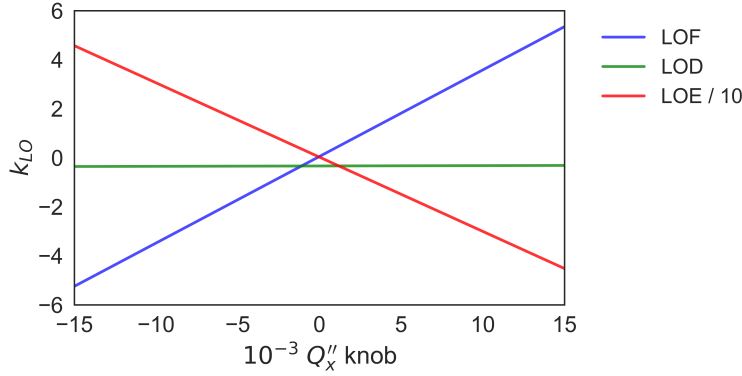


Figure 7.3: Predictions from the SPS Q20 MAD-X/PTC model on the strengths  $k_{LO}$  (LSA trim values) required in the three octupole families for the  $Q''_x$  knob free of detuning with transverse amplitude ( $a_{xx} = a_{xy} = 0 \text{ m}^{-1}$ ).

Table 7.1: Main beam and machine parameters used for all the nonlinear optics and collective effects studies in the SPS.

Parameter		Value
Optics configuration		Q20
Beam energy (total)	$E_0$	26 GeV
Bunch intensity	$N$	$2 \times 10^{10}$ p
1 <sup>st</sup> -, 2 <sup>nd</sup> -order chromaticities	$Q'_{x,y}, Q''_{x,y}$	<i>various</i>
Norm. horizontal emittance	$\epsilon_x^{\text{norm}}$	1.0 $\mu\text{m rad}$
Norm. vertical emittance	$\epsilon_y^{\text{norm}}$	0.6 $\mu\text{m rad}$
Bunch length	$\sigma_z$	0.21 m
Rf voltages (1 <sup>st</sup> , 2 <sup>nd</sup> harmonic)	$V_1, V_2$	1.5, 0.15 MV

Here, the goal is to confirm experimentally whether a second-order chromaticity knob, free of detuning with transverse amplitude, can indeed be realised in the SPS as demonstrated by the MAD-X/PTC model in Section 7.1.2. There are two main sets of measurements that need to be performed for each of the three octupole families. First, the amount of detuning with transverse amplitude introduced by every family. This will, among others, clarify whether the MAD-X model can be used to predict the strengths required in the three families to cancel out the transverse amplitude detuning coefficients. Second, a good knowledge of the nonlinear chromaticity contributions from each octupole family is required to assess whether the amount of  $Q''_x$  calculated by the model is indeed introduced in the machine.

### 7.2.1 Detuning with transverse amplitude

Detuning with transverse amplitude can be measured, for example, by exciting a low transverse emittance (and low intensity) beam to large transverse amplitudes by means of a kicker magnet. The reason for using a beam with small transverse emittances is to maximise the available aperture defined by the vacuum chamber or other accelerator structures and hence the reachable amplitude of the kicks. A

larger kick amplitude can improve the sensitivity of the measurements. Furthermore, the decoherence and the associated transverse emittance increase of the beam after the exciting kick is weaker for a beam with a smaller transverse amplitude spread. The plane of excitation, i.e. the direction in which the beam receives the kick, and the plane where the betatron tune is measured define which of the three detuning coefficients is determined. To obtain  $a_{xx}$ , for example, the beam is excited in the horizontal plane and the change of the horizontal tunes as a function of kick strength is measured. Here, the objective was to validate the SPS MAD-X model against measurements in terms of amplitude detuning through the horizontal detuning coefficient  $a_{xx}$  introduced by the three octupole families installed in the machine.

The beam is excited at different amplitudes by means of the SPS tune kicker and the betatron tune is measured for each kick strength. Both the amplitude of the kick and the betatron tune are extracted from the same beam position monitor (BPM) data. For each setting of the kick strength, between five and ten individual shots are recorded to reduce the statistical error mainly on the tune measurement. Non-conforming shots in terms of bunch length and intensity are filtered out. At the beginning of the measurement campaign in 2017, we discovered that the SPS orbit BPMs do not provide the correct amplitudes due to a calibration error, particularly pronounced at higher kick strengths. This was likely the main explanation for the discrepancies between model and measurements observed in Ref. [106]. For that reason, the LHC-type BPMs installed in the SPS were used instead to compute the action ( $2J_x$ ) of the beam. The maximum peak-to-peak amplitude  $A_{ptp}$  is measured from the first turns after the kick, squared and divided by the beta function at the location of the BPM

$$2J_x = \frac{A_{ptp}^2}{\beta_x^{BPM}}. \quad (7.2)$$

The beta function is extracted from a MAD-X Twiss analysis. The kicker magnet excites large bunch oscillations which allows to accurately determine the betatron tunes from the same LHC-type BPMs. Due to the decoherence of the centroid signal, one uses only a few hundred turns (here: 250 turns) directly after the kick. A SUSSIX frequency analysis is performed on this data and the most prominent peak (main tune) is stored for further evaluation.

Figures 7.4 to 7.6 summarise the final results for the three octupole families LOF, LOD, and LOE respectively. Measurements with positive (blue) and negative (red) polarities were taken with the same absolute strength in each family. The data points correspond to the average tune values obtained from five to ten individual shots and the data were binned with respect to the measured action. The error bars are defined by the error of the mean of each group of shots. The detuning coefficients are obtained from a linear fit and the predictions calculated with MAD-X/PTC are given by the solid lines (gold). The second-order detuning with amplitude  $\partial^2 Q_x / \partial (2J_x)^2$ , introduced by the octupole magnets as a higher-order contribution, is negligible given the field strengths and the range of excitation amplitudes accessible in the experiment. The plots demonstrate that the model makes accurate predictions on the  $a_{xx}$  parameter. By taking the difference between the slopes determined for the two octupole polarities, one can directly infer the amplitude detuning coefficient introduced purely by the corresponding family, independent of the bare amount of detuning in the machine. With this approach, one can also define the amount of amplitude detuning introduced per unit of the LSA knob  $k_{LO}$  since  $a_{xx}$  scales linearly with this parameter. All the numerical values of the analysis are listed in Table 7.2.

From the acquired data, one can also determine the amount of detuning with transverse amplitude in

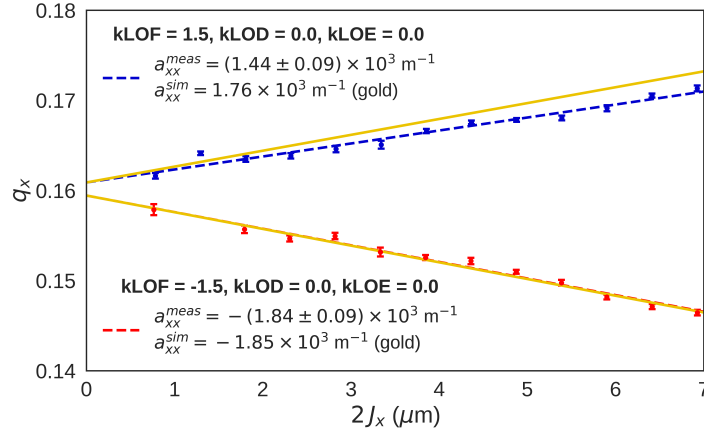
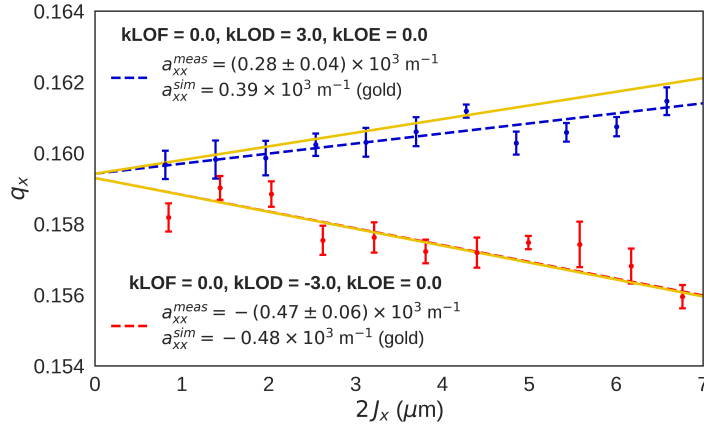
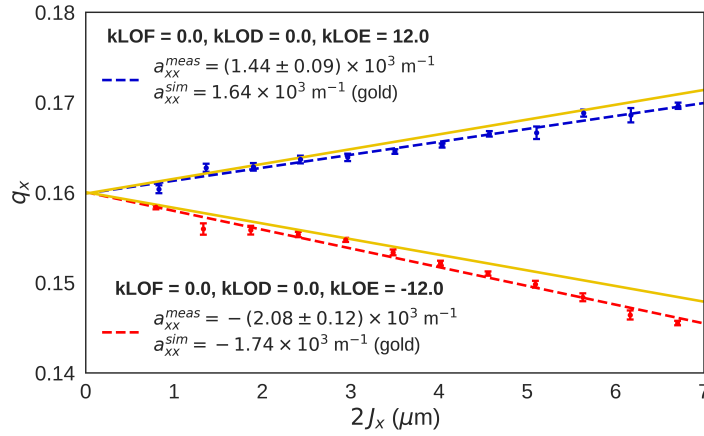
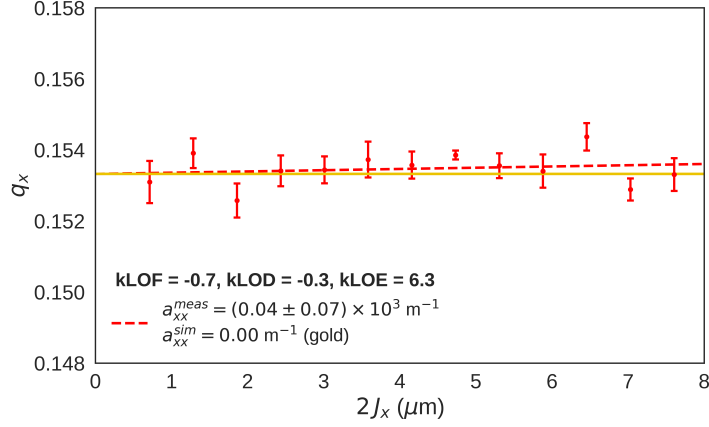

 Figure 7.4: Measurement of  $a_{xx}$  for the LOF family and comparison with MAD-X/PTC calculations.

 Figure 7.5: Measurement of  $a_{xx}$  for the LOD family and comparison with MAD-X/PTC calculations.

 Figure 7.6: Measurement of  $a_{xx}$  for the two LOEs and comparison with MAD-X/PTC calculations.

Table 7.2: Overview of the transverse amplitude detuning measurements with SPS Q20 optics for the three different families of octupole magnets. The very last row corresponds to the amount of amplitude detuning in the bare machine. Comparisons with MAD-X/PTC are also shown.

kLOF	kLOD	kLOE	$a_{xx}$ ( $10^3 \text{ m}^{-1}$ )			$\Delta a_{xx}/\Delta k_{LO}$ ( $10^3 \text{ m}^{-1}$ )	
			Measured	Simulated		Measured	Simulated
1.5	0.0	0.0	$1.44 \pm 0.09$	1.76	}	$1.09 \pm 0.04$	1.20
-1.5	0.0	0.0	$-1.84 \pm 0.09$	-1.85			
0.0	3.0	0.0	$0.28 \pm 0.04$	0.39	}	$0.13 \pm 0.01$	0.15
0.0	-3.0	0.0	$-0.47 \pm 0.06$	-0.48			
0.0	0.0	12.0	$1.44 \pm 0.09$	1.64	}	$0.15 \pm 0.01$	0.14
0.0	0.0	-12.0	$-2.08 \pm 0.12$	-1.74			
-0.7	-0.3	6.3	$0.04 \pm 0.07$	0.00			
0.0	0.0	0.0	$-0.21 \pm 0.04$	-0.05			


 Figure 7.7: Proof-of-principle measurement to demonstrate compensation of the  $a_{xx}$  coefficient using the  $Q_x''$  knob and MAD-X/PTC predictions.

the bare machine, i.e. the amount of transverse amplitude detuning  $a_{xx,0}$  present with the octupole magnet strengths set to zero (without degaussing them). This is achieved by computing the average of the two detuning coefficients measured for opposite polarities of each family, assuming that the detuning coefficient is perfectly antisymmetric with respect to  $k_{LO}$ . One obtains

$$\begin{aligned}
 a_{xx,0}^{\text{LOF}} &= -(0.20 \pm 0.06) \times 10^3 \text{ m}^{-1}, \\
 a_{xx,0}^{\text{LOD}} &= -(0.10 \pm 0.04) \times 10^3 \text{ m}^{-1}, \\
 a_{xx,0}^{\text{LOE}} &= -(0.32 \pm 0.08) \times 10^3 \text{ m}^{-1},
 \end{aligned} \tag{7.3}$$

demonstrating that the bare amount of horizontal amplitude detuning in the machine is negative and of the order of a few hundred units  $\bar{a}_{xx,0} = -(0.21 \pm 0.04) \times 10^3 \text{ m}^{-1}$  (MAD-X/PTC:  $\bar{a}_{xx,0} = -0.05 \times 10^3 \text{ m}^{-1}$ ).

Since the model makes accurate predictions on the amount of amplitude detuning, it can be reliably used to predict the strengths required in the three families to achieve compensation of the transverse amplitude detuning coefficients for a certain setting of the  $Q_x''$  knob. One example is shown in Fig. 7.7 where the three octupole families were powered simultaneously to introduce  $Q_x'' = -2 \times 10^3$  and cancel out  $a_{xx}$  (and  $a_{xy}$ ) at the same time. The measurement proves that the horizontal tune is indeed independent of the amplitude within errors [ $a_{xx} = (0.04 \pm 0.07) \times 10^3 \text{ m}^{-1}$ ]. Without compensation from the LOEs, the detuning coefficient predicted by MAD-X/PTC would be significantly higher ( $a_{xx} = -0.99 \times 10^3 \text{ m}^{-1}$ ). The same result is found using a combination of the individual measurements listed in Table 7.2 [ $a_{xx} = (-0.97 \pm 0.06) \times 10^3 \text{ m}^{-1}$ ].

Attempts were made to verify also the cross-detuning coefficient  $a_{yx} = a_{xy}$  from the same dataset. The strategy was to measure the vertical tune as a function of the horizontal kick strength. However, due to the cross talk introduced by linear coupling, it was difficult to identify the vertical tune from the data. The horizontal tune peak was more prominent in the frequency spectrum for the majority of the cases. Since MAD-X/PTC makes very accurate predictions on  $a_{xx}$ , we are relying on the model for the cancellation of the cross-detuning coefficient.

### 7.2.2 Nonlinear chromaticity

There are various techniques to determine the nonlinear chromaticity in a machine. One main method is based on changing the momentum deviation  $dp/p$  of the beam, for example through an rf modulation of the main rf frequency as introduced in Section 6.1. Alternatively, one can create a momentum deviation through a DC change of the main rf frequency. As a result of the frequency change, the beam receives an energy error which in turn leads to a radial change of the closed orbit (mostly horizontally) through dispersion, called radial steering. Ultimately this is observed as a change in the revolution frequency. Measuring the latter is hence a way to accurately determine the momentum deviation  $dp/p$ . By measuring the betatron tune for different settings of  $dp/p$  one can infer the chromaticity (linear and nonlinear terms) through a polynomial fit to the data. The maximum order of the nonlinear chromaticity terms that is accessible with this type of measurement is strongly dependent on the reach in  $dp/p$ . The tunes are determined by means of a SUSSIX frequency analysis and by taking the mean value of five consecutive shots in the SPS for each setting of  $dp/p$ .

Table 7.3: Nonlinear chromaticity measurement in the SPS for the bare machine in Q20 optics up to order four (compare Fig. 7.8).

Plane	$Q'$	$10^{-2} Q''$	$10^{-5} Q'''$	$10^{-7} Q^{(4)}$
Horizontal	$12.5 \pm 0.2$	$-7.1 \pm 0.6$	$-31.6 \pm 0.4$	$18.4 \pm 0.4$
Vertical	$1.6 \pm 0.1$	$22.5 \pm 0.5$	$26.3 \pm 0.3$	$-66.7 \pm 0.5$

Figure 7.8 displays an example measurement for the bare machine in Q20 optics with the octupole magnets switched off (again without degaussing them). The error bars on the tune measurement are smaller than the markers and are hence not visible in the plots. The results demonstrate that there are higher-order terms of chromaticity present in the machine. The values can be inferred from a polynomial fit to the data and are summarised in Table 7.3 up to the fourth order. For an accurate measurement of chromaticity, the reach in  $dp/p$  should be maximised. Here, we reached maximum

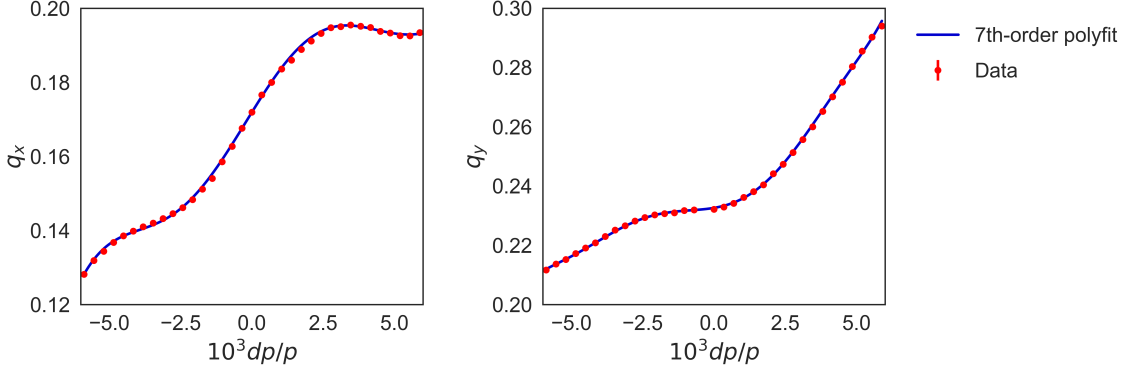


Figure 7.8: Measurement of horizontal (left) and vertical (right) tune vs. momentum deviation  $dp/p$  in the bare machine for Q20 optics. The error bars are smaller than the size of the markers. The numerical values of the polynomial fit (blue) to the data (red) are listed in Table 7.3 up to order four.

momentum deviations of  $\pm 6 \times 10^{-3}$ . This was possible by preparing a highly optimised, low intensity, low transverse emittance beam which can be steered radially to high amplitudes (up to about 19 mm) without causing strong losses from aperture limitations. Other parameters that need to be optimised to reach such high momentum deviations are the linear chromaticities in the two transverse planes. To avoid a collective instability triggered by a local negative slope of the tune vs.  $dp/p$  function for specific settings of the momentum deviation,  $Q'_{x,y}$  had to be set to a certain minimum value. This comes at the cost of a reduced precision in the tune measurement due to a broadening of the peaks and the excitation of synchrotron sidebands in the frequency spectra. This chromaticity measurement is valid only for the specific structure of the SPS supercycle used for the study. Naturally, it depends also on the settings of the sextupole knobs designed to control the first-order chromaticity.

Figure 7.8 demonstrates that there are many sources of higher-order chromaticity in the SPS. To accurately measure the contribution from each octupole family to  $Q''_x$ , given such a strong background, the following method was applied. For each octupole family two measurements of  $Q$  vs.  $dp/p$  were performed, one with positive  $k_{LO}^+$  and one with negative  $k_{LO}^-$  polarity with the same absolute strengths  $|k_{LO}^+| = |k_{LO}^-|$ . To make sure that the machine and beam conditions would remain identical, the measurements for the two polarities were always taken one directly after the other. By taking the difference between the two measurements one can determine the pure contribution from the specific octupole family to the nonlinear chromaticity, cancelling out all the other sources of chromaticity that may be present in the machine. Figures 7.9 to 7.11 summarise the measurements that were carried out for the three families. The change in the tune is shown as a function of momentum deviation. The plots on the left and right correspond to the measurements in the horizontal and vertical plane respectively. The data points (red) are fitted with a fourth-order polynomial (blue). Calculations from MAD-X/PTC are overlaid (dashed line). The main contribution from the octupole magnets, given that they are located in dispersive regions, is indeed a second-order chromaticity. This explains why the curves are predominantly parabolic. The numerical values are summarised in Table 7.4.

Concerning the measurements of the LOF and LOD families, the amount of second-order chromaticity is in good agreement with the predictions. The MAD-X/PTC model employed for comparison here does not include any misalignment errors or other imperfections. The  $Q''_x$  produced by the LOEs, on

the other hand, shows a large discrepancy of a factor four with respect to the model. This may be a result of the strong localised powering of the two magnets which can strongly enhance any local errors. However, due to the small contribution of the LOEs to  $Q_x''$  (since  $D_x \approx 0$ ), this discrepancy does not affect the performance of the  $Q_x''$  knob as discussed in more depth in Section 7.3 together with the effects of magnet misalignment errors. The contributions from the octupole magnets to the third-order chromaticity stem most likely from off-momentum beta-beating and/or second-order dispersion effects. They are not accurately predicted by the model. However, they are small enough as to not have a significant impact on the study.

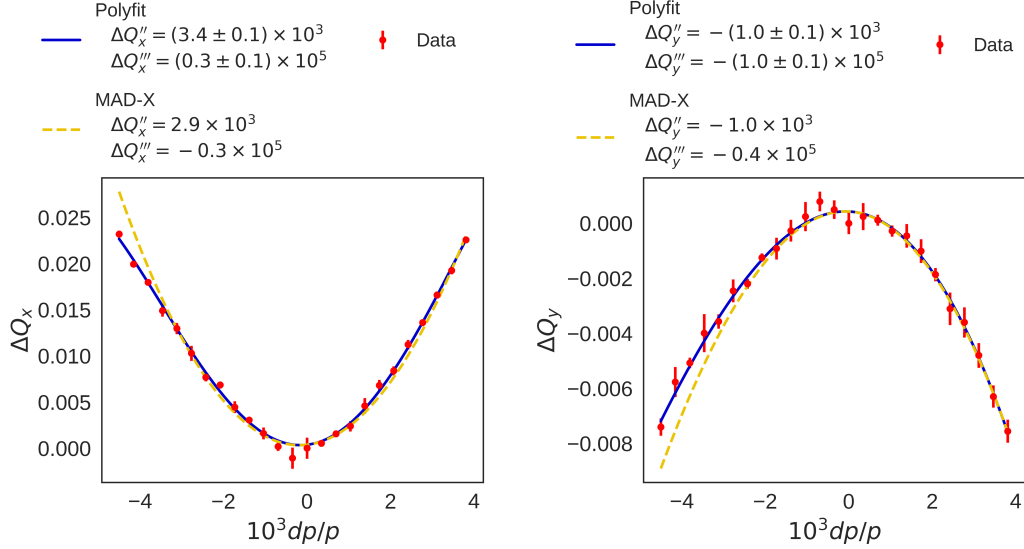


Figure 7.9: Contribution to the horizontal (left) and vertical (right) nonlinear chromaticity from the LOF family. Measurements (red), a fourth-order polynomial fit (blue), and MAD-X/PTC calculations (gold) are shown.

Table 7.4: Overview of the nonlinear chromaticity measurements (*meas.*) with SPS Q20 optics for the three different families of octupole magnets. Comparisons with MAD-X/PTC (*sim.*) are also listed.

Family	$k_{LO}^+$	$k_{LO}^-$	$10^{-3} Q_x''$		$10^{-5} Q_x'''$		$10^{-3} Q_y''$		$10^{-5} Q_y'''$	
			Meas.	Sim.	Meas.	Sim.	Meas.	Sim.	Meas.	Sim.
LOF	0.5	-0.5	$3.4 \pm 0.1$	2.9	$0.3 \pm 0.1$	-0.3	$-1.0 \pm 0.1$	-1.0	$-1.0 \pm 0.1$	-0.4
LOD	2.0	-2.0	$1.7 \pm 0.2$	1.6	$2.9 \pm 0.2$	-0.5	$-3.6 \pm 0.3$	-4.5	$-11.2 \pm 0.4$	0.9
LOE	20.0	-20.0	$1.2 \pm 0.1$	0.3	$-1.4 \pm 0.2$	0.5	$0.0 \pm 0.1$	-0.1	$-1.3 \pm 0.1$	-0.2

### 7.3 Beam stability studies

This section discusses measurements and PYHEADTAIL simulations that were performed to study single-bunch stabilisation in the SPS with Q20 optics employing the previously designed  $Q_x''$  knob. The first subsection contains all the experiments carried out in 2017. They include: (1) growth rate measurements for a head-tail mode zero as a function of  $Q_x'$  to validate the real component of the

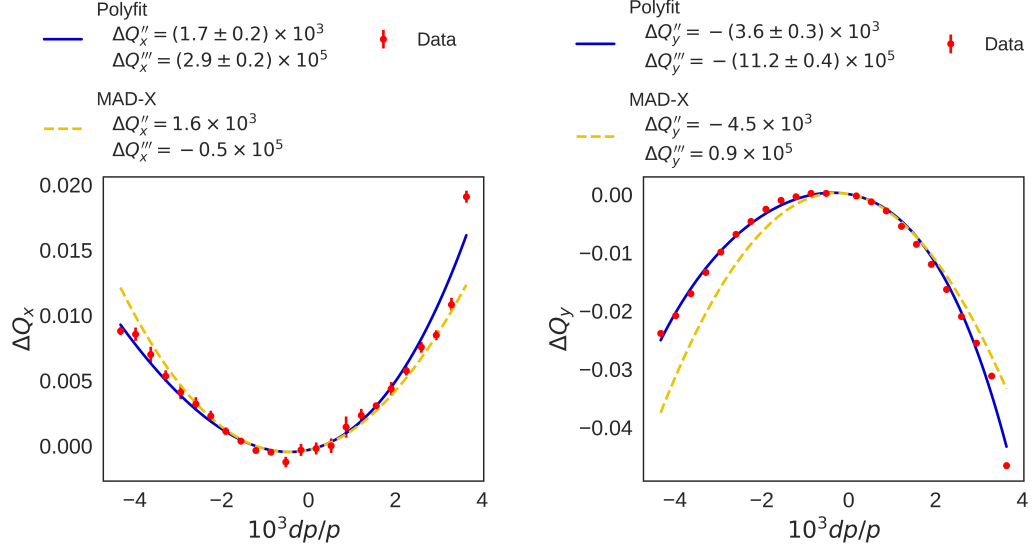


Figure 7.10: Contributions to the horizontal (left) and vertical (right) nonlinear chromaticity from the LOD family. Measurements (red), a fourth-order polynomial fit (blue), and MAD-X/PTC calculations (gold) are shown.

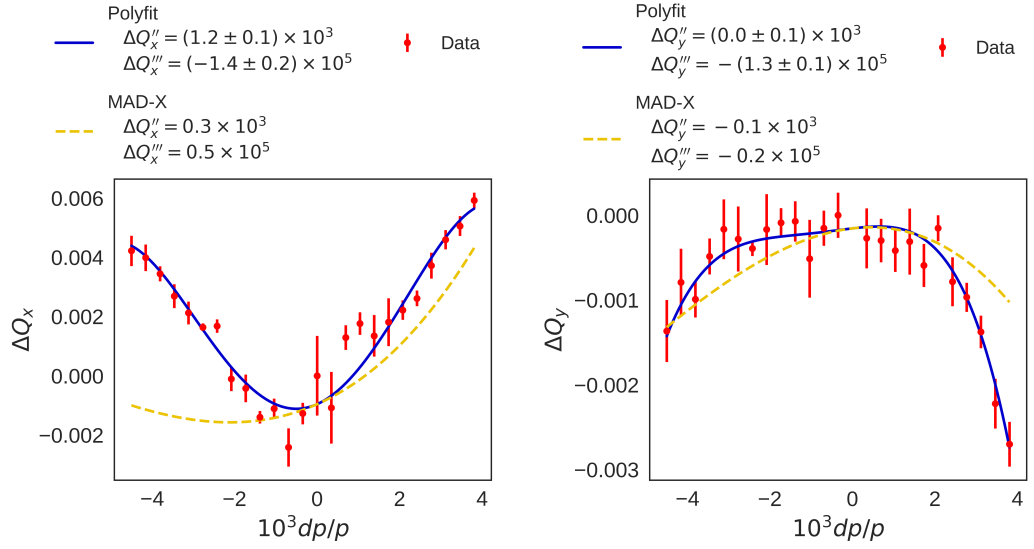


Figure 7.11: Contributions to the horizontal (left) and vertical (right) nonlinear chromaticity from the two LOEs. Measurements (red), a fourth-order polynomial fit (blue), and MAD-X/PTC calculations (gold) are shown.

horizontal dipolar impedance model of the machine; (2) the effect of the  $Q_x''$  knob on the instability growth rate for a head-tail mode zero (*main study*); and (3) a discussion of the observations made and comparisons against PYHEADTAIL simulations. The latter will reveal important quantitative and qualitative discrepancies between the model and the measurements. One possible explanation for



the observed differences is that the  $Q_x''$  knob introduces a strong first-order chromaticity from feed-down. This hypothesis will be studied with a detailed analysis of the data from all the available beam instrumentation and will eventually be confirmed with additional experiments made in 2018.

### 7.3.1 Measurements in 2017

#### Validation of the SPS impedance model

Detailed validation campaigns with single-bunch beams have already been made in previous years demonstrating a good accuracy of the dipolar and quadrupolar impedance models of the SPS (see, e.g., Refs. [63, 108, 109]). Among others, it was shown from beam-based measurements that: (1) the model accounts for more than 90 % of the actual *vertical* machine impedance in both the imaginary (real coherent tune shift with intensity) and real (growth rates vs. first-order chromaticity) components; and (2) the imaginary component of the *horizontal* impedance accurately reproduces the measured tune shift with intensity. No reports on recent benchmarks of the real component of the horizontal impedance model were available at this stage, however. The latest published report dates back to 2001 where both the horizontal and vertical growth rates were assessed for different first-order chromaticities [110]. As a first step towards the stability tests with a  $Q_x''$  knob, the objective was hence to study the growth rates of the head-tail mode zero instability as a function of  $Q_x' < 0$  to fill in the missing benchmark. The measurements as well as the simulations were performed using the beam and machine parameters listed in Table 7.1. The values of nonlinear chromaticity were taken from the polynomial fit in Fig. 7.8 (Table 7.3) and the detuning with transverse amplitude  $\bar{a}_{xx,0}$  in the bare machine from the average of the three measurements given in Eq. (7.3).

The comparison of the experimental data with PYHEADTAIL simulations is shown in Fig. 7.12. The measurements are represented by the red markers and correspond to the average growth rates obtained from exponential fits to the horizontal bunch centroid data of five to ten individual shots per  $Q_x'$  set point. The error bars are computed from the error of the mean in each dataset. An automatic fitting algorithm was used, but the results were also cross-checked manually to validate the quality of the

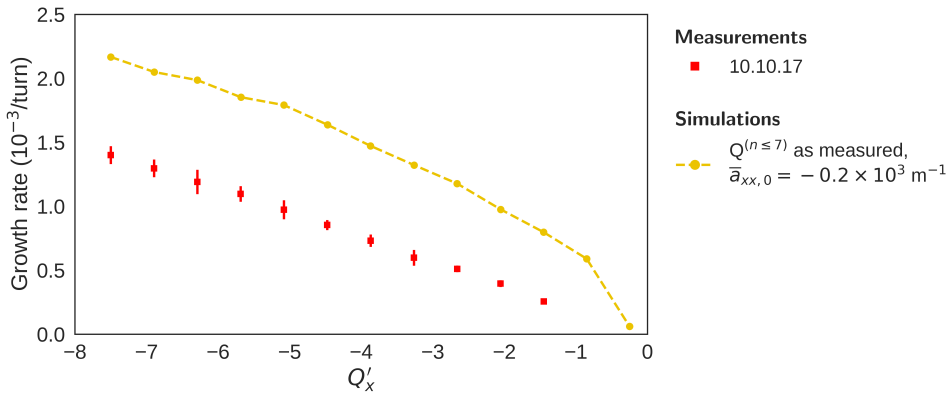


Figure 7.12: Measurements (red) vs. PYHEADTAIL simulations (gold) of the instability growth rate of a head-tail mode zero in the SPS as a function of  $Q_x'$  including measured values of nonlinear chromaticity up to order three and  $a_{xx,0}$  from Eq. (7.3). Other beam and machine parameters used are listed in Table 7.1.

fits. The PYHEADTAIL model includes the full wakefield of the SPS with dipolar and quadrupolar contributions. Qualitatively, the simulations are in agreement with the experimental data as they reproduce the trend of the curve. They predict, however, faster instability growth rates than what is actually observed in the machine. The discrepancy lies between a factor 1.6 at  $Q'_x = -7.5$  and a factor three at  $Q'_x = -1.5$ . This could be due to various reasons of which the following should be considered a priori: (1) a systematic error in the measurement of  $Q'_x$ ; (2) a missing stabilising mechanism in the simulation model, e.g. additional Landau damping from detuning with transverse or longitudinal amplitude, space charge, etc.; (3) inappropriate modelling of the longitudinal bunch distribution (or bunch spectrum); and (4) an overestimation of the real component of the horizontal dipolar impedance model.

It is unlikely that explanation (1) is the main reason for the observed discrepancies. While at  $Q'_x = -1.5$ , a systematic shift in the first-order chromaticity measurement of one unit could, in principle, explain the difference between the experimental data and the model, at  $Q'_x = -7.5$  the error would have to be larger than three units. The statistical uncertainty in the  $Q'_x$  measurement used for the calibration of the main LSA sextupole knob QPH was found to be  $\pm 0.2$  (see Table 7.3). Furthermore, the linear dependence of  $Q'_x$

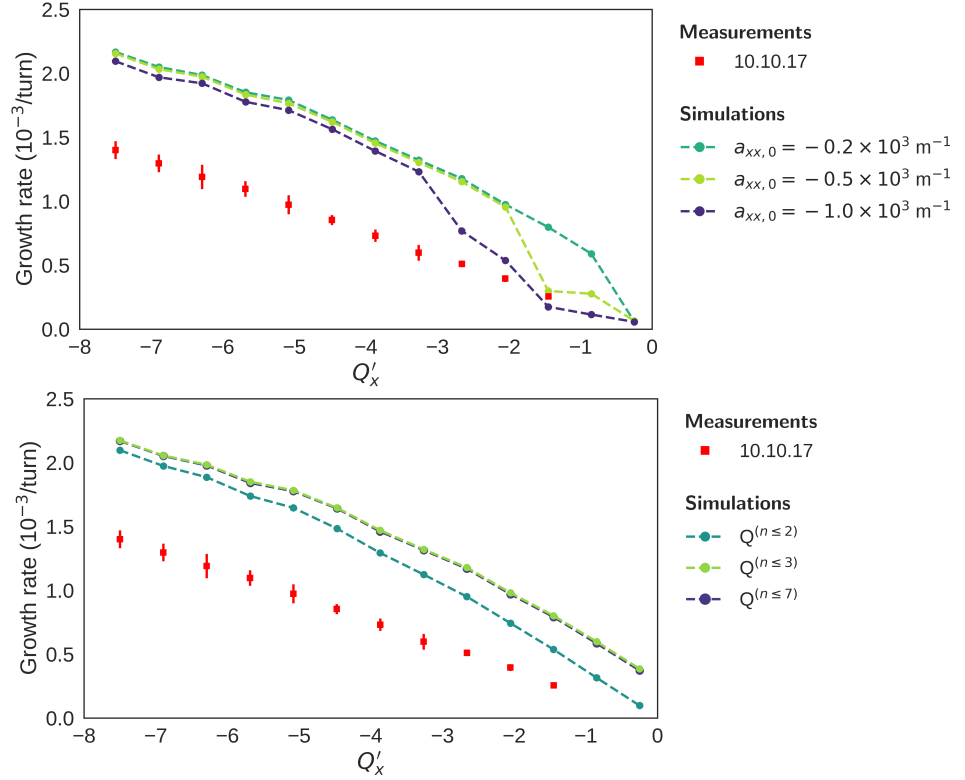


Figure 7.13: Measurements vs. PYHEADTAIL simulations of the head-tail mode zero instability growth rates as a function of  $Q'_x$  to validate the real component of the horizontal SPS impedance model. Various simulation scenarios are shown. *Top:* Effect of the bare horizontal detuning coefficient  $a_{xx,0}$  on the instability growth rates. *Bottom:* Dependence of the growth rate on various orders of nonlinear chromaticity included in the model.

on QPH in absence of magnetic octupoles was also confirmed by measurements in 2018 (see Fig. 7.21, green data samples). A systematic error in the measurement of  $Q'_x$  can hence be excluded as the main reason for the observed discrepancies. To study option (2), additional PYHEADTAIL simulations were performed including different nonlinear orders of chromaticity and different values for the transverse amplitude detuning coefficient  $a_{xx,0}$  in the bare machine. The outcome of these simulations is summarised in Fig. 7.13. The upper and lower plots show simulation scenarios respectively for different amounts of  $a_{xx,0}$  and including various orders of nonlinear chromaticity in the model. The upper plot indicates that even a large absolute value of the transverse amplitude detuning coefficient would not explain the differences on the full range of the  $Q'_x$  scan. While it may bring the model and the data into agreement for  $Q'_x$  close to zero, it practically has no impact on the growth rates for  $Q'_x < -3$ . Although a stronger transverse amplitude detuning could be introduced to remove the discrepancy in the growth rates for  $Q'_x \in [-8, -6]$ , for example, this would lead to a full stabilisation of the head-tail mode for the values of  $Q'_x$  closer to zero and hence again would not provide agreement over the full range of  $Q'_x$ . In addition,  $a_{xx}$  has been measured accurately and consistently as reported in Section 7.2. It is hence unlikely that transverse amplitude detuning is the missing factor in the model. The lower plot illustrates that the nonlinear chromaticities of order larger than three do not significantly contribute to the growth rates of the instability under study here either. The third-order chromaticity, on the other hand, could have an impact on the growth rates over the full range of  $Q'_x$  shown here. By consequence, an error in the measurement of  $Q'''_x$  could explain, to some extent, the differences between the model and the measurement. However, again it cannot be the only reason for the observed discrepancy. The effect of space charge may have to be assessed in dedicated studies in the future. Here, the idea was to limit its impact on the study by using a very low intensity beam of only  $2 \times 10^{10}$  p. The stabilising effect from the remaining amplitude detuning was also reduced by using small transverse emittance beams. One should also keep in mind that these stabilising mechanisms would also be present in the vertical plane where the agreement between simulation and experiment is better than 90%. Finally, concerning points (3) and (4), an overestimation of the real component of the horizontal impedance and/or an inaccurate representation of the actual bunch distribution in the model may explain part of the discrepancy. To clarify whether these are the actual reasons, however, more studies will be performed by the impedance group at CERN in the future. Again, if the effects of point (3) were present, they would also be observed in the vertical plane where the agreement between simulations and experiment is very good.

For the following beam stability study with the  $Q''_x$  knob, the model makes predictions that are accurate enough in terms of the instability growth rates and the discrepancy observed here is thus not a show-stopper. This is true, in particular, when making qualitative statements about beam stabilisation with  $Q''_x$ .

#### Beam stabilisation with the $Q''_x$ knob

The goal of the scan in  $Q''_x$  is to demonstrate the stabilisation of a slow head-tail mode purely from detuning with longitudinal amplitude. The study is performed for an azimuthal mode zero excited by introducing a small, negative, first-order chromaticity of  $Q'_x \approx -2$ . The reason for performing the study for this type of instability are its reproducibility and clear signature. Besides, higher-order modes, expected from theoretical considerations for  $Q'_x > 0$  cannot be observed in the SPS when operating with low intensity single bunches only. At  $Q'_x \approx -2$ , the rise time of the head-tail mode zero is about  $2 \times 10^3$  turns corresponding to a growth rate of  $0.5 \times 10^{-3}$  1/turn as shown in Fig. 7.12. PYHEADTAIL

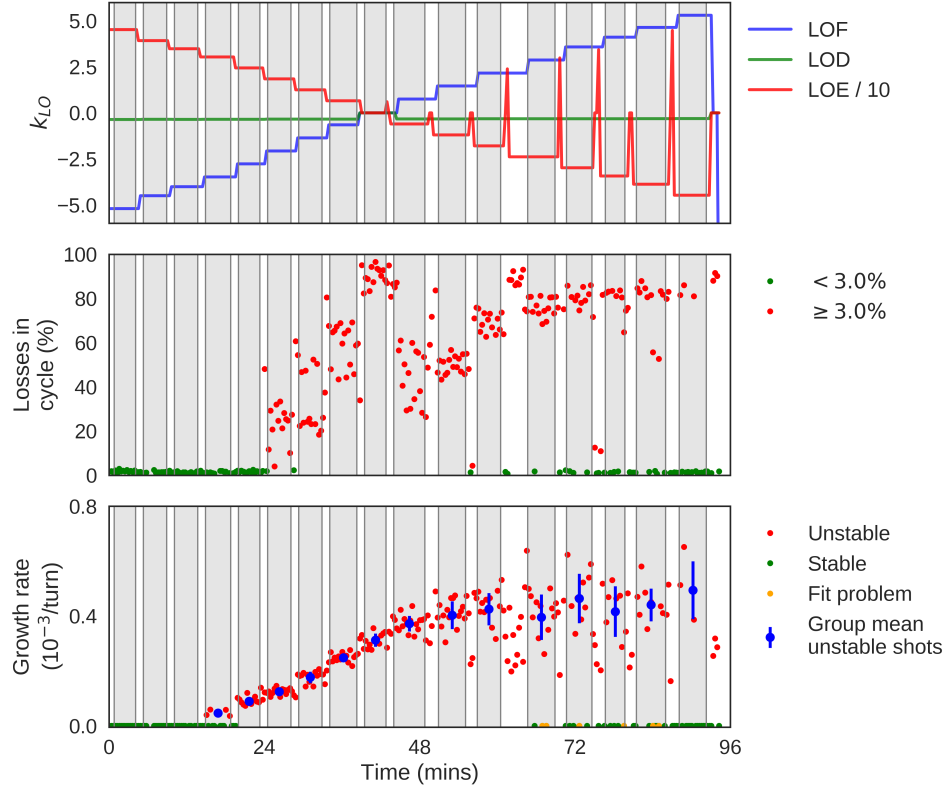


Figure 7.14: Overview of all the individual shots acquired during the beam stability study with the  $Q''_x$  knob. *Top*: LSA settings in the three octupole families over time. *Middle*: Particle losses observed over 3s of the machine development cycle. *Bottom*: Growth rate of the head-tail mode zero as obtained from exponential fits to bunch centroid data.

simulations indicate that an amount of about  $-3 \times 10^3$  units of second-order chromaticity would be enough to stabilise the head-tail mode under consideration, bearing in mind that the model predicts even faster growth rates than actually measured in the machine. This will be discussed below.

Figure 7.14 summarises the main observables acquired during the measurement period. The upper plot displays the LSA trim editor settings in the three octupole families employed to generate  $Q''_x$  while cancelling out the transverse amplitude detuning coefficients  $a_{xx}$  and  $a_{xy}$ . The first half of the measurement period corresponds to  $Q''_x < 0$  while the second half is for  $Q''_x > 0$ . The spikes in the LOE trims observed in the second half of the series are related to an LSA issue which did not allow negative values for  $k_{LOE}$ . This problem was bypassed by executing the trim directly on the current in the magnets. The specific values of current for a given  $k_{LOE} < 0$  were obtained by trimming first  $|k_{LOE}|$  and reading off the corresponding amount from the equipment state metre resulting in the observed spikes. The periods that include these spikes were excluded from the analysis. The plot in the middle shows the particle losses observed over 3s of the SPS cycle (total length of 3.6s) used during the machine study. The measured growth rates, obtained with an automatised procedure that performs exponential fits to the bunch centroid data, are given in the lower plot for each individual shot. Unstable and stable shots are marked red and green respectively. Whether or not a shot is classified as unstable depends on the

growth rate obtained from the exponential fit and on the observed amount of particle losses. In the event that the growth rate is larger than  $2 \times 10^{-5}$  1/turn (rise time  $< 5 \times 10^4$  turns) and that the losses over 3 s are  $\geq 3\%$ , a shot is classified as unstable. The few shots for which it was impossible to obtain a plausible exponential fit to the data are marked orange. The grey areas indicate periods of stable machine settings and each one corresponds to a specific setting of the  $Q''_x$  knob. About ten individual shots were acquired per setting. The blue markers denote the average growth rate and error of the mean for every group of shots taking into account only the unstable cases. At the same time, the SPS Head-Tail Monitor was set up to continuously acquire data. This was done to verify that the instability was indeed of mode zero throughout the measurement period. This is of particular importance as the nonlinear chromaticity can change the unstable mode as discussed in Chapters 4 and 6.

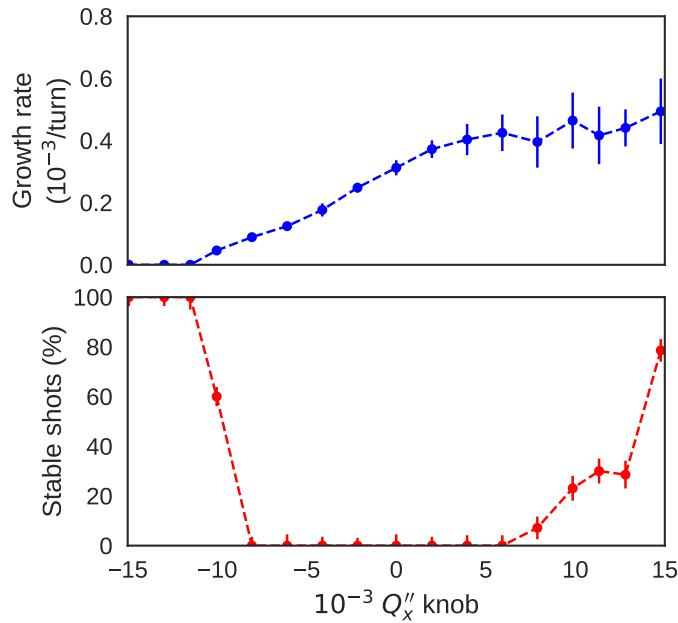


Figure 7.15: Summary plots of the beam stability study with the  $Q''_x$  knob. The growth rate of the head-tail mode zero (top) and the fraction of stable shots within each dataset (bottom) is shown as a function of the amount of  $Q''_x$  expected from the knob.

Figure 7.15 summarises the results in a more illustrative manner. The upper and lower plots show the growth rate of the head-tail mode zero and the fraction of stable shots within every sample as a function of the  $Q''_x$  knob. For increasing absolute values of  $Q''_x < 0$  the growth rate becomes slower and the instability is eventually suppressed at about  $-10^4$  units of the knob. This is confirmed by the fraction of stable shots in the lower plot which indeed reaches 100% for  $Q''_x < -1.1 \times 10^4$ . On the other hand, for  $Q''_x > 0$  the growth rate of the instability becomes faster, roughly linearly with increasing knob strength. In addition, the variation in the growth rate within each dataset becomes much larger as indicated by the error bars. This can be seen more clearly in the bottom plot of Fig. 7.14 and will be addressed in the following. Simultaneously with the increase in the growth rate, the fraction of stable shots in the acquired datasets increases as illustrated in the lower plot. This is counter-intuitive: for  $Q''_x > 0$ , more and more shots are classified as stable, but at the same time those which are unstable exhibit faster and faster growth rates. An attempt to explain this phenomenon will be made in the

following paragraphs. It is worth mentioning already here that according to the PYHEADTAIL model, a reduction of the growth rate, and eventually beam stabilisation, is expected for both positive and negative  $Q''_x$ . This issue is also addressed in the following.

### **$Q'$ feed-down hypothesis**

As explained above, the observed impact on the growth rate from the  $Q''_x$  knob does not agree with tracking simulations, not even qualitatively. In the following, we will evaluate whether the observations could instead be explained by a change in the *first-order* chromaticity introduced by the knob (in addition to  $Q''_x$ ). The source of a change in  $Q'_x$  could be feed-down induced by the closed orbit offsets at the three octupole families that are powered to generate  $Q''_x$ . This was discussed already in Section 2.1.1: a beam passing through an octupole magnet with a transverse closed orbit offset experiences, among others, an additional sextupole kick which translates into a change in chromaticity, denoted  $\Delta Q'_x$  in the following.

As illustrated in Fig. 7.12, the growth rate of the head-tail mode zero is reduced when moving closer to  $Q'_x = 0$ . And, although not shown in the figure, for positive  $Q'_x$ , single bunches are stable in the SPS, and higher-order modes cannot be observed either. On the other hand, when moving to more negative values of  $Q'_x$ , the head-tail mode zero exhibits faster growth rates. The latter is consistent with theoretical predictions [25]. Let us assume now that for negative values of the  $Q''_x$  knob, the first-order chromaticity actually increases ( $\Delta Q'_x > 0$ ) due to the feed-down mechanism described above. In that scenario, the stabilisation of the head-tail mode observed in Fig. 7.15 for negative values of the  $Q''_x$  knob could be explained simply by the fact that the effective first-order chromaticity, which is given by  $Q'_{x,\text{eff}} = Q'_{x,0} + \Delta Q'_x$  has become positive. Since the experiment was performed at an initial value of  $Q'_{x,0} = -2$ , beam stability would be observed as soon as  $\Delta Q'_x$  grows larger than 2 units. In that scenario, assuming a closed orbit distortion that remains constant over time, positive values of the  $Q''_x$  knob would produce negative  $Q'_x$  feed-down. This would result in faster growth rates which is again consistent with the observations made. It is worth noting that the sign of  $\Delta Q'_x$  depends on the applied global correction of the closed orbit when setting up the machine and the beam at the beginning of the study. There is no unique solution for this global correction, meaning that locally, i.e. at the octupole magnets, the closed orbit distortion could be positive or negative every time the orbit is optimised. The local distortion determines the sign of  $\Delta Q'_x$  as a function of the  $Q''_x$  knob.

The effect of a  $Q''_x$  knob introducing a chromatic feed-down can be illustrated qualitatively by means of PYHEADTAIL simulations. This is achieved by performing a 2D scan with  $\Delta Q'_x$  (feed-down) and  $Q''_x$  being the scan parameters.  $Q'_{x,0}$  was set to  $-2$  units. Such a study allows to analyse  $Q''_x$  knobs with “arbitrary”  $Q'_x$  feed-down effects. Figure 7.16 summarises the outcome of the simulation campaign. The upper plot displays the growth rate as a function of  $Q''_x$  and  $\Delta Q'_x$  from feed-down. Two specific lines are chosen that can be interpreted as two different realisations of a  $Q''_x$  knob. The green dashed line corresponds to a “perfect” knob, free from chromatic feed-down, while the blue one represents a knob that also introduces  $Q'_x$  with  $\Delta Q'_x = 11$  units over the full range of the knob. The growth rates of the instability for the two cases are displayed in the lower plot. A knob that introduces no feed-down effects would eventually lead to beam stability. Although not visible in the plot for  $Q''_x > 0$ , both positive and negative settings of the knob will eventually stabilise the beams. The asymmetry between  $Q''_x > 0$  and  $Q''_x < 0$  has already been explained in Chapter 4. On the other hand, the blue line, where the amount of  $Q'_x$  feed-down is significant, shows a dependence of the growth rate that matches qualitatively the experimental observations: negative values of the  $Q''_x$  knob lead to stabilisation, mostly due to

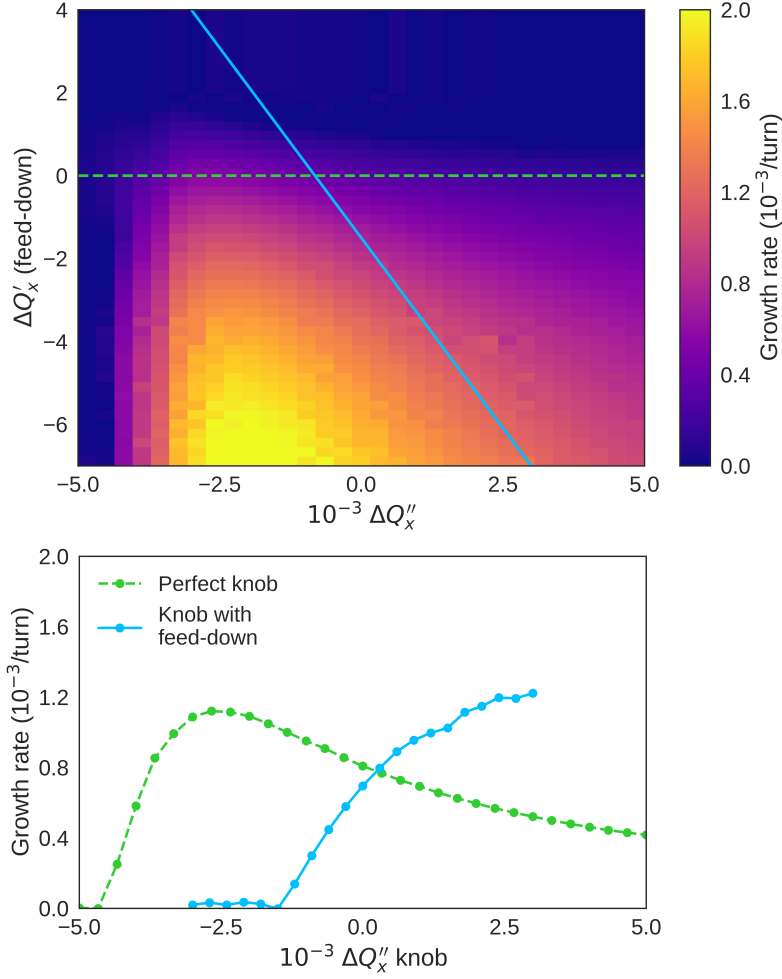


Figure 7.16: PYHEADTAIL simulations illustrating the effect of a  $Q''_x$  knob on the instability growth rates of a head-tail mode zero with (blue) and without (green)  $Q'_x$  feed-down. *Top*: 2D scan of  $Q''_x$  vs.  $Q'_x$  and the effect on the instability growth rates. Two cuts through the plane are chosen – one mimicking a perfect knob (green, dashed) without feed-down, and one that introduces a significant amount of  $Q'_x$  (blue, solid). *Bottom*: Cuts along the two realisations of  $Q''_x$  knobs showing the difference in their effects on the instability growth rate.

feed-down  $\Delta Q'_x > 0$ , while positive values lead to an increase in the growth rate due to  $\Delta Q'_x < 0$ . This study hence supports the hypothesis of  $Q'_x$  feed-down introduced by the knob described above.

To back up the hypothesis further we can determine the average horizontal closed orbit displacements  $\Delta x_{\text{CO}}^{\text{LOF}}$ ,  $\Delta x_{\text{CO}}^{\text{LOD}}$ , and  $\Delta x_{\text{CO}}^{\text{LOE}}$  at the three octupole families on a per-shot basis using continuously acquired orbit data during the scan presented in Fig. 7.14. One example measurement of the horizontal orbit is displayed in Fig. 7.17 for the full circumference of the SPS (116 BPMs). The measured orbit displacements can then be used in a MAD-X/PTC model to misalign the three octupole families accordingly (equivalent to an inverse orbit displacement), which allows to compute, among others, the chromatic feed-down for each individual shot. In doing so, it is possible to verify the hypothesis made

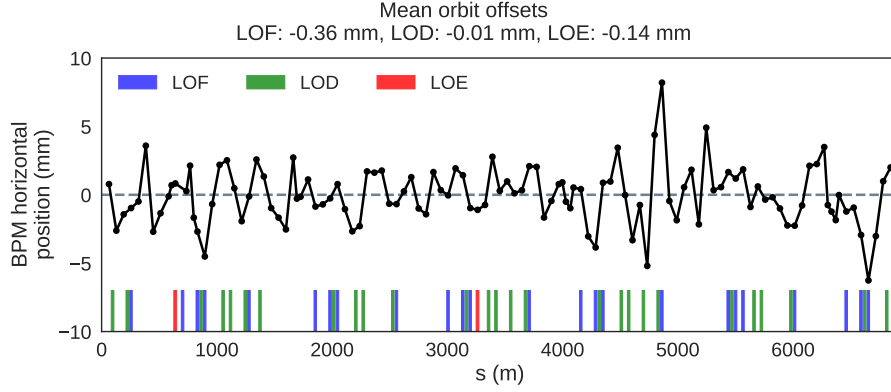


Figure 7.17: Example measurement of the horizontal closed orbit in the SPS acquired during the  $Q_x''$  scan over the full circumference of the machine. The locations of the octupole magnets are indicated by the coloured bars.

above. Figure 7.18 summarises the results. The two upper plots are taken from Fig. 7.14 and depict the LSA settings for the three octupole families over the measurement period and the instability growth rates for every shot respectively. The feed-down  $\Delta Q_x'$  obtained from orbit data in combination with MAD-X/PTC calculations is given in the plot at the bottom. Again, the red, green, and orange markers correspond to unstable, stable, and “undefined” shots respectively. The gaps in the feed-down data are due to missing orbit acquisitions or because of too many faulty BPMs in a given acquisition.

The data demonstrate that there is indeed a change of first-order chromaticity when varying the  $Q_x''$  knob. The trend of the curve is such that negative values of the knob introduce positive  $\Delta Q_x'$ , consistent with the assumptions made above based on the experimentally measured instability growth rates. The dependence of  $\Delta Q_x'$  on the strength of the knob is approximately linear. This is expected assuming that the local closed orbit distortions at the octupole magnets stay the same over time. It can be seen, furthermore, that in the second half of the acquisition period, where  $Q_x'' > 0$ , there is a shot-by-shot variation of the  $Q_x'$  feed-down which originates from orbit variations. From about minute 60 onwards, there are two separate branches of  $\Delta Q_x'$  that emerge, one with a roughly constant  $\Delta Q_x'$  of approximately  $-1$  unit and one that reaches a  $\Delta Q_x'$  of almost  $-3$ . It is conspicuous that there is not a single stable shot on the lower branch of  $\Delta Q_x'$  while most of the shots on the upper branch are found to be stable. While the source of this suddenly appearing variation in the closed orbit and in  $\Delta Q_x'$  is unclear, the shot-by-shot orbit variation is a likely explanation for the inconsistency that was observed in Fig. 7.15 concerning the increase of the fraction of stable shots vs. the faster and faster growth rates for  $Q_x'' > 0$ .

Unfortunately, this data can only be used to make a qualitative statement since the SPS orbit BPMs are not accurately calibrated and not available at the locations of all the individual octupole magnets (corresponding orbit excursions at specific locations were obtained through linear interpolation). Furthermore, the calculations with MAD-X/PTC are idealised and hence may contain systematic uncertainties. The change in first-order chromaticity of about three to four units over the full range of the knob measured here is much smaller than assumed in the PYHEADTAIL study shown in Fig. 7.16. The objective was hence to perform additional measurements with the  $Q_x''$  knob in order to confirm that it indeed introduces an important  $Q_x'$  feed-down and to quantify the latter more accurately.



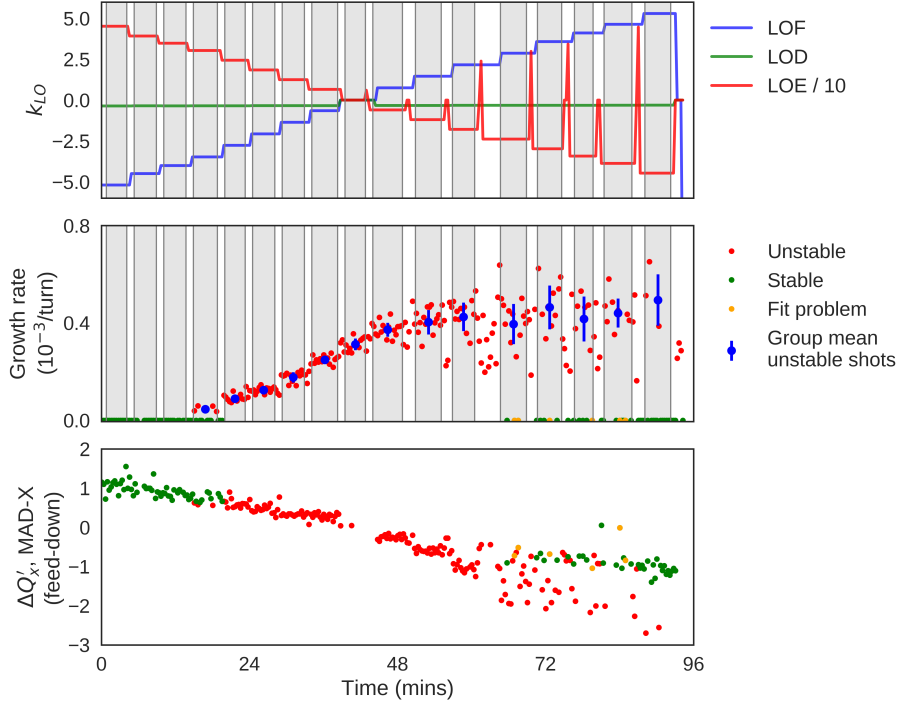


Figure 7.18: Overview of  $Q'_x$  feed-down calculated with MAD-X/PTC from SPS orbit data acquired during the scan with the  $Q''_x$  knob. *Top*: LSA settings for the three octupole families. *Middle*: Growth rate of the instability as obtained from exponential fits to bunch centroid data. *Bottom*: Feed-down calculated with MAD-X/PTC for each individual shot.

### 7.3.2 Measurements in 2018

To make a definite statement about the  $Q'_x$  feed-down introduced by the  $Q''_x$  knob, dedicated chromaticity measurements were taken in 2018. As discussed in the previous section, one issue that was observed in 2017 is the shot-by-shot variation of the closed orbit that would introduce a shot-by-shot variation of the feed-down. For that reason, a measurement method for chromaticity was used based on a fast modulation of the rf frequency, similarly to the technique employed in the LHC in Chapter 6. This method allows to measure chromaticity on a per-shot basis instead of over a one-hour period as it is the case with the DC variation of  $dp/p$ . It is clear that the feed-down can be different every time a global or local correction of the closed orbit is applied in the machine. Hence, the amount, or even the sign, of chromatic feed-down as a function of the  $Q''_x$  knob is expected to be different in 2018 compared to 2017. The measurements discussed in the following were performed all at once with identical orbit corrector settings to rule out inconsistencies.

#### Measurement of chromatic feed-down from the $Q''_x$ knob

The shot-by-shot measurement of chromaticity as a function of the  $Q''_x$  knob is displayed in Fig. 7.19. The upper plot again shows the settings in the three octupole families over the measurement period. The two lower plots contain the first- and second-order chromaticities measured for every shot respectively (red). The blue markers correspond to the mean value for every group of shots acquired for fixed

machine settings (grey area). The individual measurements demonstrate that occasionally there are variations from one shot to another. However, for the most part, the measured chromaticity is stable for a given strength of the knob. Most importantly, the  $Q'_x$  data clearly confirm that the  $Q''_x$  knob introduces significant chromatic feed-down. Despite the fact that the main sextupole strengths were kept the same throughout the measurement period, the first-order chromaticity changed by about 7 units over the full range of the knob, entirely due to feed-down from the octupole magnets. As explained above, the amount of feed-down depends on the closed orbit correction performed at the beginning of the measurement and hence varies between machine development sessions. This becomes clear when comparing Figs. 7.18 and 7.19. The data acquired in 2018 indicate that  $\Delta Q'_x$  is positive for positive values of the  $Q''_x$  knob while the situation was opposite in 2017. This is a result of the local orbit distortions at the octupole magnets. It is also possible that for the same global quality of the closed orbit correction that the feed-down is stronger in one case compared to another. Considering that a variation of  $\Delta Q'_x = 7$  was measured over the full range of the knob demonstrates that the 11 units assumed for the PYHEADTAIL simulations in Fig. 7.16 are in fact plausible. The lower plot in Fig. 7.19 illustrates the dependence of  $Q''_x$  on the knob. For a given setting, the measured second-order chromaticity is stable and follows the correct trend.

Figure 7.20 provides a clearer view of the measurements from Fig. 7.19. It displays, respectively, the  $Q'_x$  from feed-down (top) and the measured amount of  $Q''_x$  (bottom) as a function of the knob. The blue dashed line indicates the values expected for a perfect knob. The plot illustrates again the

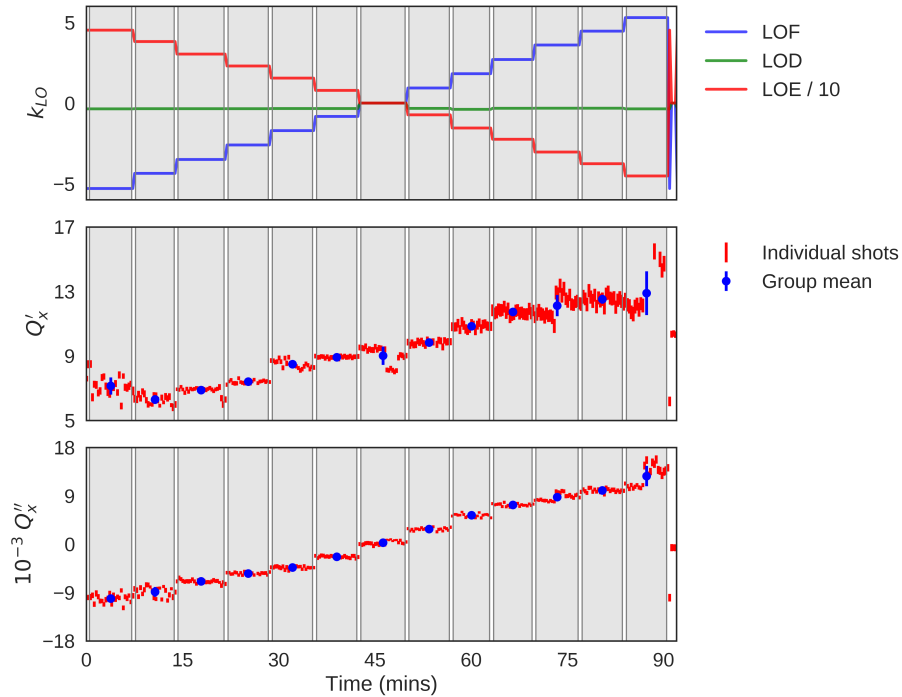


Figure 7.19: Overview of all the individual shots (red) acquired during the feed-down study with the  $Q''_x$  knob. *Top*: LSA settings of the three octupole families. *Middle*: Measured  $Q'_x$  on a per-shot basis. *Bottom*: Measured  $Q''_x$  on a per-shot basis. Blue markers represent mean values per data set (grey area).

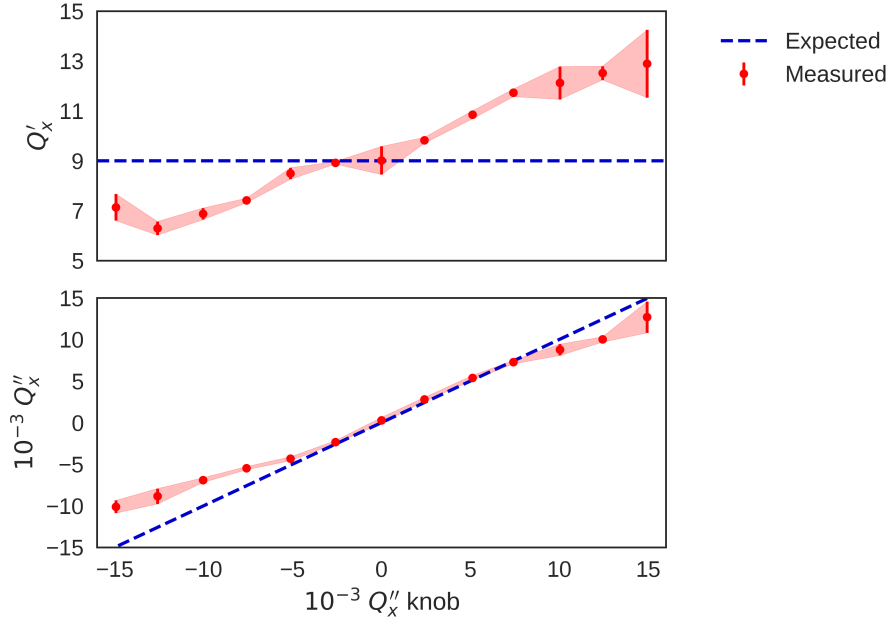


Figure 7.20: Summary plots of Fig. 7.19 showing respectively the measured  $Q'_x$  feed-down (top) and  $Q''_x$  (bottom) as a function of the  $Q''_x$  knob. The expected trends (dashed lines) are also given assuming a perfect knob.

importance of the feed-down. Furthermore, it demonstrates that the knob follows the expected amount of  $Q''_x$  well up to  $+10^4$  units and down to  $-5 \times 10^3$  units respectively. However, deviations of about  $5 \times 10^3$  units and  $2 \times 10^3$  units are measured at the two extreme values  $Q''_x = -1.5 \times 10^4$  and  $Q''_x = 1.5 \times 10^4$  respectively. Some of this discrepancy can be attributed to the measurement method. As the absolute amount of second-order chromaticity increases, the parabolic shape of the dependence of  $Q_x$  on  $dp/p$  becomes more pronounced. In that case, the range in  $dp/p$  is more and more limited due to coherent instabilities (head-tail mode zero) excited by the local negative slope of  $Q_x$  vs.  $dp/p$ . Furthermore, it will be demonstrated with additional data below that the amount of  $Q''_x$  for a fixed setting of the knob also depends significantly on the magnetic strength in the main sextupoles.

#### Attempt to correct chromatic feed-down from the $Q''_x$ knob

A correction of the closed orbit to zero at all the octupole magnets is unfortunately not feasible due to the limited number of orbit BPMs and corrector magnets. An alternative proposal was hence to measure  $Q'_x$  at each setting of the  $Q''_x$  knob and apply a correction to match again the target value (for instability studies:  $Q'_x = -2$ ), compensating for the feed-down introduced by the knob. However, it is not possible to accurately measure chromaticity with an unstable beam. This means that in order to calculate the amount of  $Q'_x$  feed-down, the chromaticity measurement would need to be performed at positive  $Q'_x$  where the beam is stable. The strategy was hence to: (1) bias  $Q'_x$  to a positive value by means of the main sextupole magnets (QPH knob) to stabilise the beam; (2) measure the chromaticity using the fast rf frequency modulation approach; and (3) correct  $Q'_x$  back to the target value accounting for both the feed-down and the bias that was artificially introduced in step (1).

To verify the method, measurements of  $Q'_x$  were taken as a function of the main sextupoles for three different settings of the  $Q''_x$  knob ( $-7.5 \times 10^3$ , 0, and  $+7.5 \times 10^3$  units). The results are summarised in Fig. 7.21. The measurements are given in absolute values in the upper plot and the dashed lines correspond to  $Q'_x$  expected purely from changing the sextupole knob (linear dependence). The reference values were chosen to match the measurement at QPH = 0.4. The curves are separated vertically due to the chromatic feed-down introduced by powering the octupole magnets when introducing  $Q''_x$ . The lower plot displays the deviation of the data with respect to the expectation for a more detailed view. For  $Q''_x \geq 0$ , the agreement with the expected value is good with deviations of about  $\pm 1$  unit in  $Q'_x$  at maximum. However, for  $Q''_x = -7.5 \times 10^3$  (red) the expected value is significantly off and the absolute deviation in the first-order chromaticity can be more than 2 units. This makes it difficult to apply the strategy presented above: when introducing the positive bias in  $Q'_x$  to make the beam stable to measure chromaticity, it is no longer possible to accurately compute the correction that needs to be applied to  $Q'_x$  to reach the target value in the machine. The difference between the expected value and the measurement most probably stems from dipole feed-down introduced by the main sextupoles. A dipole feed-down modifies the closed orbit which in turn affects the chromatic feed-down introduced by the octupole magnets.

While acquiring this set of data it became clear that the amount of  $Q''_x$  in the machine also depends on the QPH setting of the main sextupoles. Dedicated measurements are presented in Fig. 7.22, again in absolute and relative terms in the upper and lower plot respectively. The data indicate that  $Q''_x$  can vary by up to as much as  $4 \times 10^3$  units. Possibly, for even lower settings of QPH, which is where the machine would be operated to excite the head-tail mode zero, the deviation from the expected amount of  $Q''_x$

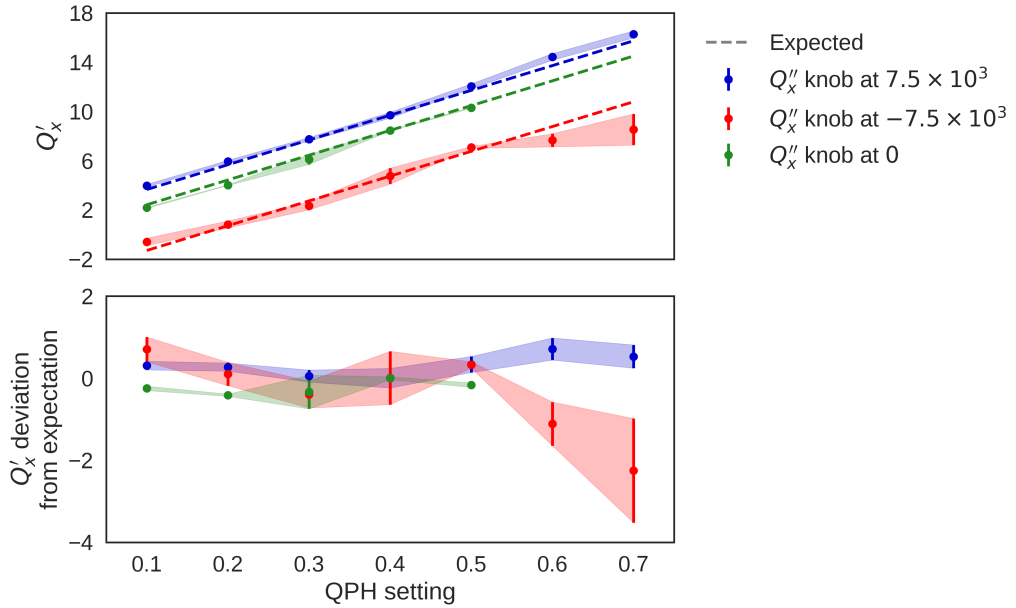


Figure 7.21: Dependence of first-order chromaticity on the main sextupole knob QPH employed to control  $Q'_x$  in the SPS for specific settings of the  $Q''_x$  knob. The plots show measurements in absolute terms (top) and their deviation from the expected value (bottom) respectively. The expected values use the measurement at QPH = 0.4 as a reference value.

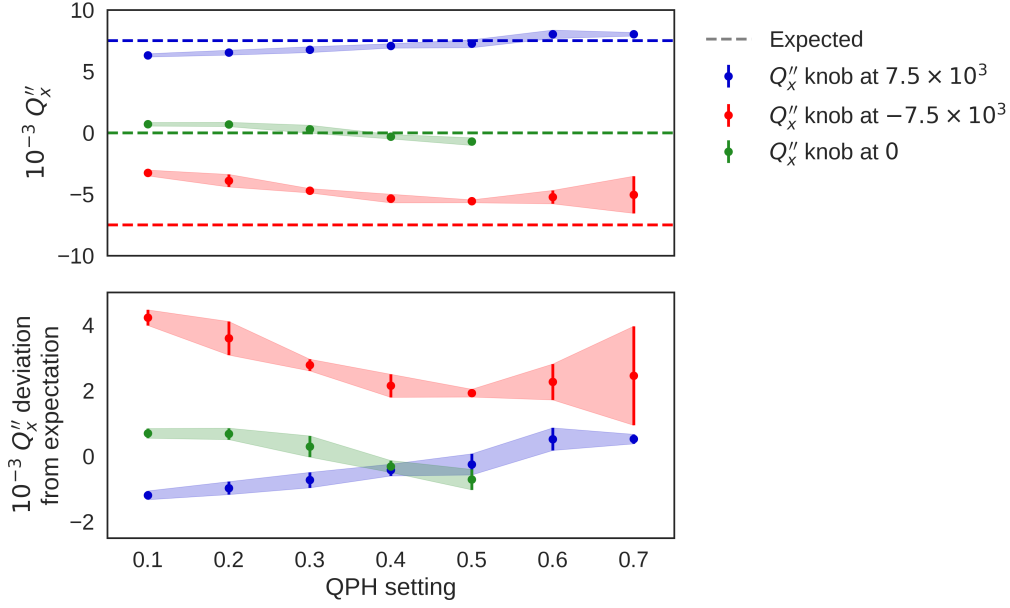


Figure 7.22: Dependence of second-order chromaticity on the main sextupole knob QPH employed to control  $Q'_x$  in the SPS for specific settings of the  $Q''_x$  knob. The plots show absolute measurements (top) and their deviation from the expected value (bottom) respectively.

grows even larger. This has actually been verified for the set point  $Q''_x = 7.5 \times 10^3$  where it was possible to perform a scan in QPH from 0.7 down to  $-0.7$  with the beam still stable thanks to the  $Q'_x$  feed-down. Indeed, at  $QPH = 0.7$ ,  $Q''_x \approx 8 \times 10^3$ , i.e. close to expectations, while at  $QPH = -0.7$ ,  $Q''_x \approx 3.3 \times 10^3$ .

To summarise, both the correction of  $Q'_x$  as well as an accurate measurement of  $Q''_x$  for each set point of the  $Q''_x$  knob cannot be easily achieved given the cross-dependencies of the knobs. The underlying source of the problem is a combination of feed-down effects from the main sextupoles (dipole feed-down) and from the octupoles (primarily sextupole feed-down).

## 7.4 Conclusions

The goal of this study was twofold. First, to design and validate a second-order chromaticity knob for the SPS that would be free of detuning with transverse amplitude, and second, to demonstrate the stabilising effect of  $Q''_x$  on a horizontal head-tail mode zero.

In the first part of the study, a  $Q''_x$  knob was engineered employing the three families of octupole magnets installed in the machine. One family was used to enhance  $Q''_x$  while the other two were powered to compensate the transverse amplitude detuning coefficients. By means of MAD-X/PTC calculations and detailed nonlinear optics measurements performed for each of the octupole families it was possible to validate the model. A good agreement was found for both chromaticity and amplitude detuning measurements demonstrating a thorough understanding of the nonlinear optics of the machine. In a second step, we attempted to use the  $Q''_x$  knob to stabilise a head-tail mode zero, excited by introducing a negative horizontal first-order chromaticity. Measurements of the instability growth rate vs.  $Q''_x$  did

not show the expected results, however: instead of a reduction in the growth rate as a function of  $Q_x''$  for both polarities, beam stabilisation was only observed for  $Q_x'' < 0$ , while faster and faster growth rates were observed for  $Q_x'' > 0$ , in contradiction to PYHEADTAIL simulations. It was suggested that the dependence of the growth rate on the strength of the knob could instead be explained by feed-down to  $Q_x'$ , introduced by closed orbit distortions at the locations of the octupole magnets. Assuming a stable closed orbit, the  $Q_x'$  feed-down from the knob would be proportional to its strength. The hypothesis was supported not only by PYHEADTAIL simulations, but also by a thorough analysis of the available closed orbit data combined with MAD-X/PTC. It was demonstrated that a  $Q_x''$  knob that introduces a strong feed-down to  $Q_x'$  would reproduce the experimental observations made, at least qualitatively.

Additional measurements performed in 2018 led to the final conclusion that indeed the experimental observations are explained predominantly by a  $Q_x'$  effect rather than Landau damping from detuning with longitudinal amplitude. This also includes the beam stabilisation that was found for negative strengths of the knob. The studies also demonstrated that a correction of the  $Q_x'$  feed-down is not straightforward, mainly because of a combination of feed-down effects introduced by the sextupole and octupole magnets (dipole and sextupole feed-downs respectively).

The bottom line is that the SPS is not a well-suited environment for the intended study. This result did not come unexpectedly given the complexity of the setup. By consequence, the measurement carried out with second-order chromaticity in the LHC and reported in Chapter 6 remains, to date, the only proof-of-principle experiment that demonstrates Landau damping of slow head-tail modes from detuning with longitudinal amplitude.

## 8 Conclusions

The performance reach of present and future hadron colliders depends to a great extent on the available active and passive transverse instability mitigation tools that are employed, for example, against impedance-driven head-tail modes. Landau damping in the transverse planes, introduced through a betatron frequency spread among the beam particles, is a powerful cure for various types of instabilities. The damping efficiency of the Landau octupoles, used for that purpose to date, depends heavily on the transverse geometric emittances of the beams. In future colliders, such as the Future Circular hadron Collider (FCC-hh), the large increase in the beam energy will result in a significant reduction of the transverse geometric emittances due to adiabatic damping. Additionally, the FCC project aims at increasing the luminosity output by actively decreasing the transverse emittances further (higher brightness beams). Considering that this results in a strong reduction of the damping efficiency of the Landau octupoles, potential alternative mitigation tools have to be developed to guarantee transverse beam stability in future machines.

This PhD thesis set out to study one possible novel approach to Landau damping in the transverse planes. The innovative idea of the method is to introduce the required betatron frequency spread through a dependence on the longitudinal instead of the transverse oscillation amplitudes of the particles. At collision energy, for example, the longitudinal emittances of the FCC-hh beams are up to six orders of magnitude larger than the transverse ones which is one of the main reasons why Landau damping from betatron detuning with longitudinal amplitude has become an attractive alternative technique to the traditional approach employing magnetic octupoles. Two possible schemes to generate the betatron frequency spread have been evaluated in parallel within the scope of this project: an rf quadrupole cavity and nonlinear chromaticity. They were both analysed from the points-of-view of theory, numerical simulations, and experiments, and consistent results were obtained from all three perspectives. The main achievements of the research carried out include: (1) the development of the analytical foundation of the novel longitudinal-to-transverse Landau damping method within the Vlasov formalism, including the successful validation of the new theory against two different accelerator physics models; (2) extensive simulation studies with the rf quadrupole to: provide a first numerical proof-of-principle of its stabilising effect, develop a more advanced two-family scheme that further enhances its overall damping performance, evaluate the requirements of an rf quadrupole system for various FCC-hh operational scenarios, and reveal the main features and potential drawbacks of the device; and (3) an experimental demonstration of the Landau damping effect on single bunches in the

LHC achieved by enhancing the second-order chromaticity, which also showed a good agreement of the measurements with predictions from the newly developed theory (qualitative) and from particle tracking simulations including single- and multi-particle dynamics models (quantitative). A more detailed discussion of the results obtained for each of the three abovementioned topics is given below.

Chapter 3 introduced the basic concepts of the novel Landau damping method, first explaining the working principle of an rf quadrupole cavity and comparing its performance to magnetic octupoles in terms of the size of the frequency spreads that can be generated. It was shown that for hadron colliders the rms frequency spread produced by magnetic octupoles typically decreases as  $1/\gamma^2$  while that from an rf quadrupole only decays with  $1/\gamma$ . The difference in the efficiencies between the two methods hence becomes more pronounced with increasing beam energy. Second, it was proven that the rf quadrupole and nonlinear chromaticity are equivalent ways to introduce the betatron frequency spread. In a first-order approximation, the betatron frequency shifts for both schemes purely depend on the longitudinal action. Other than the rf quadrupole, whose construction and test were not feasible within the timescale and budget of this thesis, nonlinear chromaticity can be enhanced and controlled in an accelerator without making any hardware changes, but by adjusting the optics of the machine. Proving the equivalence of the two detuning schemes was an essential step to pave the way for the validation of the numerical and analytical models with experimental studies later on in the project.

In Chapter 4 the Vlasov formalism was extended to correctly describe the beam dynamics in presence of nonlinear chromaticity. The derivation is based on the existing Vlasov theory for transverse instabilities with linear chromaticity. This was a major milestone of the project as it laid the analytical foundation for all the simulation and experimental studies that were carried out. It is also worth noting that even though the formalism was developed for nonlinear chromaticity, the lessons learned are equally valid for the rf quadrupole. The new theory was thoroughly benchmarked against a circulant matrix model and PYHEADTAIL particle tracking simulations showing an excellent agreement. The theory also revealed and unambiguously confirmed that detuning with longitudinal amplitude (1) indeed introduces Landau damping, and (2) modifies the head-tail instability mechanism by changing the effective impedance, similarly to the first-order chromaticity (head-tail phase). It was demonstrated that effect (1) can only be introduced by even orders of chromaticity, while (2) is present for both odd and even orders. The reason is that the frequency “spread” generated by odd orders of chromaticity vanishes over the synchrotron period and hence does not provide Landau damping of weak head-tail modes. The fact that there is an interplay between mechanisms (1) and (2) has important consequences. It greatly increases the complexity of the problem of making predictions on the beam stability with the new Landau damping approach. For example, effect (2) can render the beam more unstable, or lead to the excitation of different head-tail modes which is undesirable. The theory also shows that the impact of mechanism (2) on the beam dynamics depends entirely on the specific beam-coupling impedance of a machine. For this reason it is difficult to employ stability diagram theory which aims at making generic predictions that are valid for different machines independent of their impedance. While this is possible for Landau octupoles, it is no longer true for an rf quadrupole or nonlinear chromaticity and thus the concept of stability boundary diagrams is of limited use for the latter. Instead, particle tracking codes are the most accurate tools to determine the required rf quadrupole strengths or amounts of nonlinear chromaticity for a specific machine configuration. Stability diagrams can, however, still be used to make qualitative statements about the underlying stabilising mechanisms. For example, the strong asymmetry in the Landau damping efficiency between the two transverse planes observed with the stability diagrams is confirmed by tracking simulations.



---

Chapter 5 showed the first numerical proof for Landau damping from an rf quadrupole. It was based on a well-studied head-tail instability observed experimentally in the LHC and shown to be stabilised through Landau damping from magnetic octupoles with a good agreement between experiments, tracking simulations, and Landau octupole theory. For this particular case, an improved efficiency of a factor five in terms of active magnetic length was observed for the rf quadrupole compared to the LHC Landau octupoles. At the same time, the required rms frequency spread was about 50 % larger for the rf quadrupole which could potentially be a disadvantage when considering single-particle incoherent effects (dynamic aperture, beam lifetime). It is important to note that the ratio of the required rms frequency spreads between magnetic octupoles and rf quadrupoles is dependent on the given machine configuration and head-tail mode. This is a result of the difference in the stabilising mechanisms as illustrated by the theory developed in Chapter 4. The issue of the strong differences in the stabilising efficiencies between the two transverse planes, discovered through analytical considerations, was also addressed by means of PYHEADTAIL simulations. A two-family scheme was proposed to reduce the asymmetry. In this scheme, a “focusing” rf quadrupole family is installed at a location of high horizontal, low vertical beta function and a “defocusing” family is located in a region of high vertical and low horizontal beta function. It was confirmed that such a configuration could not only significantly improve the overall efficiency of the Landau damping from an rf quadrupole system, but also equalise the required cavity strengths to stabilise the beam in both planes. Based on the two-family scheme, the requirements for an rf quadrupole system for the FCC-hh were evaluated, both for injection and collision energies and for various likely operational scenarios. In the worst case scenario, 15 m of active length of rf quadrupoles would provide enough Landau damping to stabilise the FCC beams according to the PYHEADTAIL model, assuming a factor three margin in the current impedance model. In comparison, external references quote required magnetic lengths of up to 1.1 km when using octupole elements of the LHC octupole type [78]. These results illustrate the potential gain that could be achieved when using an rf quadrupole for Landau damping instead of octupole magnets and the results are indeed very promising in terms of the collective beam dynamics. The main possible drawbacks of the new technology were also identified and briefly discussed. They are mostly related to single-particle dynamics and will require further dedicated studies in the future. Among the potential downsides are resonances of the synchro-betatron type, possibly reduced dynamic aperture and beam lifetime due to the large betatron frequency spreads that are introduced, and rf dipole feed-down effects. The strong, localised kicks from rf quadrupoles facilitate the excitation of synchro-betatron resonances. On the other hand, it was shown that this type of resonance is less likely an issue as long as the betatron tunes are far away from the integer values and when the synchrotron tunes are low. The reason is that in this configuration, the resonances are of higher orders and hence only weakly excited by the device. The feed-down effects can be addressed using dipole correctors at the location of the rf quadrupole to ensure that the beam passes through the cavity centre. Dynamic aperture and beam lifetime, on the other hand, need to be analysed by means of dedicated single-particle simulations. In particular, the objective will be to compare the impact on the dynamic aperture from magnetic octupoles and an rf quadrupole system for the kick strengths required for beam stabilisation.

Chapter 6 discussed the experiments carried out in the LHC. The goal of the study was to introduce detuning with longitudinal amplitude to demonstrate in a proof-of-principle experiment its stabilising effect on single bunches. For this reason, a knob was designed in a first step in order to gain control over the second-order chromaticity in the machine. This was achieved by powering the main LHC sextupoles in a specific configuration. Independent and accurate control of the second-order chromaticity in both beams and both transverse planes was demonstrated by comparing MAD-X calculations with

results from measurements. In a second step, single bunches were accelerated to an energy of 6.5 TeV and attempted to be stabilised purely by using the second-order chromaticity knob. Two observations were made: (1) detuning with longitudinal amplitude indeed provided a significant stabilising effect which was reflected in the strongly reduced Landau octupole stability thresholds (from  $\approx 100$  A it could be lowered down to 0 A); and (2) a change of the most unstable head-tail mode was recorded when introducing nonlinear chromaticity. The two observations confirmed the analytical model which predicted both effects qualitatively. Furthermore, in PYHEADTAIL, both experimental observations were reproduced with the correct transition between the two different head-tail modes seen during the experiment. This confirmed that the involved single- and multi-particle dynamics are accurately modelled and well understood. Since second-order chromaticity could be successfully introduced without installing any additional hardware, the experiment also raised the question of whether the rf quadrupole or nonlinear chromaticity is a more suitable detuning scheme. The main advantage of the rf quadrupole is that it is an independent, dedicated device that is not limited by any other constraints. To enhance nonlinear chromaticity in an existing machine, however, optics constraints need to be taken into account which limits the performance reach of the knob. Furthermore, without dedicated magnets, the reach in the amount of nonlinear chromaticity may not be large enough to have a significant positive impact on the beam stability. For future machines where the lattice can be designed from scratch, the advantages of an rf quadrupole over nonlinear chromaticity are less obvious. For the FCC-hh, for example, a feasibility study would have to be conducted to determine whether a lattice configuration with additional dedicated sextupoles could provide the required degrees of freedom as well as the required amounts of nonlinear chromaticity to guarantee beam stability in all machine configurations.

Finally, Chapter 7 summarised the experimental studies performed in the SPS. The objective was the same as in the LHC experiment explained above. Again, a second-order chromaticity knob was designed, but this time employing octupole magnets rather than sextupoles. The main challenge was to make sure that the knob would be free of detuning with transverse amplitude to demonstrate the stabilising effect of detuning with longitudinal amplitude alone. It was shown in MAD-X calculations that this can in principle be achieved by powering the three independent families of octupole magnets in the SPS in a specific manner. To verify that this can indeed be realised in the actual machine, systematic nonlinear optics measurements were performed to characterise the three octupole families in terms of their contributions to the nonlinear chromaticity and to the amount of detuning with transverse amplitude. In general, comparisons with MAD-X predictions demonstrated a very good agreement with the measurements confirming the high accuracy of the SPS optics model. In particular, it was proven that the cancellation of detuning with transverse amplitude was indeed successful. The beam stability measurements performed in the second part of the study, on the other hand, did not produce the desired outcome. The instability growth rate of the excited head-tail mode zero measured as a function of the second-order chromaticity knob could not be explained by a pure second-order chromaticity dependence. Extensive analyses of all the available data from measurements performed in 2017, combined with PYHEADTAIL simulations, suggested instead that a large amount of first-order chromaticity had been introduced through feed-down effects at the octupole magnets which could explain the measured dependence of the instability growth rates. This hypothesis was eventually confirmed with further dedicated measurements acquired in 2018. The observed stabilisation of the head-tail mode zero was, after all, mainly a result of a change in first-order chromaticity. It was concluded that the SPS is not a well-suited environment for the planned study due to the large complexity of the setup employing different families of octupole magnets to generate nonlinear chromaticity and to cancel out

---

the detuning with transverse amplitude at the same time. The example of the SPS underlines that it can be complicated to design a nonlinear chromaticity knob in existing machines. This is mostly due to other, (possibly) undesired, optics effects entangled with the knob.

Overall, the research carried out within the framework of this PhD thesis has largely improved the understanding of the Landau damping mechanism in particle accelerators. In particular, the study provides a systematic analysis of the beam dynamics effects from detuning with longitudinal amplitude. It sheds light on the collective beam dynamics introduced by an rf quadrupole or nonlinear chromaticity and demonstrates a possible application of these techniques to the mitigation of weak head-tail instabilities. The project also serves as a solid starting point for additional studies in the future. Specifically, the single-particle dynamics needs to be evaluated to make another step towards the realisation of an rf quadrupole system for Landau damping.



# A Vlasov theory on nonlinear chromaticity

## A.1 Solution for an airbag beam with linear chromaticity

The goal here is to prove that assuming a purely linear chromaticity, the expression for the coherent frequency shifts given in Eq. (4.19) for an airbag beam reduces to Chao's Eq. (6.188) derived in Ref. [25]. For a first-order chromaticity  $\xi^{(1)}$ , the betatron frequency changes as  $\Delta\omega_\beta = \omega_{\beta,0}\xi^{(1)}\delta$ . In that case, Eqs. (4.10) and (4.12) are easily evaluated

$$\begin{aligned}\langle\Delta\omega_\beta\rangle_\varphi(r) &= 0 \\ B(r,\varphi) &= \xi^{(1)} \frac{\omega_s \omega_{\beta,0}}{\eta c} r (1 - \cos\varphi).\end{aligned}\tag{A.1}$$

It can be shown, furthermore, that the  $H_l^k(r)$  functions reduce to the Bessel functions of the first kind  $J_l(x)$  under these circumstances

$$\begin{aligned}H_l^k(r) &= \frac{1}{2\pi} \int_0^{2\pi} e^{il\varphi} e^{-\frac{i\omega'}{c} r \cos\varphi} e^{-i\xi^{(1)} \frac{\omega_{\beta,0}}{\eta c} r (1 - \cos\varphi)} d\varphi \\ &= \frac{1}{2\pi} e^{-i\xi^{(1)} \frac{\omega_{\beta,0}}{\eta c} r} \int_0^{2\pi} e^{il\varphi} e^{-i\left(\omega' - \xi^{(1)} \frac{\omega_{\beta,0}}{\eta}\right) \frac{r}{c} \cos\varphi} d\varphi \\ &= i^{-l} e^{-i\xi^{(1)} \frac{\omega_{\beta,0}}{\eta c} r} J_l \left[ \frac{\omega' - \omega_\xi}{c} r \right].\end{aligned}\tag{A.2}$$

with  $\omega' = k\omega_0 + \omega_{\beta,0} + l\omega_s$  (approximating  $\Omega \approx \omega_{\beta,0} + l\omega_s$ ), and  $\omega_\xi = \xi^{(1)}\omega_{\beta,0}/\eta$ . Using the last result on  $H_l^k(r)$  in Eq. (4.19), one finds

$$\Omega^{(l)} - \omega_{\beta,0} - l\omega_s = -i \frac{Ne^2 c}{2\omega_{\beta,0} T_0^2 E} \sum_{k=-\infty}^{\infty} Z_1^\perp(\omega') J_l^2 \left( \frac{\omega' \hat{z}}{c} - \chi \right),\tag{A.3}$$

where  $\chi = \omega_\xi \hat{z}/c$  is the head-tail phase parameter. Equation (A.3) is indeed equivalent to Chao's Eq. (6.188) in Ref. [25].

## A.2 Equivalence of dispersion relation to existing theory

This section demonstrates that the stability diagram theory developed by Scott Berg and Ruggiero in Ref. [28] for detuning with longitudinal action which corresponds to a detuning from second-order chromaticity as explained in [35], is a special solution of Eq. (4.21) derived in Chapter 4. Scott Berg and Ruggiero's dispersion relation reads

$$\begin{aligned} \left(\Delta\Omega_{\text{lin}}^{(l)}\right)^{-1} &= \frac{1}{\mathcal{N}} \int_0^\infty \frac{J_s^{|l|} \lambda(J_s)}{\omega - \omega_\beta(J_s) - l\omega_s} dJ_s, \\ \mathcal{N} &= \int_0^\infty J_s^{|l|} \lambda(J_s) dJ_s, \end{aligned} \quad (\text{A.4})$$

where  $l$  is the azimuthal mode number of the instability under consideration, and  $\lambda$  represents the unperturbed, stationary particle distribution in the longitudinal phase space.  $\omega_\beta(J_s) = \omega_{\beta,0} + \Delta\omega_\beta(J_s)$  describes the betatron frequency dependence on the longitudinal action  $J_s$ . The latter is related to the longitudinal amplitude  $r$  via  $r = \sqrt{2J_s\beta_z}$ . In their paper, Scott Berg and Ruggiero also include a dependence of  $\omega_s$  on  $J_s$ . This has been excluded here, but could be included also in our formalism. Scott Berg and Ruggiero assume in their derivations that: (1) the frequency of the impedance is much smaller than the beam spectrum, and (2) that the longitudinal wakefield term caused by the transverse wakefield can be ignored. The first approximation means that the impedance drops out of the equation, similarly to Section 4.2.2, where a strongly peaked impedance was assumed. The second approximation has also been made in this study when deriving the Vlasov equation in Section 2.2.3. It is valid as long as synchro-betatron resonance conditions are avoided and given that the transverse beam sizes are small enough [25].

The derivations made in Chapter 4 led to the dispersion relation [see Eq. (4.23)]

$$\begin{aligned} \left(\Delta\Omega_{\text{lin}}^{(l)}\right)^{-1} &= \frac{1}{\mathcal{N}} \int_0^\infty \frac{r g_0(r) \left|H_l^{k_0}(r)\right|^2}{\omega - \omega_\beta(r) - l\omega_s} dr, \\ \mathcal{N} &= \int_0^\infty r g_0(r) \left|H_l^{k_0}(r)\right|^2 dr, \end{aligned} \quad (\text{A.5})$$

where all the functions have been defined in the main text. To demonstrate that this equation is equivalent to Eq. (A.4), we start off by approximating the  $H_l^{k_0}(r)$  function. Assuming that the second-order effects from chromaticity accounted for by the phase terms in  $H_l^{k_0}(r)$  can be neglected, and using Eq. (A.2), one obtains

$$H_l^{k_0} \approx i^{-l} e^{-i\xi^{(1)} \frac{\omega_{\beta,0}}{\eta c} r} J_l \left[ \frac{\omega' - \omega_\xi}{c} r \right], \quad (\text{A.6})$$

$$\left|H_l^{k_0}\right|^2 \approx \left|J_l \left[ \frac{\omega' - \omega_\xi}{c} r \right]\right|^2 \quad (\text{A.7})$$

By assumption (1), there is a contribution from the impedance only at low frequencies, meaning that the argument of the Bessel function in the previous equation is small. Hence,  $J_l(x)$  can be expanded

## A.2. Equivalence of dispersion relation to existing theory

around  $x = 0$

$$\begin{aligned} J_l(x) &\approx i^{-l+|l|} \left( \frac{x^{|l|}}{2^{-|l|} \Gamma(1+|l|)} \right) = i^{-l+|l|} \left( \frac{x^{|l|}}{2^{-|l|} |l|!} \right), \\ |J_l(x)|^2 &\approx \frac{x^{2|l|}}{2^{-2|l|} |l|!^2}, \end{aligned} \quad (\text{A.8})$$

since the Gamma function  $\Gamma$  is defined as

$$\Gamma(1+|l|) = |l|!, \text{ for } |l| \in \mathbb{N}_0. \quad (\text{A.9})$$

After changing the integration variable  $r \rightarrow J_s$ , using  $r = \sqrt{2J_s\beta_z}$ , one finds

$$\begin{aligned} \left( \Delta\Omega_{\text{lin}}^{(l)} \right)^{-1} &= \frac{C_l}{\mathcal{N}} \int_0^\infty \frac{g_0(J_s) J_s^{|l|}}{\omega - \omega_\beta(J_s) - l\omega_s} dJ_s, \\ \mathcal{N} &= C_l \int_0^\infty g_0(J_s) J_s^{|l|} dJ_s, \end{aligned} \quad (\text{A.10})$$

with

$$C_l = \frac{\beta_z^{1+|l|} \left[ \frac{\omega' - \omega_\xi}{c} r \right]^2}{4|l|!^2}. \quad (\text{A.11})$$

The constant  $C_l$  drops out of the equation. After redefining  $\mathcal{N}$  accordingly, one indeed reveals Scott Berg and Ruggiero's dispersion relation

$$\begin{aligned} \left( \Delta\Omega_{\text{lin}}^{(l)} \right)^{-1} &= \frac{1}{\mathcal{N}} \int_0^\infty \frac{J_s^{|l|} g_0(J_s)}{\omega - \omega_\beta(J_s) - l\omega_s} dJ_s, \\ \mathcal{N} &= \int_0^\infty J_s^{|l|} g_0(J_s) dJ_s, \end{aligned} \quad (\text{A.12})$$

with  $g_0(J_s) \equiv \lambda(J_s)$ .





# Bibliography

- [1] S. L. Glashow, “Partial Symmetries of Weak Interactions”, Nucl. Phys. **22**, 579–588 (1961).
- [2] S. Weinberg, “A Model of Leptons”, Phys. Rev. Lett. **19**, 1264–1266 (1967).
- [3] Salam, A. and Ward, J. C., “Weak and electromagnetic interactions”, Il Nuovo Cimento **11**, 568–577 (1959).
- [4] F. Englert and R. Brout, “Broken Symmetry and the Mass of Gauge Vector Mesons”, Phys. Rev. Lett. **13**, 321–323 (1964).
- [5] P. W. Higgs, “Broken Symmetries and the Masses of Gauge Bosons”, Phys. Rev. Lett. **13**, 508–509 (1964).
- [6] G. S. Guralnik, C. R. Hagen, and T. W. B. Kibble, “Global Conservation Laws and Massless Particles”, Phys. Rev. Lett. **13**, 585–587 (1964).
- [7] O. S. Brüning, P. Collier, P. Lebrun, S. Myers, R. Ostojic, J. Poole, and P. Proudlock, *LHC Design Report*, CERN Yellow Reports: Monographs, 10.5170/CERN-2004-003-V-1 (CERN, Geneva, Switzerland, 2004).
- [8] H. Bohr and H. B. Nielsen, “Hadron production from a boiling quark soup: A thermodynamical quark model predicting particle ratios in hadronic collisions”, Nucl. Phys. B **128**, 275–293 (1977).
- [9] E. Mobs, *The CERN accelerator complex*, tech. rep. OPEN-PHO-ACCEL-2016-009 (CERN, Geneva, Switzerland, July 2016).
- [10] The ATLAS Collaboration, “Observation of a new particle in the search for the Standard Model Higgs boson with the ATLAS detector at the LHC”, Phys. Lett. B **716**, 1–29 (2012).
- [11] The CMS Collaboration, “Observation of a new boson at a mass of 125 GeV with the CMS experiment at the LHC”, Physics Letters B **716**, 30–61 (2012).
- [12] H. Damerau, A. Funken, R. Garoby, S. Gilardoni, B. Goddard, K. Hanke, A. Lombardi, D. Manglunki, M. Meddahi, B. Mikulec, G. Rumolo, E. Shaposhnikova, M. Vretenar, and J. Coupard, *LHC Injectors Upgrade, Technical Design Report, Vol. I: Protons*, tech. rep. CERN-ACC-2014-0337 (CERN, Geneva, Switzerland, Dec. 2014).
- [13] L. Arnaudon, P. Baudrenghien, M. Baylac, G. Bellodi, Y. Body, J. Borburgh, P. Bourquin, J. Broere, O. Brunner, L. Bruno, et al., *Linac4 Technical Design Report*, tech. rep. CERN-AB-2006-084 (CERN, Geneva, Switzerland, Dec. 2006).
- [14] L. Rossi and O. S. Brüning, *The High Luminosity Large Hadron Collider: the new machine for illuminating the mysteries of Universe*, Advanced series on directions in high energy physics, ISBN: 978-9-81-467546-8 (World Scientific, Hackensack, NJ, 2015).

## Bibliography

---

- [15] CERN, *LHC / HL-LHC plan*, (2017) [Accessed: 14/05/2018].
- [16] CERN, *FCC-hh machine and beam parameters*, (2016) [Accessed: 14/05/2018].
- [17] CERN, *FCC-hh machine and beam parameters (alternative source)*, (2018) [Accessed: 14/05/2018].
- [18] G. Apollinari, I. Béjar Alonso, O. S. Brüning, M. Lamont, and L. Rossi, *High-Luminosity Large Hadron Collider (HL-LHC): Preliminary Design Report*, CERN Yellow Reports: Monographs, ISBN: 978-9-29-083423-6 (CERN, Geneva, Switzerland, 2015).
- [19] F. Zimmermann, “HE-LHC: design status and operation parameters”, *presented at the “Workshop on the physics of HL-LHC, and perspectives at HE-LHC”*, CERN, Geneva, Switzerland, Oct. 2017.
- [20] E. Todesco and F. Zimmermann, eds., *Proceedings, EuCARD-AccNet-EuroLumi Workshop: The High-Energy Large Hadron Collider (HE-LHC)*, EUCARD-CON-2011-001, CERN-2011-003, CERN (Geneva, Switzerland, 2011).
- [21] E. Shaposhnikova, “RF system for FCC-hh”, *presented at the “FCC-hh impedance and beam screen workshop”*, CERN, Geneva, Switzerland, Mar. 2017.
- [22] E. Shaposhnikova, *Longitudinal beam parameters during acceleration in the LHC*, tech. rep. LHC-Project-Note-242 (CERN, Geneva, Switzerland, Dec. 2000).
- [23] J. F. Esteban Müller, “Longitudinal intensity effects in the CERN Large Hadron Collider”, CERN-THESIS-2016-066, PhD thesis (École Polytechnique Fédérale de Lausanne, Switzerland, July 2016).
- [24] L. D. Landau, “On the vibration of the electronic plasma”, *Zh. Eksp. Teor. Fiz.* **16**, 574 (1946), [*J. Phys. USSR* **10**, 25 – 34 (1946)].
- [25] A. W. Chao, *Physics of collective beam instabilities in high energy accelerators*, Wiley Series in Beam Physics and Accelerator Technology, ISBN: 978-0-47-155184-3 (Wiley, 1993).
- [26] L. R. Carver, J. Barranco, N. Biancacci, X. Buffat, W. Höfle, G. Kotzian, T. Lefèvre, T. Levens, E. Métral, T. Pieloni, et al., “Current Status of Instability Threshold Measurements in the LHC at 6.5 TeV”, in *Proc. of International Particle Accelerator Conference 2016 (IPAC’16)*, Busan, Korea (June 2016), pp. 1434–1437.
- [27] E. Métral, G. Arduini, L. Barranco Navarro, X. Buffat, L. R. Carver, G. Iadarola, K. Li, T. Pieloni, A. Romano, G. Rumolo, et al., “Measurement and Interpretation of Transverse Beam Instabilities in the CERN Large Hadron Collider (LHC) and Extrapolations to HL-LHC”, in *Proc. of ICFA Advanced Beam Dynamics Workshop on High-Intensity and High-Brightness Hadron Beams 2016 (HB’16)*, Malmö, Sweden (July 2016), pp. 254–259.
- [28] J. Scott Berg and F. Ruggiero, “Stability diagrams for Landau damping”, in *Proc. of Particle Accelerator Conference 1997 (PAC’97)*, Vancouver (British Columbia), Canada (May 1997), pp. 1712–1714.
- [29] A. Grudiev, “Radio frequency quadrupole for Landau damping in accelerators”, *Phys. Rev. ST Accel. Beams* **17**, 011001 (2014).
- [30] V. Shiltsev, Y. Alexahin, A. Burov, and A. A. Valishev, “Landau damping of beam instabilities by electron lenses”, *Phys. Rev. Lett.* **119**, 134802 (2017).

- [31] K. Li, W. Höfle, G. Rumolo, J. Cesaratto, J. Dusatko, J. Fox, M. Pivi, K. Pollock, C. Rivetta, and O. Turgut, “Modelling and Studies for a Wideband Feedback System for Mitigation of Transverse Single Bunch Instabilities”, in Proc. of International Particle Accelerator Conference 2013 (IPAC’13), Shanghai, China (May 2013), pp. 3019–3021.
- [32] K. Li, H. Bartosik, E. Bjorsvik, J. Fox, W. Höfle, G. Kotzian, C. Rivetta, B. Salvant, and O. Turgut, “Wideband feedback system prototype validation”, CERN Proceedings **2**, 95–102 (2017).
- [33] M. Schenk, A. Grudiev, K. Li, and K. Papke, “Analysis of transverse beam stabilization with radio frequency quadrupoles”, Phys. Rev. Accel. Beams **20**, 104402 (2017).
- [34] M. Schenk, X. Buffat, K. Li, and A. Maillard, “Vlasov description of the effects of nonlinear chromaticity on transverse coherent beam instabilities”, Phys. Rev. Accel. Beams **21**, 084402 (2018).
- [35] M. Schenk, X. Buffat, L. R. Carver, R. De Maria, K. Li, and E. Métral, “Experimental stabilization of transverse collective instabilities in the LHC with second order chromaticity”, Phys. Rev. Accel. Beams **21**, 084401 (2018).
- [36] S. Y. Lee, *Accelerator Physics*, Third edition, ISBN: 978-9-81-437494-1 (World Scientific, Singapore, 2011).
- [37] E. J. Wilson, *An introduction to particle accelerators*, ISBN: 978-0-19-850829-8 (Oxford University Press, Oxford, United Kingdom, 2001).
- [38] S. Peggs and T. Satogata, “Octupoles, Detuning and Slow Extraction”, in *Introduction to Accelerator Dynamics*, ISBN: 978-1-31-645930-0 (Cambridge University Press, Cambridge, 2017) Chap. 10, pp. 107–115.
- [39] E. D. Courant, M. S. Livingston, and H. S. Snyder, “The Strong-Focusing Synchrotron – A New High Energy Accelerator”, Phys. Rev. **88**, 1190–1196 (1952).
- [40] G. W. Hill, “On the part of the motion of the lunar perigee which is a function of the mean motions of the sun and moon”, Acta Math. **8**, 1–36 (1886).
- [41] G. Floquet, “Sur les équations différentielles linéaires à coefficients périodiques”, Annales scientifiques de l’École Normale Supérieure **12**, 47–88 (1883).
- [42] H. Wiedemann, *Particle Accelerator Physics*, Fourth edition, ISBN: 978-3-319-18317-6 (Springer International Publishing, Berlin, Germany, 2015).
- [43] A. Piwinski, “Synchro-betatron resonances”, in Proc. of International Conference on High-Energy Accelerators 1980, Geneva, Switzerland (July 1980), pp. 638–649.
- [44] E. M. McMillan, “The Synchrotron – A Proposed High Energy Particle Accelerator”, Phys. Rev. **68**, 143–144 (1945).
- [45] V. I. Veksler, “A New Method of Accelerating Relativistic Particles”, Dokl. Akad. Nauk SSSR **43**, 346–348 (1944), (in Russian).
- [46] V. I. Veksler, “About the New Method of Accelerating Relativistic Particles”, Dokl. Akad. Nauk SSSR **44**, 393–396 (1944), (in Russian).
- [47] A. M. Sessler, *Collective Phenomena in Accelerators*, tech. rep. LBL-1326 (Berkeley, California, Sept. 1972).
- [48] B. W. Zotter and S. A. Kheifets, *Impedances and Wakes in High-Energy Particle Accelerators*, ISBN: 978-9-81-44991-8 (World Scientific, Singapore, 1998).

## Bibliography

---

- [49] B. Salvant, “Impedance model of the CERN SPS and aspects of LHC single-bunch stability”, CERN-THESIS-2010-087, PhD thesis (École Polytechnique Fédérale de Lausanne, Switzerland, Mar. 2010).
- [50] T. Levens, K. Lasocha, and T. Lefèvre, “Recent Developments for Instability Monitoring at the LHC”, in Proc. of International Beam Instrumentation Conference 2016 (IBIC’16), Barcelona, Spain (Sept. 2016), pp. 852–855.
- [51] V. V. Danilov and E. A. Perevedentsev, “Feedback system for elimination of the transverse mode coupling instability”, Nucl. Instrum. Methods Phys. Res. A **391**, 77–92 (1997).
- [52] X. Buffat, “Transverse beams stability studies at the Large Hadron Collider”, CERN-THESIS-2014-246, PhD thesis (École Polytechnique Fédérale de Lausanne, Switzerland, Jan. 2015).
- [53] S. White, X. Buffat, N. Mounet, and T. Pieloni, “Transverse mode coupling instability of colliding beams”, Phys. Rev. ST Accel. Beams **17**, 041002 (2014).
- [54] X. Buffat, “The circulant matrix formalism and the role of beam-beam effects in coherent instabilities”, *presented at the* “International Workshop on Impedances and Beam Instabilities in Particle Accelerators”, Benevento, Italy, Sept. 2017.
- [55] W. Herr, “Introduction to Landau Damping”, in CERN Accelerator School (CAS): Advanced Accelerator Physics Course 2013, Trondheim, Norway (Aug. 2014), pp. 377–404.
- [56] X. Buffat, W. Herr, N. Mounet, T. Pieloni, and S. White, “Stability diagrams of colliding beams in the Large Hadron Collider”, Phys. Rev. ST Accel. Beams **17**, 111002 (2014).
- [57] S. Y. Lee, “Transverse Motion”, in *Accelerator Physics*, Third edition, ISBN: 978-9-81-437494-1 (World Scientific, Singapore, 2011) Chap. 2, pp. 33–227.
- [58] A. Bazzani, G. Servizi, E. Todesco, and G. Turchetti, *A normal form approach to the theory of nonlinear betatronic motion*, CERN Yellow Reports: Monographs, ISBN: 978-9-29-083059-7 (CERN, Geneva, Switzerland, 1994).
- [59] S. C. Leemann and A. Streun, “Perspectives for future light source lattices incorporating yet uncommon magnets”, Phys. Rev. ST Accel. Beams **14**, 030701 (2011).
- [60] J. Gareyte, J.-P. Koutchouk, and F. Ruggiero, *Landau damping, dynamic aperture and octupoles in LHC*, tech. rep. LHC-Project-Report-91 (CERN, Geneva, Switzerland, Feb. 1997).
- [61] E. Métral, T. Argyropoulos, H. Bartosik, N. Biancacci, X. Buffat, J. F. Esteban Müller, W. Herr, G. Iadarola, A. Lasheen, K. Li, et al., “Beam Instabilities in Hadron Synchrotrons”, IEEE Transactions on Nuclear Science **63**, 1001–1050 (2016).
- [62] G. Rumolo and F. Zimmermann, “Electron cloud simulations: beam instabilities and wakefields”, Phys. Rev. ST Accel. Beams **5**, 121002 (2002).
- [63] C. Zannini, “Electromagnetic Simulation of CERN accelerator Components and Experimental Applications”, CERN-THESIS-2013-076, PhD thesis (École Polytechnique Fédérale de Lausanne, Switzerland, Mar. 2013).
- [64] R. Bartolini and F. Schmidt, *A Computer Code for Frequency Analysis of Non-Linear Betatron Motion*, tech. rep. SL-Note-98-017-AP (CERN, Geneva, Switzerland, Feb. 1998).
- [65] M. Schenk, X. Buffat, L. R. Carver, A. Grudiev, K. Li, A. Maillard, E. Métral, and K. Papke, “RF Quadrupole Structures for Transverse Landau Damping in Circular Accelerators”, in Proc. of International Particle Accelerator Conference 2017 (IPAC’17), Copenhagen, Denmark (May 2017), pp. 2516–2519.

- [66] M. Schenk, A. Grudiev, K. Li, and K. Papke, “Use of RF Quadrupole Structures to Enhance Stability in Accelerator Rings”, in Proc. of ICFA Advanced Beam Dynamics Workshop on High-Intensity and High-Brightness Hadron Beams 2016 (HB’16), Malmö, Sweden (Aug. 2016), pp. 505–510.
- [67] A. Grudiev, K. Li, and M. Schenk, “Radio Frequency Quadrupole for Landau Damping in Accelerators: Analytical and Numerical Studies”, in Proc. of ICFA Advanced Beam Dynamics Workshop on High-Intensity and High-Brightness Hadron Beams 2014 (HB’14), East Lansing (Michigan), USA (Apr. 2014), pp. 315–319.
- [68] K. Papke and A. Grudiev, “Design of an rf quadrupole for Landau damping”, *Phys. Rev. Accel. Beams* **20**, 082001 (2017).
- [69] Benedikt, M. and Zimmermann, F., “Future Circular Colliders”, in Proc. of International School of Physics “Enrico Fermi”: Future Research Infrastructures: Challenges and Opportunities, Varenna, Italy (July 2015), pp. 73–80.
- [70] M. Schenk, “RF quadrupole for Landau damping for HL-LHC”, *presented at the “72nd HiLumi WP2 Meeting”*, CERN, Geneva, Switzerland, Aug. 2016.
- [71] I. M. Kapchinski and V. A. Tepliakov, “Linear Ion Accelerator with Spatially Homogeneous Strong Focusing”, *Prib. Tekh. Eksp.* **19** (1970).
- [72] W. K. H. Panofsky and W. A. Wenzel, “Some Considerations Concerning the Transverse Deflection of Charged Particles in Radio-Frequency Fields”, *Rev. Sci. Inst.* **27** (1956).
- [73] V. V. Danilov, “Increasing the transverse mode coupling instability threshold by RF quadrupole”, *Phys. Rev. ST Accel. Beams* **1**, 041301 (1998).
- [74] E. A. Perevedentsev and A. A. Valishev, “Synchrotron dynamics with a radio-frequency quadrupole”, in Proc. of European Particle Accelerator Conference 2002 (EPAC’02), Paris, France (June 2002), pp. 1574–1576.
- [75] N. Mounet, “The LHC Transverse Coupled-Bunch Instability”, CERN-THESIS-2012-055, PhD thesis (École Polytechnique Fédérale de Lausanne, Switzerland, Mar. 2012).
- [76] M. Schenk, L. R. Buffat X. Carver, K. Li, A. Maillard, and E. Métral, “Experiments and Theory on Beam Stabilization with Second-Order Chromaticity”, in Proc. of ICFA Advanced Beam Dynamics Workshop on High-Intensity and High-Brightness Hadron Beams 2018 (HB’18), Daejeon, Korea (June 2018), pp. 32–37.
- [77] E. Métral, B. Salvant, and N. Mounet, “Stabilization of the LHC single bunch transverse instability at high-energy by Landau octupoles”, in Proc. of International Particle Accelerator Conference 2011 (IPAC’11), San Sebastián, Spain (Sept. 2011), pp. 775–777.
- [78] V. Kornilov and O. Boine-Frankenheim, “Landau damping and tune-spread requirements for transverse beam stability”, in Proc. of International Particle Accelerator Conference 2018 (IPAC’18), Vancouver (British Columbia), Canada (Apr. 2018), pp. 3168–3171.
- [79] CERN, *Methodical Accelerator Design (MAD)*.
- [80] R. Calaga, E. Jensen, G. Burt, and A. Ratti, “Crab Cavity Development”, in *The High Luminosity Large Hadron Collider: the new machine for illuminating the mysteries of Universe*, Advanced series on directions in high energy physics, ISBN: 978-9-81-467546-8 (World Scientific, Hackensack, NJ, 2015) Chap. 7, pp. 137–156.

## Bibliography

---

- [81] J. Laskar, “Introduction to Frequency Map Analysis”, in *Hamiltonian Systems with Three or More Degrees of Freedom*, edited by C. Simó, ISBN: 978-9-40-114673-9 (Springer Netherlands, Dordrecht, 1999), pp. 134–150.
- [82] G. Ripken and F. Schmidt, *A Symplectic six-dimensional thin lens formalism for tracking*, tech. rep. CERN-SL-95-12-AP, DESY-95-063 (CERN, Geneva, Switzerland, Apr. 1995).
- [83] F. Schmidt et al., *SixTrack User Manual – Single Particle Tracking Code Treating Transverse Motion with Synchrotron Oscillations in a Symplectic Manner*, tech. rep. CERN-SL-94-56-AP (CERN, Geneva, Switzerland, Nov. 2017).
- [84] P. Collier, K. Cornelis, A. Hofmann, S. Myers, and H. Schmickler, “Experimental Observation of Synchro-Betatron Resonances in LEP”, in Proc. of European Particle Accelerator Conference 1994 (EPAC’94), London, United Kingdom (July 1994), pp. 1063–1065.
- [85] P. Collier, K. Cornelis, S. Myers, and H. Schmickler, “Synchro-Betatron Resonances in LEP”, in Proc. of European Particle Accelerator Conference 1996 (EPAC’96), Barcelona, Spain (June 1996), pp. 418–420.
- [86] Y. Funakoshi, “Operational experience with crab cavities at KEKB”, in ICFA Mini-Workshop on Beam-Beam Effects in Hadron Colliders, CERN, Geneva, Switzerland (Mar. 2013), pp. 27–36.
- [87] E. H. Maclean, “Modelling and correction of the non-linear transverse dynamics of the LHC from beam-based measurements”, CERN-THESIS-2014-135, PhD thesis (Hertford College, University of Oxford, Oxford, United Kingdom, 2014).
- [88] E. H. Maclean, R. Tomás, F. Schmidt, and T. H. B. Persson, “Measurement of nonlinear observables in the Large Hadron Collider using kicked beams”, Phys. Rev. ST Accel. Beams **17**, 081002 (2014).
- [89] E. H. Maclean, “LHC Single Beam DA: measurements vs simulations”, presented at the “ICFA Mini-Workshop on Dynamic Apertures of Circular Accelerators”, Beijing, China, Nov. 2017.
- [90] J. Barranco García, R. De Maria, A. Grudiev, R. Tomás García, R. B. Appleby, and D. R. Brett, “Long term dynamics of the high luminosity Large Hadron Collider with crab cavities”, Phys. Rev. Accel. Beams **19**, 101003 (2016).
- [91] L. R. Carver, M. Schenk, R. De Maria, K. Li, D. Amorim, N. Biancacci, X. Buffat, E. H. Maclean, E. Métral, K. Lasocha, et al., *MD1831: Single Bunch Instabilities with Q” and Non-Linear Corrections*, tech. rep. CERN-ACC-NOTE-2017-0012 (CERN, Geneva, Switzerland, Feb. 2017).
- [92] M. Schenk, D. Amorim, N. Biancacci, X. Buffat, L. R. Carver, R. De Maria, K. Li, E. Métral, and B. Salvant, “Practical Stabilisation of Transverse Collective Instabilities with Second Order Chromaticity in the LHC”, in Proc. of International Particle Accelerator Conference 2017 (IPAC’17), Copenhagen, Denmark (May 2017), pp. 4477–4480.
- [93] F. C. Iselin, *The MAD Program (Methodical Accelerator Design) Version 8.13/8, Physical Methods Manual*, tech. rep. SL-92-199 (CERN, Geneva, Switzerland, Sept. 1994).
- [94] S. D. Fartoukh, *Second order chromaticity correction of LHC V6.0 at collision*, tech. rep. CERN-LHC-Project-Report-308 (CERN, Geneva, Switzerland, Oct. 1999).
- [95] F. Schmidt, E. Forest, and E. McIntosh, *Introduction to the polymorphic tracking code: Fibre bundles, polymorphic Taylor types and “Exact tracking”*, tech. rep. CERN-SL-2002-044-AP. KEK-REPORT-2002-3 (CERN, Geneva, Switzerland, July 2002).

- 
- [96] M. Gasior and R. Jones, *The principle and first results of betatron tune measurement by direct diode detection*, tech. rep. LHC-Project-Report-853 (CERN, Geneva, Switzerland, Aug. 2005).
- [97] L. R. Carver, D. Amorim, N. Biancacci, X. Buffat, G. Iadarola, K. Lasocha, K. Li, T. Levens, E. Métral, B. Salvant, and C. Tambasco, *MD1228: Validation of Single Bunch Stability Threshold & MD1751: Instability Studies with a Single Beam*, tech. rep. CERN-ACC-NOTE-2017-0013 (CERN, Geneva, Switzerland, Feb. 2017).
- [98] M. Schenk, S. D. Fartoukh, K. Li, L. Malina, E. Métral, and R. Tomás Garcia, *MD2190: Q" Stabilization during injection*, tech. rep. CERN-ACC-NOTE-2018-0003 (CERN, Geneva, Switzerland, Jan. 2018).
- [99] H. Bartosik, "Beam dynamics and optics studies for the LHC injectors upgrade", CERN-THESIS-2013-257, PhD thesis (Technische Universität, Vienna, Austria, Oct. 2013).
- [100] H. Bartosik, G. Arduini, T. Argyropoulos, T. Bohl, S. Cettour-Cave, K. Cornelis, J. F. Esteban Müller, W. Hofle, Y. Papaphilippou, G. Rumolo, B. Salvant, and E. Shaposhnikova, "Increasing instability thresholds in the SPS by lowering transition energy", in Proc. of International Particle Accelerator Conference 2012 (IPAC'12), New Orleans (Louisiana), USA (May 2012), pp. 3096–3098.
- [101] H. Bartosik, G. Arduini, and Y. Papaphilippou, "Optics considerations for lowering transition energy in the SPS", in Proc. of International Particle Accelerator Conference 2011 (IPAC'11), San Sebastián, Spain (Sept. 2011), pp. 619–621.
- [102] H. Bartosik, V. Kain, A. Oeftiger, M. Schenk, F. Schmidt, and M. Titze, "Impact of remnant fields on non-linear chromaticity in the SPS", *presented at the "MSWG meeting 2016 #12"*, Sept. 2016.
- [103] F. Velotti, H. Bartosik, J. Bauche, M. Buzio, K. Cornelis, M. Fraser, and V. Kain, "Investigation of the Remanent Field of the SPS Main Dipoles and Possible Solutions for Machine Operation", in Proc. of International Particle Accelerator Conference 2017 (IPAC'17), Copenhagen, Denmark (May 2017), pp. 4069–4072.
- [104] G. Kruk, S. Deghaye, M. Lamont, M. Misiowiec, and W. Sliwinski, "LHC Software Architecture [LSA] – Evolution toward LHC Beam Commissioning", in Proc. of International Conference on Accelerator and Large Experimental Physics Control Systems 2007 (ICALEPCS'07), Knoxville (Tennessee), USA (Oct. 2007), pp. 307–309.
- [105] G. Arduini, A. Faus-Golfe, and F. Zimmermann, *Measurements and Modelling of Nonlinear Chromaticity and Detuning with Amplitude at 26 GeV*, tech. rep. SL-Note-2001-030-MD (CERN, Geneva, Switzerland, Aug. 2001).
- [106] R. Tomás, G. Arduini, R. Calaga, A. Faus-Golfe, G. Rumolo, and F. Zimmermann, "Improved Algorithms to determine the Non-Linear Optics Model of the SPS from Non-Linear Chromaticity", in Proc. of Particle Accelerator Conference 2007 (PAC'07), Albuquerque (New Mexico), USA (June 2007), pp. 4231–4233.
- [107] H. Bartosik, A. Oeftiger, M. Schenk, F. Schmidt, and M. Titze, "Improved Methods for the Measurement and Simulation of the CERN SPS Non-linear Optics", in Proc. of International Particle Accelerator Conference 2016 (IPAC'16), Busan, Korea (June 2016), pp. 3464–3467.
- [108] C. Zannini, H. Bartosik, G. Rumolo, and B. Salvant, "SPS: impedance model and instability in the transverse plane", *presented at the "LIU Day 2014"*, Apr. 2014.

## Bibliography

---

- [109] C. Zannini, H. Bartosik, G. Iadarola, G. Rumolo, and B. Salvant, “Benchmarking the SPS transverse impedance model: headtail growth rates”, *presented at the “LIU-SPS Beam Dynamics Working Group Meeting”*, Oct. 2014.
- [110] H. Burkhardt, G. Rumolo, and F. Zimmermann, *Measurements of SPS Single-Bunch Coherent Tune Shifts and Head-Tail Growth Rates in the Year 2001*, tech. rep. CERN-SL-Note-2001-043-MD (CERN, Geneva, Switzerland, Dec. 2001).



# Acronyms

BBQ	base-band tune metre. 98, 100
BPM	beam position monitor. 116, 129, 130, 133
BSM	Physics Beyond the Standard Model. 1, 2, 4
BTF	beam transfer function. 34
c.m.	centre-of-mass. 2, 4, 5, 83
CERN	Centre Européen pour la Recherche Nucléaire (European Organization for Nuclear Research). 1–4, 8, 11, 38, 40, 41, 61, 90, 111, 125
CMM	circulant matrix model. 31, 32, 40, 75, 76
DA	dynamic aperture. 91, 92
DC	direct current. 99, 119, 131
FCC	Future Circular Collider project. 5
FCC-ee	Future Circular Collider (electron-positron configuration). 5
FCC-hh	Future Circular Collider (hadron-hadron configuration). 5, 7, 9, 41, 42, 48, 49, 71, 77, 83–85, 91–93
FMA	frequency map analysis. 88–90
HE-LHC	High Energy Large Hadron Collider. 5, 41, 42, 49, 77
HL-LHC	High Luminosity Large Hadron Collider. 4, 5, 7, 41, 42, 48, 49, 71, 72, 77, 78, 81, 82, 86, 90, 92, 93, 112
LEP	Large Electron Positron collider. 90
LHC	Large Hadron Collider. 2–9, 19, 28, 46–48, 51–53, 69, 71, 73–79, 81–83, 91–93, 95–105, 107–109, 111, 114, 116, 131, 136
LIU	LHC Injectors Upgrade. 4, 112
LOD	SPS defocusing Landau octupoles. 112, 113, 116, 117, 120, 122
LOE	SPS extraction Landau octupoles. 112–114, 116, 117, 119–122

## Acronyms

---

LOF	SPS focusing Landau octupoles. 112, 114, 116, 117, 120, 121
LSA	LHC Software Architecture. 114–116, 124, 126, 130–132
MS	main sextupoles. 96, 104
QPH	SPS main sextupole knob (LSA) to control horizontal first-order chromaticity. 124, 125, 133–135
rf	radio-frequency. 6–12, 19, 20, 22–24, 26, 33, 38, 39, 41–53, 55, 56, 69–73, 76–93, 98–100, 108, 109, 119, 131, 133
rms	root mean square. 4, 7, 16, 17, 39, 47–49, 52, 77
SBR	synchro-betatron resonances. 86–90
SM	Standard Model of Particle Physics. 1, 2, 4, 5
SPS	Super Proton Synchrotron. 2, 3, 8–10, 27, 61, 87–91, 93, 99, 111–116, 118–121, 123–131, 134–136
TMCI	Transverse Mode Coupling Instability. 6, 26–28, 45, 57, 86, 112

# Michael Schenk

LinkedIn | [michuschenk@gmail.com](mailto:michuschenk@gmail.com)  
211C Rue Chantepie, 01280 Prévessin-Moëns, France

Swiss citizen  
born 14/10/1988

## Education

**Doctoral studies in Accelerator Physics** since 08/2015  
CERN, Geneva and EPFL, Lausanne (CH)

Thesis title: *A novel approach to Landau damping of transverse collective instabilities in future hadron colliders*

Supervisors: Prof. L. Rivkin (EPFL), Dr. G. Rumolo & Dr. K. Li (CERN)

- Studied novel technique to improve beam stability in future colliders, analytically, numerically, and experimentally.
- Proposed, organised, and carried out experiments in the LHC and SPS.
- Realised data processing and visualisation in Python and performed analysis of experiments demonstrating good agreement with models (PyHEADTAIL, MAD-X).
- Authored three peer-reviewed articles and gave invited talks at international conferences.

**Master of Science in Applied Physics** 09/2011 - 09/2014  
*Summa cum laude* and Springer 'BestMasters' award  
Laboratory for High-Energy Physics, University of Bern (CH)

Thesis title: *Study of cosmic muon and UV laser induced events with a large liquid argon TPC*  
Grade: 6.0/6.0

Supervisors: Prof. A. Ereditato, Prof. I. Kreslo

- Studied and operated the ARGONTUBE prototype detector for 3D reconstruction of charged particle tracks and achieved record electron drift distance.
- Carried responsibility in planning of detector runs as member of a small R&D team.
- Developed event reconstruction tool with pattern recognition algorithm in CUDA.

**Bachelor of Science in Physics** 09/2008 - 09/2011  
*Summa cum laude*  
University of Bern (CH)

## Work and Teaching Experience

**Short-Term Invited Fellow** (three weeks) 07/2017  
with Prof. Y.H. Chin at KEK & J-PARC, Tsukuba (J)

- Introduced KEK beam dynamics group to PyHEADTAIL & PyECLOUD tracking codes.
- Gave two seminars on beam dynamics modelling.

**Teaching assistant** 09/2016 - 01/2017  
for Prof. L. Rivkin, EPFL, Lausanne (CH)

- Guided 20 master students through exercise sessions (weekly), gave MAD-X tutorial, and prepared and corrected final exams.
- Prepared and delivered a two-hour guest lecture on accelerator physics at EPFL.

**Technical student** 05/2014 - 06/2015  
CERN, Geneva (CH)

- Co-developed collective effects and tracking modules for PyHEADTAIL code in Python.

## Work and Teaching Experience *cont.*

<b>Teaching assistant</b> Laboratory for High-Energy Physics, University of Bern (CH)	10/2012 - 02/2014
<ul style="list-style-type: none"><li>• Supervised twelve undergraduate students during their physics lab sessions.</li><li>• Responsible to receive lab reports in due time, and to correct and grade them.</li></ul>	
<b>Summer Student</b> CERN, Geneva (CH)	06/2012 - 09/2012
<ul style="list-style-type: none"><li>• Implemented test module in C++ for multiple scattering models in Geant4.</li></ul>	
<b>Language stay</b> EF language school, Bristol (UK)	03/2012 - 06/2012

## Languages

<b>German</b>	Native language
<b>English</b>	Fluent in reading, writing, and speaking <i>Grade C2 in EFCELT exam (7<sup>th</sup> June 2012)</i>
<b>French</b>	Proficient in reading and writing; conversant in speaking <i>Grade 5.5/6.0, Matura level (21<sup>st</sup> June 2007)</i>
<b>Greek</b>	Basic knowledge

## IT Skills

<b>Programming</b>	C/C++ ( <i>good knowledge</i> ), Nvidia CUDA ( <i>basic knowledge</i> ), Python & scientific libraries ( <i>excellent knowledge</i> ), Shell scripting, Tensorflow ( <i>basic knowledge</i> )
<b>Devel. tools</b>	git, github, spyder
<b>Software tools</b>	Geant4, MAD-X, Mathematica, MatLab, Octave, PyHEADTAIL, Root
<b>Office</b>	L <sup>A</sup> T <sub>E</sub> X, Microsoft Office
<b>OS</b>	Linux, Microsoft Windows

## Selection of Journal Publications

08/2018	<b>M. Schenk</b> , X. Buffat, K. Li, A. Maillard, <i>Vlasov description of the effects of nonlinear chromaticity on transverse coherent beam instabilities</i> , <a href="#">Phys. Rev. Accel. Beams <b>21</b>, 084402</a> .
08/2018	<b>M. Schenk</b> , X. Buffat, L. R. Carver, R. De Maria, K. Li, E. Métral, <i>Experimental stabilization of transverse collective instabilities in the LHC with second order chromaticity</i> , <a href="#">Phys. Rev. Accel. Beams <b>21</b>, 084401</a> .
04/2018	L. R. Carver, X. Buffat, K. Li, E. Métral, and <b>M. Schenk</b> , <i>Transverse beam instabilities in the presence of linear coupling in the Large Hadron Collider</i> , <a href="#">Phys. Rev. Accel. Beams <b>21</b>, 044401</a> .
10/2017	<b>M. Schenk</b> , A. Grudiev, K. Li, and K. Papke, <i>Analysis of transverse beam stabilization with radio frequency quadrupoles</i> , <a href="#">Phys. Rev. Accel. Beams <b>20</b>, 104402</a> .
01/2015	<b>M. Schenk</b> , <i>Studies with a liquid argon Time Projection Chamber – Addressing technological challenges of large-scale detectors</i> , Springer BestMasters 2014 (book).

*A complete overview of my publications and conference talks is available on ORCID (ID: 0000-0001-9438-812X).*



